2020

Multiscale Modeling of Structure-Function Relationships of Organic Semiconductors

Shi Li

University of Kentucky, sli259@g.uky.edu
Author ORCID Identifier:
https://orcid.org/0000-0003-0505-6751
Digital Object Identifier: https://doi.org/10.13023/etd.2020.240

Right click to open a feedback form in a new tab to let us know how this document benefits you.

MULTISCALE MODELING OF STRUCTURE–FUNCTION
RELATIONSHIPS OF ORGANIC SEMICONDUCTORS

_____

DISSERTATION

_____

A dissertation submitted in partial fulfillment of the
requirements for the degree of Doctor of Philosophy in the
College of Arts and Sciences
at the University of Kentucky

By

Shi Li

Lexington, Kentucky

Co-Director: Dr. Chad Risko, Professor of Chemistry

and   Dr. John Anthony, Professor of Chemistry

Lexington, Kentucky

2020

ABSTRACT OF DISSERTATION

MULTISCALE MODELING OF STRUCTURE–FUNCTION

RELATIONSHIPS OF ORGANIC SEMICONDUCTORS

While optoelectronic devices built from organic semiconductors (OSC) continue to find their way into the commercial landscape, there remain numerous challenges to overcome to supplant traditional semiconductors in many technologies. Chief among these are low performance metrics relative to devices with conventional semiconductors and device stability. In order to overcome these challenges, a wide range of new OSC and processing technologies have been developed. However, there remains limited fundamental understanding of the relationship between molecular structure, packing in the solid state, and the resulting materials properties. Here, we make use of multiscale molecular models and utilize classical all-atom molecular dynamic (MD) simulations and quantum-chemical density functional theory (DFT) to explore the molecular structure-function relationships. Our results have provided distinctive insights into how the chemistries and processing of the OSC impact the material characteristics.

KEYWORDS: Organic Semiconductor, Molecular Dynamics, Density Functional Theory

_____Shi Li_____

_____04/01/2020_____

MULTISCALE MODELING OF STRUCTURE–FUNCTION

RELATIONSHIPS OF ORGANIC SEMICONDUCTORS

By

Shi Li

Chad Risko
Co-Director of Dissertation

John Anthony
Co-Director of Dissertation

YinanWei
Director of Graduate Studies

04/01/2020

ACKNOWLEDGMENTS

TABLE OF CONTENTS

LIST OF TABLES

LIST OF FIGURES

xiii

CHAPTER 1

ORGNIC SEMICONDUCTORS FOR ELECTRONIC APPLICATIONS –

ADVANTAGES AND CHALLENGES

1.1   Organic semiconductors (OSC)

Since the first discovery in the 1940s,[1] organic semiconductors (OSC) have received substantial academic and commercial interest. Electronic devices made with OSC as the active layer can be lighter, more flexible, and less costly than their inorganic semiconductor counterparts. OSC can be processed at low temperatures, reducing energy consumption during device development, and solution-based printing of OSC can enable large-scale fabrication. Perhaps most importantly, the electronic and optical properties of the organic molecules that comprise OSC can be synthetically tailored to enable a wide range of functionality. These advantages make OSC attractive replacements for traditional inorganic semiconductors in electronic applications, including organic field-effect transistors (OFET),[2, 3] light-emitting diodes (OLED),[4] and photovoltaics (OPV).[5, 6]

Despite the potential advantages of OSC, there remain many scientific and technological challenges that need to be overcome. One such challenge is long-term chemical stability.[7] OSC can degrade when exposed to light, heat, or react with the oxygen or water in the environment,[7, 8] limiting the material lifetime. A second challenge relates to the generally small charge-carrier mobilities (μ) that OSC possess when compared to inorganic semiconductors. Charge-carrier mobility, which is a critical factor in electronic devices, is defined as the speed (cm/s) of the charge carrier moving through the material under an applied electric field (V/cm), therefore, the units of μ are $cm^2/(Vs)$. Generally, for an

OSC to be competitive with at least amorphous silicon, μ must approach or surpass 1 $cm^2/(Vs)$. This metric, though, is not readily achieved in OSC. As opposed to the band-like electronic structures of inorganic semiconductors, which arise from the overlap of atomic orbitals (one-electron wavefunctions), the important electronic characteristics of OSC begin with the π molecular orbitals (linear combination of atomic orbitals) of the building blocks. In lieu of the covalent or ionic bonds in inorganic semiconductors that lead to large wavefunction overlap among neighbors (and the formation of electronic bands), the molecular building blocks of OSC are held together by relatively weak non-covalent intermolecular interactions that impact molecular packing, dynamic motion of the molecules in the solid state, and intermolecular electronic coupling. These weaker intermolecular interactions generally necessitate that charge-carrier transport not be treated in the band regime as in inorganic semiconductors, but rather the charge-hopping regime, or variations thereof. Hence, there is a tremendous need to be able to control not only the molecular characteristics of the OSC components, but also how these components pack in the solid state to ensure sufficient electronic communication amongst neighboring molecules to allow for efficient charge-carrier transport.

1.2 Molecular structure and crystal packing

While there are numerous solid-state packing configurations available to OSC, from completely amorphous to varied crystalline motifs, there are four packing structures that are often discussed in OSC, as shown in Figure 1.1. Here, packing motif A has a perfect co-facial arrangement among adjacent molecules, which is expected to present the largest electronic couplings due to the maximized π orbital overlap. However, this configuration is not realistic in OSC due to strong exchange repulsion interactions. Other packing motifs

such as slipped stack (B) and brickwork (C) can both present fairly large π-π overlap. A critical difference is that the slipped-stack structure presents only one-dimensional charge-carrier pathways, while the brickwork packing motif can provide a two-dimensional pathway for charges to follow; empirically, materials with brickwork packing structures show better μ when compared to slipped-stack. On the contrary, the herringbone packing motif (D) has no co-facial overlap of the π orbitals on neighboring molecules due to the edge-to-face packing structure. However, there remains sufficient overlap of the wavefunctions in materials with these configurations that molecules such as C8-BTBT have among the largest performance metrics in OFET.[7]
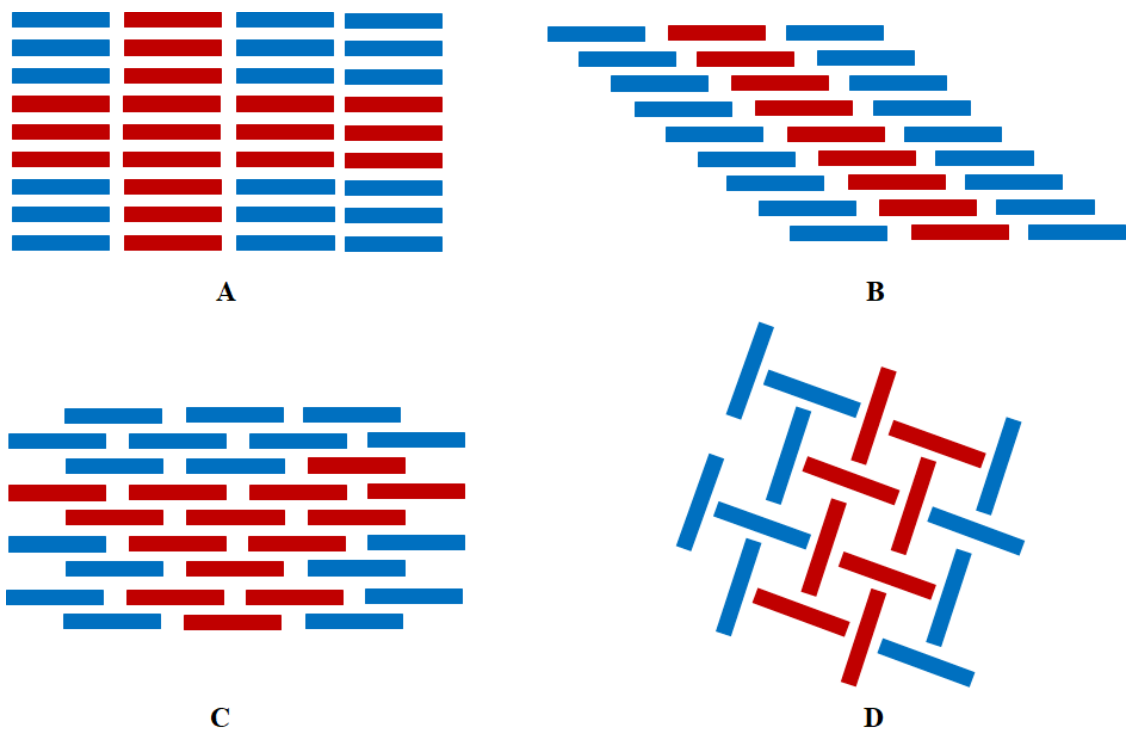
Figure 1.1. Pictorial representation of four packing motifs in OSC crystals. A: co-facial packing with one dimensional π-π interactions. B: slipped-stack packing with one dimensional π-π interaction. C: brickwork stacking with two dimensional π-π interactions. D: herringbone packing with two-dimensional, edge-to-face interactions among adjacent molecules. The structures marked in red demonstrate potential charge-carrier pathways.

As noted, an important feature of OSC is that their molecular-scale properties can be readily tailored through organic synthetic chemistry. Common approaches of such chemical modification are to append halogen atoms (*e.g.* fluorine, F) or flexible alkyl side chains to the periphery of the π-conjugated backbone. These chemical modifications can promote changes to the crystal packing motifs, and alter the intermolecular wavefunction overlap.[8] As an example system that is studied in this thesis is anthradithiophene (ADT). As shown in Figure 1.2, the chemical structure of ADT (A) consists five fused aromatic rings, creating a large π surface. It should be noted that the sulfur atoms can be arranged in two ways, referred to as *anti* (sulfur atoms on different sides of the molecular long axis) and *syn* (sulfur atoms on the same side of the molecular long axis). The crystal structures of both *anti* and *syn* ADT feature the herringbone packing motif. With this framework, the addition of bis(triethylsilylethynyl) (TES) groups on the ADT unit produce two different structures: *anti* TES-ADT (B) and *syn* TES-ADT (C). The small variation of the sulfur atom placement on the ADT backbone induces a dramatic change in the molecular packing configurations, where the *anti* TES-ADT presents a brickwork packing motif, and the *syn* TES-ADT has a slipped-stack packing feature. Further modification on the *anti* TES-ADT by adding two fluorine atoms to the 2 and 8 positions of the ADT backbone gives *anti* diF-TES-ADT (D). Intermolecular fluorine-fluorine and fluorine-sulfur interactions between adjacent molecules in *anti* diF-TES-ADT are hypothesized to improve crystallinity and stability[9-12] As a result, the single crystal form of diF-TES-ADT has a measured μ up to 6 $cm^2\ V^{-1}\ s^{-1}$.[8]
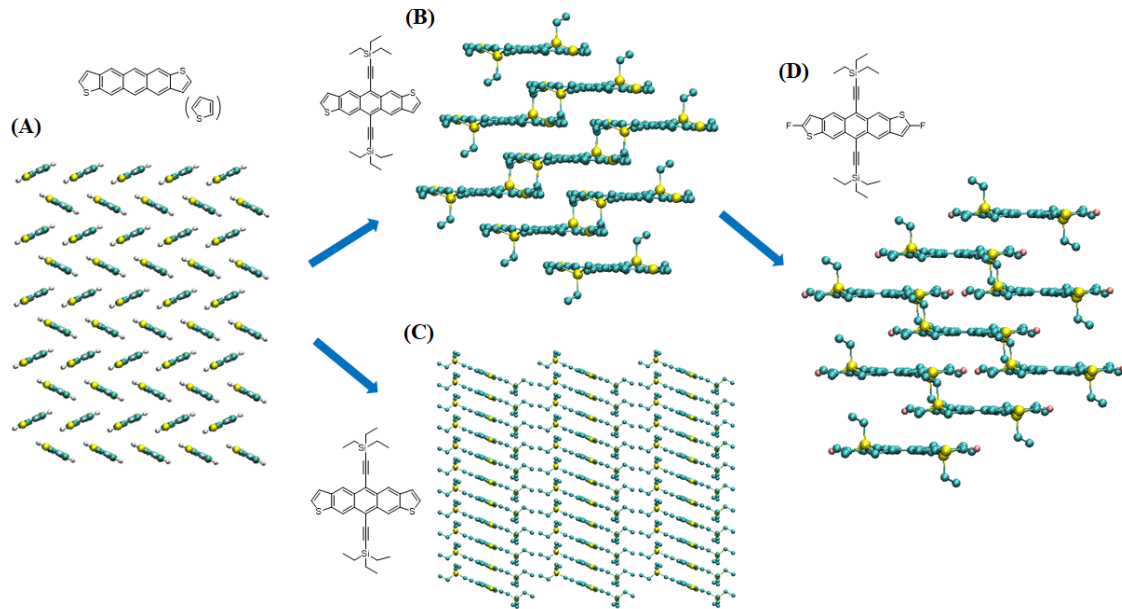
Figure 1.2. Chemical and crystal packing structures of *anti* ADT (A), *anti* TES-ADT (B), *syn* TES-ADT (C) and *anti* diF-TES-ADT (D). Select hydrogen atoms were omitted for clarity.

Though OSC crystal packing motifs can be tailored through chemical modification, there remains challenge to achieve desired packing arrangements in the solution-processed thin-films used in electronic devices. Organic crystals typically feature polymorphs, and liquid-liquid, liquid-solid, and solid-solid phase transitions can occur during processing.[13, 14] In fact, it has been reported that one-third of all organic materials display polymorphism under ambient conditions.[15, 16] These features are attributed to the weak noncovalent intermolecular interactions among neighboring molecules in the crystal and the often non-rigid structural features of organic molecules. Such polymorphism can be trigged through different thermal treatment or processing conditions. For example, it has been shown that TES-ADT exhibits different polymorphs during heating and cooling cycles,[17] suggesting that there is a solid-solid phase transition state during the thermal annealing processes. Another example is the 6,13-bis(triisopropylgermanylethynyl) pentacene (TIPGe-Pn),

which can exhibit several different packing motifs as shown in Figure 1.5. While the bulk

crystal of TIPGe-Pn grown from solution typically shows a herringbone motif with

insignificant intermolecular π-π overlap, other polymorphs can be achieved from different

processing methods such as spin-casting or drop-casting.[18] As a result, the mobilities in

thin-film transistors can vary from 10^{-5} cm^2 V^{-1} s^{-1} to about 1 cm^2 V^{-1} s^{-1}, depending on the

different polymorphs of the TIPGe-Pn.
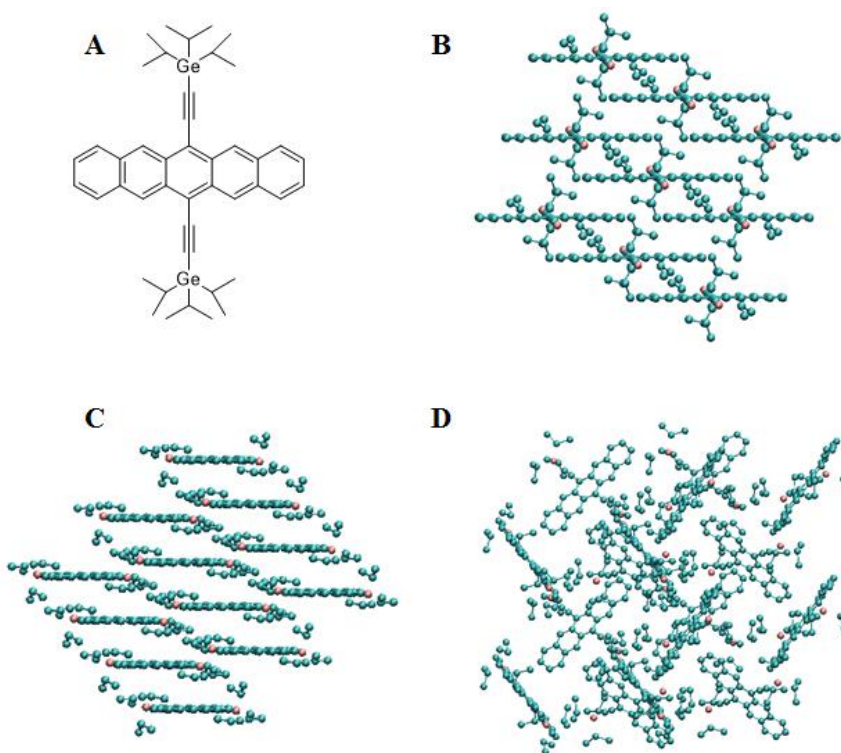
Figure 1.3. Chemical structure of (A) TIP-Ge Pn and three crystal packing motifs (B): brickwork, (C): slip-stack and (D): herringbone.

1.3   Thin film and solid-state morphologies

It is generally hypothesized that the charge-carrier transport properties of semi-crystalline

OSC films can be described (ideally) by the characteristics of the bulk crystal structure.

Therefore, to achieve efficient charge-carrier transport properties, it is critical to control

the crystallization of OSC to form films with sufficient long-range order that mimics the idealized packing of the preferred crystal structure. The fabrication of OSC is typically achieved through vapor or solution deposition. For vapor deposition, the OSC is first vaporized, and then it condenses onto the substrate.[19, 20] This method, however, requires ultrahigh vacuum environments and requires care to control the growth of single crystals; hence, this technology typically does not merge with the concept of creating low-cost electronics. Solution deposition methods take advantage of the solubility of OSC building blocks in common organic solvents and allows for the development of OSC thin films through various printing techniques. This approach, however, is more complex than vapor deposition as all of the components that comprise the solution (*i.e.* the ink) can impact the multi-scale structure of the final thin film.[21-23] In addition, external factors, such as the deposition substrate and temperature, can impact the final OSC morphology. Hence, *a priori* predictions as to the final thin-film structure, and determining structure–processing–function relationships, is extremely complicated.

1.4   Challenges and approaches

Tremendous efforts have been made to develop solution processable OSC and improve thin-film morphologies through different deposition methods.[23-33] Due to the complexity of the chemical structures and the intricate mechanisms of thin-film formation, there remains a lack of fundamental understanding concerning the structure–processing–function relationships of OSC. Hence, the development of new OSC relies heavily on the Edisonian screening of a large number of organic compounds and processing conditions. Such a scenario is both costly and time-consuming, and limits the progress of the field.

Advances in computational power and development in computational and theoretical methods have made computational materials chemistry approaches to solving materials problems and guiding materials design ever more feasible. Of particular interest to this thesis are molecular dynamics (MD) approaches and quantum chemical techniques in the context of density functional theory (DFT). MD simulations follow the physical movements of atoms and molecules within a period of time by numerically solving Newton's equations of motion, and are often used to study the interactions and properties of multi-body systems. However, the MD modeling of crystallization or film formation requires large time and length scale simulations, which are very challenging due to the computational cost. Hence, there remains a need to establish methods and models that provide insight into various aspects of the full OSC processing procedure that can be used to inform materials development.

Quantum-chemical calculations are often employed to study the electronic and optical properties of OSC. DFT-based approaches are widely used, providing information on the geometric, electronic, and excites-state properties of OSC. The results derived from the quantum-chemical calculations provide valuable insight across materials scales that can be used to understand connections between molecular and material characteristics, and assist in the design of new OSC.

In this thesis, I explore the structure–processing–function relationships of OSC. I designed and developed multiscale computational models using MD and DFT methods, described in detail in Chapter 2, to examine the physicochemical characteristics of OSC under a variety of conditions. In particular, I aimed to address the following questions:

1. Can we derive atomic-scale models to accurately predict thermal transitions in crystalline OSC and reveal solid-solid and solid-liquid phase transitions?

Polymorphism is a common feature of OSC and often arises during thermal treatment or solution processing. Understanding the causes of phase transition of OSC and how the morphologies change during the annealing process can help to control the film morphology and improve device performance. MD can be used to study the phase transitions, however, the ability to accurately predict phase transitions are challenging due to the nature of MD simulations, such as ultra-fast heating rates, lack of boundaries and interfaces, etc. The results of these limitations are commonly seen in the form of superheating effects, which lead to overestimations of phase-transition temperatures by 1.2 times of the actual melting temperature.[34, 35] Therefore, the study the phase transition of OSC with MD requires not only the accurate force field for novel structures, but also new designs of computational models that will eliminate the superheating effect.

We investigated several OSC and adapted modified simulation models to study the phase transition and morphology change during the thermal annealing process. While for some OSC the computational models and methods led to good agreement with the experimental results, the impact of these modifications seems to be nuanced for other derivatives. On the other hand, we confirmed the presence of solid-solid phase transitions through the simulation that also observed from the experiment. The descriptions of the molecular features associated with these thermal transitions provide distinctive insight into the how the chemistries of such materials direct their solid-state packing characteristics.

2. How does the solvent environment impact the processing of OSC?

Depending on the OSC and intended application, the formulation of the printing solutions can vary greatly in complexity. In bulk heterojunction (BHJ) OPV, for instance, controlling the degree of phase separation of binary or ternary material blends is critical to material performance.[36, 37] Early efforts to print OPV relied solely on halogenated solvents, while recent work demonstrated that the addition of a small fraction of a secondary solvent enables a dramatic change to the nanoscale phase separation in the OSC thin film.[38] In most applications, OSC deposited with such binary solution show improved OPV performance.[39-44] However, the understanding of how this binary solvent impacts the phase separation of OSC is very limited and the choice of primary solvent and additive remains highly empirical. Hence, there is a tremendous need to understand the role of the solvent environment on a fundamental level.

In Chapter 4, we explored phase separation of binary and ternary systems. Particularly, we made use of molecular and Lennar-Jones (LJ) particle models to evaluate the free energy change as a function of the component composition. Considering that the relative concentrations of the solvent and additive are continuously changing during solvent drying, it is important to explore the free energy of the mixture across a wide range of concentrations.

3. What is the role of the processing environment on the geometry of OSC and how does the environment affect the formation aggregates in solution?

In addition to the molecular structure, the morphology of the thin-film OSC is strongly influenced by the solvent environment during process.[10, 45, 46] Although the choice of the

primary and secondary solvents are often arrived through an Edisonian approach, the idea of using such binary solution as the processing agent is commonly accepted and applied to control solid-state morphology. To further understand the role of the solvent environment and continue establishing the structure–packing–function relationships of OSC, we developed simulation protocols for several OSC in different solution environments in Chapter 5. Particularly, we were interested in exploring the impact of different solvent on the molecular conformation and to study the factors that affect the aggregation of the OSC. Moreover, it has been suggested that the phase separation and crystallization of OSC can be carefully controlled in supersaturated solutions.[47, 48] We aim to use the computational models to observe the nucleation of OSC and understand the driving force for crystal formation.

4. *How does the construction of multi-chromophore dyes and the solid-state environment impact the electronic and optical properties of OSC?*

Theoretical approaches have been entensively developed to help understand the properties of OSC and bridge the gap between chemical design and material functionality, and collaborations among theoretical and experimental chemists are becoming more and more frequent to build a fundamental understanding of the structure–property relationships of OSC. To connect our theoritical work with experimental chemistry targets, in Chapter 6 we worked in collaboration with two synthetic chemistry groups to study a serise of novel dyes that show distinct changes in the optical characteristics in the solid state upon post-deposition annealing. We applied DFT and time-dependent (TDDFT) to understand relationships among molecular geometry, electronic strucutre, redox characteristics, and

how the optical properties can change due to the formation of multi-molecule complexes in the solid state.

CHAPTER 2

COMPUTATIONAL METHODS

Over the past few decades, there has been considerable growth of computational chemistry techniques developed and applied to determine the structure and properties of molecules and materials.[1-3] These techniques, such as empirical approaches based on Newton's laws of motion and *ab initio* approaches based on quantum mechanics, have been extensively developed to bridge the gap between chemical design and material functionality, offering fundamental insights to develop materials.[4-6] The empirical approach, such as molecular dynamics (MD), uses either quantum mechanics (QM),[7] molecular mechanics (MM),[8] or a combination thereof (QM/MM)[9] to calculate the forces that are then used to solve Newton's laws of motion to examine the time-dependent behavior of a given system. The result of the MD simulation is a trajectory that describes how the position and velocity of particles varies with time. From here, different methods can be used to analyze the trajectories and explore the property of the systems. The *ab initio* approach, on the contrary, does not (necessarily) include empirical or semi-empirical parameters, as they are ideally derived directly from theoretical principles. The simplest example of this technique is the Hartree-Fock (HF) equation, which assumes that the wavefunction of many electrons is generally a linear combination of many simpler functions.[10] Another technique, such as density functional theory (DFT), expresses the wavefunction of an electron in terms of total one-electron density, and has become a popular and versatile methods in computational chemistry.[11] In this section, we will discuss different analysis methods that made use of

both classical MD as well as DFT to understand the properties of organic semiconductor (OSC) and materials.

2.1 An overview of MD simulations

MD simulations are valuable computational tools to study the physical movements of atoms and molecules in an N-body system.[12-14] In MD simulations, the molecules and their constituent atoms can be considered as classical particles whose chemical properties are parameterized into a force field. The atoms and molecules interact for a fixed period of time, giving a view of the dynamical evolution of the system. The results of MD simulations are usually trajectories that specify the changes of position and velocity of particles in the simulation box. In the most common version, the trajectories of atoms and molecules are obtained by numerically solving Newton's equations of motion of interacting particles, such as:

$$\frac{d^2 x_i}{dt^2} = \frac{F_{x_i}}{m_i} \qquad\qquad \textit{Equation 2.1}$$

where m_i is the mass of the particle, (x_i) is the coordinate particle moving along with and F_{x_i} is the force on the particle in that direction.

Although integrating Newton's equations of motion allows researchers to explore the constant energy surface of a system, in order to mimic experimental conditions, some state variables, such as temperature and pressure of the system, should be kept constant during the molecular simulation. Depending on which state variables (for example, the energy E, volume V, temperature T, pressure P, and number of particles N) are fixed, different statistical ensembles can be generated. A variety of structural, energetic, and dynamic

properties can then be calculated from the averages or the fluctuations of these quantities over the ensemble generated. In MD simulations, the two most common ensembles are the constant *NVT* and the constant *NPT* ensembles.

2.2 *NVT* ensemble

The constant-number, constant-temperature, constant-volume ensemble (*NVT*), also referred to as the canonical ensemble, is obtained by controlling the temperature through direct temperature scaling during the initialization stage and by temperature-bath coupling during the data collection phase. The volume is kept constant throughout the simulation. There are several reasons to maintain or otherwise control the temperature during a MD simulation. A constant temperature simulation may be required to determine how the behavior of the system changes with temperature, such as the unfolding of protein or film formation. Simulated annealing algorithms also require the temperature of the system to be reduced gradually while the system explores its degree of freedom. Additionally, *NVT* is an appropriate choice when conformational searches of molecules are carried out in the vacuum without periodic boundary conditions. Without periodic boundary conditions, volume, pressure, and density are not defined. Constant-pressure dynamics cannot be carried out. Even if periodic boundary conditions are used, if pressure is not a significant factor the *NVT* ensemble provides the advantage of less perturbation of the trajectory, due to the absence of coupling to a pressure bath.

2.3 *NPT* ensemble

The constant-number, constant-temperature, constant-pressure ensemble (*NPT*) allows control over both the temperature and pressure. The unit cell vectors are allowed to change,

and the pressure is adjusted by adjusting the volume. This is the ensemble of choice when the correct pressure, volume, and densities are important in the simulation. This ensemble can also be used during equilibration to achieve the desired temperature and pressure before changing to the constant-volume or constant-energy ensemble when data collection starts.

Many experimental measurements are made under conditions of constant temperature and pressure, and so simulations in the isothermal-isobaric ensemble are most directly relevant to experimental data. Certain structural rearrangements may be achieved more easily in an isobaric simulation than in a simulation at constant volume.

2.4   Force field

The force field refers to the parameters of the potential used to calculate the forces (via a gradient) in MD simulations. Most force fields in chemistry consist of a summation of bonded forces associated with chemical bonds, bond angles, and bond dihedrals, and non-bonded forces associated with van der Waals forces and electrostatic charges. These force fields contain free parameters such as atomic charge, van der Waals parameters reflecting estimates of atomic radius, and equilibrium bond length, angle, and dihedral; these parameters are obtained by fitting against detailed electronic calculations (quantum chemical simulations) or experimental physical properties such as elastic constants, lattice parameters, and spectroscopic measurements.

The main force field used in this work is the OPLS[15] (Optimized Potential for Liquid Simulations) force field, developed by William L. Jorgensen. The force field has been found to provide reasonable estimates for the solid-state and solution properties of the system.[14, 16-18] The distinctive feature of the OPLS-AA (where AA stands for All Atom)

16

parameters is that they are optimized to fit experimental properties of liquids, such as density and heat of vaporization, in addition to fitting gas-phase torsional profiles. The simple functional form of OPLS-AA can be written as:

$$E_{tot} = E_{bond} + E_{angle} + E_{torsion} + E_{n.b.} \qquad \text{Equation 2.2}$$

where

$$E_{bond} = \Sigma K_r \ (r - r_0)^2 \qquad \text{Equation 2.3}$$

$$E_{angle} = \Sigma k_\theta (\theta - \theta_0)^2 \qquad \text{Equation 2.4}$$

describes the energetics for bond stretching and angle bending respectively, where r_0 and θ_0 are the reference bond length and angle, K_r and k_θ are the force constant,

$$E_{torsion} = \sum \left\{ \frac{V_1}{2}[1 + cos(\phi)] + \frac{V_2}{2}[1 - cos(2\phi)] + \frac{V_3}{2}[1 + cos(3\phi)] \right.$$
$$\left. + \frac{V_4}{2}[1 - cos(4\phi)] \right\}$$

Equation 2.5

describes the energetics of intramolecular torsion, where ϕ is the dihedral angle, V_1, V_2, V_3 and V_4 are the coefficients in the Fourier series. The total torsional energy, $E_{torsion}$, is the sum of this series for each dihedral angle, and

$$E_{n.b.} = \Sigma_{i=1}^{a} \Sigma_{j=i+1}^{b} \left\{ 4\epsilon_{ij} \left[\left(\frac{\sigma_{ij}}{r_{ij}}\right)^{12} - \left(\frac{\sigma_{ij}}{r_{ij}}\right)^{6} \right] + \frac{q_i q_j e^2}{r_{ij}} \right\} f_{ij} \qquad \text{Equation 2.6}$$

is the nonbonded interactions between particles a and b, represented by the Lennard-Jones terms plus Coulomb, where ϵ_{ij} is the depth of the potential well, σ is the finite distance at which the inter-particle potential is zero, r_{ij} is the distance between the particles, q is the signed magnitudes of the charge, e is the electron charge and f_{ij} is the scaling factor.[15, 16]

2.5 MD software packages

In this thesis, most of the MD simulations are carried out with GROMACS[19, 20] software package, version 5.0.5 or later with OPLS-AA force field.[16, 17, 21] GROMACS is a free, open-source software package[20, 22] and can run on central processing units (CPUs) and graphics processing units (GPUs).

We also used the LAMMPS[23] (18Aug2017) software suite for simulations involving Lennard-Jones particles due to the easy assignment of intermolecular interactions.

2.6 General simulation protocol

In all simulations carried out in this thesis, once the initial system was created, a general simulation protocol was applied to ensure the system was under equilibration for data collection and analysis. The protocol includes an initial steepest descent energy minimization (EM) step, followed by one NVT and two NPT ensembles that made use of the leap-frog integrator with a time step of 2 fs. Three-dimensional periodic boundary conditions (PBC) were applied using the velocity rescaling thermostat. Then, an NPT ensemble using the Berendsen[24] barostats was applied to stabilize the volume, followed by the Parrinello-Rahman[25] barostat that allows additional dynamic shape change (both with a coupling time of 1.0 ps). A compressibility of 4.5×10^{-5} bar^{-1} was used for both NPT ensembles. A spherical cut-off of 1.4 nm for the summation of van der Walls (vdW)

interaction and the particle-mesh Ewald (PME)[26] solver for long-range Coulomb interactions (with a cut-off of 1.4 nm) were used throughout all simulations. The time for *NVT* and *NPT* ensembles were varied according to the system size and simulation purpose, the final *NPT* ensemble was used for data collection.

2.7 Force field parametrization for new molecules

One of the key factors for an accurate MD simulation is to apply the correct force field for the system. As mentioned before, the idea of force field is to create a certain number of atom types upon which any bonds, angles, proper and improper dihedrals and long-range interactions may be described. More atom types than elements are necessary, since the chemical surroundings greatly influence the parameters. The angle between carbons in alkyne side chains will obviously differ from that of carbons in a benzene ring, so two different atom types are used to describe them. Since all simulations rely greatly upon the correctness of these parameters, it is important to generate adequate force field for novel organic semiconductor molecules.

Since some of the parameters for the novel organic molecules studied here may not be available, particularly the proper dihedrals, the OPLS-AA force field parameters were acquired through fitting potential energy surface (PES) profile of designed molecular dihedral torsion angle with classical QM calculations. The PES of target dihedrals was first determined at the B3LYP/6-31G(d,p) level of theory and then the change in potential energy was calculated for optimized geometry at each step. In the MM calculation, the unknown dihedral parameters were initially set to zero, then the EM step was performed to compute potential energy of each optimized configuration. For each optimized

configuration, the EM energy was subtracted from *ab initio* results and the resulted curve

was fitted into following equation to get the parameters,

$$V(\{r\}) = C_n \cdot (1 + cos(n\phi))$$ *Equation 2.7*

where C_n is the dihedral parameter, ϕ is the torsion angle. The new parameters were used

in a new series of MD simulation to compare the PES with *ab initio* calculation.

2.8   Methods for data analysis

2.8.1   Heat capacity

Since the data collection step is simulated under constant pressure, the change of heat

capacity of the simulation system over a temperature range was calculated from the

enthalpy and simulation temperature using the equation:

$$\Delta C_p = \frac{\Delta H}{\Delta T}|P$$ *Equation 2.8*

The enthalpy can be directly acquired through GROMACS energy package (*gmx energy*),

for a simulation involving temperature change, the temperature can also be acquired

through the same package. To ensure an accurate calculation of the heat capacity as a

function of the temperature, we applied a moving average method to calculate the enthalpy

and temperature change.

2.8.2   Potential of mean force (PMF) simulations

PMF simulations were used to determine how the intermolecular interaction energies

change as a function of the distance between two molecules. Various methods have been

proposed for calculating PMF. The simplest type is the free energy change as the separation

(r) between two particles is changed. It is anticipated that PMF can be calculated from the

radial distribution function $g(r)$ using the following expression from Helmholtz free

energy:

$$A(r) = -k_B T \ln g(r) + constant \qquad\qquad Equation\ 2.9$$

where k_B is the Boltzmann constant and T is the temperature. The constant term is often

chosen so that the most probable distribution corresponds to a free energy of zero. However,

the PMF may vary by several multiples of $k_B T$ over the relevant range of the parameter r,

which means a small change in the free energy may correspond to $g(r)$ changing by an

order of magnitude from its most likely value.

The MD simulation method does not adequately sample regions where the radial

distribution function differs drastically from the most likely value, leading to inaccurate

values for the PMF. This problem is traditionally avoided by a technique called umbrella

sampling. Umbrella sampling attempts to overcome the sampling problem by modifying

the potential function so that the unfavorable states are sampled sufficiently. The

modification of the potential function can be written as a perturbation:

$$Y^{'}(r^N) = Y(r^N) + W(r^N) \qquad\qquad Equation\ 2.10$$

where $W(r^N)$ is a weighting function, which often takes a quadratic from:

$$W(r^N) = k_w(r^N - r_0^N)^2 \qquad\qquad Equation\ 2.11$$

For configurations that are far from the equilibrium state r_0^N, the weighting function will be large and so a simulation using the modified energy function $Y'(r^N)$ will be biased away from the configuration r_0^N. The resulting distribution will be non-Boltzmann. The corresponding Boltzmann averages can be extracted from the non-Boltzmann distribution using a method introduced by Torrie and Valleau[27] as:

$$\langle A \rangle = \frac{\langle A(r^N) exp[+W(r^N)/k_B T] \rangle_W}{\langle exp[+W(r^N)/k_B T] \rangle_W} \qquad \qquad Equation\ 2.12$$

The subscript W indicates that the average is based on the probability $P_w(r^N)$, which in turn is determined by the modified energy function $Y'(r^N)$. It is usual to perform an umbrella sampling calculation in a series of stages, each of which is characterized by a particular value of the coordinate and an appropriate value of the forcing potential $W(r^N)$. These are usually referred as "windows". Therefore, umbrella sampling consists of running separate "windows" along the reaction coordinate simultaneously. This parallelization can also greatly increase the efficiency of the overall simulation. First, the reaction coordinate space is divided into windows, and, for each independent simulation, the system can only sample within that window. By allowing neighboring windows to overlap and ensuring there are enough windows to cover the entire reaction coordinate space. A PMF can be calculated by properly combining the data from each window, giving statistical weighting to the overlapping regions between windows.

Weighted histogram analysis method (WHAM) was first introduced by Kumar[28] in 1992, and provides a scheme for obtaining the optimal estimate of the unbiased probability distribution from biased probability distributions in the presence of biasing potentials. The biasing potential, $V_i(\xi)$, serves to confine the variations in the reaction coordinate, ξ, around some fixed value ξ_i, and therefore enables a more efficient sampling in the region around ξ_i [28, 29]. In short, WHAM provides a scheme for "stitching" individual biased probability distributions from each window together to yield a single unbiased property distribution. The WHAM equations for a one-dimensional reaction coordinate are:[29]

$$\rho(\xi) = \frac{\sum_{i=1}^{Nw} n_i \rho_i^{(b)}(\xi)}{\sum_{j=1}^{Nw} n_j e^{-\beta\left(V_j(\xi) - F_j\right)}} \qquad\qquad \textit{Equation 2.13}$$

$$e^{-\beta F_i} = \int e^{-\beta V_i(\xi)} \beta(\xi) d\xi \qquad\qquad \textit{Equation 2.14}$$

The PMF simulations carried out in this thesis were started by placing two target molecules in the simulation box, separated by an initial distance. A pull code was used to apply umbrella sampling method to generate a series of sample windows. Two energy minimization processes (one of 1000 steps to remove potential overlap and one of 20,000 steps for minimization) were then run for each sample window, followed by an *NVT* ensemble to equilibriate the system. According to the natural of the box, an additional *NVT* ensemble (for system in vacuo) or an *NPT* ensemble (for solvent system) using a velocity rescaling thermostat with a coupling time of 2.0 ps was then run for data collection. The PBC were turned off and the cut-off was set to zero for the in vacuo simulations. The force

data from the final ensemble was then averaged and the GROMACS WHAM package (*gmx wham*) was used to obtain the PMF profile.

2.8.3 Mean square displacement and diffusion coefficients

Since molecular diffusion rates change as a function of phase, the mean square displacement (MSD) was used to determine the crystalline melting point during simulated annealing. MSD is defined as:

$$MSD = \langle (r - r_0)^2 \rangle = \frac{1}{N} \sum_{n=1}^{N} \left(r_i(t) - r_i(0) \right)^2 \qquad \textit{Equation 2.15}$$

where $r_i(t)$ is the location of the center-of-mass (COM) of molecule i at time t and N is the total number of molecules in the system. Therefore, the diffusion constant of the additive can be computed by fitting a straight line:

$$MSD(t) = D \times t + c \qquad \textit{Equation 2.16}$$

through the *MSD(t),* where D is the diffusion constant and t is the time from the reference positions.

2.8.4 Solubility parameters

The Hildebrand[30] and Hansen[31] solubility parameters have found wide use in the experimental literature. For a pure substance, the Hildebrand solubility parameter is defined as the square root of the cohesive energy density.[32]

$$\delta = \sqrt{CED} = \left[\frac{\Delta H_{vap} - RT}{V_m}\right]^{1/2} \qquad\qquad \textit{Equation 2.17}$$

where CED is the cohesive energy density, ΔH_{vap} is the heat of vaporization, R is the gas constant, T is the temperature and V_m is the molar volume. Hansen proposed an extension of the Hildebrand parameter to estimate the relative miscibility of polar and hydrogen bonding systems,

$$\delta^2 = \delta_d^2 + \delta_p^2 + \delta_h^2 \qquad\qquad \textit{Equation 2.18}$$

where δ_d, δ_p and δ_h represent the dispersion, dipolar and hydrogen bond intermolecular forces among molecules, respectively. However, the determination of hydrogen component requires a separation of the Coulombic interaction into a dipole-dipole and hydrogen bond interaction, while in MD simulation, this is determined through an arbitrary cutoff length.[33] Therefore, in this study, we did not extract the individual dipolar and hydrogen bond component and only the Hildebrand parameter, the contribution from dispersion δ_d and the global Coulombic interaction $(\delta_p + \delta_h)$ were reported.

2.8.5 Enthalpy, entropy and free energy of mixing calculation

2.8.5.1 Ideal, regular and real solutions

A solution is defined as any phase containing more than one component, such as gas, liquid, or solid. In order for mixing to occur, the free energy of mixing must be less than zero, such as:

$$\Delta G_{mix} = \Delta H_{mix} - T\Delta S_{mix} < 0 \qquad\qquad \textit{Equation 2.19}$$

For an ideal solution, the enthalpy of mixing (ΔH_{mix}) is zero and therefore the change in Gibbs free energy (ΔG_{mix}) is determined only by the entropy of mixing (ΔS_{mix}).

$$\Delta G_{mix} = RT(x_A \ln x_A + x_B \ln x_B) \qquad \text{Equation 2.20}$$

where x_A and x_B are the mole fraction of the component A and B. In this condition, the components in the system are considered non-interactive and behave as ideal gases.

On the other hand, a regular solution occurs when there are weak interactions between components of a mixture. In such a system the enthalpy of mixing behaves in a non-ideal manner, but the entropy still follows that of the ideal solution with random mixing. Therefore:

$$\Delta G_{mix} = \left(\sqrt{\Delta E_A} - \sqrt{\Delta E_B}\right)^2 N x_A x_B + NRT(x_A \ln x_A + x_B \ln x_B) \qquad \text{Equation 2.21}$$

where $\sqrt{\Delta E_{A/B}}$ is the vaporization energy of component A or B and N is the number of moles of the two components. This formulation is only valid in the absence of strong specific interactions, such as hydrogen bonding.

The enthalpy of mixing may also be expressed as:

$$\Delta H_{mix} = H_{mixture} - \sum x_i H_i \qquad \text{Equation 2.22}$$

26

where $H_{mixture}$ is the total enthalpy of the system after mixing, x_i is the mole fraction of I and H_i is the enthalpy of pure i.

For a real solution, we need an accurate measurement of the entropy component to calculation the free energy of mixing, which in this case the is not based on the ideal gas law. The entropy of mixing can be expressed as:

$$\Delta S_{mix} = S_{mixture} - \sum x_i S_i \qquad\qquad \textit{Equation 2.23}$$

therefore, the free energy of mixing for the real solution can be expressed as:

$$\Delta G_{mix} = H_{mixture} - \sum x_i H_i + RT(S_{mix} - \sum x_i S_i) \qquad \textit{Equation 2.24}$$

2.8.5.2 Two-phase thermodynamic (2PT) method and the DoSPT code

From the standpoint of MD simulation methods, the determination of ΔG_{mix} is complicated by the fact that the determination of the entropy of mixing (ΔS_{mix}) is not straightforward. Methods such as umbrella sampling,[34] Widom particle insertion,[35] and thermodynamic integration,[36] can effectively probe the entropy of an ensemble, though each has potential complications depending on the system under investigation. Another means to determine entropy is to evaluate the vibrations of the system. Here, the system thermodynamic characteristics can be evaluated within the context that the ensemble density of states (DoS) is comprised of harmonic oscillators. While such an assumption is generally valid for solids, the anharmonic nature of low-frequency and diffuse vibrational modes in liquids and gases renders severely limits the assumption.[37] To overcome this constraint for liquids, Lin,

Blanco, and Goddard proposed the two-phase thermodynamic (2PT) model.[38] Here, the thermodynamics characteristics of a liquid are determined from the DoS obtained from the Fourier transform of the velocity autocorrelation function,[39] with the total DoS ($DoS(v)$) being the sum of two components – a gas component that contains the anharmonic diffusive vibrations ($DoS_{diffuse}(v)$) and a solid component that contains the harmonic vibrations ($DoS_{solid}(v)$) – as shown below:

$$DoS(v) = f \times DoS_{diffuse}(v) + (1 - f) \times DoS_{solid}(v) \qquad \textit{Equation 2.25}$$

A key feature of 2PT theory is the fluidicity parameter (f), which is a function of the system properties (*e.g.* self-diffusion, density, and temperature) that is solved self-consistently from the MD simulation.[40] The system thermodynamics are recovered by applying statistical weighting functions to each respective component. Since the inception of the 2PT method, it has been shown to provide accurate determinations of the absolute entropies and free energies for a variety of liquid systems, including those with considerable chemical and physical complexity.[37, 38, 41-56]

In the work presented in this thesis, the free energy of different mixtures was calculated through the 2PT method. Each system was equilibrated using the general simulation protocol introduced in Section 2.5, followed by a 20 ps MD simulation with the same NVT ensembles using the previous equilibrium system. The DoSPT code developed by Caro and co-workers[57, 58] was used for the 2PT calculations; DoSPT is Fortran implementation that

allows the computation of entropies from MD simulation within the framework of the 2PT method. More detailed explanation of DoSPT can be found in http://dospt.org/.

2.8.6   Free energy of solvation

Solvation describes the interactions among the solvent and the dissolved solute molecules, and provides insight into how solvent and solute behave in different environments. The solvation of a component is only favorable when the overall Gibbs energy of the solution is decreased in comparison to the separated two components, (ΔG_{solv} is negative). Here, we used a free energy perturbation method to determine the free energy of solvation of several solvents.

If we consider a process of solute molecule A solvated into a solvent environment S, the imaginary start and end states can be expressed as the Figure 2.1:
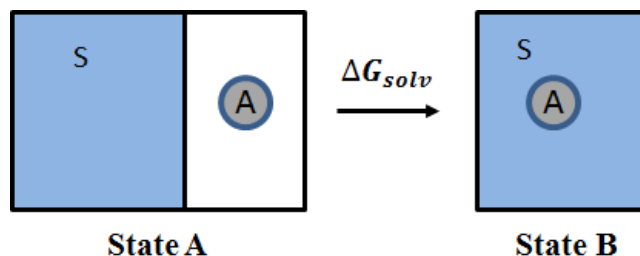
State A   State B

Figure 2.1. Pictorial representation of the starting (State A) and ending (State B) of solvation.

Here, state A can be described as the molecule A is isolated from solvent S and state B is the when molecule A is dissolved in solvent S. The free energy difference between these two states determines the relative probability p_A and p_B,

$$\frac{p_A}{p_B} = exp\frac{F_B - F_A}{k_B T}$$
Equation 2.26

where k_B is Boltzmann's constant and T is the temperature. Principally, the free energy can be calculated by forcing the system into a situation that the system does not want to be, and then calculate how much it does not want to be there. In the free energy perturbation method, this is expressed by coupling the two components in the system with an interaction variable λ, such that:

$$E_{total} = E_{A-A} + E_{B-B} + \lambda \times E_{A-B}$$
Equation 2.27

The variable λ is varied from 0 to 1; as a point of reference, the molecule A is effectively turned off from the system (when $\lambda = 0$).

In this study, the solvation energy were calculated using the Bennett acceptance ratio (BAR)[59] perturbation method as implemented in the GROMACS software suite. According to BAR, the free energy difference can be calculated directly if the two states A and B are close enough. In this case, the switching between two states becomes possible in both directions, as demonstrated in Figure 2.2 by the double arrows.
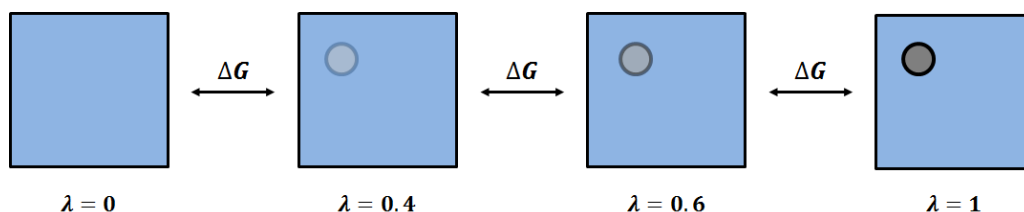
Figure 2.2. Pictorial representation of solving the particle into the solvent by varying interaction variable λ.

By creating many λ values between the initial and end states, we can effectively turn on

and off the interaction between the solute and solvent molecules. For each λ value, a series

of MD simulations is conducted, and we use the same workflow as described above. The

simulation will calculate the energy difference between two neighboring λ values, while

all the energy difference combined will provide the total energy of solvate the molecule A

into the solvent environment (ΔG_{solv}).

2.8.7 Natural order parameter

Order parameters were determined using the method described by Dewar and Camp[60]. In

this method, the global ordering of the model molecule is assumed to involve preferential

ordering of a set of molecular axes. The unit vectors and $\hat{e}_2$ describe the orientations of

the two bending "arms" of the molecule, with $\hat{e}_1 \times \hat{e}_2 = -cos\gamma$. The molecular frame is

defined by three orthonormal vectors given by:

$$\hat{a} = \frac{\hat{e}_1 - \hat{e}_2}{|\hat{e}_1 - \hat{e}_2|} \qquad\qquad Equation\ 2.28$$
$$\hat{b} = \frac{\hat{e}_1 + \hat{e}_2}{|\hat{e}_1 + \hat{e}_2|} \qquad\qquad Equation\ 2.29$$
$$\hat{c} = \hat{a} \times \hat{b} \qquad\qquad Equation\ 2.30$$

Uniaxial and biaxial ordering of the molecules are described by the parameters Q_{00}^2 and

Q_{22}^2 given by:

$$Q_{00}^2 = \frac{1}{2}(3\ cos^2\theta - 1) \qquad\qquad Equation\ 2.31$$

$$Q_{22}^2 = \frac{1}{2}(1 + cos^2\theta)\ cos\ 2\phi\ cos2\psi - cos\ \theta\ sin\ 2\phi\ sin\ 2\psi \qquad Equation\ 2.32$$

31

where (θ, ϕ, ψ) are the Euler angles in the rotation matrix mapping the molecular frame defined by Equation 3.14 - 3.16 to the laboratory frame[61]. The laboratory frame is assigned in each molecular model by taking the director of the most aligned molecular axis to define the laboratory Z axis, while the second-most aligned molecular axis is taken to be the laboratory Y axis, and the X axis is orthogonal to Y and Z. Therefore, $Q_{00}^2 = 1$ and $Q_{22}^2 = 0$ denote a phase with perfect uniaxial orientational ordering. In their simulations, the directors and order parameters were obtained by diagonalizing the order tensors[60], shown in Equation 3.19, where I is the second-rank unit tensor.

$$Q_{aa} = \frac{1}{2N_m} \sum_{i=1}^{N_m} \left(3\hat{a}_i \hat{a}_j - I \right) \qquad \text{Equation 2.33}$$

2.8.8 Radial distribution function

Radial distribution functions (RDF), also called pair distribution functions or pair correlation functions $g(r)$, define the probability of finding a particle in a shell dr at the distance r of another particle chosen as a reference point, such as:

$$dn(r) = \frac{N}{V} g(r) \, 4\pi r^2 dr \qquad \text{Equation 2.34}$$

where V is the model volume and N is the total number of atoms. If we consider dividing the physical space volume V into shell dr, then it is possible to compute the number of atoms $d_n(r)$ at a distance between r and $r + dr$ from a given atom. The RDF is strongly dependent on the type of matter, therefore the profile of solids, liquids and gases are significantly different.

In the solid state, the materials structure is specific over a long range, therefore the profile of RDF for solid state materials appears as discrete peaks. Each peak has a broadened shape which is caused by the vibration of the particle around its lattice site. In liquids, due to the more dynamic nature of the molecules, the liquid does not maintain a constant structure and loses the long-range structure. Therefore, the first coordination spheres will occur as a sharp peak that indicates the first sphere. At longer ranges, the molecules become more independent of each other and the distribution returns to the bulk density. Because of the loosely packed nature, the RDF for liquids does not have exact intervals. In gases, because of the non-existence of regular structure, the RDF only has a single coordination sphere then rapidly decays to the normal bulk density of gas.

2.8.9   Simulation of x-ray diffraction patterns

X-ray diffraction (XRD) is a powerful nondestructive technique used to obtain the structural information of crystalline materials. The intensities shown on XRD patterns are produced by constructive interference of a monochromatic beam of x-rays that scattered by atoms in a periodic lattice. The diffraction of x-rays by crystals is described by Bragg's Law as shown below:

$$n\lambda = 2d \sin\theta \hspace{4cm} Equation\ 2.35$$

where n in an integer, λ is the characteristic wavelength of the X-rays impinging on the crystallize sample, d is the interplanar spacing between rows of atoms, and θ is the angle of the x-ray beam with respect to these planes. While the Equation 3.35 is satisfied, x-rays scattered by the atoms in the plane of a periodic structure are in phase and diffraction occurs

in the direction defined by the angle θ. From the experimental measurement, the x-ray diffraction patterns consist of a set of diffracted peaks with the angles at which they are observed. These patterns are the fingerprint of periodic atomic arrangements in a given material, and can be used to identify the chemicals by comparing this diffraction pattern to a database of known patterns.

2.9 Quantum mechanics approaches

Classical mechanics uses Newton's law ($F = ma$) to predict the behavior of a physical system under given conditions. The solution of this equation provides the position and momentum of the system as a function of the force F. The physical state of the system can then be described with these two parameters. In quantum mechanics (QM), the role of Newton's law is played by Schrödinger's equation, which can be generally written as:

$$\widehat{H}|\Psi\rangle = E|\Psi\rangle \qquad\qquad \text{Equation 2.36}$$

where $\widehat{H}$ is the Hamiltonian operator, E is the energy eigenvalue for the system and Ψ is the wave function. In Schrödinger's equation, the kinetic and potential energies of the system are part of the Hamiltonian ($\widehat{H}$), which acts upon the wavefunction (Ψ) to generate the evolution of the wavefunction in time and space.

For a simple two-dimensional square potential or even the hydrogen atom, the Schrödinger's equation can be solved exactly to get the wavefunction of the system, then, the allowed energy states of the system can be determined. However, it is impossible to use the equation to solve N-body systems due to repulsion potential between electrons. Therefore, approximate methods, such as Hartree-Fock (HF) theory and variational Monte

Carlo approaches, have been implemented to solve systems with many electrons. Among different *ab initio* approaches, density functional theory (DFT) is quite versatil,[11] and is a standard approach to study the ground-state electronic structure of molecules and solid-state materials.

2.10 Born-Oppenheimer approximation

N-body systems cannot be solved exactly by Schrödinger's equation due to the difficulty to solve the Coulombic repulsion terms. Therefore, the approximations have to be made to reduce the number of degrees of freedom. The most basic approximation is called Born-Oppenheimer approximation, which assumes that the motion of the atomic nuclei and electrons in a molecule can be treated separately due to the large mass differences between electron and nuclei. Because the motion of nuclei is much slower than electrons, the nuclei can then be treated as stationary and the electronic wavefunction only depends on the positions of the nuclei. This allows the separation of the Hamiltonian into nuclei term and electron term, such that:

$$\widehat{H}(r_1, \ldots, r_n, R_1, \ldots, R_N) = \widehat{H_n}(R_1, \ldots, R_N) + \widehat{H_e}(r_1, \ldots, r_N; R_1, \ldots, R_N)$$

Equation 2.37

where r_i are the electronic coordinates and R_I are the nuclear coordinates, H_e then depends parametrically on the nuclear coordinates, therefore the wavefunction can be taken to be the product of the electronic and nuclear parts.

$$\Psi(r_1, \ldots r_n, R_1, \ldots, R_N) = \Psi_e(r_1, \ldots, r_n; R_1, \ldots, R_N) \, \Psi_n(R_1, \ldots, R_N)$$

Equation 2.38

This product wavefunction is called the Born-Oppenheimer wavefunction, where the $\Psi_n(R_1, \ldots, R_N)$ is the vibrational wavefunction and $\Psi_e(r_1, \ldots, r_n; R_1, \ldots, R_N)$ is the function of both the nuclei and electronic coordinates, but only depends on the electronic quantum number or electron state. This separation of the Hamiltonian into a sum of nuclear and electronic parts and the wavefunction into a product of nuclear and electronic parts allows the separation of the Schrödinger equation. Electronic structure calculations aim to solve the electronic Schrödinger equation as a function of the nuclear coordinates.

2.11 Basics of DFT

2.11.1 Density functional theory

Density functional theory (DFT) states that the properties of a many-electron system can be determined by using a function of the electron density. The electron density is a function of space and time. Therefore, the density function of the function of space and time is referred as functional. Because the electron density is only a function of three coordinates (x, y, z), the treatment of the many-body electronic wavefunction is reduced to a function of $3N$ variables, where N is the number of atoms in the system.

This method, first introduced by Thomas and Fermi in 1927,[62] has gone through subsequent development over the years. Among these efforts, Hohenberg and Kohn (H-K) proved that the ground state in quantum mechanics is only a function of the electron density and demonstrated that the electron density uniquely determines the Hamiltonian operator and thus all the properties of the system.[63] Kohn and Sham (K-S) further developed the Kohn-

Sham equation for non-interacting electrons in an effective potential and stated that the functional pertaining to the ground-state energy of the system delivers the lowest energy if and only if the input density is the true ground state density.[64] The Kohn-Sham equation is written as:

$$E[\rho] = T_s[\rho] + \int dr\, v_{ext}(r)\rho(r) + E_H[\rho] + E_{xc}[\rho] \qquad \textit{Equation 2.39}$$

where $T_s[\rho]$ is the Kohn-Sham kinetic energy term, which is expressed in terms of Kohn-Sham orbitals $\phi_i(\mathbf{r})$, such as:

$$T_s[\rho] = \sum_{i=1}^{N} \int dr\, \phi_i^*(r) \left(-\frac{\hbar^2}{2m} \nabla^2 \right) \phi_i(r) \qquad \textit{Equation 2.40}$$

v_{ext} is the external potential acting on the interacting system, $E_H[\rho]$ is the Hartree (or Coulomb) energy and $E_{xc}[\rho]$ is the exchange-correlation (XC) energy. Nowadays, the develop of DFT are focus on the improvement of both accuracy and efficiency of the methods, which depend on the basis-set expansions of the Kohn-Sham orbitals, particularly, upon the quality of the applied exchange-correlation functionals.[64]

2.11.2 The functionals

2.11.2.1 Local density approximation (LDA)

There are many different approaches to model the exchange-correlation functionals, the most basic one is the local density approximation (LDA)[65], which states that the exchange-correlation functionals depends only on the value of the electronic density at each point in space:

$$E_{xc}^{LDA}[\rho] = \int \rho(r) \, \varepsilon_{xc}(\rho(r)) \, dr \hspace{3cm} Equation \ 2.41$$

In the LDA model, the exchange-correlation energy (ε_{xc}) of each particle is derived from a homogeneous electron gas with a density of $\rho(\boldsymbol{r})$ and the exchange and correlation terms are composed linearly. Slater[66] further included electron spin into the LDA model and developed local-spin density approximation (LSDA). This model proves a good estimation of bond lengths, however, often overestimates the binding energies and underestimates the barriers, therefore, is not sufficient for many applications.

2.11.2.2 Generalize gradient approximation (GGA)

The development of the LDA model is important to construct more sophisticated approximations to solve the XC energy. The first logical improvement is to consider the non-homogeneity of the true electron density, and such an approximation is referred as the generalized gradient approximation (GGA). Many GGA functionals have been derived over the years and provide good approximation to total energies and structural properties, such as, PW91 by Perdew-Wang,[67] PBE by Perdew-Burke-Ernzerhof,[68] BLYP by Lee-Yang-Parr[69] and AM05 by Armiento-Mattsson.[70] However, they still underestimate the energy barriers and fail to describing van der Waal interactions.

In addition to the GGA model, the meta-GGAs[71] include additional Kohn-Sham kinetic energy for the occupied orbitals and can give more accurate equilibrium properties of condensed matters.[72] A typical example of such functional is TPSS developed by Tao, Perdew, Staroverow and Scuseria.[73] This model, however, is often subject to convergence issues and limited application.

2.11.2.3 Hybrid functional

The hybrid functionals, first introduced in 1993 by Axel Becke,[74] are approximation models that incorporate the GGA model (or meta-GGA) with exact exchange from Hartree-Fock (HF) theory. Although the combination with HF makes the calculation more expensive, such hybridization improves the accuracy to calculate many molecular properties, such as atomization energies, bond lengths and vibration frequencies.[75] The most popular hybrid functionals includes the B3LYP[74, 75] which stands for "Becke, 3-parameter, Lee-Yang-Parr" and the M06.[76] The B3LYP is one of the first DFT methods that can predict molecule properties and reaction barriers with an accuracy comparable to the wavefunction based methods and is among the most popular functionals to calculate electronic structures.

2.11.2.4 Range-separated (RS) functional

Despite the popularity of hybrid functionals in electronic structure calculations, they are only able to reliably capture the short-range interactions. The problem of hybrid functionals relys on the treating of Coulomb interactions at long range. Since hybrid functionals were developed from the LDA model, which only considers the electron density at a particular point and has problems describing long-range behavior. Recent efforts have improved the global hybrid functionals and use a range-separated (RS) functional to solve this problem.[77, 78] In the RS functional, the Coulomb interaction ($1/r_{12}$) is split into two parts, the short-range (SR) term is handled by the exchange from the GGA functional, while the long-range (LR) term is handled by Hartree-Fock, and uses a function to smoothly scales between the two terms, such that:

$$\frac{1}{r_{12}} = \frac{1-g(r)}{r_{12}} + \frac{g(r)}{r_{12}} \qquad\qquad \text{\textit{Equation 2.42}}$$

where $r_{12} = |r_1 - r_2|$ for the coordinate vectors of electrons and $g(r)$ is the scale function that defined as:

$$g(r) = \alpha + \beta \, erf(\omega r) \qquad\qquad \text{\textit{Equation 2.43}}$$

the α and β are functional dependent mixing parameters, and the error function erf smoothly connects the SR to the LR part of the operator under the governance of a range-separation parameter ω, which is determined empirically.[77-80] Recent work has shown that the ω is strongly depended on the target system,[79, 81] therefore, it is important to determine the optimal ω for individual systems.

Among different RS functionals, the ωB97X-D functional developed by Chai and Gordon is widely used.[82] With this long-range corrected (LRC) method, the exact exchange included in the long-range term increases with the interelectronic distance, which leads to the correct behavior for the exchange potential and an improved description of charge-transfer process.

2.11.3 Basis sets

In computational chemistry, the basis set is used to turn the partial differential equations of the models into algebraic equations for efficient implementation on a computer, which is a set of functions that used to represent the electronic wave function in the HF method or DFT. The commonly used the expression of the molecular orbitals (MO) in quantum

chemistry is the linear combination of atomic orbitals (LCMO). Several types of LCMO include Slater-type orbitals (STO), Gaussian-type orbitals (GTO) or numerical atomic orbitals, out of these three, the GTOs are the most often used due to their efficient computation of molecular integrals.

2.11.3.1 Gaussian function

The single Gaussian function is also called a primitive Gaussian function, or primitive GTO, which can be used as Cartesian primitive GTOs or Spherical primitive GTOs. The Cartesian GTOs is defined with the angular momentum quantum number l and the number k, m and n, where $l = k + m + n$,

$$g_v(r) = x^k y^m z^n e^{-\zeta_v r^2} = x^k y^m z^n \, e^{-\zeta_v(x^2 + y^2 + z^2)} \qquad \text{Equation 2.44}$$

while the Spherical GTO was defined with the angular momentum quantum number l and its components $m = -l, \dots, l$, such that:

$$g_v(r) = Y_{l,m}(\theta, \phi) r^l e^{-\zeta_v r^2} = Y_{l,m}(\theta, \phi) r^l e^{-\zeta_v(x^2 + y^2 + z^2)} \qquad \text{Equation 2.45}$$

2.11.3.2 Contracted Gaussian-type orbitals (CGTO)

The STO's can provide more accurate results but at the same time, it takes longer computation time to compute the integrals. A solution to this is to use a fixed linear combination of GTO's to mimic a STO, which are often referred as "STO-nG", even though it is made of GTOs. Such basis set are called "Contracted Gaussians" (CGs):

$$G_a(r) = \sum_{v=1}^{N_\alpha} c_v \, g_v(r) \qquad\qquad \textit{Equation 2.46}$$

There are many improvements can be made on the STO-nG basis sets, such as including more than one CG on each AO, $e.g.$ Double zeta (DZ), triple zeta (TZ) and quadruple zeta (QZ). Or, split-valence basis, which including one CG per core AO and more than one for the valence AOs. $e.g.$ 3-21G, 4-31G, 6-31G, 6-311G, etc.

2.11.3.3 Polarization and diffusion

Simply increasing the number of CGs on each AO does not guarantee a good computational result, as other factors also need to be considered. For example, the AO may shift to one side or the other due to the polarization, such that the s orbital can be polarized if it is mixed with a p orbital, and the p orbital can be polarized if mixed with d orbitals, which requires a polarized basis function to encounter this situation. Normally, the inclusion of polarization function can be defined with symbol "*", or "**" (d, p), which refers to including polarization function on heavy atoms or both heavy atoms and hydrogen, respectively. Others include the correlation-consistent basis sets, such as cc-pVDZ, cc-pVTZ, etc, where "cc-p" stands for "correlation-consistent polarized" and "V" indicates they are "valence-only" basis sets. The use of these polarization functions enhances the flexibility of atoms to form chemical bonds in any direction and improves the calculation of molecular structures.

In the case that CGs extend further from the nucleus than the AO, the diffuse function also needs to be included into the basis sets. The symbol to include diffuse functions is "+", such as 3-21+G, 6-311++G, where single "+" refers to including diffuse function on heavy

atoms, and "++" includes diffuse function on both heavy atoms and hydrogen. For the molecules that form hydrogen bonds, the inclusion of diffuse functions improves the prediction of the extended electronic densities. In practice, the basis sets often include both polarization and diffuse functions to provide the best calculation results, such as 6-31+G, 6-311++G**, aug-cc-pVDZ (augmented versions of the preceding basis sets with added diffuse functions).[83, 84]

2.11.4 Time-dependent DFT (TDDFT)

As the name applies, time-dependent DFT (TDDFT)[85] is an extension of DFT which is used to investigate the properties and dynamics of N-body systems in the presents of time-dependent potentials. In computational chemistry, TDDFT is mostly used to calculate the excited states of isolated systems and extract features like absorption or emission spectra. The energies that associated with TDDFT calculation are presented in Figure 2.3. Generally, the energy of most interests from the TDDFT calculations is the one between ground state (GS) and excited state (ES) at ground state geometry [R(GS)], which corresponds to the idealized (vertical) absorption energy and can be expressed as:

$$E^{vert-abso.} = E^{ES}(R^{GS}) - E^{GS}(R^{GS}) \qquad \qquad \textit{Equation 2.47}$$

As a contrary, the energy calculated with the geometry of excited state [G(ES)] corresponds to the fluorescence if ES is a singlet state, or to the phosphorescence if the ES is a triplet state.

$$E^{vert-fluo.} = E^{ES}(R^{ES}) - E^{GS}(R^{ES})$$ *Equation 2.48*

The adiabatic contribution is then the energy difference between these two states at each minimum:

$$E^{adia.} = E^{ES}(R^{ES}) - E^{GS}(R^{GS})$$ *Equation 2.49*
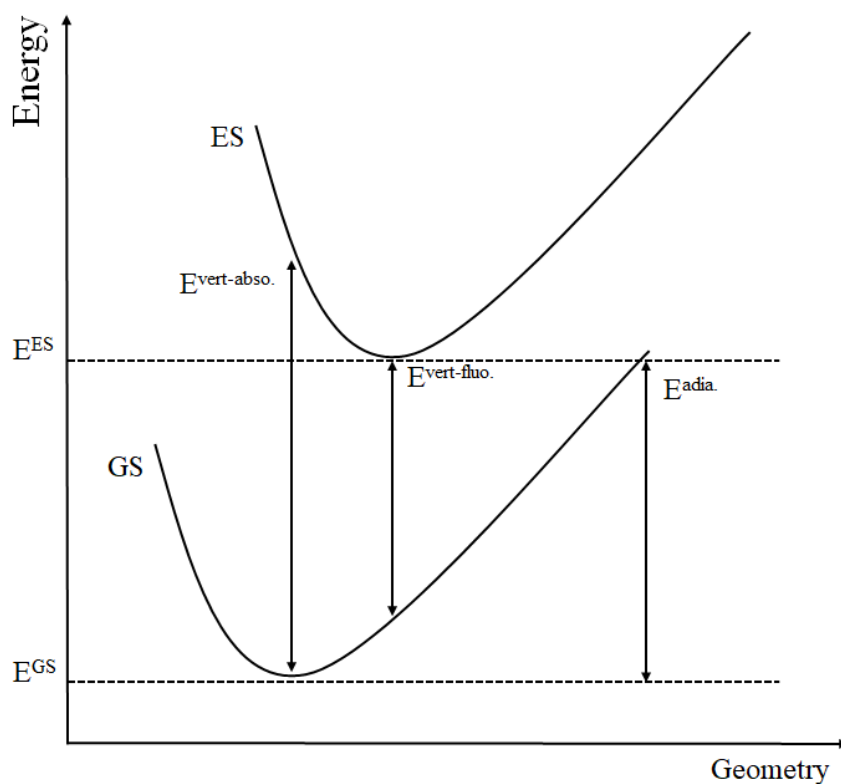
Figure 2.3. Energy diagram representing the energies associated with TD-DFT calculation.

44

2.11.5 Natural transition orbitals

TDDFT is very useful to study the excited states of systems. The results of such calculation are a summary of all the excitation energies of the selected transitions as well as the coefficients that describing the contributions of each particle-hole pairs to the excited states. In several cases, a single dominate transition can be characterized from the results indicating the associated excited states, however, in many other situations, the excited state is a combination of many transitions, which makes the straightforward identification of the dominate transition difficult. The suggested solution to this problem is called natural transition orbitals (NTOs) analysis introduced by Martin in 2003.[86] The NTO approach uses the corresponding orbital transformation by Amos and Hall.[87] In this effort, the original transition density matrix is transformed into a more compact form where each excited state is expressed as a single pair or orbital, so that the transition occurs from excited "particle" to the empty "hole".[86]

CHAPTER 3

EXPLORE PHASE TRANSITION AND MORPHOLOGIES CHANGE DURING

THERMAL ANNEALING PROCESS

3.1 Introduction

As discussed in Chapter 1, OSC morphology is critical to the performance of these materials in electronic devices. OSC performance is dictated by a hierarchal morphology, starting with intermolecular interactions (i.e. exchange repulsion, dispersion, electrostatics, and induction)[1-9] that define local molecular packing and electronic interactions through long range (dis)order that can, for instance, dictate the mobility of charge carriers through the material, mechanical characteristics, and operational stability.[2, 5-6, 10-19] Currently, the OSC community relies mostly on trial-and-error approaches to design, create, and apply OSC, as there are few rational guidelines that can direct the chemistry and processing to control material assembly or organization. To move away from such Edisonian approaches, direct correlations among these parameters need to be made, necessitating the advance of synthetic, analytical, and computational/theoretical techniques and the development and application of models that can probe this complex morphological hierarchy.

Thermoanalytical techniques – which can provide details of phase transitions, such as the glass transition (T_g), melt transition (T_m), and crystallization temperatures (T_c) – are particularly useful experimental tools to gauge the strengths of and interplay between intermolecular interactions and packing arrangements in OSC.[20-23] Data from such techniques, however, are inherently macroscale and provide a time and space averaged result for a given sample, limiting the amount of microscopic insight that can be obtained

and provided as feedback for synthetic chemists interested in controlling solid-state packing and materials characteristics through molecular design. Hence, computational approaches that can probe these types of thermal transitions with atomic-scale resolution can provide invaluable connections with experiment.[24-26]

Classical MD approaches, which bridge the gap between size-limited quantum mechanical calculations and macroscopic experimental analyses, are widely employed to explore phase transitions, as they are capable of simulating thousands to millions of atoms on time-scales that approach relevance to capture such events.[23, 27-29] A critical issue that needs to be overcome when implementing MD simulations to study thermal transitions is the so-called superheating effect,[28, 30-32] which can lead to overestimates of T_m of $1.2 \times T_m$.[30, 33] Superheating has been attributed to (i) the PBC used during the MD simulations (*i.e.* an infinite, periodic system is being heated equally throughout its entirety) and (ii) the large-temperature ranges that are traversed over very short timescales (in particular with respect to experiment) during the simulations. PBC can be problematic as they do not account for the interfaces, defects, or disorder that one might expect for a real material, *i.e.*, sites in the material where one might expect phase transformations to first begin. To overcome this limitation, Jayaraman and co-workers[34] suggested the introduction of voids into simulated atomic crystals, wherein random point/atom deletions are made within a crystal to create disorder. Alternatively, Takahashi and co-workers simulated polymer melting using explicit surfaces and found that the melting at the surface initiated below the T_m of the bulk material;[1, 35] Chen and co-workers have also worked with free surfaces to determine T_m in polymers.[32] Importantly, both the point-defect and surface methods show promise for mitigating superheating effects and delivering T_m closer to experimental measures.

We are interested in exploring the phase transitions of OSC developed from rigid, anthradithiophene (ADT) chromophores (Figure 3.1),[36-40] with a particular emphasis on understanding how the molecular structure and chemical substitution (here the alkylsilylethynyl functionalization approach that is often used to govern solubility) impact the molecular-scale features of the phase transitions. It is our aim to determine how these molecules transition from ordered to disordered phases during heating, and to look for hallmark characteristics that may lead to further insight into the crystal nucleation and growth in these and similar systems. Experimentally, ADT are challenging materials as they result in a 1:1 mixture of *syn* and *anti* configurations of the thiophene moieties during synthesis. The presence (or lack) of *syn* and *anti* ADT isomers in molecular materials has been shown to direct both the molecular order in the solid state and the resulting OSC characteristics, in particular the charge-carrier mobilities extracted from OFET architectures.

Here, we investigate the thermal transitions of the *syn* and *anti* isomers of both the ADT chromophore and 5,11-bis(triethylsilylethynyl) anthradithiophene (TES ADT). We demonstrate the impact of superheating in the MD simulations on the determination of T_m, and how the enhanced probability for disorder from both the void and interface methods can alter T_m. Interestingly, while the results for the unsubstituted ADT chromophores are clear cut, the impact of these different methods for the TES ADT derivatives is more nuanced. The descriptions of the molecular features associated with these thermal transitions provide distinctive insight into the how the chemistries of ADT-based materials direct their solid-state packing characteristics.
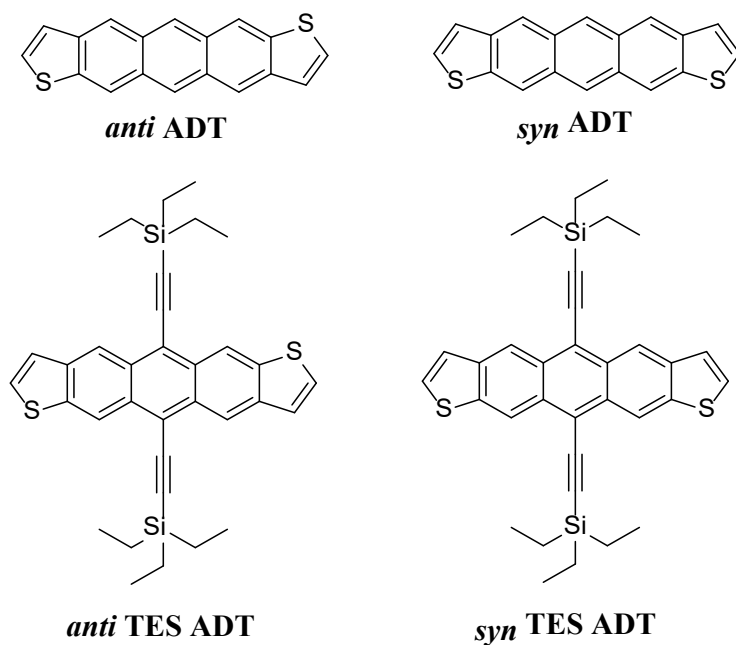
Figure 3.1. Chemical structures of the *anti* and *syn* isomers of [top] anthradithiophene (ADT) and [bottom] 5,11-bis(triethylsilylethynyl) anthradithiophene (TES ADT).

3.2 Computational methodology

All MD simulations were performed using the GROMACS 2016.1 software package.[41-42]

The intra- and inter-molecular interaction parameters for the ADT molecules were built

from the OPLS-AA force field.[43-44] Bonded force field parameters for the thiophene moiety

were adapted from Schwarz and co-workers[45] and the TES moiety were adapted from Do

and co-workers[46]. All parameters were evaluated by comparing ADT energy minimized

structures from molecular mechanics (MM) minimizations to molecular geometries

optimized via density functional theory (DFT) at B3LYP/6-31G(d,p) level. Data from the

comparisons are given in Tables 3.1 and 3.2 of and suggest that the OPLS-AA-based force

field parameters provide molecular structures similar to the DFT optimized geometries.

anti ADT
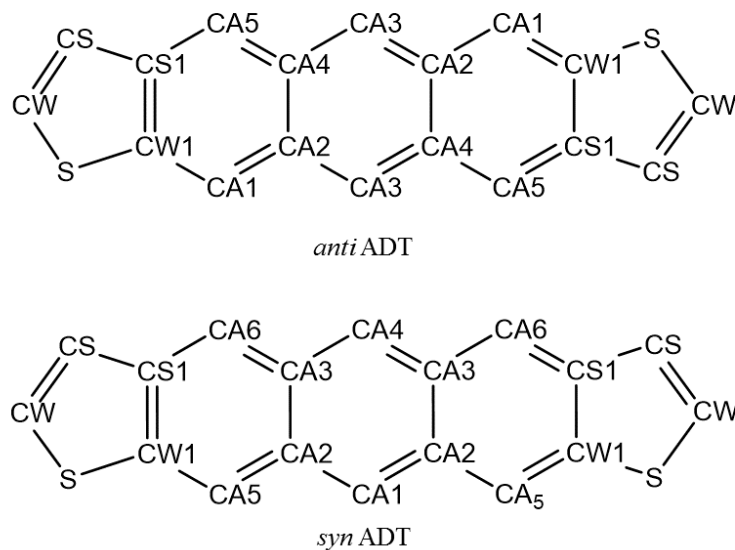
syn ADT

Figure 3.2. Chemical structures of *anti* and *syn* ADT with atom labels used for the bond and angle analyses.

Table 3.1. Select bond lengths for *anti* and *syn* ADT as determined by molecular mechanics (MM) energy minimization using the OPLS-AA force field and density functional theory (DFT) optimizations at B3LYP/6-31G(d,p) level. Atom labels are given in Figure 3.2.

	anti ADT			*syn* ADT		
Bond #	DFT [Å]	MM [Å]	SD	DFT [Å]	MM [Å]	SD
S-CW	1.761	1.753	0.004	1.761	1.768	0.004
CW-CS	1.353	1.365	0.006	1.353	1.358	0.003
CS-CS1	1.446	1.458	0.006	1.446	1.446	0.000
CS1-CA5	1.379	1.386	0.003	-	-	-
CA4-CA5	1.422	1.424	0.001	-	-	-
CA3-CA4	1.402	1.409	0.004	1.402	1.409	0.004
CA2-CA3	1.400	1.412	0.006	-	-	-
CA1-CA2	1.427	1.427	0.000	1.401	1.418	0.008
CA1-CW1	1.370	1.370	0.000	-	-	-
CW1-S	1.769	1.769	0.000	1.769	1.767	0.001
CW1-CS1	1.444	1.450	0.003	1.444	1.453	0.005
CA2-CA3	1.453	1.451	0.001	1.453	1.462	0.004
CS1-CA6	-	-	-	1.379	1.374	0.002
CA3-CA6	-	-	-	1.423	1.430	0.003
CA5-CW1	-	-	-	1.370	1.385	0.007

Table 3.2. Select bond angles for *anti* and *syn* ADT determined by molecular mechanics (MM) energy minimization using the OPLS-AA force field and density functional theory (DFT) optimizations at B3LYP/6-31G(d,p) level. Atom labels are given in Figure 3.2.

Angle	*anti* ADT			*syn* ADT		
	DFT [°]	MM [°]	SD	DFT [°]	MM [°]	SD
S-CW1-CS1	113.893	114.584	0.346	113.887	113.713	0.087
CW1-CS1-CS2	113.228	112.540	0.344	113.224	113.679	0.227
CS1-CS2-CW2	110.476	110.980	0.252	110.477	110.761	0.142
CS2-CW2-S	110.767	111.361	0.297	110.768	111.385	0.309
CW2-S-CW1	90.637	90.536	0.050	90.644	90.460	0.092

To evaluate the nonbonding parameters, supercells created from the bulk crystal structure reported by Mamada and co-workers[47] containing 400 ADT molecules were subjected to MD simulation at 113 K and 1 bar, the temperature at which the crystal structure was obtained. Following an initial steepest descent energy minimization, these supercells were treated by one *NVT* (constant number, *N*, volume, *V*, temperature, *T*) and two *NPT* (number, *N*, pressure, *P*, temperature, *T*) steps using a leap-frog integrator with a 1 fs time step. Both *NPT* runs used a velocity rescaling thermostat[48] with a coupling time of 1.0 ps and a compressibility of 4.5×10^{-5} bar^{-1}. The first NPT step used the Berendsen[49] barostat, which is an efficient way to scale the system for initial equilibration yet produces artificially narrow distributions of pressure. The second *NPT* step used the Parrinello-Rahman[50] barostat for further equilibration. Three-dimensional PBC were applied and a spherical cut-off of 1.4 nm was used for van der Waals (vdW) interactions and particle-mesh Ewald (PMD)[51] with 1.4 nm cutoff for long-range electrostatic interactions are used throughout the simulations. Each *NVT* and *NPT* simulation was carried out for 2 ns with

the geometry from the second *NPT* ensemble used to generate crystal parameters for comparison with the experimentally derived parameters. Our results indicate that the nonbonding parameter applied for both the *anti* and *syn* ADT supercells effectively maintains the experimental crystal packing during the entire simulation time. The comparison of the experimental crystal parameters and the packing results derived from these MD simulations are provided in Table 3.3.

Table 3.3. Unit cell parameters and densities determined from MD simulations using the OPLS-AA force field in comparison to those from the experimental crystal structure reported in ACS Applied Materials & Interfaces 2013, 5, 9670.

	anti ADT			*syn* ADT		
	MD	CIF	SD	MD	CIF	SD
a [Å]	5.972	5.916	0.028	5.916	5.887	0.014
b [Å]	7.846	7.772	0.037	7.545	7.508	0.018
c [Å]	14.125	13.991	0.067	14.418	14.347	0.035
α [°]	86.600	86.589	0.005	96.160	96.100	0.030
β [°]	78.300	78.271	0.014	94.300	94.300	0.000
γ [°]	86.400	86.424	0.012	89.600	90.400	0.400
Density [g/cm^3]	1.490	1.540	0.025	1.510	1.530	0.010

Potential of mean force (PMF) calculations, using constrained simulations, were performed *in vacuo* to determine the strength of the intermolecular interactions between the various ADT chemistries considered. For each PMF simulation, two ADT molecules were placed in a $10 \times 10 \times 10$ nm^3 simulation box. Two energy minimization processes (one of 1000 steps to remove potential overlap and one of 20,000 steps for minimization) were run for each sample window, followed by an *NVT* simulation to_equilibriate the system. An additional *NVT* simulation using a velocity rescaling thermostat with a coupling time of

2.0 ps was then run for data collection. The PBC were turned off and the cut-off was set to zero for the *in vacuo* simulations, and the production run was carried out at 298 K for 5 ns with a time step of 2 fs. The force data from the final 2 ns was averaged and the weighted histogram analysis method (WHAM)[52] in GROMACS was used to obtain the PMF profile.

To explore phase transformations during heating and eventual melting, supercells of the *anti* and *syn* ADT and *anti* and *syn* TES ADT crystals were created. The *anti* and *syn* ADT and *syn* TES ADT supercells included 1600 molecules, while the *anti* TES ADT supercell included 1350 molecules. These differences reflect the different number of molecules in each of the respective unit cells and a strategy to retain cube-like supercells. Thermal annealing simulations were carried out using a methodology similar to that employed by Palczynski and co-workers,[53] following a two-step protocol as demonstrate in Figure 3.3:

Unit Cell   Solid   Liquid   Gas
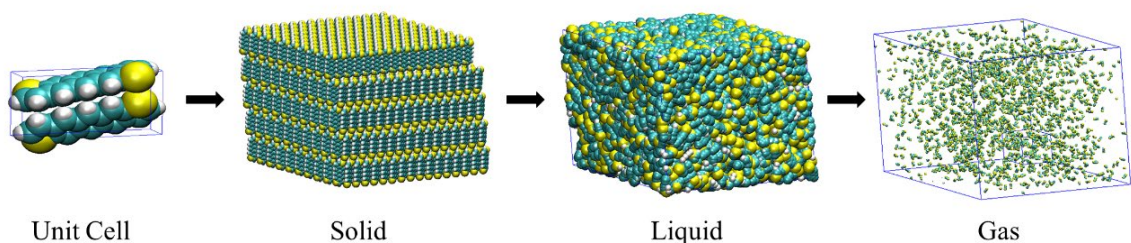
Figure 3.3. Annealing simulation work protocol.

- The pre-equilibrium simulations were carried out with the method described above, with each *NVT* and *NPT* ensemble was carried out for 2 ns.

- We simulated the thermal annealing process using the final geometry of the previous step within the *NPT* ensemble with the Parrinello-Rahman barostat. Using a 2 fs time

step, the system was heated linearly from 300 K at a rate of 60 K/ns until an isotropic melt was achieved. This was followed by additional heating to 1200 K at a rate of 40 K/ns with a 1 fs time step to achieve a gaseous state.

Since molecular diffusion rates change as a function of phase, we evaluated the mean square displacement (MSD) to determine the crystalline melting point during simulated annealing. Within a given phase, the molecular COM MSD varies linearly with time. A fitting procedure was applied to the unit phases and the intersection of these linear trends was assigned as the melting point.

X-ray powder diffraction (XRD) calculation were applied on selected bulk *anti* TES ADT configuration at different temperature steps during thermal annealing simulation with Mercury 3.6[54-57] at wavelength of 1.033 Å.

Two additional supercell constructs were used to examine their impact on the processes and temperatures at which melting occurred in the simulations. The first was a supercell where voids were purposefully created by removing small groups of molecules.[34] A cluster of 12 molecules was defined as one void unit; this number was chosen so that each dimension of the void space was similar to the length of the ADT backbone, and that the overall shape of the void was cube-like, allowing the ADT molecules exposed to the void to freely move into the open space during heating. Each void was randomly inserted into the supercell. The overall void percentage was calculated based on the total number of molecules removed. Simulations for each void configuration were repeated 10 times to test the impact of the randomness of the voids on the melting temperature.

The second construct inserted a vacuum gap along select crystalline lattices to create surfaces (slabs). These structures were created using the *gmx editconf* and *gmx genconf* packages in GROMACS. Each of the void and slab constructs were subjected to the previously described MD heating protocol. To maintain the gap configuration during initial *NPT* equilibrium stage of the slab calculations, a semi-isotropic coupling was used to turn off the pressure along *z* direction.

3.3   Results and Discussion

In the following, we begin with a brief description of the potential of mean force (PMF) simulations that were used to examine the strength of the intermolecular interactions of all ADT systems considered here. These results are then followed by those from the thermal annealing simulations of the bulk, void, and slab ADT structures. We then conclude with a description of the impact of the triethylsilylethynyl (TES) substitution on the ADT thermal transitions.

3.3.1   Intermolecular interaction via PMF simulations

The PMF simulations are used as a preliminary means to examine the impact of the molecular chemistry and symmetry on the strength of the intermolecular interactions (Figure 3.4). As expected, the intermoleuclar interactions are similar for both the ADT and TES ADT systems regardless of the symmetry of the thiophene groups (*syn* or *anti*) in the ADT core. For the unsubtituted ADT, the molecules begin to interact at ≈1.5 nm (15 Å) COM distance. When the TES groups are added, the turn-on of the intermolecular interactions begins at ≈1.9 nm (19 Å), a function of the stronger dispersion interactions induced by the TES groups; these results confirm the importance of the trialkylsilylethynyl (TAS) groups on the packing of TAS-acene molecular materials.[58-59] These distances will

be of importance when the slab simulations are considered. The potential energy minima arise at COM distances of approximately 0.4 nm for both sets of ADT, though the geometries differ whether or not that TES groups are considered. We note that at the PMF minima, the ADT COM are slightly smaller than those observed in the bulk crystal structures, and that the interaction geometries differ from those found in the respective crystal structures, with the variation being larger for the TES ADT systems as shown in Table 3.4.

Table 3.4. Potential of mean force (PMF) minima center- of-mass (COM) distances and those obtained from the respective crystal structures.

	PMF		Bulk Crystal (nm)
	Minima (nm)	Plateau (nm)	
anti ADT	0.389	1.510	0.474
syn ADT	0.400	1.520	0.488
anti TES ADT	0.404	1.910	0.673
syn TES ADT	0.404	1.910	0.630

These differences can be attributed to (i) effects that arise from many-body nature of the packing in the bulk crystals – in the PMF, the interactions only consider two molecules in vacuum – and (ii) intrinsic errors based on the deviations in the force field parameters to describe the systems.
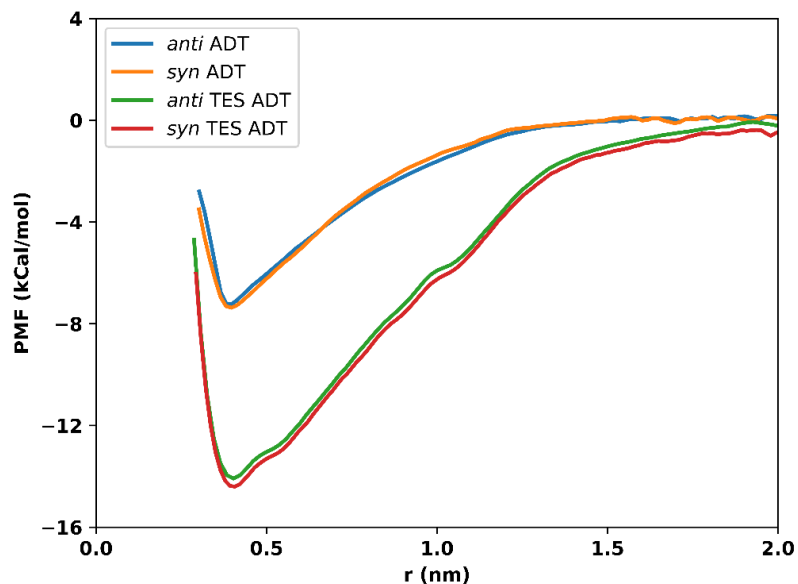
Figure 3.4. Potential of mean force (PMF) profiles of *anti* and *syn* ADT and TES ADT molecular pairs pulling along the axis perpendicular to the molecular planes.

3.3.2 ADT phase transformations during thermal annealing

Thermal annealing of bulk crystals. Among the more straightforward ways to determine the melting point (T_m) of bulk, periodic systems from simulations is via density *vs.* temperature plots (Figure 3.5), where discontinuities in the density indicate a phase change or some manner of molecular rearrangement. The heat capacity at constant pressure (C_p) *vs.* temperature also serves as an efficient indicator of phase change since sharp peaks indicate exothermic or endothermic processes. Notably, C_p sharply peaks at discontinuities in the density plots, providing another identification of T_m. Finally, we use the total energy of the system to identify first-order transitions (Figure 3.6). Melting transitions are identified as sharp discontinuities in the total system energy (sum of the potential and kinetic energies) *vs.* temperature plots. The simulated T_m was identified as the temperature at the center of the discontinuity.
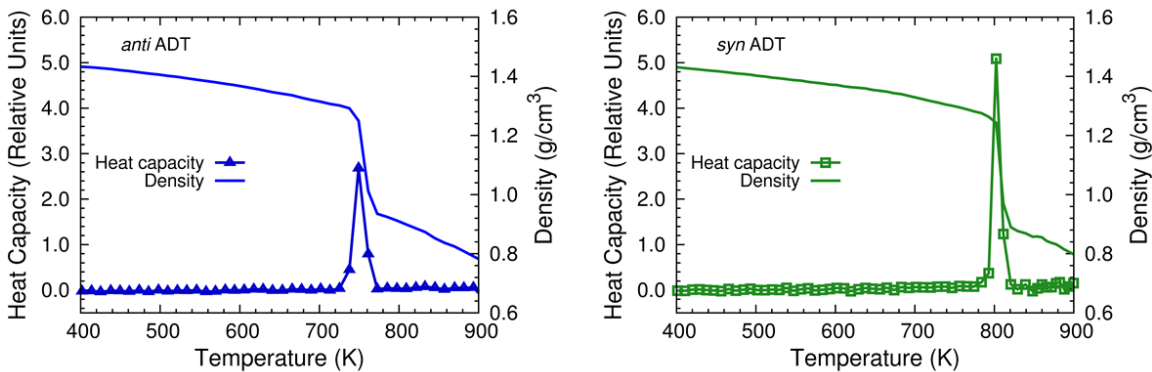
Figure 3.5. Density and heat capacity (C_p) *vs.* temperature plots for [top] *anti* and [bottom] *syn* ADT bulk crystals.
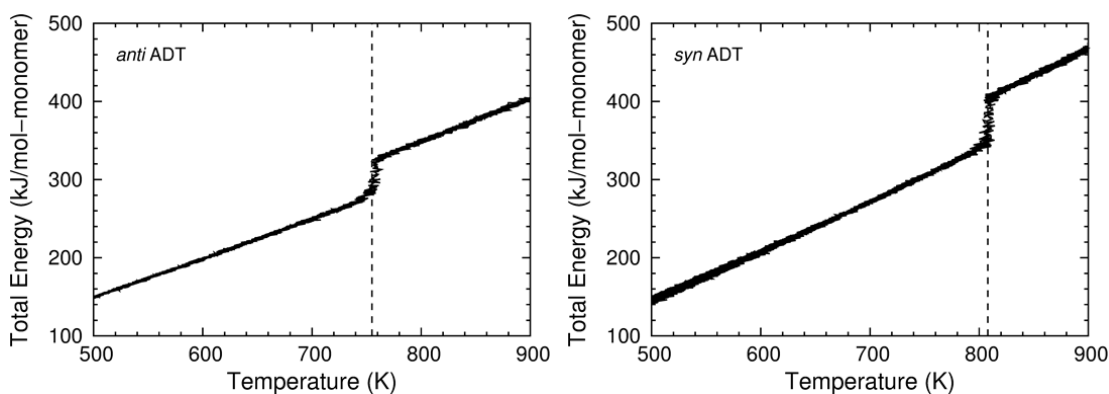
Figure 3.6. Total energy profiles for [top] *anti* and [bottom] *syn* ADT crystals during thermal annealing.

From the density and energy *vs.* temperature analyses of the bulk, periodic structures, the simulated T_m of *anti* and *syn* ADT are estimated to be 750 K and 808 K, respectively. Differential scanning calorimetry (DSC) experiments[47] provide T_m for *anti* and *syn* ADT of 725 K and 720 K, respectively. Hence, these bulk simulations overestimate T_m by 25 K and 83 K, respectively. It is notable that the solid-liquid (SL) phase transitions occur over short temperature ranges in the simulations, shown as sudden discontinuities in the density and total energy *vs.* temperature plots or as sharp peaks in the heat capacity *vs.* temperature plots. Such sharp peaks, in part, can be assigned to the fact that the simulated heating took

58

place equally throughout the entire simulation box, which is unlike experiments where melting might be expected to first occur on the materials surface. Overall, these results demonstrate qualitative and quantitative failures that arise from spurious superheating due to the simulation constraints.

Thermal annealing of bulk crystals with voids. The T_m derived using the fully periodic systems are clearly too large. Hence, it is important to evaluate if different methods can allow for more representative descriptions. To explore alternative methods, we begin with the so-called void method, where groups of molecules are removed from the bulk structure.[34] There are a number of considerations that need to be made when implementing this method. It is important to note that the ADT molecules are essentially rigid rods packed in tight configurations (density = 1.53 g/cm^3). Hence, if only single, isolated molecules are removed from the system, the neighboring molecules can readily occupy the resulting voids through only small translations or rotations during equilibration. Here, such defects are not sufficient to modify the T_m significantly from the periodic bulk simulations, unless many voids are created. For such simulations, a sufficient amount of the crystal must be kept to maintain the integrity of the crystal structure; if too many voids are introduced, the crystal becomes mechanically unstable and collapses without the hallmark discontinuity expected for SL phase transitions.[60-62]

Instead of removing only a single molecule from many points in the supercell, we removed small groups consisting of 12 molecules to create the voids. In this case, the ADT molecules exposed to the void can move more freely, and over larger distances, into the open space during heating. The total void percentage was calculated according to the total number of molecules removed from the system. We randomly made 10 configurations for

each void percentage to generate appropriate data for statistical relevance. A comparison of the resulting void systems by removing either a one molecule or 12 molecule unit is shown in Figure 3.7.
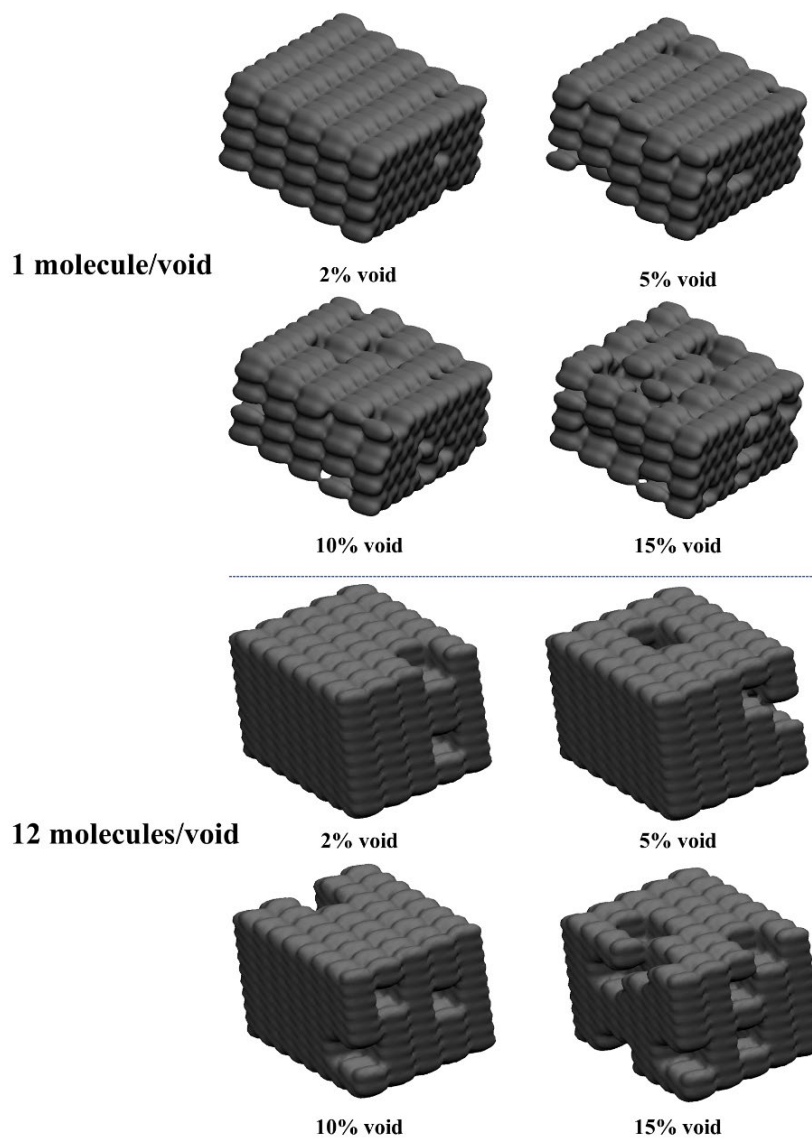
Figure 3.7. Representations of the void models implemented. (Top) Each void was created by removing one molecule to create the void. (Bottom) Each void was created by removing a group of 12 molecules to create the void. The void percentage was calculated based on the total number of molecules removed from the bulk crystal.

The relative MSD as a function of the annealing temperature for the (12 molecule) void systems are given in Figure 3.8. T_m is interpreted by the points of intersection found for two linear fits in different regions of the curves. The results from these methods follow the trends established by the fully periodic bulk calculations, though the T_m decrease. With 2% voids, T_m decreases from 775 K (bulk) to 752 K for *anti* ADT and 804 K (bulk) to 753 K for *syn* ADT. As the number of voids increases, the shifts of the MSD profiles become less pronounced. From 10-30 % voids, the calculated T_m is independent to the number of voids, as show in Figure 3.9. The temperature corresponding to this plateau region is taken to be the T_m of the unsubstituted ADT, and are estimated at 720 K for *anti* ADT and 710 K for *syn* ADT. While there is still a 10 K to 20 K variation in T_m, these results are qualitatively consistent with experiment, and provide insight into the impact of increased disorder in ADT materials upon heating. A series of snapshots (Figure 3.9) from the void simulations reveal that the voids allow larger degrees of translational and rotational freedom when compared to the bulk simulations, with adjacent molecules filling the void space during the annealing process.
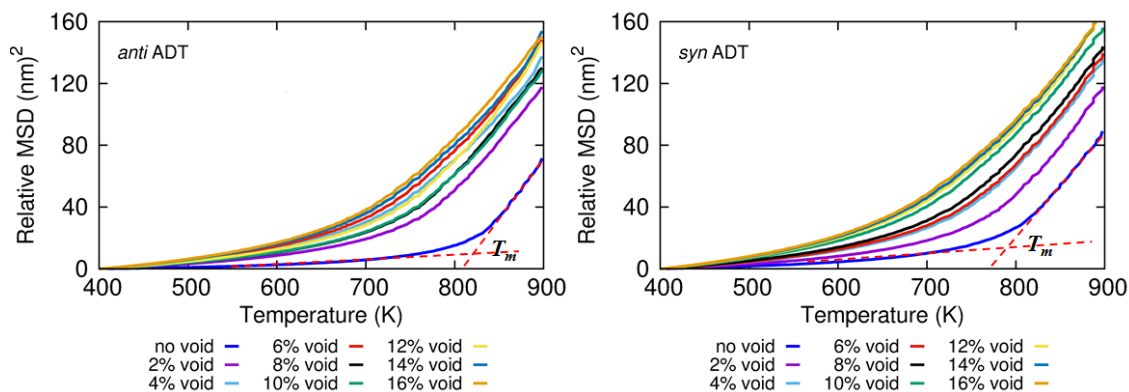
Figure 3.8. Relative MSD as a function of anneal temperature of the *anti* and *syn* ADT systems with voids of varying percentage. The MSD of the void free supercell for each system is also included. Dashed lines indicate the two linear trend lines of solid and liquid phases, and the intersection T_m is marked for reference; one example is given in each plot.
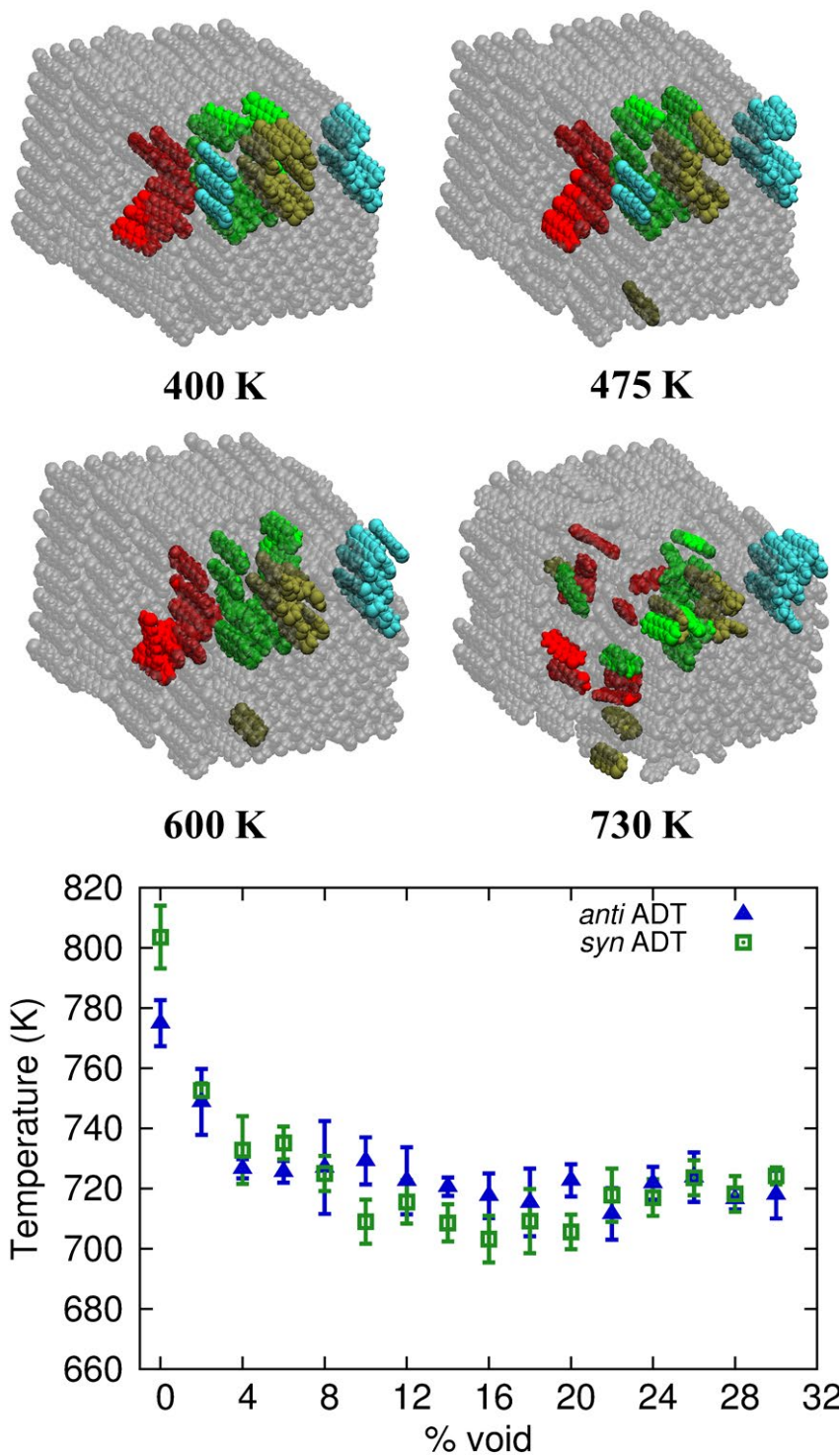
Figure 3.9. [top] Snapshots from one of the *anti* ADT systems with 14 % voids shows the melting process from 400 K to 730 K. [bottom] Melting point as function of void percentage determined from the MSD.

Thermal annealing of slabs. While the defects induced in the void systems lead to better agreement with the experimental T_m, one may question how such a system relates to those used in DSC experiments. During DSC, for instance, there are definite free/exposed surfaces that will first encounter the heat applied during the experiment. To examine such a consequence, a series of periodic structures were created in which a vacuum gap was installed along explicit crystallographic planes to create slabs – here, the (001), (100), and (010) crystal faces – and these structures were then used in the thermal annealing simulations (Figure 3.10).
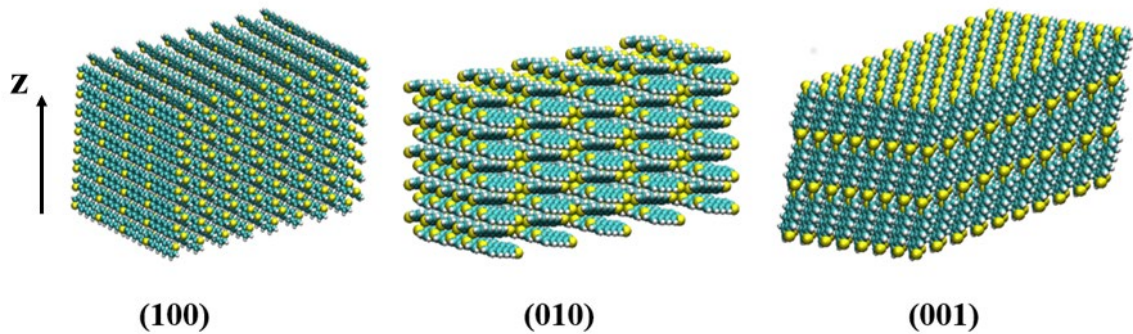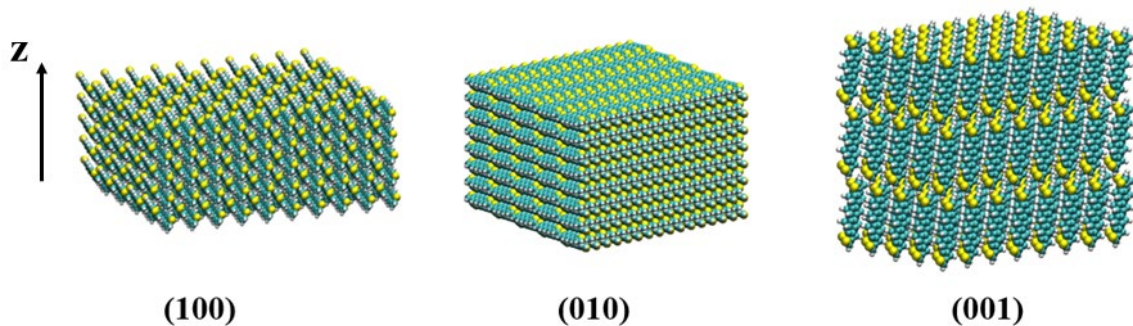
Figure 3.10. *Anti* (top) and *syn* (bottom) ADT slabs; the vacuum gap is along *z*-direction.

As shown in Figure 3.11, the (001) slabs present similar C_p as the fully periodic ADT, while the (100) and (010) slabs show significantly decreased C_p and T_m. For both *anti* and *syn* ADT, the (010) slab presents a T_m around 700 K, which is in close agreement with experiment. For the (010) slab, the molecules lie with their long axes parallel to the surface, with the molecules underneath arranged in a herringbone packing configuration. Hence, each molecule on the surface is only held in place by relatively weak C–H•••π noncovalent interactions that are readily broken upon heating. Figure 3.11 depicts the melting process at this surface: As the temperature increases, thermally induced translational and rotational modes become more active. These modes eventually lead to the surface molecules breaking away to enter the vacuum gap, while the lower layers of the bulk-like molecules maintain the crystal packing. Further heating leads to the remaining molecules in the solid melting, and eventually the full liquid state being formed. The temperature range of this entire process covers about 100 K, as is represented as the broad peak in the heat capacity profile.
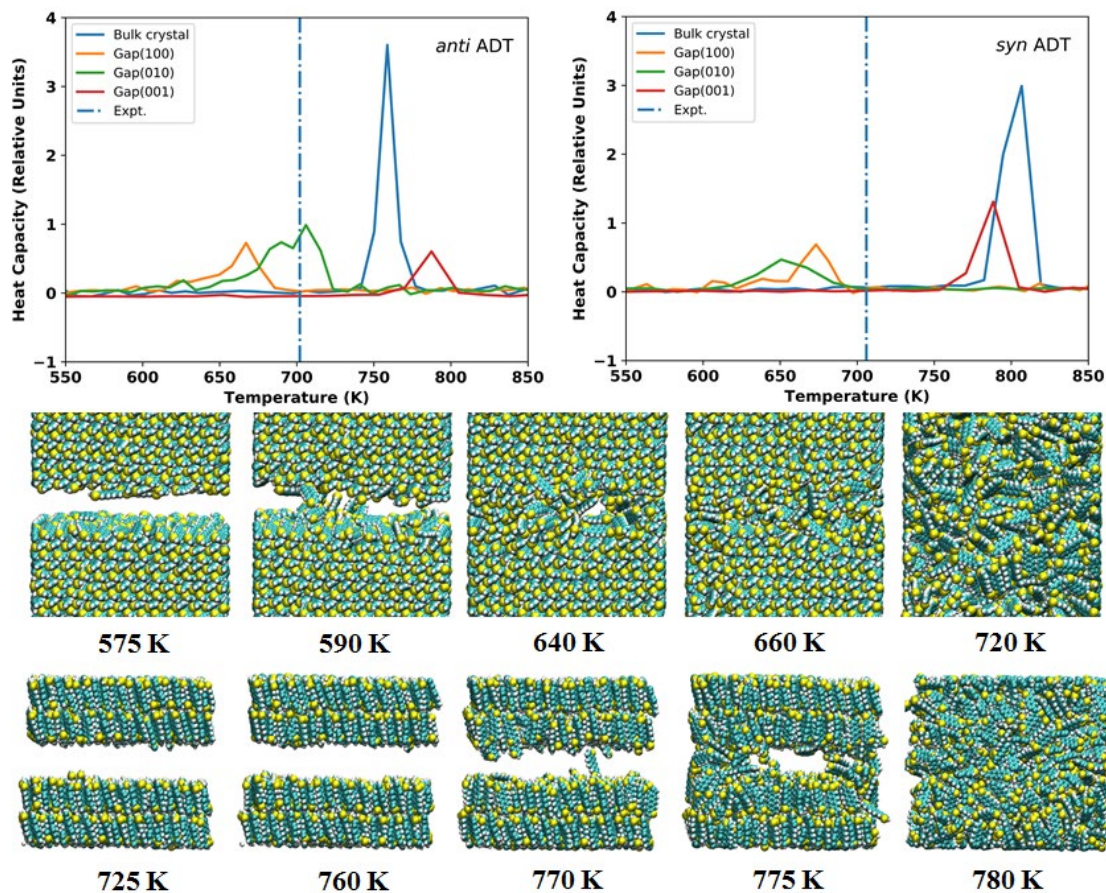
Figure 3.11. [top] Change of heat capacity as a function of temperature of bulk crystals and various slab structures. [bottom] Snapshots of *anti* ADT with gaps along the (010) (upper structures) and (001) (bottom structures) taken at different temperatures during the annealing process.

On the contrary, the (001) slab exposes the ADT short axis. Now, to escape the solid state, the molecules need to overcome intermolecular interactions that cover a larger portion of the molecular volume. As shown in Figure 3.11, even at 700 K where the (010) structure is melted, the top molecular layer of the (001) slab maintains a crystal-like packing. It is only as the temperature keeps increasing from 725 K to 770 K that the molecules in this slab escape the solid. However, once a few molecules enter the gap, the system breaks apart rapidly, and at 780 K the entire system is in the liquid state. This process is represented by a sharp peak in the heat capacity profile, which is similar to that observed from the

65

simulations on bulk crystal. More snapshots of each slab system may be found in the Figure 3.12 and 3.13.

anti ADT (100)

| 508 K | 522 K | 570 K | 600 K |

| 640 K | 660 K | 700 K | 710 K |

anti ADT (010)

| 575 K | 590 K | 640 K | 660 K | 720 K |

anti ADT (001)

| 725 K | 760 K | 770 K | 775 K | 780 K |
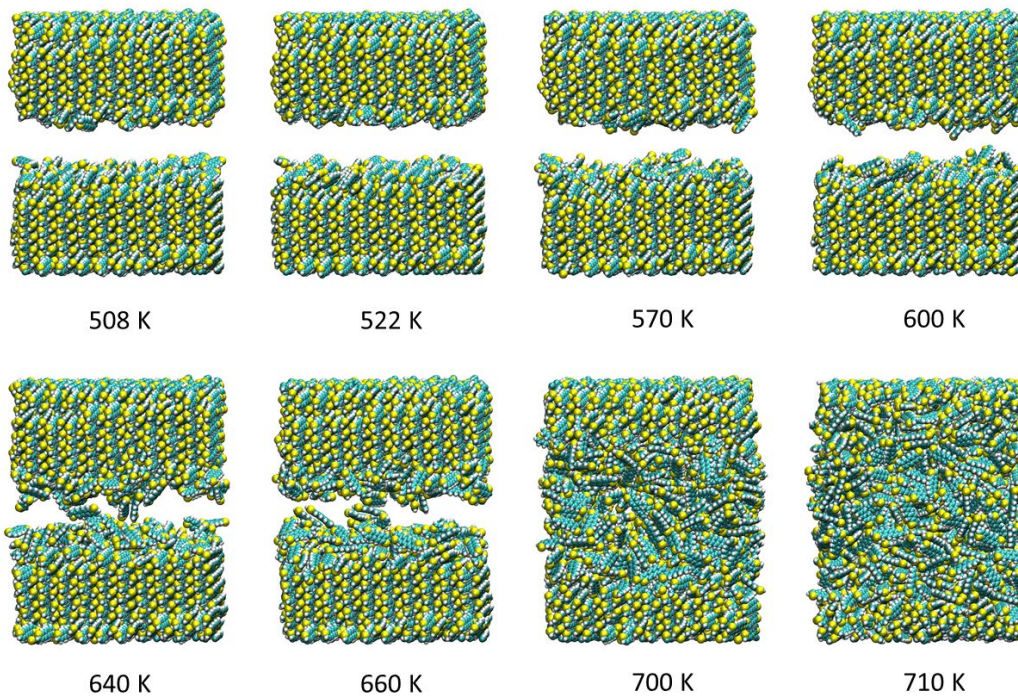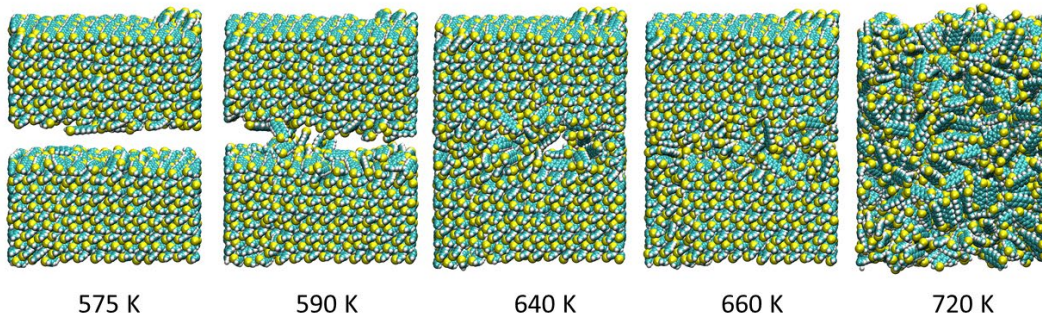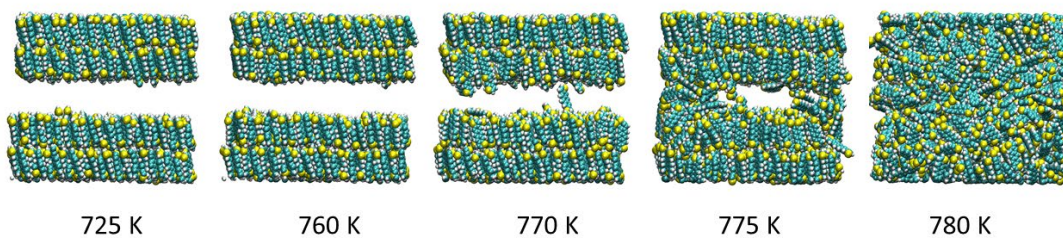
Figure 3.12. Snapshots of select *anti* ADT slabs during annealing.

syn **ADT (100)**
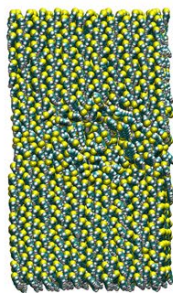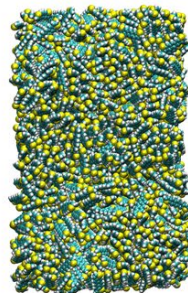
| 490 K | 550 K | 600 K |

| 620 K | 640 K | 700 K |
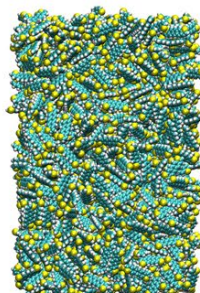
syn **ADT (010)**
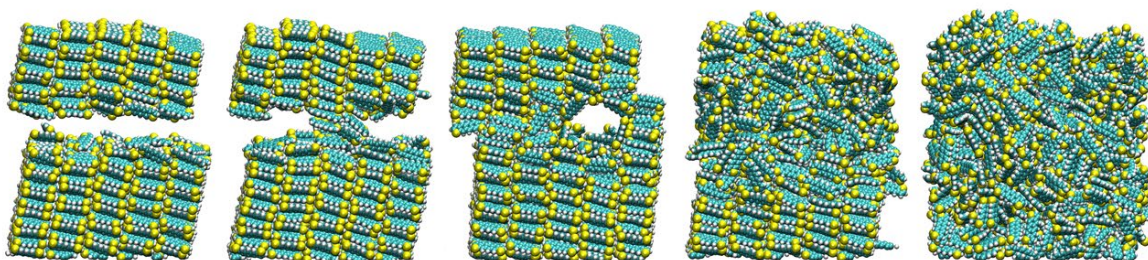
| 550 K | 580 K | 640 K | 700 K | 740 K |

syn **ADT (001)**
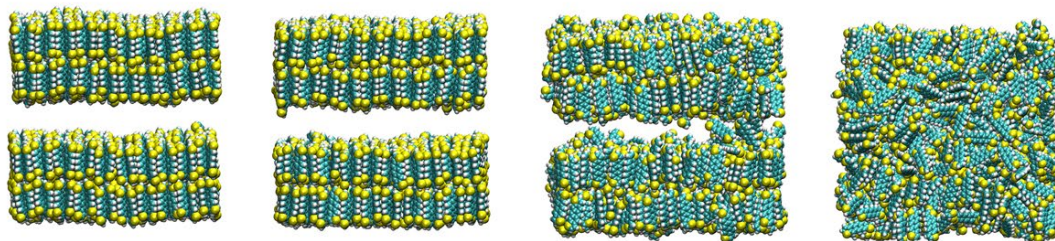
| 700 K | 760 K | 765 K | 770 K |

Figure 3.13. Snapshots of select *syn* ADT slabs during annealing.

For these slab structures, plots of the system total energy *vs.* temperature reveal the phase transitions (Figure 3.14). The T_m (onset of melting) and T_{end} (fully melted) can be acquired from the plots, which appear to be composed of three sections: (i) a linear region with increasing heat capacity followed by (ii) a roughly quadratic rise in the C_p that is followed by (iii) a linear rise in C_p. The onset of T_m was determined from the regression analysis method used by Chen and co-workers:[32] Sections (i) and (iii) were fit with linear functions, while part (ii) was fit with a constrained quadratic function. Notably, the width of each parabola can be related with a force constant that represents the force required to move the molecules from the surface into the gap. The wider parabolic curves for the (100) and (010) surfaces arise from smaller coefficients in the quadratic functions, suggesting a small force constant for melting, while the narrower quadratic curve for the (001) slab indicates that a larger force is required to extract the molecules from the solid. In general, the melting along the various slabs differs rather dramatically, as one might expect given the very different intermolecular interactions at play on each surface. We note that this conclusion diverges from that of Chen and co-workers for the isotatic polypropylene,[32] but makes physical sense given the anisotropic nature of the ADT.

We do note that the T_m derived from the total energy *vs.* temperature plots differ from those derived from the C_p *vs.* temperature plots. This variation is due to how the T_m are assigned: In the C_p plots, sharp peaks are used to identify T_m, while in the total energy plots, the T_m was defined as the "onset of melting", while the T_{end} represents the temperature when system is fully melted. Here, the onset of melting commences when the surface molecules being to migrate into the gap, though the majority of the systems remain crystal-like.
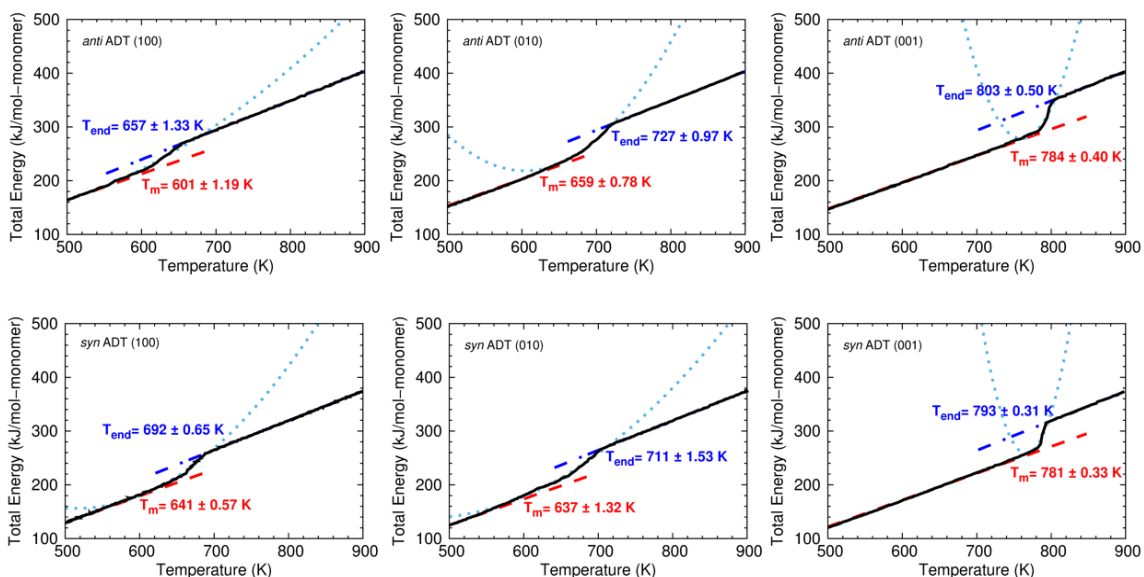
Figure 3.14. Total energy *vs.* temperature profiles for *anti* and *syn* ADT slab systems.

For the slab systems, an additional aspect to consider is whether the width of the vacuum layer is large enough to prevent intermolecular forces acting across the gap to influence the melting, and how different gap widths influence the determination of T_m; ideally, T_m should be independent of the size of the gap. To explore this feature, a series of *anti* and *syn* ADT systems with different gap widths were created for the (010) surface and the same melting approach was applied. Figure 3.15 shows T_m as a function of the gap width, which decreases with increasing gap width up to a critical point at 15 Å, after which no further change in T_m is observed with increasing gap width. This in part can be explained by the PMF simulations, which show that the intermolecular interactions become very weak to nonexistent for ADT at approximately 15 Å – *i.e.* this is the point at which molecules on the two surfaces that form the gap do not "feel" each other. It is also notable that to maintain the gap during initial equilibrium step, a sufficient gap width is required to overcome the interaction between two building blocks across the vacuum (see Figure 3.16).
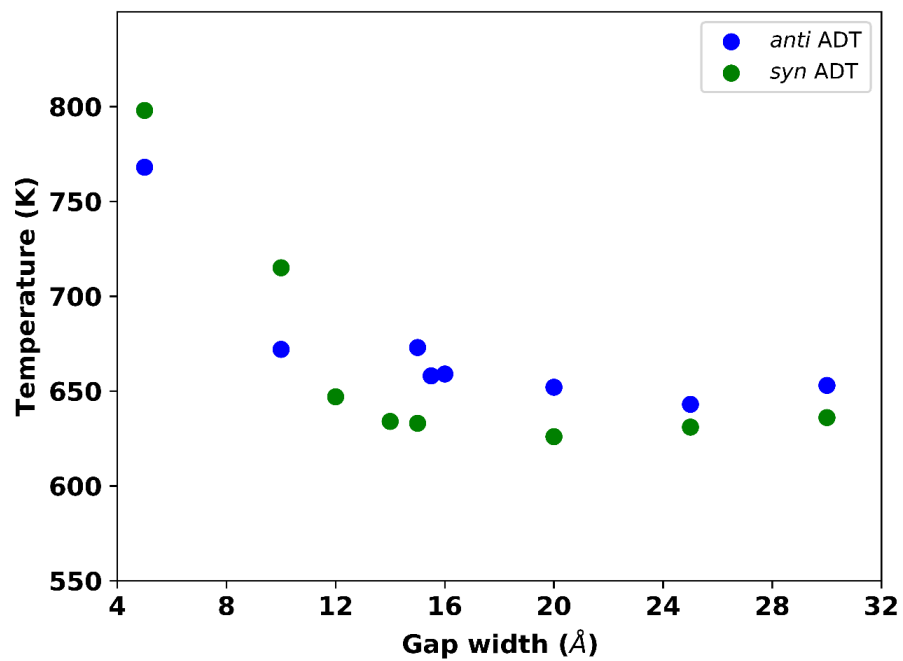
Figure 3.15. T_m as a function of the (010) gap width for *anti* (blue dot) and *syn* (green dot) ADT.
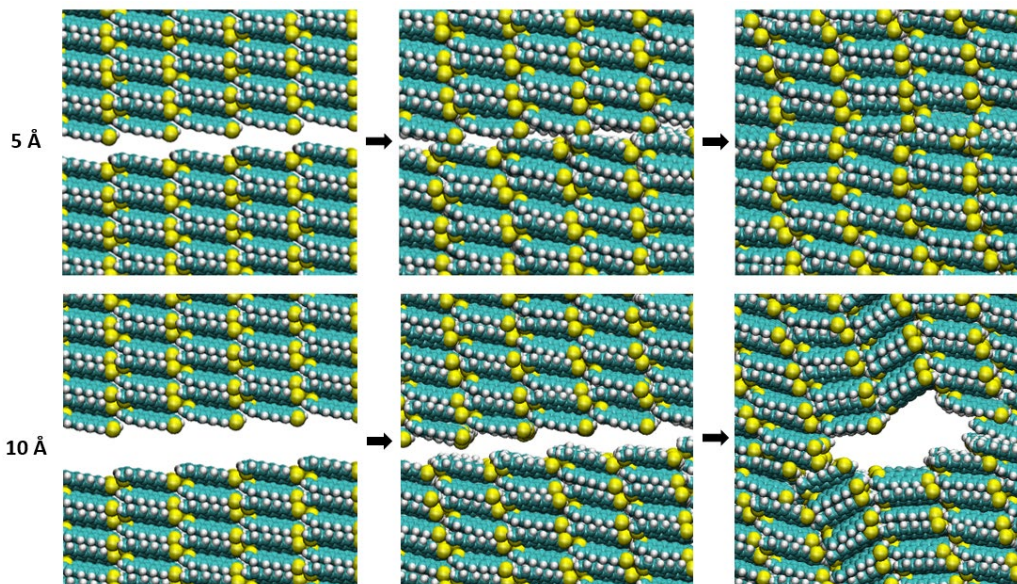
Figure 3.16. *Anti* ADT with 5 Å and 10 Å vacuum gap along the (010) surface to demonstrate differences in the melting process as a function of vacuum gap width during NVT equilibrium.

3.3.3 Thermal annealing of the anti and syn TES ADT systems.

We now turn to the TES ADT systems. Here, it is important to recall two important distinctions: (i) the ADT now contain the triethylsilylethynyl (TES) arms that are appended synthetically to enhance solubility and (ii) these groups change the ADT herringbone packing configuration to one that is brickwork for *anti* TES ADT[63-64] or a one that adopts a monoclinic lattice with two molecules per unit cell for *syn* TES ADT.[65] Starting with the bulk thermal annealing approach as applied to *anti* and *syn* ADT bulk crystals, the change in C_p as function of temperature for both *anti* and *syn* TES ADT exhibit small peaks prior to reaching the melting point, which corresponds with discontinuities in the respective density *vs*. temperature profiles (Figure 3.17). Deeper inspection reveals solid-solid (SS) phase transitions, wherein the molecules reorient. In *anti* TES ADT, the original crystal at 100 K has a brickwork packing configuration, and the SS phase transition can be described by a change in the angle formed between the ADT backbone and z-direction (defined in Figure 3.18), which changes from 70° to 100° in the temperature range from 400 K to 518 K. At 518 K, all molecules in the bulk crystal are aligned in a new brickwork-like orientation, which is maintained until 850 K when the solid melts.
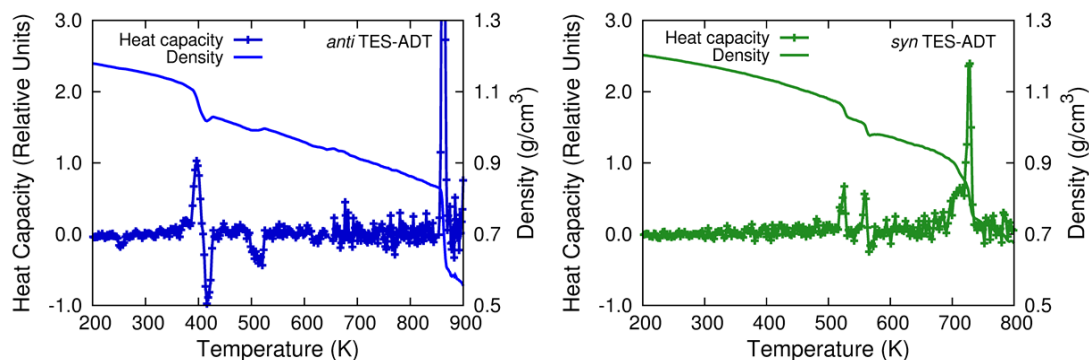
Figure 3.17. Density and heat capacity as function of temperature of [top] *anti* and [bottom] *syn* TES ADT bulk crystals.
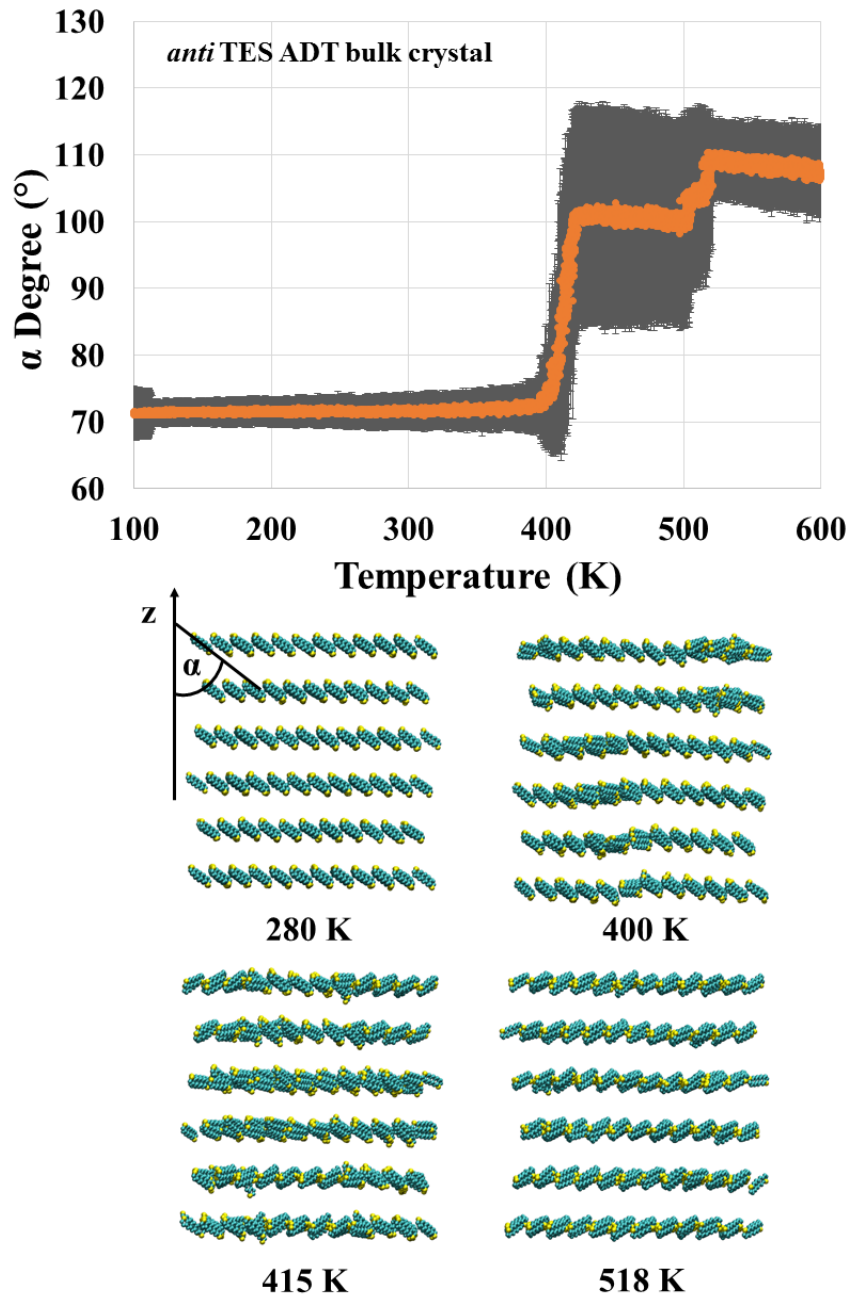
Figure 3.18. [Top] Change in angle between the *anti* TES ADT backbone and the *z*-direction as a function of temperature. [Bottom] Snapshots of the *anti* TES ADT bulk crystal during thermal annealing to demonstrate the reorientation of ADT backbone.

To further investigate the SS transition of *anti* TES ADT during thermal annealing, XRD of several geometries was calculated (Figure 3.19). Four distinct phases were identified from the powder pattern: An initial state of the bulk crystal at low temperature (100 K and

280 K; Figure 3.19), a transition morphology during thermal treatment (415 K; Figure 3.19), a reoriented morphology before melt (518 K; Figure 3.19) and a liquid TES ADT phase (870 K; Figure 3.19). Interestingly, such metastable states were observed experimentally by Yu *et al.*[66] In their differential scanning calorimetry (DSC) measurements, three crystalline structures and one amorphous state were identified within two heating cycles. Comparison of the experimental X-ray scattering patterns with our simulated XRD shows that the initial bulk crystal (100 K and 280 K; Figure 3.19) and transition morphology (415 K; Figure 3.19) showed similar patterns to the experimental α and γ phases, where α phase is the as-cast TES ADT at room temperature and the γ phase was developed during the heating process of an amorphous phase, which was formed from cooling of isotropic melt. The pattern shown at 518 K also shared similar features with another crystalline state from experiment (β phase), which was observed during the first heating cycle of TES ADT thin film, especially the distinct peak at 0.6 Å^{-1} and more narrowed peaks from 0.75 Å^{-1} to 1.25 Å^{-1}, which were not observed in other geometries at lower temperature in both experiment and simulation. This comparison suggests that upon heating, *anti* TES ADT shows three different polymorphs, while two initial and ending morphologies are more crystal-like, the intermediate transition state is a mixture of two crystalline phases. This can also be supported by the polarized optical microscopy (POM),[66] as comparing with the α and β phases, the γ phase presents a less defined morphology with smaller domain size.
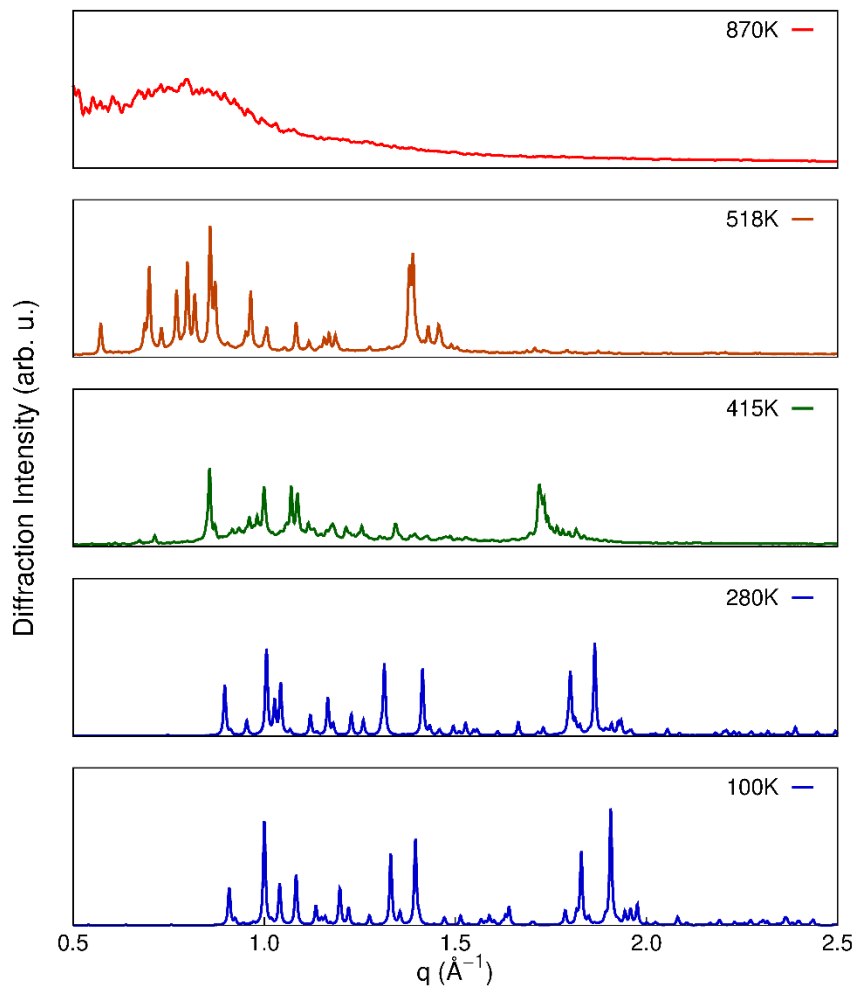
Figure 3.19. Variable-temperature XRD pattern of *anti* TES ADT during thermal annealing simulation.

Such a reorientation is also observed in the *syn* TES ADT bulk crystal. The unit cell of *syn* TES ADT contains two molecules, with an angle between two molecular planes of about 42°. As the temperature increases, the angle between the two molecules decreases and both molecules change their orientation to a more brickwork packing, as shown in Figure 3.20. Unlike the *anti* TES ADT reorientation, which occurs for all the molecules before melting, the reorientation in *syn* TES ADT occurs in only a portion of the bulk crystal, while different regions of the crystal undergo a simple increase in disorder and melting. As the

temperature continues to increase, these disordered regions act as seeds that expand to melt the entire crystal.
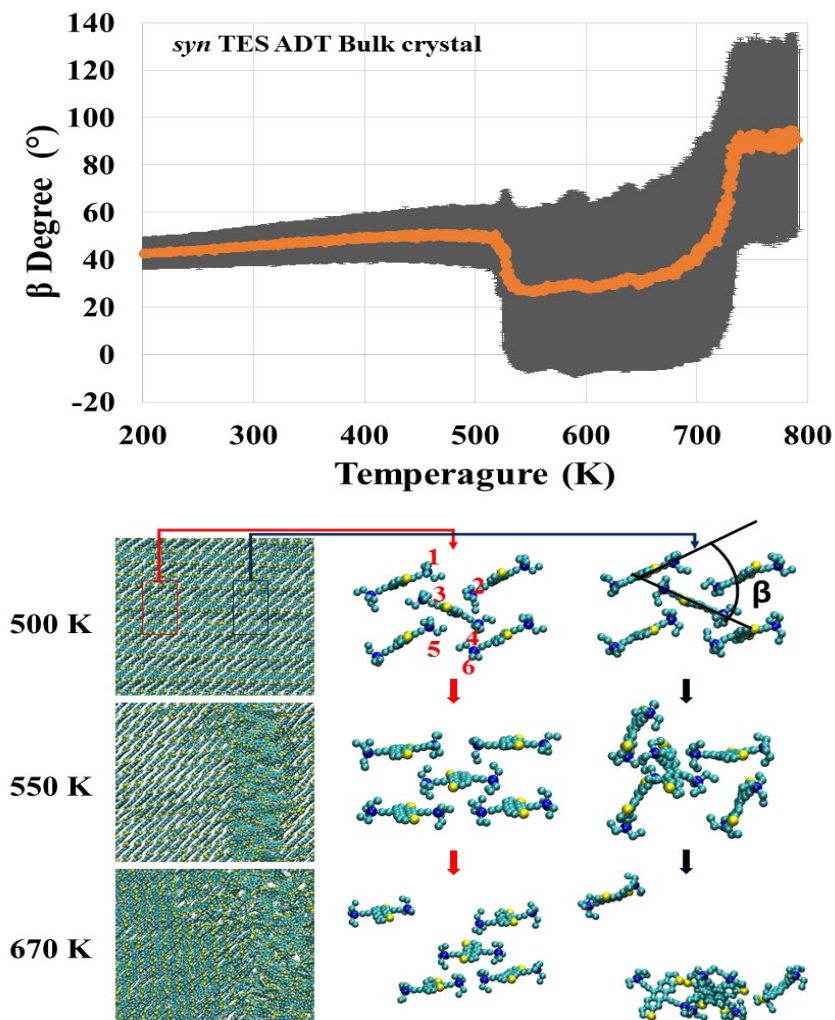
Figure 3.20. [Top] Change in angle between the backbone planes of two *syn* TES ADT as a function of annealing temperature. [Bottom] Snapshots of two parts of the *syn* TES ADT bulk crystal during thermal annealing process.

Moving to slab simulations, the *anti* TES ADT slabs show similar transitions in the heat capacity profiles, indicating that the molecules reorient in a like fashion for all surfaces considered (Figure 3.21). For the (100) and (010) slabs, the ADT backbone is more exposed, leading to a decrease in T_m compared with the bulk crystal. The (001) slab has the TES

side group exposed, and this surface shows a similar heating profile with the bulk crystal. The reported melting point for *anti* TES ADT is around 405 K,[65] which is much lower than the simulated melting range in all systems; however, this melting point falls within the reorientation temperature range noted above, suggesting there may be connections between the experimental melting process and reorientation seen in the simulations. (Figure 3.22).
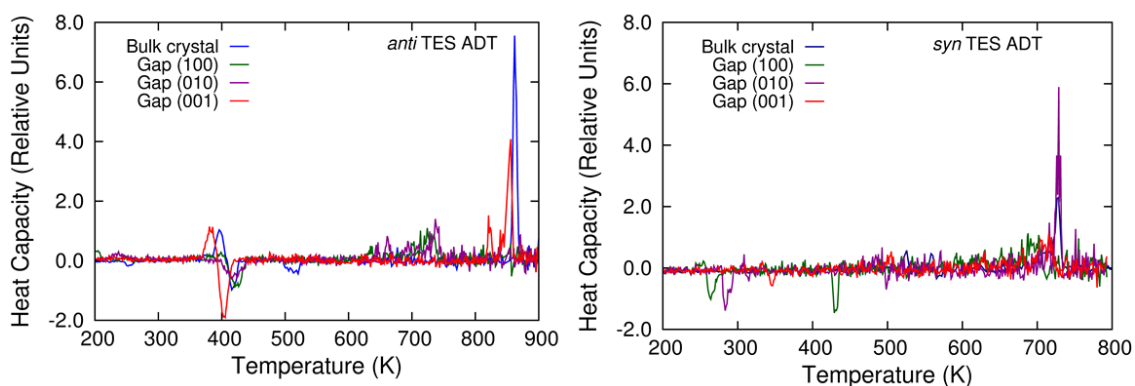
Figure 3.21. Change of heat capacity as a function of temperature of for [top] *anti* and [bottom] *syn* TES ADT bulk crystals and crystals with gaps along different surfaces.
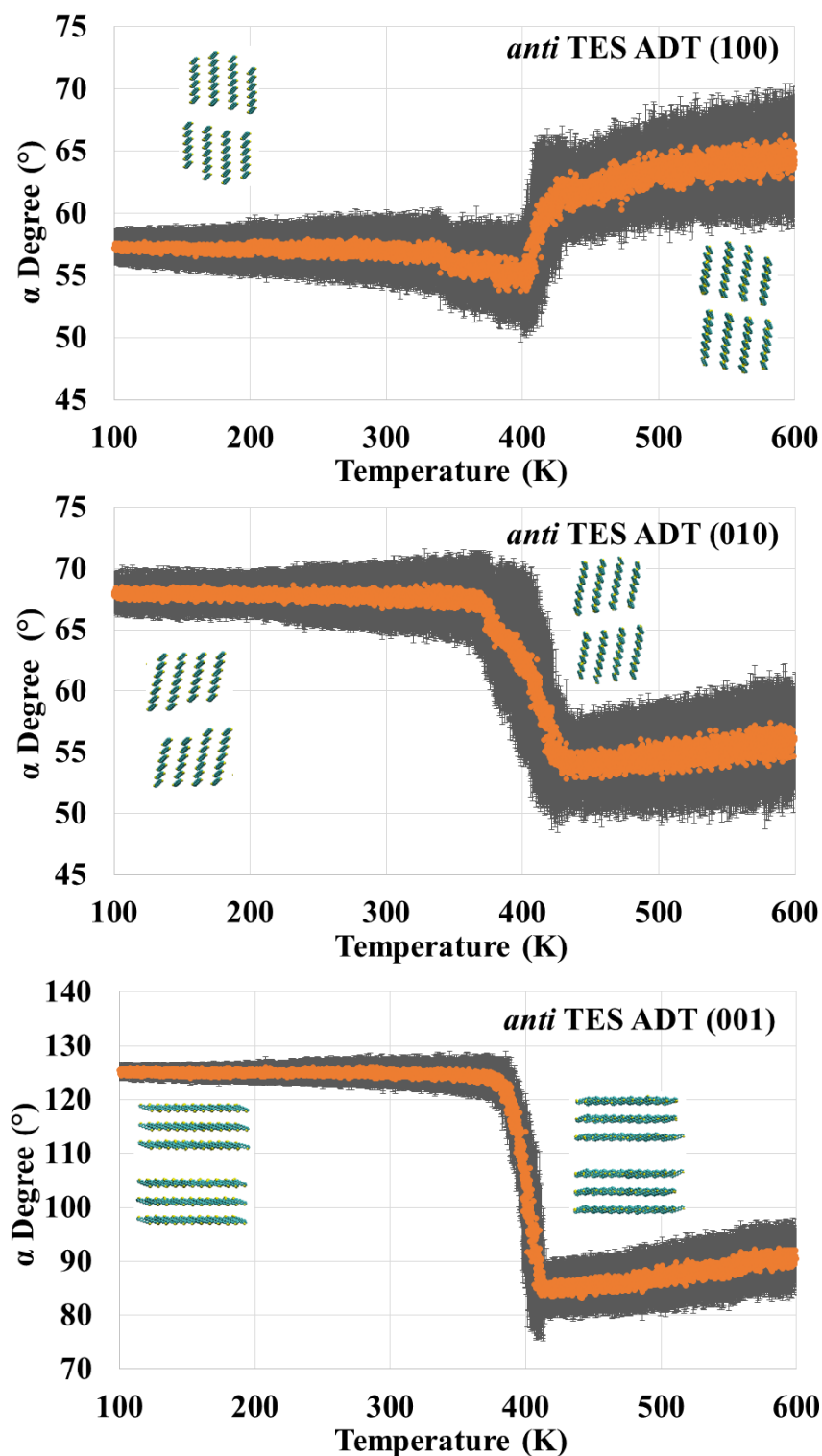
Figure 3.22. The angle between *anti* TES ADT backbone long-axis vector with respect to the *z*-direction as function of the annealing temperature of different slab systems. The inset snapshots show the backbone directions before and after reorientation.

The *syn* TES ADT gap systems exhibit distinct thermal ranges in terms of molecular reorientation events. Particularly, the (100) surface exhibits an additional peak at 430 K. Deeper analysis of the angle distributions between the two molecules in the same unit cells reveals that the (100) slabs go through two steps to form the final brickwork-like packing feature: At 270 K, the angle between two molecules decreases from $38 \pm 4°$ to $26 \pm 16°$, and this configuration is maintained until 430 K, where the angle further decreases to $16 \pm 9°$ until the system starts to melt at 580 K (Figure 3.23). The (001) slab system exhibits the lowest melting temperature at 510 K, which is still significantly larger than the experimental melting temperature at 390 K. From these results, it is hypothesized that disorder in the experimental *syn* TES ADT sample also contributes to the lower melting temperature. Additional snapshots of the *syn* TES ADT slabs showing the reorientation during annealing process can be found in Figure 3.24.
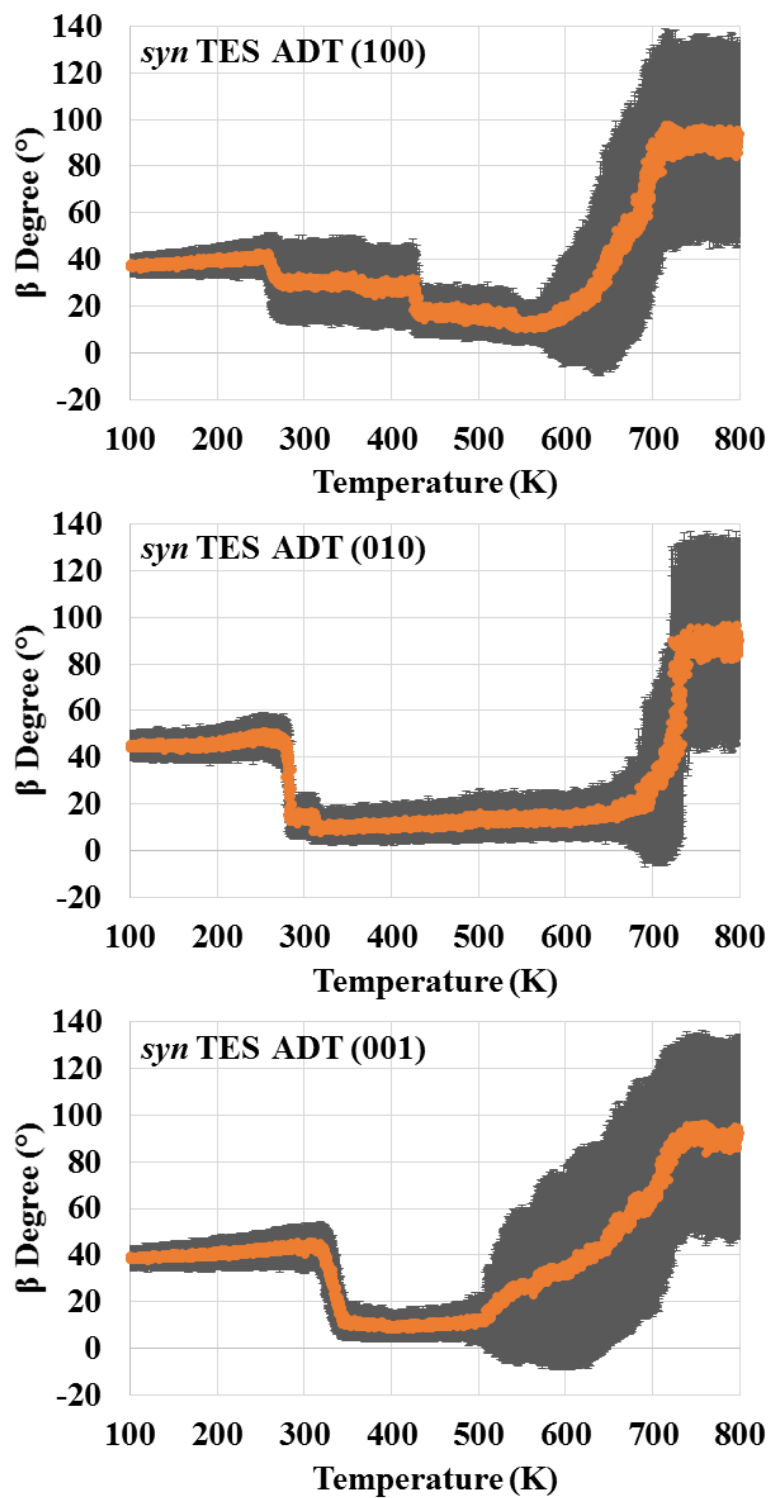
Figure 3.23. Angle between the two molecular planes in the same unit cell as a function of temperature.
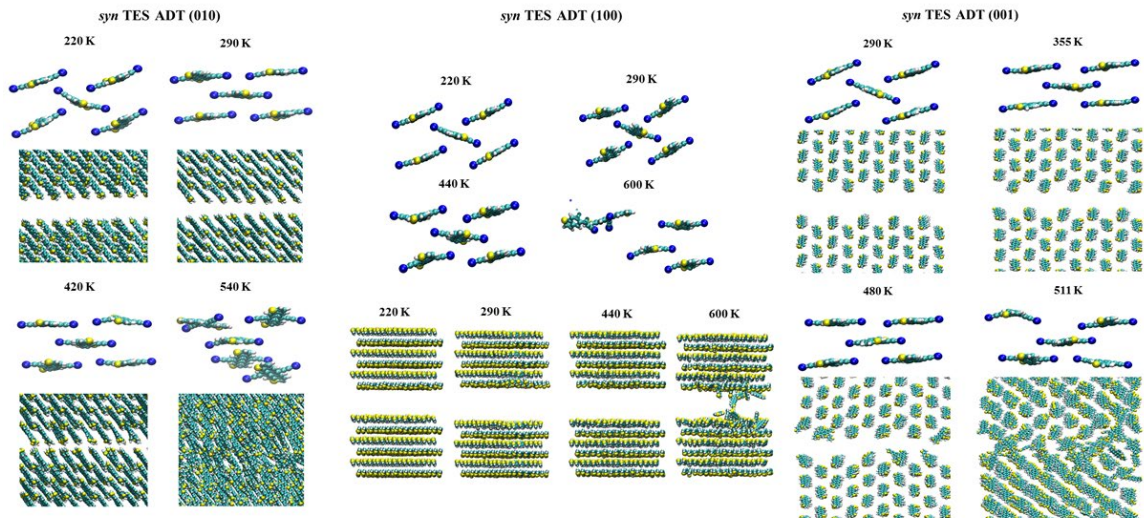
Figure 3.24. Snapshots of three *syn* TES-ADT slab systems during thermal annealing, showing the molecular reorientation before melting.

The reorientation of the *syn* TES ADT systems during thermal annealing can also be determined through the radial distribution functions (RDF) of Si-Si pairs among molecules in different layers. As shown in Figure 3.25, the peak at 0.7 nm represents the Si-Si distance between two adjacent layers, which as the temperature increases, decreases from 0.7 nm to around 0.5 nm (Pair: 1-2). This change indicates a reorientation of two layers from a monoclinic lattice[65] to a head-to-tail configuration. Another significant change of the RDF is the peak at 1.4 nm, corresponding to the long Si-Si distance between two molecules in the same unit cell, which shifts from 1.4 nm to 1.0 nm. This shift indicates that the reorientation of the molecules in the unit cell changes from edge-to-face to a brick-work configuration.
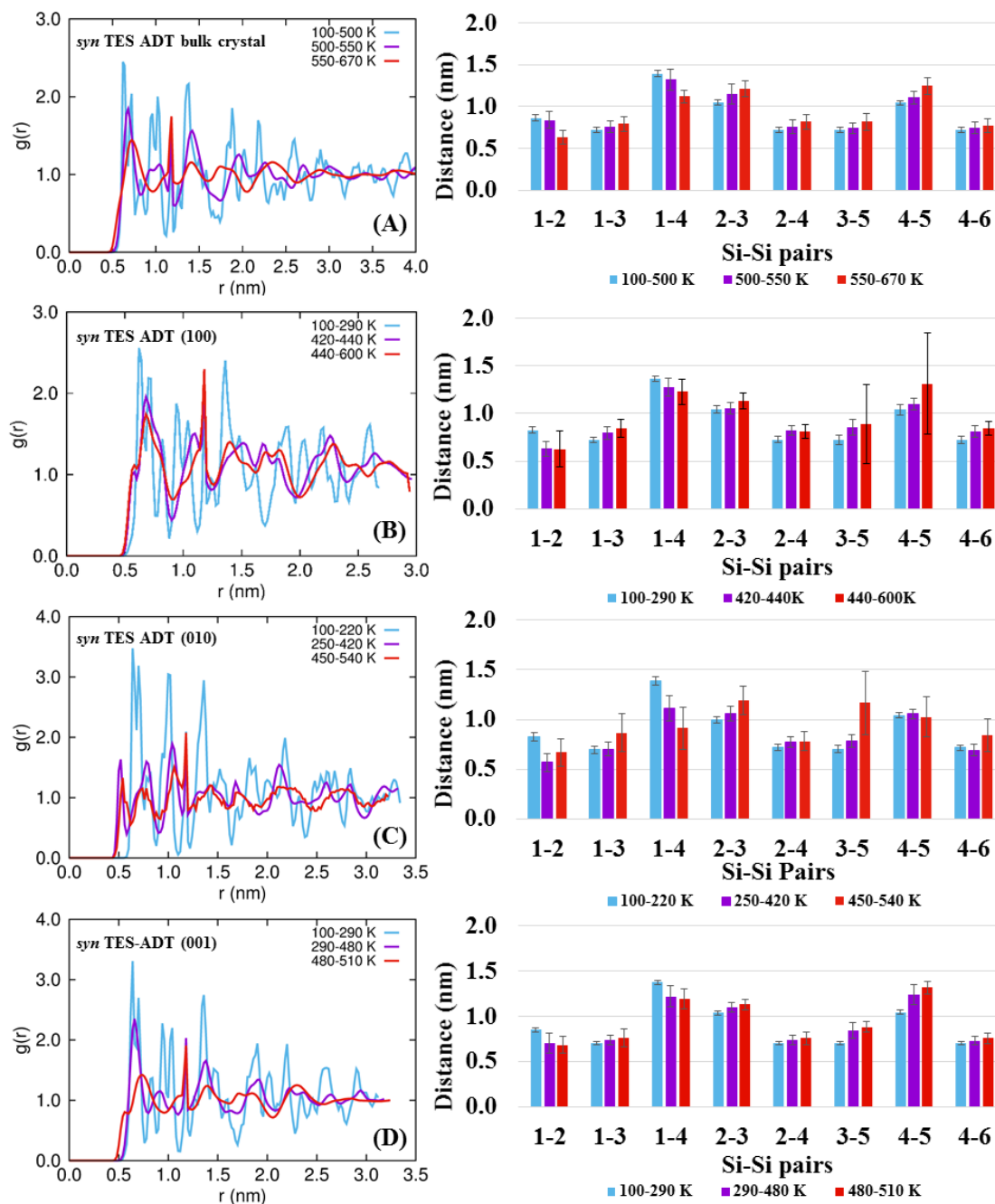
Figure 3.25. (Left) Radial distribution functions $[g(r)]$ for Si-Si pairs in the *syn* TES ADT bulk crystal and slab systems. (Right) Distances of Si-Si pairs at various stages of the thermal annealing process. The Si numbering is given in Figure 3.20.

81

3.4   Conclusion

Thermoanalytical techniques offer distinctive capabilities to employ a macroscopic measurement to understand how molecular-scale features impact the solid-state packing of OSC. Further insight can be derived through atomistic MD simulations, provided that the simulations deliver results that are in line with experiment. Here we explore the phase transitions upon the heating of *anti* and *syn* ADT and TES ADT derivatives. Simulations of the melting process using PBC bulk crystals show strong superheating effects, with the effect more significant for the TES ADT molecules. Providing free space for molecules to move and the opportunity for increased disorder – either through the introduction of voids into the supercell or the creation of free surfaces – reduces superheating effects rather dramatically. For the *anti* and *syn* ADT systems, a small number of voids accelerates the melting process, and can result in good agreement with experimentally determined T_m. The slab systems show a strong dependence of T_m with respect to the exposed surface, which is a consequence of the molecular anisotropy. Again, good agreement with experiment can be obtained with the slab simulations, with these models providing opportunities to mimic the melting processes expected in these crystals. For the TES ADT molecules, the free surfaces had minimal effect on accelerating the melting process, with the T_m derived for all exposed surfaces being similar to the bulk crystals. However, distinct SS transformations were observed for the TES ADT systems, with the temperature range for these transitions similar to the reported T_m . Investigation of the molecular packing configurations reveals significant TES ADT reorientations during these SS transitions.

Notably, the atomic-level details pertaining to the nature of the phase transitions in these ADT-based OSC provide critical information as to how changes in chemical structure impact molecular motion during annealing. Such information pertaining to how the molecules move and disperse upon heating can be correlated with expectations as to how changes in molecular chemistry may affect the nucleation and growth of these materials. Simulations are currently ongoing into the nucleation and growth of these systems in order to demonstrate the robustness of these correlations, with the goal of increasing the knowledge required to rationally engineer OSC crystal packing.

DETERMINING THE FREE ENERGY OF MIXING THROUGH MOLECULAR

DYNAMICS SIMULATIONS

4.1 Introduction

Phase separation is a process that takes a mixture from a homogeneous nonequilibrium

state to an inhomogeneous equilibrium state, and is a common phenomenon that occurs in

multicomponent systems. The process can be triggered by several conditions, such as

concentration,[1, 2] pH differences,[3] or thermal variations.[4] For a liquid–liquid solution, the

phase separation separates the system into two immiscible liquid fractions, which differ in

concentration, and can occur when the intermolecular interactions within a single

component are stronger than those interactions among the different components that

comprise the mixture, overcoming the entropic tendency to maintain the system as a

mixture.[5]

Controlling phase separation is critical in a diverse array of applications, such as the

separation of oils from wastewater via membranes,[6] the fabrication of nanofibrous

scaffolds for tissue engineering,[4,7] and drug delivery.[8] Another widely used application is

to control the morphologies of organic thin films. In addition to the structures and chemical

compositions of the individual molecules or polymers, the solid-state morphologies of thin-

film organic semiconductors (OSC) are determined by the processing conditions. While

the current application of organic light-emitting diodes (OLED) in display technologies

relies on vapor deposition, there is a tremendous push to optimize solution processing (*i.e.*

printing) capabilities to enable low-cost production at large scale and realize conformal

additive manufacturing. Depending on the OSC and intended application, the formulation of the printing solution (*i.e.* ink) can vary in complexity. In bulk heterojunction (BHJ) organic photovoltaics (OPV), for instance, controlling the degree of phase separation of the binary or ternary material blend is critical to material performance.[9, 10] While much of the early efforts to print BHJ OPV relied solely on halogenated solvents, work by Bazan and co-workers demonstrated that the addition of a small fraction of a high boiling point solvent, such as 1, 8-diiodooctane (DIO), 1-chloronaphthalene (CN), or diphenyl ether (DPE), to the solution could enable a dramatic change to the nanoscale phase separation in the OSC thin film.[11] Across the literature, OSC deposited with these low-volatility solution additives have facilitated generally improved OPV performance when compared to OSC active layers printed from halogenated solvents on their own,[12-17] though this is not always the case. The most commonly used host solvents to for OSC are halogenated solvents, such as chlorobenzene (CB), *o*-dichlorobenzene (*o*-DCB) or chloroform, which show excellent solubility of many materials. However, it should be noted that there is a desire to move away from these types of solvents due to toxicity and environmental and safety hazards for large-scale industrial applications. Recently, several non-halogenated solvents and additives have been introduced as "green solvents" to make low toxicity, eco-friendly solutions for the processing of OSC, including 1,2,4-trimethylbenzene (TMB) and 1-phenylnaphthalene (PN)[18, 19], and isopropyl alcohol (IPA) and tetrahydrofuran (THF)[17]. Notably, the choice of primary solvent and additive to implement in such ink formulations remains highly empirical, and it is often through trial-and-error approaches that appropriate ratios of the ink components are determined. If such Edisonian tactics are to be overcome

and *a priori* processing design guidelines established, there is a tremendous need to understand at a fundamental level how the primary solvent and additive work in concert.

A crucial parameter that is required to develop this requisite insight is the free energy of mixing (ΔG_m) for all components that comprise the solution. From the standpoint of molecular dynamics (MD) simulation methods, the determination of ΔG_m is complicated by the fact that the determination of the entropy of mixing (ΔS_m) is not straight forward. Methods such as umbrella sampling,[20] Widom particle insertion,[21] and thermodynamic integration,[22] can effectively probe the entropy of an ensemble, though each has potential complications depending on the system under investigation. Another means to determine entropy is to evaluate the system vibrations. Here, the system thermodynamic characteristics can be evaluated within the context that the ensemble density of states (DoS) is comprised of harmonic oscillators. While such an assumption is generally valid for solids, the anharmonic nature of low-frequency and diffuse vibrational modes in liquids and gases severely limits the assumption.[23] To overcome this constraint for liquids, Lin, Blanco, and Goddard proposed the two-phase thermodynamic (2PT) model,[24] as described in Chapter 2, which has been shown to provide accurate determinations of the absolute entropies and free energies for a variety of liquid systems, including those with considerable chemical and physical complexity.[23-40]

Given this background, we are particularly interested in exploring the solution processing of OSC during the post annealing process, which often involves multi-components in the solution. Here, as a first step, we apply a series of Lennard-Jones particle simulations to explore the phase separation of binary and ternary systems and determine the ΔG_m by applying the 2PT approach to extract the entropic contribution to mixing. We then repeat

the analysis with atomistic MD simulations of binary and ternary mixtures of small molecules. Finally, we report on the application of this method to determine ΔG_m for of organic solvents and additives that are widely used in the OSC processing. By varying the concentrations of the components in these systems, we aim to chart the entire ΔG_m surface the solution may follow during the drying process. The methods developed here provide a framework for further investigations of such multicomponent systems across a range of applications.

4.2   Computational Models

4.2.1   Lennard-Jones (LJ) model

We built the LJ models for binary and ternary mixtures using the parameters of argon. This simple model system allowed us to precisely tune the intermolecular interactions to achieve different mixing conditions. From these models, we used the 2PT method to determine the entropy of each mixture, and in turn ΔG_m for a range of concentrations.

4.2.2   Molecular models

4.2.2.1   Mixtures of simple solvents

We selected several common solvents to make binary and ternary solutions in order to extend the knowledge developed from the LJ models. These solvents were chosen based on their known solubilities to give a range of expected phase separation. Each of these solutions corresponds to one mixing condition as listed in Table 4.1.

Table 4.1. Selected solvents to make ternary solutions

	Molecule A	Molecule B	Molecule C
Miscible	1, 2- Dichlorobenzene (*o*-DCB)	Hexane	Toluene
Immiscible	Water	Hexane	Benzyl alcohol
Partially Miscible	Water	Methanol	Hexane

4.2.2.2   Organic solvent – additive mixtures

We selected organic solvents and additives that are widely used in solution based OSC

processing method, as shown in Figure 4.1. We also selected one non-halogenated solvent

(as a "green solvent"), introduced by Zhao. et al, [41] 1, 2, 4-trimethylbenzene (TMB), and

1-phenylnaphthalene (PN) as the additive. Notably, the OPV processed with this

hydrocarbon solution system showed improved OSC morphology and performance when

compared to the same material processed from traditional halogenated solvents.[17, 19]
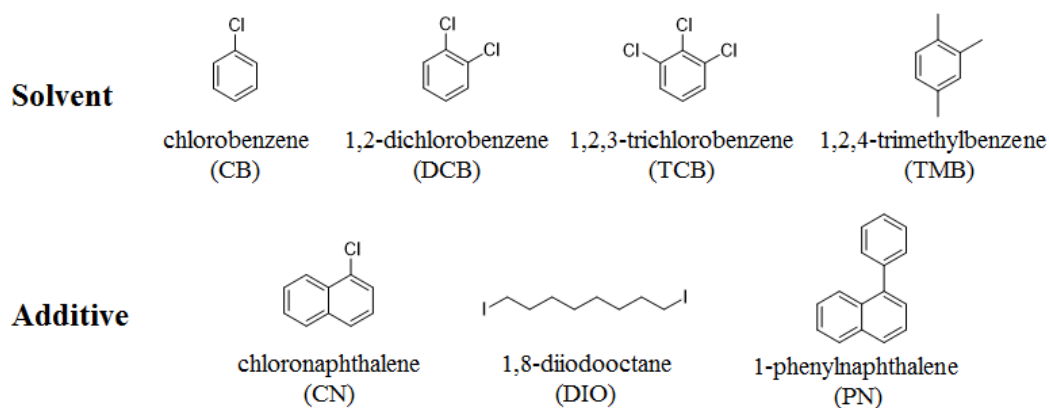
Figure 4.1. *Primary solvents and high boiling-point solvent additives studied in this chapter.*

4.3 Computational Methods

4.3.1 Computational models

All model systems were built in GROMACS 2016.1 package[42, 43] using the *gmx insert-molecule* tools. We first determined the number of molecules/atoms needed for each system, then estimated the box size considering the system to be in the liquid phase. We then inserted molecules/atoms randomly into a box that was slightly larger than the estimated box size. This was to make sure that the correct number of molecules/atoms could be inserted into the box to achieve the right composition of the components. The system box will shrink during the equilibration step to achieve the liquid phase.

4.3.1.1 LJ model

The LJ systems were first prepared in GROMACS, and then converted to LAMMPS format using a code that I developed. In order to obtain a complete picture of the thermodynamic properties, unary, binary, and ternary systems were each created using the same method. The LJ pair potential:

$$\phi_{12}(r) = 4\varepsilon_{12} \left[\left(\sigma_{12}/r\right)^2 - \left(\sigma_{12}/r\right)^6 \right] \qquad \text{Equation 4.1}$$

was used for the interatomic interaction. The parameter σ relates to the diameter of the atom, the parameter ε indicates the potential depth, and *r* is the distance between two particles. For the LJ models, the potential parameter, diameter, and atom masses were taken as the same as argon atom. To balance the computation cost and achieve an appropriate system size for data collection, each binary LJ model contained 4000 argon atoms, while each ternary LJ model contained 6000 atoms with 5% mole fraction interval. We also made

single component LJ models with 4000 and 6000 atoms to represent the pure solution system.

4.3.1.2   General molecular models

The general binary solutions were created with 10% mole fraction intervals for the binary and ternary mixtures. To make sure that a sufficient number of molecules were used to for the low concentration solutions and be consistent with the system size used in LJ simulation, the binary and ternary molecular models were made with 4000 and 6000 molecules, respectively.

4.3.1.3 Organic solvent – additive models

When considering solution drying, *e.g.* as the solvent in an ink formulation dries to leave behind a thin film, the relative concentrations of the primary solvent and all solution components are continuously changing. Hence, it is important to determine ΔG_m over a wide range of concentrations. Also, due to the small fraction of additive used in the mixture, it was important to establish the appropriate system size for the simulations, so that there were enough additives in the system at the lowest concentration model for analysis. Therefore, we first calculated the number of each type of molecules needed base on weight percentage. The number of solvent and additive for each system were listed in Table 4.2 and Table 4.3. Each system contained a total of 10,000 molecules, a system size that was determined to balance the need for statistically relevant data sets and computation cost, as will be discussed in Section 4.4.

Table 4.2. Number of solvent and additive molecules in each binary solution containing chlornaphthalene (CNP) as the additive.

Weight %	Solvent CB	Additive CN	Solvent DCB	Additive CN	Solvent TCB	Additive CN
0.0%	10000	0	10000	0	10000	0
0.1%	9993	7	9991	9	9989	11
0.2%	9986	14	9982	18	9978	22
0.3%	9979	21	9973	27	9967	33
0.4%	9972	28	9964	36	9955	45
0.5%	9965	35	9955	45	9944	56
0.6%	9958	42	9946	54	9933	67
0.7%	9951	49	9937	63	9922	78
0.8%	9944	56	9928	72	9911	89
0.9%	9938	62	9919	81	9900	100
1.0%	9931	69	9910	90	9889	111
2.0%	9861	139	9819	181	9777	223
3.0%	9790	210	9728	272	9666	334
4.0%	9720	280	9637	363	9556	444
5.0%	9649	351	9546	454	9445	555
6.0%	9577	423	9454	546	9335	665
7.0%	9505	495	9363	637	9225	775
8.0%	9432	568	9271	729	9116	884
9.0%	9359	641	9179	821	9006	994
10%	9286	714	9087	913	8897	1103
20%	8525	1475	8157	1843	7819	2181
30%	7712	2288	7208	2792	6765	3235
40%	6843	3157	6240	3760	5735	4265
50%	5910	4090	5252	4748	4727	5273
60%	4906	5094	4244	5756	3740	6260
70%	3824	6176	3216	6784	2775	7225
80%	2653	7347	2166	7834	1831	8169
90%	1383	8617	1095	8905	906	9094
100%	0	10000	0	10000	0	10000

Table 4.3. Number of solvent and additive molecules in each binary solution containing 1,8-diiodooctane (DIO) as the additive.

Weight %	Solvent	Additive	Solvent	Additive	Solvent	Additive
	CB	DIO	DCB	DIO	TCB	DIO
0.0%	10000	0	10000	0	10000	0
0.1%	9997	3	9996	4	9995	5
0.2%	9994	6	9992	8	9990	10
0.3%	9991	9	9988	12	9985	15
0.4%	9988	12	9984	16	9980	20
0.5%	9985	15	9980	20	9975	25
0.6%	9981	19	9976	24	9970	30
0.7%	9978	22	9972	28	9965	35
0.8%	9975	25	9968	32	9960	40
0.9%	9972	28	9964	36	9955	45
1.0%	9969	31	9960	40	9950	50
2.0%	9938	62	9919	81	9900	100
3.0%	9906	94	9877	123	9849	151
4.0%	9873	127	9835	165	9798	202
5.0%	9841	159	9793	207	9746	254
6.0%	9807	193	9750	250	9693	307
7.0%	9774	226	9707	293	9640	360
8.0%	9740	260	9663	337	9587	413
9.0%	9705	295	9618	382	9533	467
10%	9670	330	9573	427	9478	522
20%	9286	714	9088	912	8897	1103
30%	8836	1164	8531	1469	8248	1752
40%	8299	1701	7888	2112	7516	2484
50%	7648	2352	7134	2866	6686	3314
60%	6843	3157	6240	3760	5735	4265
70%	5822	4178	5162	4838	4637	5363
80%	4484	5516	3836	6164	3353	6647
90%	2654	7346	2167	7833	1831	8169
100%	0	10000	0	10000	0	10000

4.3.2 Atomic charges

To obtain the atomic charge for each atom, density functional theory (DFT) calculations were performed at the ωB97X-D/6-311g(d,p) level of theory in the Gaussian 09, Revision A.02 program.[44] The CM5 model[45] was used to determine the atomic charges of each target

molecules. For DIO, a split-basis set was used in order to calculate the charge on the iodine atom.

4.3.3 MD simulations

The LJ models were simulated using the LAMMPS (18Aug2017)[46] software suite, as this code has reliable and efficient LJ capabilities. All molecular models were simulated on GROMACS (version 2016[42, 47] and later).

4.3.3.1 LJ simulations

All the systems were pre-equilibrated before being fed to the DoSPT[29, 30] code for the 2PT analysis. The LJ parameters and atomic masses for the particles A, B, and C are listed below. All intra-particle parameters are the same, ensuring similar behavior for each species. The interparticle interactions ($\varepsilon_{AB}, \varepsilon_{AC}, \varepsilon_{BC}$), however, were modified to be a fraction of the intraparticle interaction parameter ($\varepsilon_A, \varepsilon_B, \varepsilon_C$) to achieve different mixing conditions.

$$\sigma_A = \sigma_B = \sigma_C = \sigma_{Argon} = 3.4 \text{ Å}$$

$$\varepsilon_A = \varepsilon_B = \varepsilon_C = \varepsilon_{Argon} = 0.238$$

$$m_{AA} = m_{BB} = m_{CC} = m_{Argon} = 39.95 \text{g/cm}^3$$

All simulations were kept at 84 K and 1 atmosphere to maintain the liquid phase of argon. The PBC condition was used with a cut-off length of 1.35 Å (about 4σ). The equilibration of the system included an *NVT* ensemble for 500 ps and *NPT* ensemble for 1 ns with a time step of 1 fs. Then a 20 ps *NVT* simulation was used to obtain the trajectory for DoSPT. Since the DoSPT code only supported trajectories with GROMACS format, we developed

code to convert the trajectory file from LAMMPS format to GROMACS format before passing it to DoSPT.

4.3.3.2 Molecular model simulations

For the simulations of the molecular models, we used the same MD protocol described in Chapter 2.5. The simulation times for the *NVT*, *NPT* Berendsen,[48] and *NPT* Parrinello-Rahman[49] were 2 ns, 5 ns, and 10 ns, respectively. All systems were visualized with Visual Molecular Dynamics (VMD) softeware[50] and the density and total energy for each system was extracted to ensure that the systems were in the condensed phase and equilibrated. Then, a 20 ps MD simulation were initiated from the *NVT* ensemble for the 2PT calculation.

4.3.4 Solvation energies

The solvation energy was determined using Bennett acceptance ratio (BAR)[51] method as introduced in Chapter 2. The *gmx bar* tool as implemented in the GROMACS software suite was used to calculate the solvation energy. Here, the parameter λ was varied within an equidistant spacing of 0.05 from 0 to 1. For each value of λ, the complete workflow as described above was followed to calculate the free energy difference (ΔG_{AB}). To validate the BAR method, the solvation energy of several common solvent mixed with water were also calculated and compared with literature value (Table 4.4).[52] Free energies of solvation determined using the BAR method show reasonable agreement with experiment.

Table 4.4. Solvation energy of several common solvents determined by BAR method.

Binary Model	Expt. (kJ/mol)	MD (kJ/mol)
Methane/Water	8.39	9.84 ± 0.22
Methanol/Water	-21.34	-17.87 ± 0.51
Ethanol/Water	-20.90	-21.90 ± 3.73
Benzene/Water	-3.21	-2.40 ± 0.37

4.3.5 Diffusion coefficients

The mean square displacement of each additive in the solvent - additive systems were calculated with the *gmx msd* tool in GROMACS software suite. For the fitting of each profile to calculate the diffusion coefficients, only the simulation within 10% - 90% time frame were used to eliminate the initial and final fluctuation.

4.3.6 Solubility parameters

The heat of vaporization is calculated as:

$$dH_{vap} = U_{gas} - {U_{liquid}}/{N} + RT \qquad \text{Equation 4.2}$$

where U is the bonded energy in the respective gas (U_{gas}) and liquid (U_{liquid}) phases, N is the number of the molecules, R is the gas constant and T is the temperature. A simulation with one isolated molecule in the gas phase was used to determine the bonded energy in gas phase, and the simulation with 10,000 molecules in the condensed phase at room temperature was applied to calculate the bonded energy in liquid phase. The solubility parameter was then calculated from the square root of the cohesive energy density as described in Chapter 2.7.4.

4.3.7 Free energies of mixing

The enthalpy component for the free energy calculation can be directly extracted from the MD simulation. In GROMACS, this is obtained by the *gmx energy* package. For LAMMPS, the term *entropy* needs to be included as an argument in *thermol_style* in the job script. We converted the trajectory file from LAMMPS format to the GROMACS format using a self-developed conversion code. The entropy component was then calculated through DoSPT program, detailed explanation of the procedure is described in http://dospt.org.

4.4 Results and Discussion

Here, we discuss the simulation results from the different models in three sections. First, we look at the simulations from binary / ternary LJ models, as this gives us the fundamental information about the free energy change at different mixing conditions and the how the variations in the interparticle interactions lead to phase separation. Then, we move on to the mixtures of common liquids to establish how the 2PT method works for atomistic molecular models. In the last section, we focus on the organic solvents and additives, which are widely used to process OSC.

4.4.1 LJ liquids

Equilibration. We extracted the density as a function of the simulation time to validate the parameters chosen for the LJ model. The experimental density of liquid argon at 84 K is 1.40 g/cm^3.[53] The MD simulation results in a density of 1.401g/cm^3, giving excellent agreement with experiment. Starting from the gas phase, the liquid was formed through condensation, which occurred rapidly. The experimental density was achieved within 100 ps and stayed stable for the rest of the simulation time as shown in Figure 4.1.
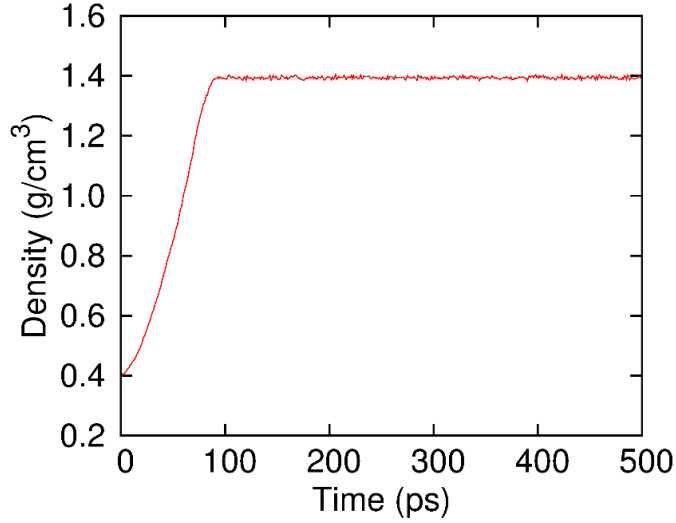
Figure 4.2. Density change as a function of time step of the pure liquid system.

Excess interface energy. The excess interface energy, ΔPE, which is used to determine the progress of phase separation in the binary systems (Figure 4.2), was defined as the potential energy differences between the binary system (PE_{binary}) and the one component homogeneous system (PE_{homo}) at the same temperature as below:

$$\Delta PE = PE_{binary} - PE_{homo}$$
<div align="right">Equation 4.3</div>

Here, since particles A and B share the same LJ parameter of argon, if no parameters are changed, their behavior should be identical to a homogeneous system. We then made a series of binary A/B mixtures and varied the interparticle interaction parameter ε_{AB} to be a fraction of the ε_A or ε_B. We then calculated the ΔPE of each of these systems.

As expected, smaller interparticle interactions among A and B in the mixtures resulted in faster phase separation. When ε_{AB} is only 10% of ε, the phase separation happens within 100 ps, while when the ε_{AB} is 85% of the original ε the binary system is almost miscible.
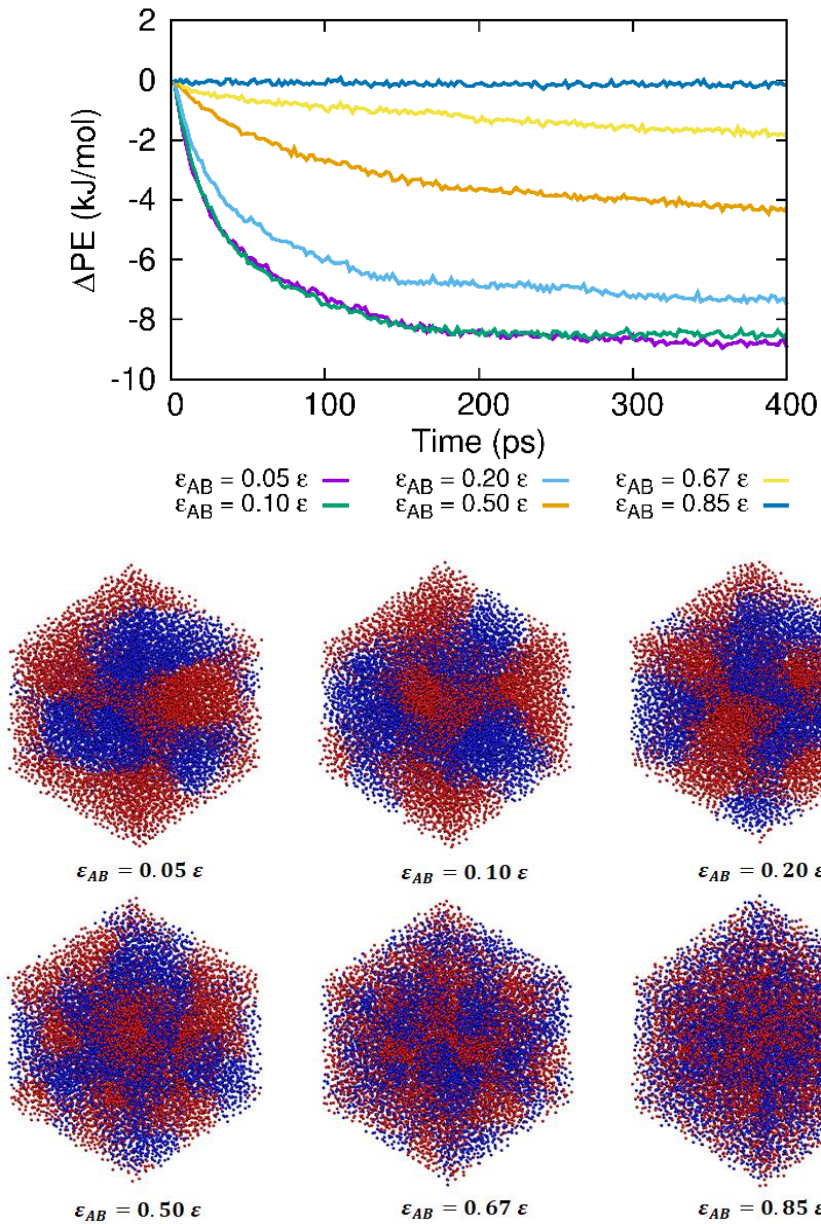
Figure 4.3. (Left) Excess interface energy (ΔPE) as a function of simulation time for different binary systems. The snapshots on the right were each taken at 200 ps.

Gibbs free energy of mixing. Solutions can be referred as a "regular" or "real" when determining the free energy of mixing. The difference between these scenarios is if the exact entropy is considered into the calculation. ΔH_{mix} and ΔG_{mix} as a function of the B composition are shown in Figure 4.3 when the solution is considered as a regular solution.

The positive ΔH_{mix} suggests that the mixing of the two components is enthalpically unfavorable. The enthalpy difference between $\varepsilon_{AB} = 0.9\ \varepsilon$ and $0.5\ \varepsilon$ was not significant. We know the $\varepsilon_{AB} = 0.5\ \varepsilon$ is a phase separated system from Figure 4.2, therefore the phase separation process is most likely driven by the entropy term, a result confirmed by ΔG_{mix}.
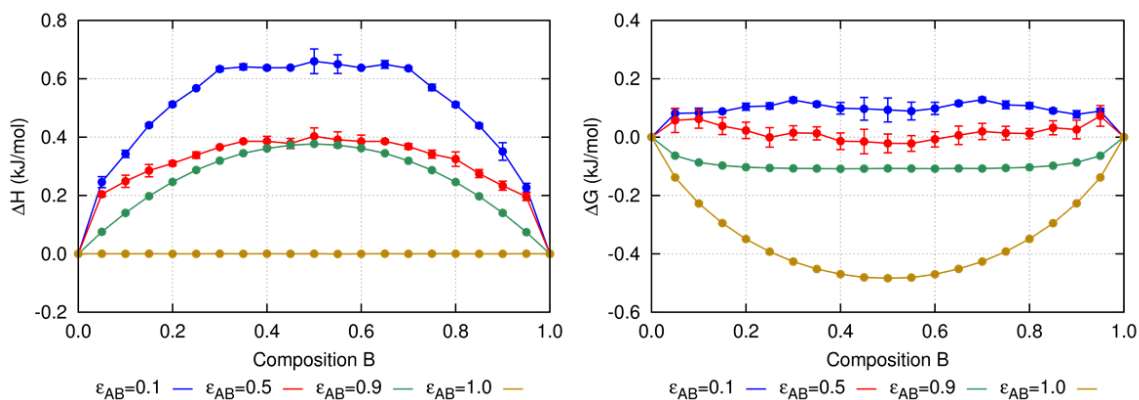
Figure 4.4. Enthalpy of mixing and free energy of mixing calculated as regular solution of the binary LJ systems.

The calculated ΔG_{mix} for the $0.9\ \varepsilon$ and $0.1\ \varepsilon$ systems agree well with the prediction that negative ΔG_{mix} is sufficient for mixing. On the other hand, the $\varepsilon_{AB} = 0.5\ \varepsilon$ system shows phase separation feature in Figure 4.2 and ΔG_{mix} is positive at most A/B ratios. This suggests that the evaluation of ΔG_{mix} is important to determine the mixing condition of the regular binary solutions and a negative ΔG_{mix} is sufficient for a system to be mixed.

Figure 4.3 summarizes data from 10 individual systems for statistical analysis. Here, it is evident that there is larger variation for the 50/50 mixtures of A and B. The upper and lower points of these values can result in two different curve shapes: The higher energy point can lead to a single parabolic curve, while the lower curve would have a double-well shape. To further investigate this phenomenon, we made 100 individual binary systems at

this composition, and used the $\varepsilon_{AB} = 0.1\ \varepsilon$ to force phase separation. For each system, we

calculated the enthalpy value and the distribution of enthalpy as shown in Figure 4.4 (A-

B). There are two major distributions of the enthalpy at this mixing condition. The

difference of these two distributions is 0.1 kJ/mol, which agrees well between the upper

and lower error bars of the ΔG_{mix} at 50/50 mixing ratio in Figure 4.3. Further investigation

of the snapshots of these systems, shown in Figure 4.4 (C-D), reveals that while the systems

are equilibrated, the morphologies of these systems were quite different. The lower energy

point at 0.67 kJ/mol presents a bilayer, while the higher energy point at 0.77 kJ/mol

presents a cylinder-shaped morphology. The formation of different morphologies is caused

by the initial random assignment of the velocity for each atom in the system. As expected,

the lower energy morphology, which formed the bilayer curve, is higher in the population

(62%) in the 100 simulations, shown in Figure 4.4 (B). Therefore, the results suggest that

the free energy of mixing curve for this system should have a double-well shape.
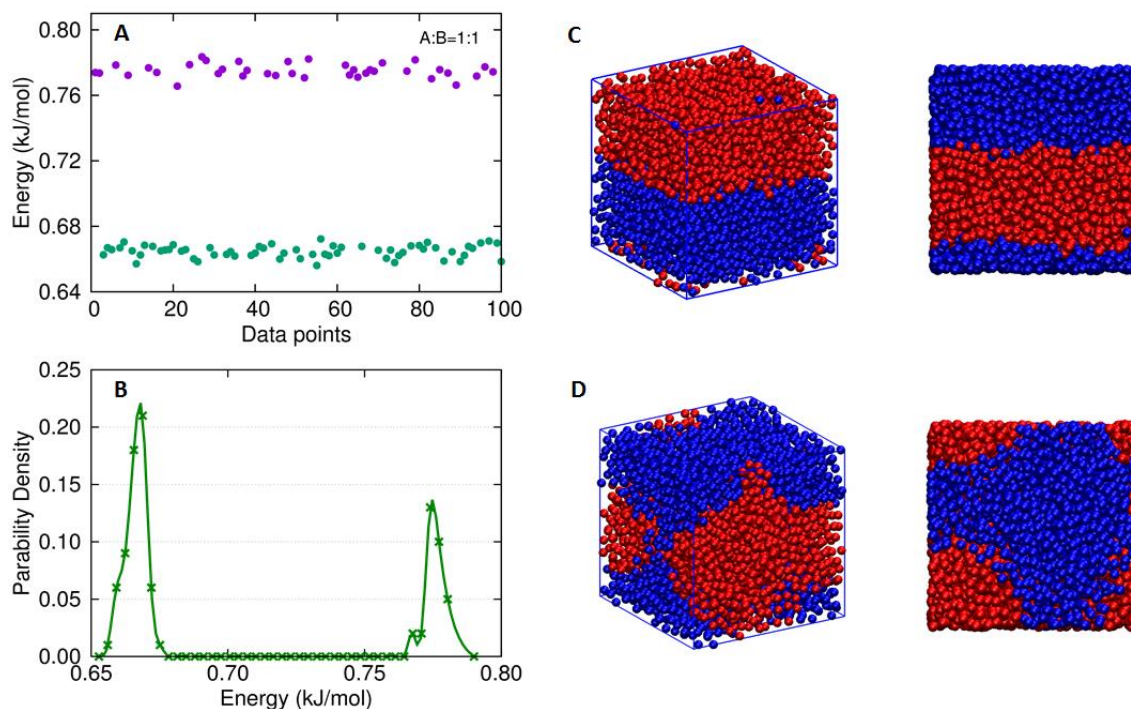
Figure 4.5. (A) Calculated enthalpy of the binary systems at 1:1 mixing ratio. (B) Enthalpy distribution of 100 systems. (C-D) Side and top view of two 50/50 mixing systems at equilibration.

So far, we treated the binary systems as regular solutions and the effect of entropy was not considered. Figure 4.5 shows the same systems treated as real solutions with the entropy of each calculated by 2PT method. The trend of entropy of mixing follows the trend of enthalpy of mixing, as shown in Figure 4.3. The ΔS_{mix} increases as the interatomic parameter decreases from 1.0 to 0.1, which is as expected due to the observed increased level of phase separation. It is worth noting that while we considered the system as a regular solution and calculated the $\Delta S_{Reg.}$ with Equation 2.21, the curve matched the ΔS_{real} at $\varepsilon_{AB} = 1.0 \, \varepsilon$, which was calculated with 2PT method. For the real solution, the interatomic interaction at this value made no difference with the intraatomic interaction, and the

entropy of mixing should be only affected by the molar fractions of the components. That the curves match suggests that the 2PT method as applied here is adequate for this calculation and can provide reasonable information of the entropy of the system.

We then used Equation 2.25 to calculate the ΔG_{mix} of these systems. We note that $\Delta G_{mix} < 0$ is a necessary but not sufficient condition for miscibility.[54] The free energy of mixing curves are concave for $\varepsilon_{AB} = 0.9\,\varepsilon$ and $\varepsilon_{AB} = 1.0\,\varepsilon$, indicating full miscibility at all compositions at these interatomic interaction value. The $\varepsilon_{AB} = 0.5\,\varepsilon$ curve is less parabolic than $\varepsilon_{AB} = 0.9\,\varepsilon$, suggesting that the systems have less miscibility. While $\varepsilon_{AB} = 0.1\,\varepsilon$, ΔG_{mix} is nearly a flat line, with a range within ~0.1 kJ/mol, which is a significantly smaller range than all the other curves. As all systems are immiscible at this ε value, it becomes difficult to use the sign of ΔG_{mix} to determine the miscibility of the components at this interatomic interaction value. We also noticed large variations in the middle of the curves, as shown in Figure 4.5, which were due to different morphologies developed during the equilibration.
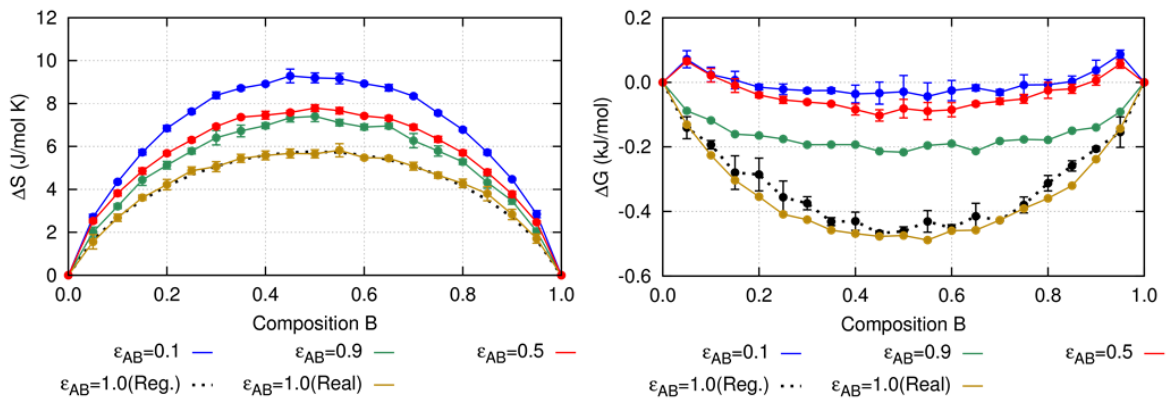
Figure 4.6. Entropy and free energy of mixing determined for real solution of the binary LJ systems.

We further determined the entropy and enthalpy of 10 systems with 50/50 mixing. The result is shown in Figure 4.6. In these 10 systems, 3 systems (Date point 3, 5, 9) formed cylinder shapes, while the others formed bilayers. The enthalpy corresponds to the cylinder conformation is slightly higher (~0.1 kJ/mol) than the bilayer conformation. However, the entropies of systems are not affected by the different morphologies, meaning that even the conformations of the systems are significantly different, their overall entropies are relatively the same at the equilibrated state.
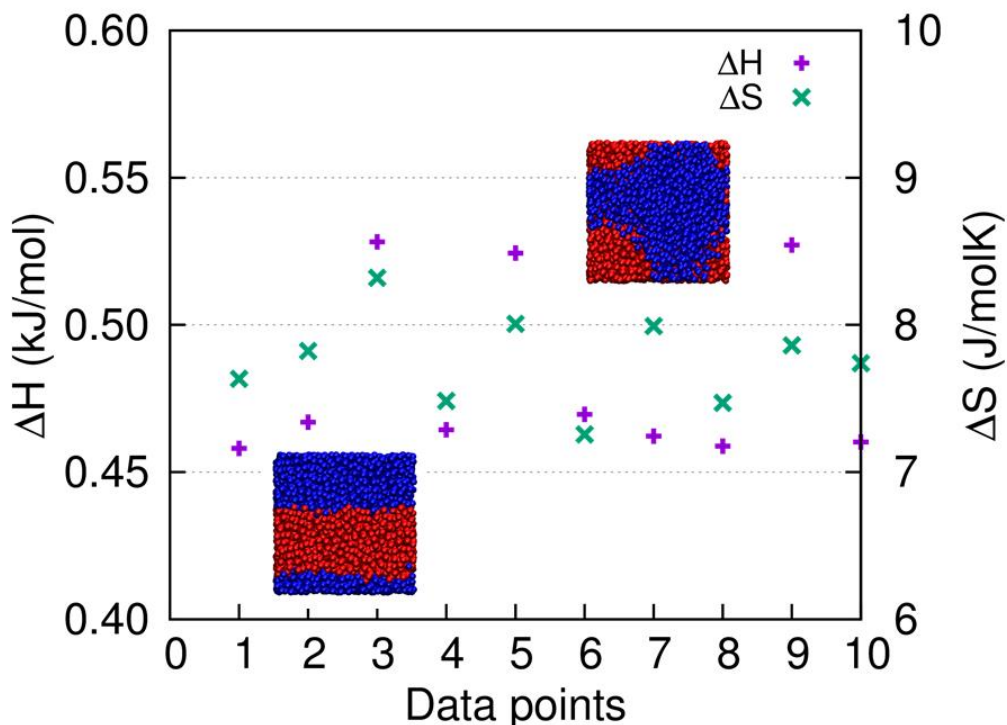
Figure 4.7. The change of enthalpy and entropy of 10 randomly made systems at 50/50 mixing ratio of A and B with $\varepsilon_{AB} = 0.1\ \varepsilon$.

We extracted the enthalpy, entropy, and free energies of mixing during the equilibration process, shown in Figure 4.7. Clearly, the ΔH_{mix} and ΔG_{mix} follow the same decreasing trend, with the entropy driving the free energy of mixing to lower energy. Figure 4.8 shows the ΔG_{mix} as a function of the composition during the equilibration process. As the system equilibrated, the ΔG_{mix} dropped across all compositions. The more equivalent in mole fraction of the two components, the faster for the ΔG_{mix} to stabilize. The dashed line in Figure 4.8 is the ΔG_{mix} of 10 fully equilibrated 50/50 mixtures. This guide-line is inserted to show where the ΔG_{mix} would be for a fully equilibrated state. As discussed before, the upper and lower points corresponded to the cylinder and bilayer morphologies.
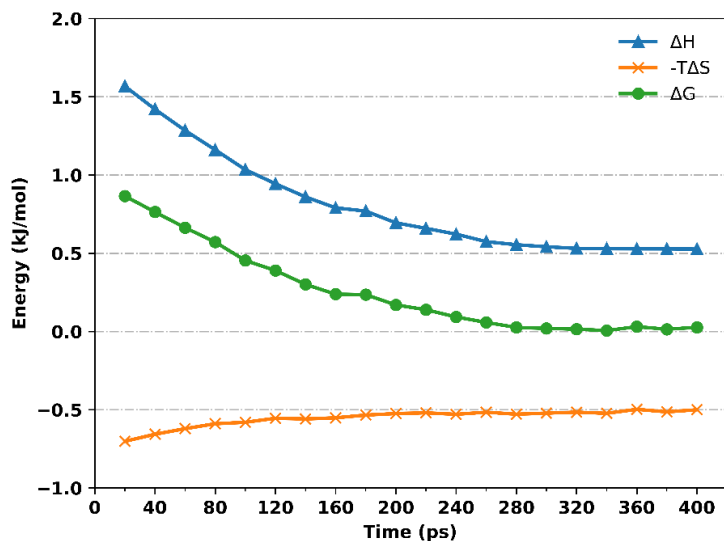
Figure 4.8. Enthalpy, entropy and free energy of mixing of a 50/50 mixed system at 0.5 ε as it equilibrated for 400 ps.
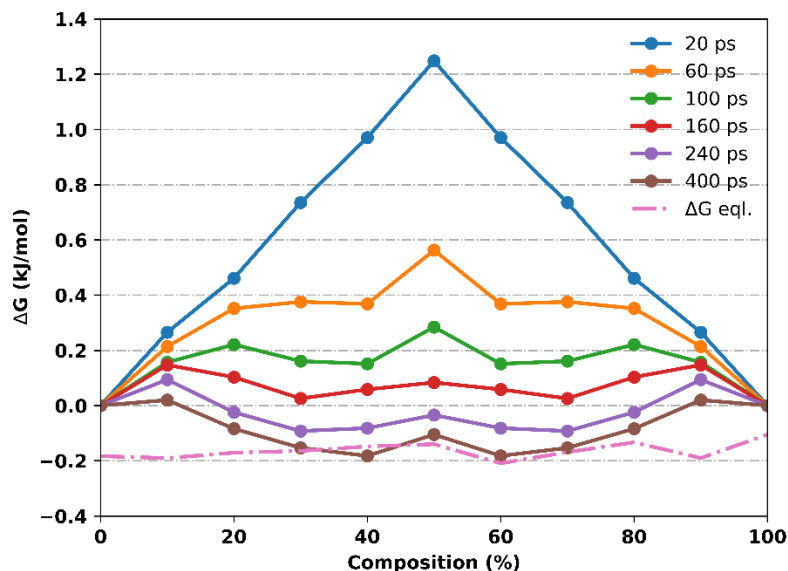
Figure 4.9. ΔG_{mix} as a function of the molar composition during equilibration in 400 ps. The dashed line presents the fluctuation of ΔG_{mix} at equilibration from 10 different simulations.

Now we want to look at how does the free energy change in the ternary LJ solutions. Three types of systems were made as below:

1. All components are miscible (M). ($\varepsilon_{AB} = \varepsilon_{AC} = \varepsilon_{BC} = 0.9\ \varepsilon$)

2. All components are immiscible (IM). ($\varepsilon_{AB} = \varepsilon_{AC} = \varepsilon_{BC} = 1.0\ \varepsilon$)

3. A system that shows partially miscibility (PM), where A and B and B and C are miscible, but A and C are immiscible. ($\varepsilon_{AB} = \varepsilon_{BC} = 0.9\ \varepsilon, \varepsilon_{AC} = 0.1\ \varepsilon$)

Each system type includes a series of solutions with 5% concentration intervals, each using 6000 LJ particles. We used the same method applied for the binary solutions to calculate the enthalpy, entropy, and free energy of mixing of these ternary solutions. Combining the results of the unary, binary, and ternary mixtures results in the contour plots of ΔG_{mix} for the ternary systems as shown in Figure 4.9. The three sides A, B and C corresponded to binary mixtures of A-C, A-B and B-C, respectively.

105
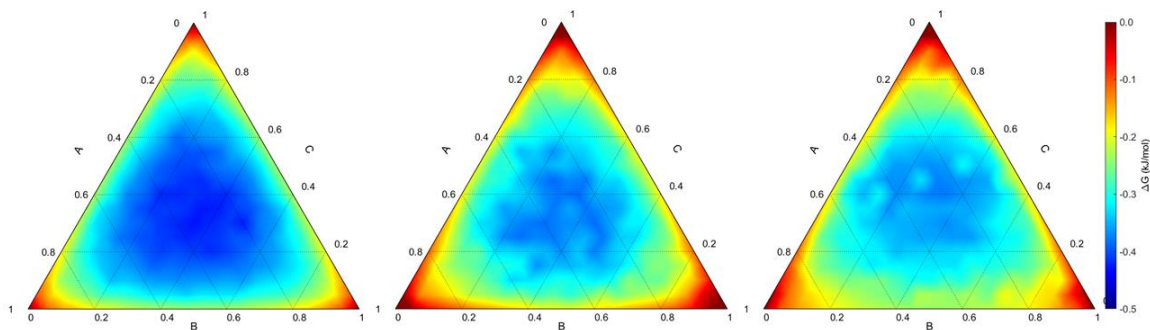
Figure 4.10. ΔG_{mix} of three ternary systems treated as real solutions.

ΔG_{mix} of the ternary solutions agree reasonably well with the results from the binary simulations. For the miscible system (System M), the ΔG_{mix} are all negative, with the lowest point around –0.4 kJ/mol at the center, which corresponds to the composition of 30% A, 30% B and 40% C. We notice that in the binary solutions, the lowest ΔG_{mix} at 0.9 ε was about −0.2 kJ/mol as shown along the three sides of the plot. Therefore, introducing an additional miscible component (C) into the binary solution further stabilized the overall ΔG_{mix}. Such behavior is also observed for other systems. In the immiscible system (System IM), the ΔG_{mix} of the binary solution has a small range of 0.1 kJ/mol, while in the ternary, the range increases to 0.2 kJ/mol. The overall ΔG_{mix} has a small positive region and large negative region. The positive ΔG_{mix} is located near the tips of the triangle, which corresponds to the mixtures that one component dominates in the composition. The range of ΔG_{mix} is near 0 while closer to the edge of the triangle, which agrees well with binary results, indicating that if one component is lower in the composition, the ΔG_{mix} of the system is close to 0 kJ/mol. ΔG_{mix} further stabilizes while moving from the edge to the center and to a lowest value about −0.2 kJ/mol, suggesting that the presence of an additional component in the solution, even though is immiscible with the other components, can

stabilize the ΔG_{mix}. As expected, the lowest ΔG_{mix} point is at the center of the plot, which suggests that the most stable composition consists 40% A, 30% B and 30% C. As A, B and C are identical atoms, this composition is the same as we find for the miscible system.

For the partially miscible system (System PM), the ΔG_{mix} along side B (A-B) and side C (B-C) are similar to the ΔG_{mix} we find in System M, due to the same miscible feature of the components. While on side A (A-C), the ΔG_{mix} is significantly higher due to the immiscibility of A and C. The ΔG_{mix} changes sign from AC binary to ABC ternary solution (moving away from A side), while a small amount of B starts to be introduced into the system. As the concentration of B increases, the ΔG_{mix} reaches the most stabile state at about −0.4 kJ/mol, which is comparable to the all miscible system (System M). Because of the partially miscibility, the ΔG_{mix} at the lowest point also shifts to the A side, comparing to the other two systems.

Synopsis. So far, we have explored the properties of unary, binary, and ternary LJ liquids. As suggested by Gedde, we find that $\Delta G_{mix} < 0$ is a necessary but not sufficient condition for miscibility.[54] We have shown this agrees with most of the binary simulations. Turning to the ternary solutions, we find that the introduction of an additional component can further stabilize the ΔG_{mix}. These simulations serve as fundamental guide for us to understand the behavior and energy change in real molecular models.

4.4.2   General molecular models

Now we focus on atomistic simulations related to mixtures of known chemicals. We designed three ternary models to make different system types as shown in Table 4.1. Each system type included a series of solutions with 10% concentration intervals and a total of

6000 molecules. We also made unary and binary solutions for each of the components. We then applied the same simulation procedure and determined the corresponding thermodynamic energies as was done for the LJ liquids.

Condensed phase properties. We equilibrated each pure solvent at room temperature and calculated the density according to the OPLS-AA force field and standard molar entropy (S_0) using the 2PT method. The results are shown in Table 4.5. The OPLS-AA force field recovered excellent agreement in terms of the density for each solvent, which was expected as the force field was developed to work best with solvent simulations. The 2PT method also gave a reasonable estimation on the S_0 for most systems. We noticed larger deviations for hexane and benzyl alcohol, which we hypothesize results from the fact that molecules were treated as spherical-like particles in the determination of the density of state. Therefore, the 2PT becomes less reliable to predict the entropy of such molecules; this is seen, in part, in the large standard deviations for the entropies determined for these systems. Comparing with reference values, the 2PT method underestimated the entropy by up to 20% for linear molecules. The deviation increased while the molecule became less sphere in shape.

Table 4.5. Density and standard molar entropy of the molecule solvent calculated by OPLS-AA force field and 2PT method.

Solvent	Density (g/cm³)			S_0 (J/mol × K)		
	OPLS-AA	**Ref.[a]**	**SD**	**2PT**	**Ref.[a]**	**SD**
Water	0.992 ± 0.18	0.997	0.003	63.900 ± 0.99	69.900	-0.746
Toluene	0.874 ± 0.12	0.867	0.004	202.890 ± 1.45	220.960	9.035
Hexane	0.661 ± 0.09	0.655	0.003	252.295 ± 6.21	296.060	21.883
Benzyl Alcohol	1.022 ± 0.46	1.040	0.009	188.714 ± 5.38	216.700	13.993
Methanol	0.775 ± 0.17	0.792	0.009	124.330 ± 1.38	127.200	1.435
1,2-Dichlorobenzene	1.306 ± 0.24	1.300	0.003	213.260 ± 0.68	N/A	N/A

[a]References were retrieved from the NIST WebBook at www.nist.gov.

While analyzing the entropy data, we noticed that the entropy of the binary system had a linear relationship with the concentration of the components, which can be expressed as:

$$S_{total} = kx_i + S \qquad \text{Equation 4.4}$$

where S_{total} is the total entropy of the mixture, x_i is the concentration of i, k is the slope and S is the intercept. When $x_i = 0$, the intercept $S = S_{total}$, which represents the S_0 of the other component in the mixture. We knew the DoSPT code became less reliable while the shape of the molecule became less sphere-like. Therefore, the slope of the linear relationship decreased as the concentration of the non-sphere molecule increased, so that the intercept S decreased and resulting an underestimated S_0 value, as shown in Table 4.6. Here, we calculated the linear trends with every two adjacent concentrations. Notice that the intercept (S_0) calculated from lower solute concentrations (10% to 20%) are slightly

larger than the those at higher solute concentrations (80% to 90%). If we use the lowest solute concentration trendline (10% and 20%) to estimate the S_0, the results are 274.647 J/mol×K for hexane and 205.657 J/mol×K for benzyl alcohol (Figure 4.10), both in better agreement with the reference values.
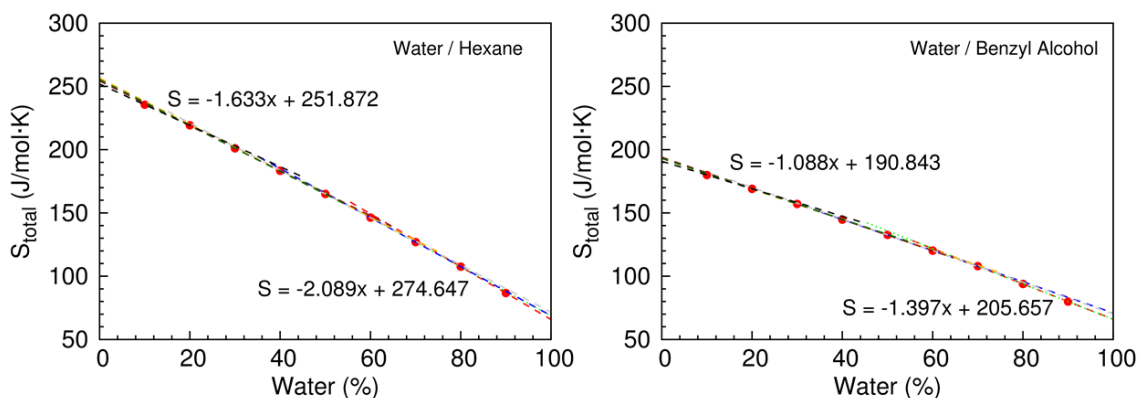
Figure 4.11. Total entropy as a function of the water composition in water-hexane (left) and water-benzyl alcohol (right) binary mixtures. The linear relations from two end concentrations were presented to show the change of linear constant and intercept.

Table 4.6. The linear constant and corresponding S_0 estimated from each water concentration for the water - benzyl alcohol and water - hexane solution. The S_0 increases as the solute concentration increases

Water (%)	Water - Benzyl Alcohol		Water - Hexane	
	k	S_0 (J/mol·K)	k	S_0 (J/mol·K)
10 – 20	-1.088	190.843	-1.831	256.543
20 – 30	-1.201	193.087	-1.776	254.367
30 – 40	-1.232	194.038	-1.813	255.474
40 – 50	-1.205	192.950	-1.633	251.872
50 – 60	-1.250	195.205	-1.870	258.523
60 – 70	-1.231	194.077	-1.937	262.501
70 – 80	-1.398	205.745	-1.942	262.879
80 – 90	-1.397	205.657	-2.089	274.647

To further confirm this trend, we made two solutions (1% solute and 5% solute) using water–hexane and water–benzyl alcohol, then applied the same simulation protocol to calculate the total entropy. As shown in Figure 4.11, the trendlines from these two compositions were inserted for each binary system. From the equations we estimate the S_0 of the hexane to be 289.737 J/mol×K and the S_0 of benzyl alcohol to be 209.262 J/mol×K, which are very close to the reference values. Therefore, the linear trend seemed to be an effective approach to estimate the S_0 of a non-spherical molecules.
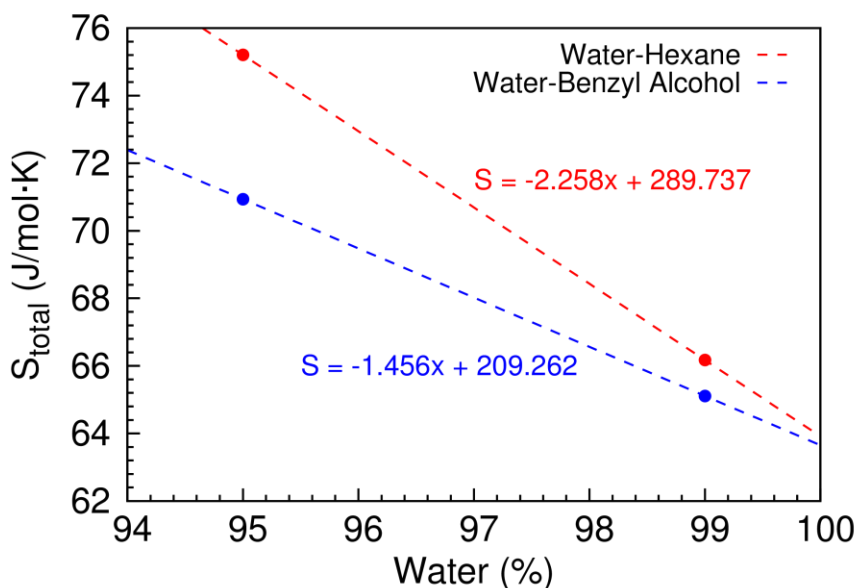
Figure 4.12. Total entropy as function of the water composition at 95% and 99% solute concentration. The linear trendline for each binary solution were presented to show the estimated standard molar entropy.

Enthalpy of mixing. The enthalpies of each mixture are calculated from Equation 2.23 and are shown in Figure 4.12. The fully miscible system (System A) is built with DCB, toluene, and hexane; the fully immiscible system (System B) is built with water, hexane, and benzyl alcohol; and the partially miscible system (System C) is built with water, methanol, and hexane, where water–methanol are miscible, but water–hexane and methanol–hexane are

immiscible. Upon investigating the system B and C, we find that while the two components are miscible, the ΔH is negative for all concentrations. When the two components are immiscible, then the ΔH becomes positive. This agrees with all the combinations in the immiscible and partial miscible systems, however, it did not agree with the miscible system, except for the DCB and toluene combinations. Toluene and hexane are miscible due to their non-polar nature. Therefore, we expect the negative trend of the ΔH in toluene-hexane binary solutions, however, the ΔH stays positive, with the largest value at 50:50 mixing ratio. This suggests that the mixing of hexane and toluene is an enthalpically unfavorable process. On the other hand, the ΔH for DCB and hexane binary solutions are partially positive (0-40% of DCB) and partially negative (60%-100% of DCB), indicating that at low DCB concentration, mixing hexane into DCB is enthalpically favorable, while the concentration of DCB exceeds 60%, the addition of hexane becomes enthalpically unfavorable.
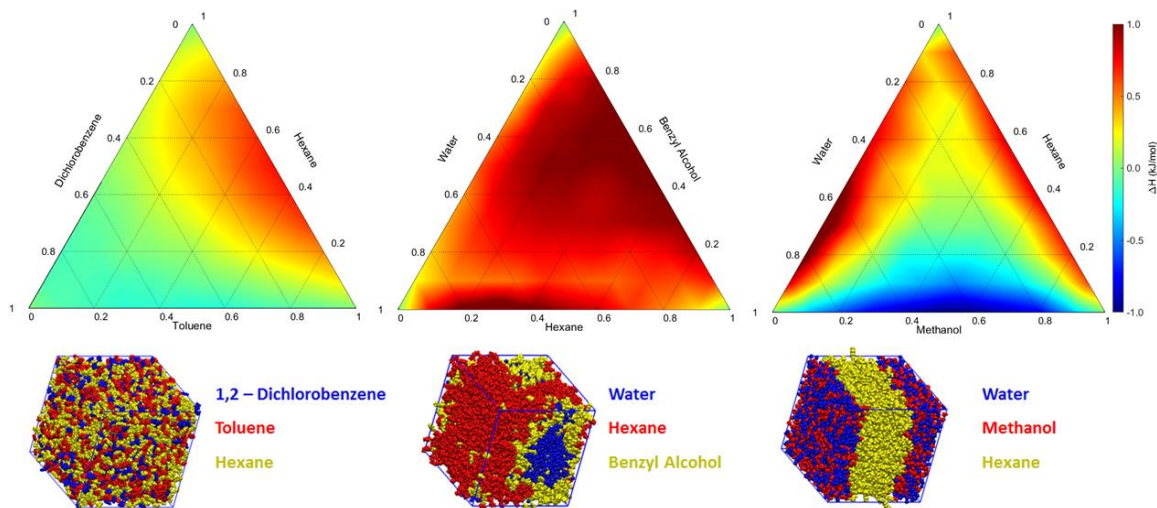
Figure 4.13. Change of enthalpy of mixing for three molecule systems. Left: all miscible, middle: all immiscible, right: partially miscible. The snapshots of each system at a mixing ratio were presented to show the different mixing conditions.

112

The ΔH for the immiscible system (water–hexane−benzyl alcohol) are positive at all concentrations. The binary systems water−hexane and hexane−benzyl alcohol present a much higher ΔH than the ternary solutions, as shown along the bottom and right sides of the triangle. The snapshot of the ternary mixture also reveals that water molecules are surrounded by the benzyl alcohol molecules and did not mix with hexane, this may due to the similar polarity between water and benzyl alcohol causing them to be moderately soluble, while hexane is non-polar and is insoluble with water or benzyl alcohol.

In the partially miscible system (water–methanol–hexane), the ΔH is positive along the two sides which corresponds to the mixture of water–hexane and hexane -methanol, and negative for the miscible solution, water–methanol. The snapshot also shows a well-mixed feature between water and methanol, and phase separated while both in mixed with hexane.

Entropy of mixing. All entropy of mixing curves for the binary and ternary mixtures are positive (Figure 4.13), which is expected as the mixing of two or more solutions to form a solution of intermediate composition should increase the entropy of the system. Ideally, the highest entropy value located at where the mole fraction was 0.5 for binary or 0.33 for a ternary mixture. For the miscible system, the highest ΔS shifts away from the center to where less DCB (10%-30%) is present in the mixture, and is also the largest ΔS in all three systems, suggesting that the complete mixture of three components increases the overall ΔS.
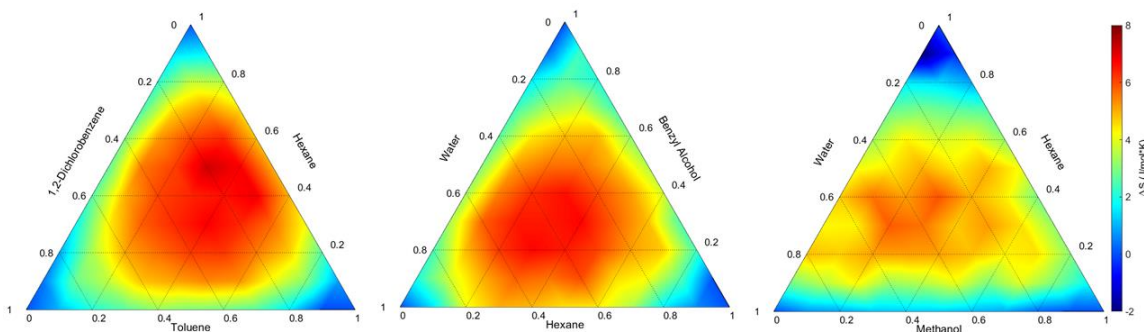
Figure 4.14. Change of entropy of mixing for the three molecule systems. Left: all miscible, middle: all immiscible, right: partially miscible.

For the immiscible system, the entropy changes of water–hexane system (bottom) is similar to the hexane–benzyl alcohol system (right side), which are both higher than the water–benzyl alcohol system (left side). This agrees with the fact that benzyl alcohol had a moderate solubility in water due to the same polarity, while hexane is a non-polar molecule, is insoluble in either water or benzyl alcohol. In the partially miscible system, the water–methanol binary mixture has the lowest ΔS (0-2 J/mol K), due to the well mixed feature between the two molecules.

Free energy of mixing. Now, we combine the results from change of enthalpy and change of entropy to calculate the free energy of mixing using Equation 2.25 (Figure 4.14). We notice that the mixing of two components generally agree with the expected solubility of the molecules. Along each side of the plots, ΔG is negative while the components are miscible and becomes positive for immiscible binary solutions. The exception is between the water–hexane, the ΔG for this binary solution is slightly negative (-0.5 kJ/mol) between 20%−65% range, as discussed before, this may result from an underestimated entropy for

the S_0 of hexane, according to Equation 2.25, this would result an overestimated ΔS and stabilize the ΔG.
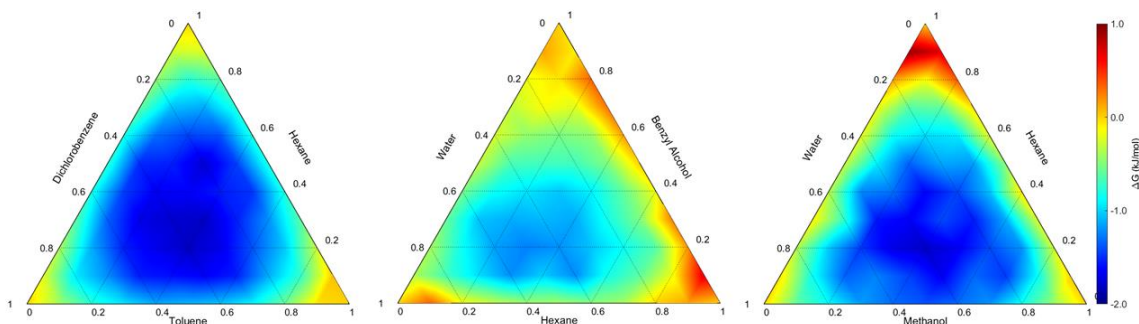
Figure 4.15. Free energy of mixing for the three molecule systems. Left: all miscible, middle: all immiscible, right: partially miscible.

The ΔG for the ternary systems are all concave in shape, indicating that the mixing of the three components, regardless the miscibility, is a spontaneous process. The largest ΔG for each system, however, varies for different systems and is due to the miscibility between each two components. For the all miscible system, the largest ΔG locates at about 0.3 mole fraction of each components. For the other two systems, the location of the largest ΔG generally shifts to where the two miscible components dominate the compositions.

Synopsis. The atomistic molecular models further confirm that 2PT model can be used to determine the entropy of complex liquid solutions. When the shape of the molecule is spherical, the 2PT method gives a good agreement with experimental measurement. For non-spherical molecules, a linear relation with the entropy determined from the low concentration aqueous solutions can provide a good estimate of the standard molar entropy of the solute. The Gibbs free energy calculations also agree with the understanding that

negative ΔG is a necessary condition for miscible to occur. These simulations now serve as fundamental guideline to investigate the properties of more complicated molecular models of interest for OSC.

4.4.3   Organic solvent–additive models

As noted earlier, processing solvents that include small amounts of additives can alter OSC morphologies, affecting the OSC characteristics. The choice of additive and host solvent and the amount of additive that should be added varies depending on the chemistry of the OSC, to date, remains highly empirical and is often determined through trial-and-error approaches. Here we investigated several solvent and additive molecules that are widely used in OSC processing. The methods developed here provide a framework for further investigations of such multicomponent systems across a range of applications.

Pure solvent equilibration. Prior to the examination of the free energies of mixing, it is important to establish the appropriate system sizes for the simulations. Since we are particularly interested in following the mixing processes at small concentrations of the additives, it is imperative that the simulation boxes be large enough to allow for this situation. Here, we begin with evaluations of the pure liquids that are subjected to the 2PT method; relevant data is summarized in Figure 4.13 and Figure 4.14. With increasing system size, the entropy changes plateau, as summarized in Figure 4.13. Importantly, as the system sizes are extended, the computational cost for the DoSPT code increases exponentially (Figure 4.15). To balance the computational cost of the exponential system size dependence of the 2PT method with enough additive molecules to ensure entropy convergence, each pure and binary system studied here contains 10,000 total molecules.
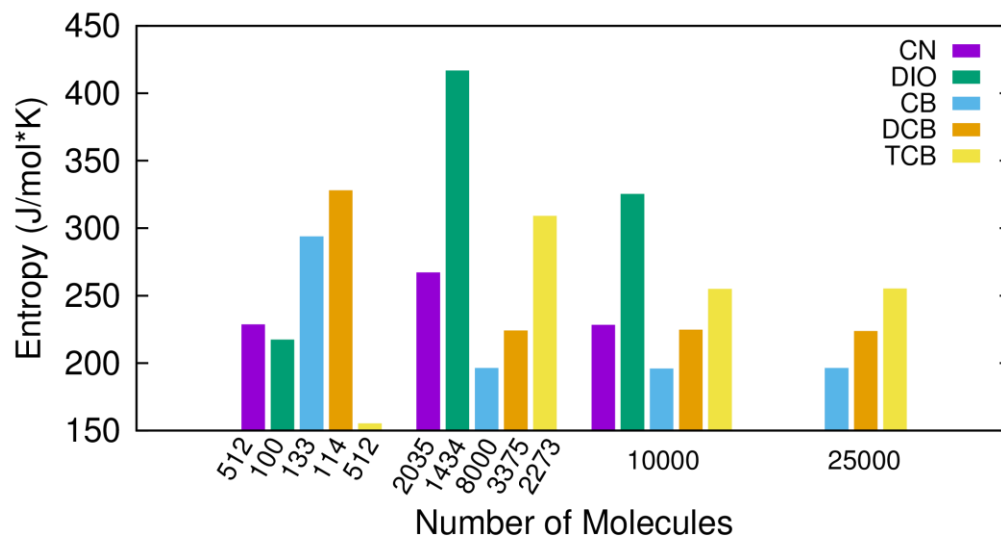
Figure 4.16. Entropy calculated from 2PT method with DoSPT code of different system size.
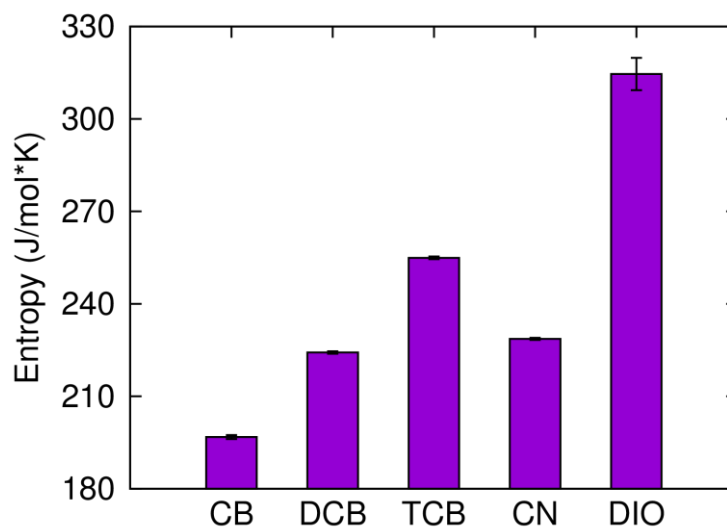
Figure 4.17. Entropy of the pure solvent from 2PT calculation

117
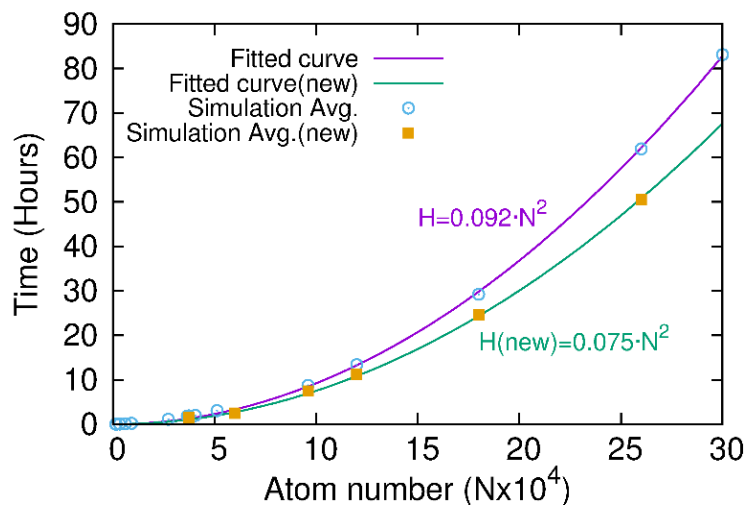
Figure 4.18. Time cost of applying DoSPT code for entropy calculation.

Table 4.7 summarizes the results from six individual simulations for each pure solvent. In general, the liquid densities and the standard molar entropies of CB and DCB show good agreement with experiment. DIO does presents a larger standard deviation of 6.5% with respect to the experimental density; this deviation could be due to the fact that the non-bonded parameter for iodine was derived for aryl halides,[55] which present slightly different chemistries than one might expect for alkyl halides; two different non-bonded parameters for iodine were evaluated and the input files are included in the SI, with the one that presented the best agreement with the experimental DIO density used in all subsequent calculations. Although the 2PT method has been widely applied to liquids and even mixtures, most of the simulation targets are ions, non-organic liquids,[11-26] or water/organic mixtures.[23-38, 56] The validation of using 2PT on pure organic solvents here provides us confidence in the application of the method to binary mixtures.

We also determined the solubility parameters of each pure solvent systems. The calculated Hildebrand and Hansen solubility parameters are in good agreement with previous

reference values.[57] The solubility parameters of each pure solvent fall within 9.4 to 10 $\text{cal}^{1/2}$ $\text{cm}^{-3/2}$, suggesting from an entropic standpoint that each additive should readily mix with the host solvent.

Table 4.7. Hildebrand and Hansen solubility parameter, density and standard molar entropy of solvent systems calculated from simulation.

	Density (g/cm³)		Standard molar entropy (J/mol K)		Hildebrand (cal$^{1/2}$ cm$^{-3/2}$)		Hansen (cal$^{1/2}$ cm$^{-3/2}$)			
	ρ		S_0		δ		δ_d		$\delta_p + \delta_h$	$\delta_p + \delta_h$
	Ref.[a]	MD	Ref.[a]	MD	Ref.[b]	MD	Ref.[b]	MD	Ref.[b]	MD
CB	1.11	1.14	197.48	196.97 ± 0.64	9.50	9.42 ± 1.64	10.30	8.35 ± 1.34	3.08	4.36 ± 0.04
DCB	1.30	1.33	211.29	224.15 ± 0.39	10.02	10.04 ± 1.14	8.94	9.02 ± 0.65	5.13	4.40 ± 0.07
TCB	1.46	1.51	N/A	254.95 ± 0.43	N/A	10.21 ± 0.26	N/A	9.22 ± 0.04	N/A	4.38 ± 0.06
CNP	1.19	1.21	N/A	228.73 ± 0.35	9.80	9.61 ± 0.78	9.73	8.79 ± 0.52	3.62	3.88 ± 0.06
DIO	1.84	1.96	N/A	312.41 ± 5.26	N/A	10.12 ± 1.01	8.94	9.39 ± 0.29	3.57	3.79 ± 0.20

[a]Density and entropy data were retrieved from the NIST WebBook at www.nist.gov. [b]The experimental solubility parameters were retrieved from literature[58] and Hansen Solubility Parameters handbook.[59]

Solutions: Free Energy of Solvation and Diffusion. Since experimental solvation energies of our target systems are not available, we first selected several common organic–aqueous solutions and determined the solvation energy for these reference solutions to validate the approach. The results, presented in Table 4.8, demonstrate that the calculated solvation energies agree reasonably well with reference experimental values.[52] In turn, we determined the solvation energy of each additive in the three host solvents. All solvation energies are negative, as shown in Figure 4.16, suggesting that the solvation of the additive into the host solvent is an exothermic process. For both CN and DIO, the ΔG is similar

across all three solvents, indicating that the energy difference associated with dissolving the additive into different solvent environment is negligible. Solutions with DIO present solvation energies about 10 kJ/mol smaller than the solutions containing CN, suggesting that DIO is more readily solvated.

Table 4.8. Salvation energy of solvent calculated using BAR method as comparing with reference values.

Binary Model	Expt. (kJ/mol)	MD (kJ/mol)
Methane/Water	8.39	9.84 ± 0.22
Methanol/Water	-21.34	-17.87 ± 0.51
Ethanol/Water	-20.90	-21.90 ± 3.73
Benzene/Water	-3.21	-2.40 ± 0.37
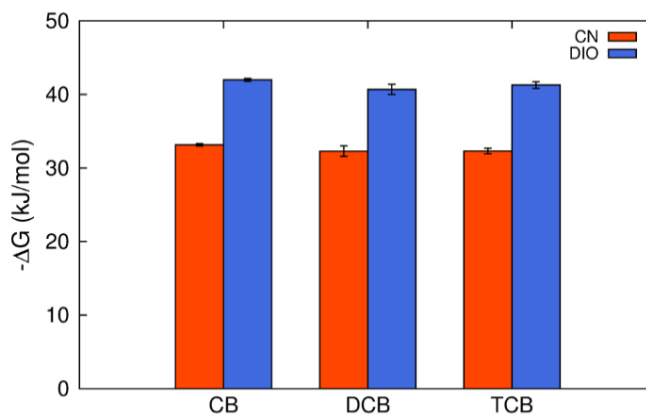
Figure 4.19. Free energy of solvation of two additives in three host solvents.

The relative free energy differences for each interval of the coupling parameter λ are presented in Figure 4.17. The value of λ where the energy changes sign is defined as the critical point (λ_c). Notably, both CN and DIO have similar λ_c, located between 0.7 and 0.8

in all host solvents.). For λ value larger than λ_C, scaling out the additive is energetically favorable, while for λ value smaller than λ_C, scaling in additive is energetically favorable. Notably, both PN and DIO has similar λ_C located between 0.7 and 0.8 across all host solvents.
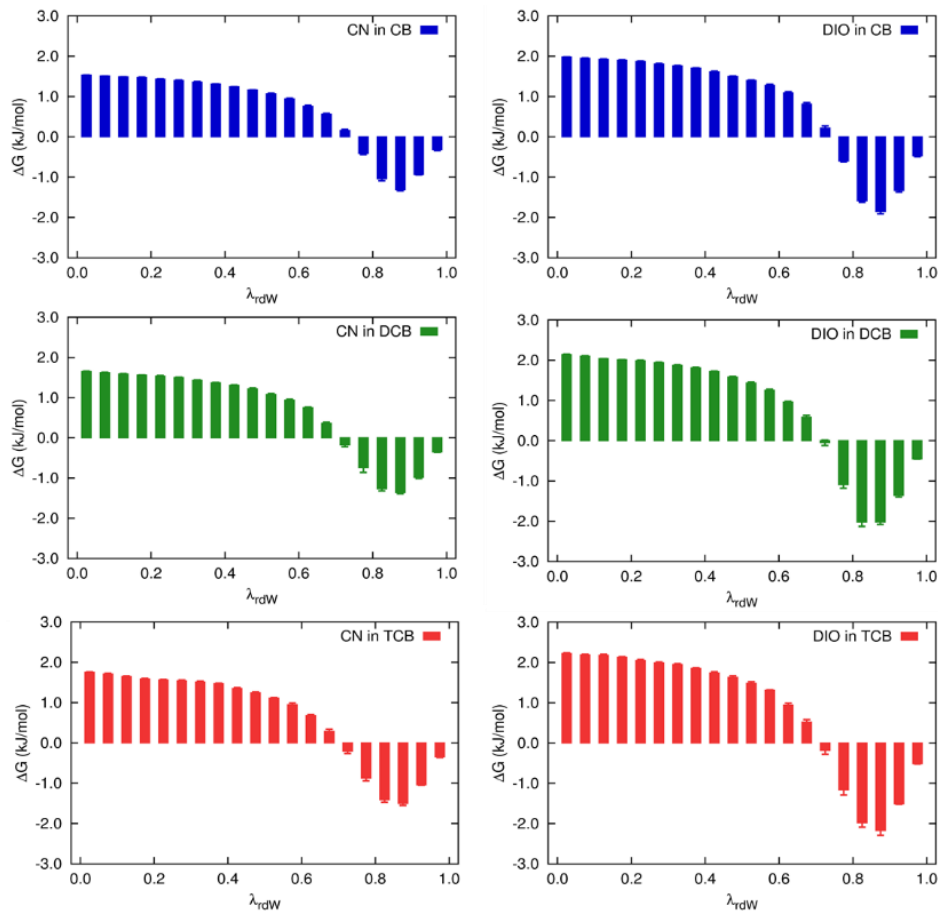
Figure 4.20. Relative free energy differences as function of each interval of λ.

Turning to diffusion, there is a large variation in the additive diffusion coefficients at low additive concentrations, Figure 4.18. At low additive concentrations, only a few additive molecules are present in the system, resulting in larger standard deviations. At concentrations larger than 10%, the diffusion constant stabilizes in all mixtures. Additive

diffusion in each host solvent follows the order of CB > DCB > TCB, which is expected in part due to the increasing size of the host molecule. When CB was the host solvent, at low additive concentrations, both CN and DIO showed the largest diffusion coefficient, around 0.8×10^{-5} cm^2/s, which then decreased significantly as the concentration increased; this suggests that there was more solvent-additive interaction at lower additive concentration in CB solution. In DCB and TCB mixtures, however, the diffusion constants for DIO and CN were less affected by the additive concentration.
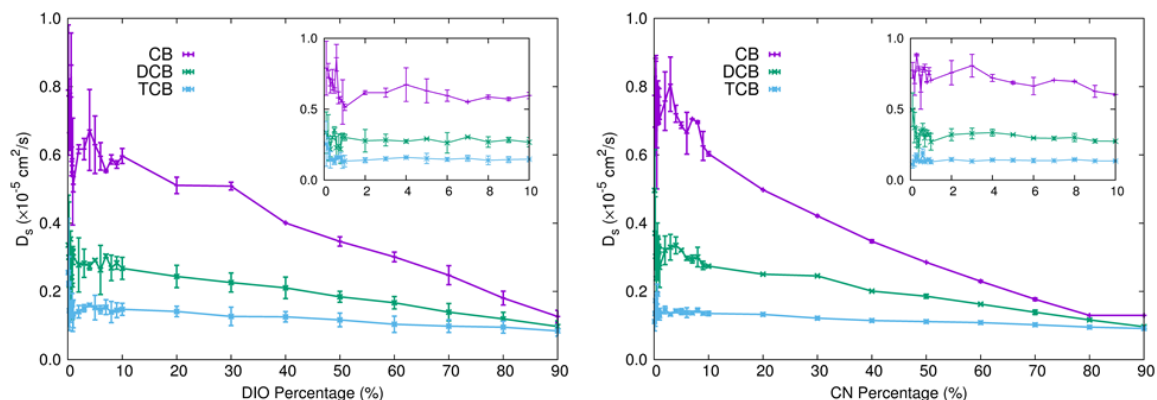
Figure 4.21. Diffusion constant of two additive, DIO (left) and CN (right), in three host solvents as a function of the additive concentration.

Gibbs free energy of mixing

The density of each binary solution at various additive concentrations was checked to guarantee a mixed condition was achieved for free energy prediction. The results were shown in Figure 4.21. Each density change was following the trend to recover the density of the two components, suggesting a complete mixed feature throughout the concentrations. We then calculated the energies with these equilibrated systems.
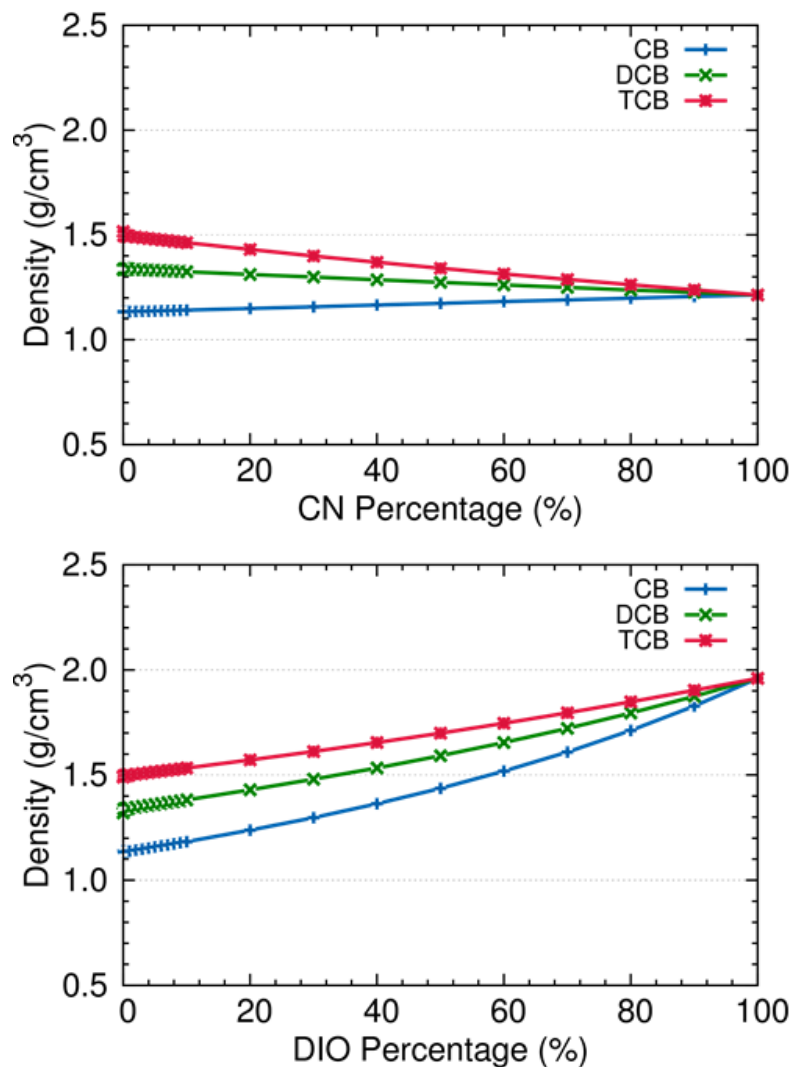
Figure 4.22. Density of the two additive mixtures, CN (top) and DIO (bottom), in the three host solvents as a function of the additive concentration.

All binary mixtures present ΔG_{mix} less than zero across all additive fractions, Figure 4.22, indicating the additives are soluble with three host solvent at various concentrations. The minimum of ΔG_{mix} occurs between $0.2 - 0.4$ additive mole fraction. Interestingly, when DIO is the additive, the enthalpy terms are all positive, suggesting that the mixing of DIO with the host solvent is enthalpically unfavorable. For mixtures containing CN as the

additive, the enthalpy is nearly unchanged and zero across all mole fractions. In every case, ΔG_{mix} follows the trends set by $-T\Delta S$, suggesting that the mixing between the additive and host solvents re driven by entropy. Notably, when CB and DCB are the host solvent, both DIO and CN show a slightly higher ΔG_{mix} than when TCB is the solvent.
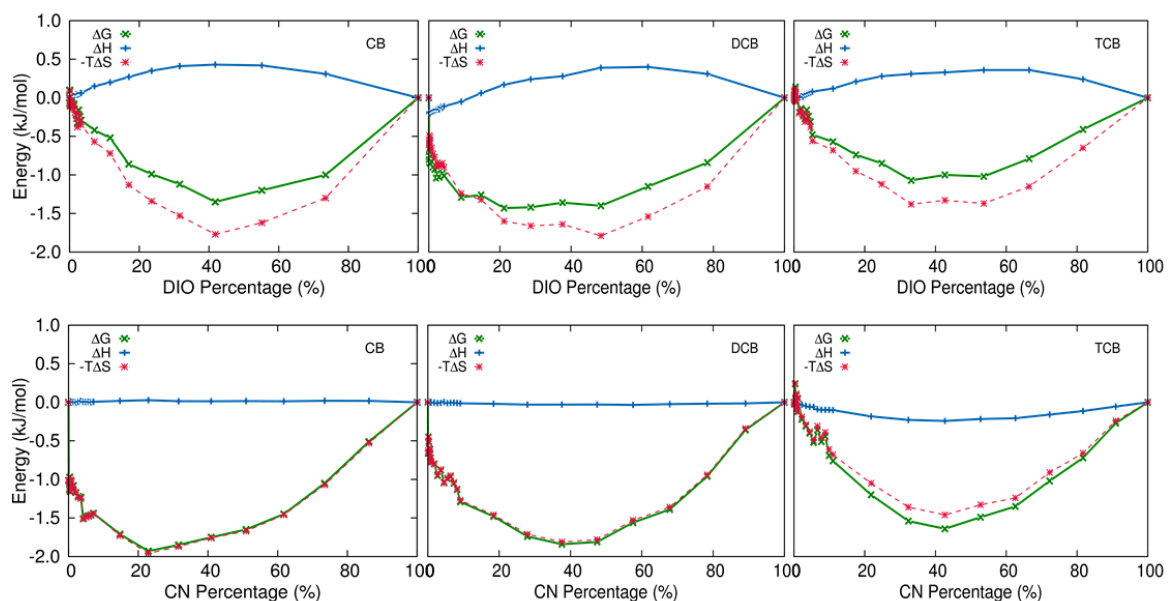
Figure 4.23. Enthalpy, entropy and Gibbs free energy of mixing as function of the additive mole fraction of the binary solutions.

For the purpose of solution printing OSC, there has been a move towards developing non-halogenated "green" solutions. To show further generality of the method, we also examined the mixing of 1,2,4-trimethylbenzene (TMB) as the host solvent and 1-phenylnaphthalene (PN) as the additive (Figure 4.23).[60] Here, the minimum of ΔG_{mix} occurs between 0.4 – 0.6 additive mole fraction. The enthalpy term is again slightly positive, suggesting that the mixing of PN with the TMB is enthalpically unfavorable. The overall entropy and free energy of mixing are similar to the halogenated solutions using CN as the additive, which is expected due to the chemical similarity of the CB–CN and TMB–PN mixtures.
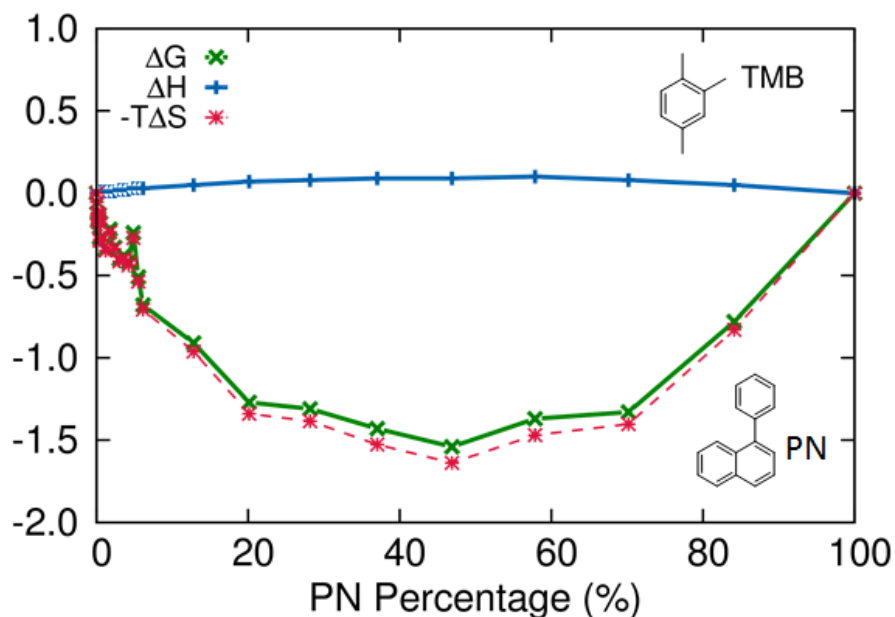
Figure 4.24. Enthalpy, entropy and Gibbs free energy of mixing as function of the additive mole fraction of the TMB–PN solutions.

4.5   Conclusion

In this chapter, we have shown that the 2PT method is a practical tool to calculate the entropy of various liquid solutions. When the shape of the molecule is spherical, 2PT gives a good agreement with experimental measurement. For the non-spherical molecules, however, a linear relation with the entropy calculated from low-concentration solutions can provide a good estimation of the standard molar entropy of the solute.

We then explored the energy properties of the LJ liquids and several common molecular models, for the pure and binary systems, our results showed reasonable agreement with experiment and expectations. $\Delta G_{mix} < 0$ was shown to be a necessary but not sufficient condition for miscibility. Turning to ternary solutions, we found that the introduction of the additional component can further stabilize the ΔG_{mix} and the lowest energy becomes

comparable to the fully mixed solution while all components are equivalent in concentration.

Accurate and expedient determinations of the free energy of mixing can hold important consequence across a number of fields, including the development of emerging technologies. Here, with a focus on beginning to develop *in silico* protocols to understand and design printing inks for OSC, we determined the free energies of mixing for commonly used halogenated solvents and additives across a range of concentrations. We show that the mixing in these systems is predominantly entropically driven, which highlights the importance of needing robust methods to determine entropic terms. This work represents a first step along the path to implementing in silico design of OSC that includes the processing conditions.

INFLUENCE OF THE SOLVENT ENVIRONMENT ON THE MOLECULAR

CONFORMATION AND AGGREGRATION DYNAMICS OF ORGANIC

SEMICONDUCTORS

5.1 Introduction

Efforts to control organic semiconductor (OSC) thin-film morophology need to consider the control of (dis)order across multiple scales. The formation of ideal molecular- and nano-scale structure can be tuned through molecular chemistry,[1-7] with considerations in these realms generally made towards the OSC electronic and optical properties. In addition to the structure of individual molecules, the morphology can also be controlled through either the thin-film deposition process or some post-deposition annealing process. During the film formation process, the relatively fast evaporation of the solvent results in limited molecular motion as the film evolves, hence films formed through this process can contain extensive disorder. As an example, the TES-ADT molecule has a strong tendency to form brickwork like crystalline, however, the deposition of such molecules in toluene with spin coating method results in a completely amorphous thin film.[8-10] In such cases, the thin-film morphology may be modified using a post-annealing process (*i.e.* vapor or thermal annealing) to more ordered morphologies.

Further, in Chapter 4, we discussed how thin-film morphologies can be modified by using a small amount of additive in the host solvent. Although the selection of primary and secondary solvent is often arrived through an Edisonian approach, the idea of using such binary system as the processing agent is commonly accepted and applied to control solid-

state morphology of the thin film. In this chapter, to bridge our previous studies and continue to establish packing–structure–function relationships of OSC, we explore the properties of several OSC molecular components in solution phase. We first explore a series chromophores synthesized by Bazan and co-workers.[11] As show in Figure 5.1, these molecules were designed with an architecture consisting electron-donating (D) and accepting (A) subunits in a D'-A-D-A-D' configuration, where the D' and D represent different electron donors. The orientation of each subunit gives rise to various rotational isomers for each molecule. The rotamers may not be equi-energetic, and lower energy conformations are expected to have higher relative populations at a given temperature, and are anticipated to play an influential role during molecular assembly and thin-film formation. As discussed in their study, the thin-film order can be improved using donor thienothiphehe (TT) and acceptor fluorinated benzothiadiazole (FBT). Moreover, while processing the molecular blend FBT-biTh / PC$_{71}$BM, Bazan, Amassian, and co-workers found that different morphologies can be achieved by changing the solvent from pure chlorobenzene (CB) to a binary CB–diiodooctane (DIO) solution,[12] and showed that there was a fundamentally different molecular behavior in these chemical environments. Here, we are perticularly interested in applying molecular dynamic (MD) simulation to study the population of rotamers in different solvent environments. We are also interested to understand how does the processing method affect the aggregation of the OSC in solution.
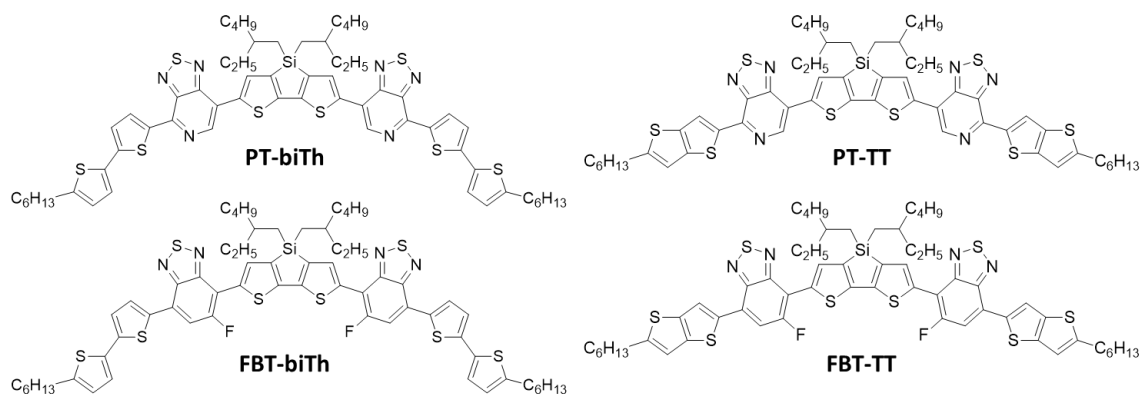
Figure 5.1. Chemical structures of oligomers of interest. PT: pyridyl-[2,1,3]thiadiazole; FBT: fluorinated benzo[c][1,2,5]thiadiazole; biTh: bithiophene; TT: thieno[3,2-b]thiophene.

We then turn to the behavior of the *anti* and *syn* isomers and fluorinated derivates of TES-ADT in concentrated, nano-confined solutions. As mentioned earlier, the optimized solid state morophologies are stongly coupled with the crystal structure that exhibit two-dimensional in-plane π-stacking, as well as the excellent continuity of the OSC through the thin film with limited domain and grain boundaries.[13-16] This scenario can be very challenging to achieve as the scale of thin film increases and strongly detemined by the processing conditions. Recently, Amassian and co-workers showed that the phase separation and crystallization of OSC can be carefully controlled through a blade coating process in a supersaturated solution.[17, 18] This study revealed the formation diF-TES-ADT polycrystalline from the supersaturated toluene solution during blade coating. These crystals were developed through a path away from the deposition point and initilly form amorphous phases that then grew into large, spherulitic cystals. Since we are interested in developing simulation models to study the aggregation and nucleation of OSC in solution phase, we made systems with derivatives of TES-ADT and explored the nucleation events at various conditions. We consider the fact that the synthesis of the ADT core presents

isomeric ratios of the thiophene orientations – *anti* or *syn*. To examine the isomer effect on nucleation and growth, models were built that contain solely anti isomers or syn isomers, and a 50:50 anti-syn mixture with the molecules shown in Figure 5.2.

anti TES-ADT   syn TES-ADT   anti diF-TES-ADT   syn diF-TES-ADT
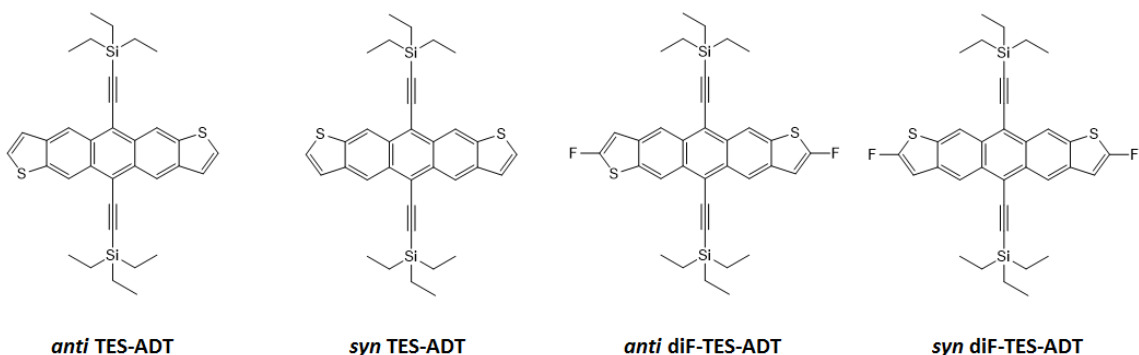
Figure 5.2. Chemical structures of *anti* and *syn* TES-ADT [5,11-bis (triethylsilylethynyl) anthradithiophene] and their fluorinated (diF-TES-ADT) derivates of interest.

5.2   Computational Methods

5.2.1   Conformational analysis through MD simulations

The MD simulations were carried out with GROMACS package 2019 or later[19, 20] using the OPLS-AA (Optimized Parameters for Liquid Simulations – All Atom) force field.[21, 22] Molecular charges and dihedral angle torsion parameters were explicitly parameterized for each molecule considered. The simulations were carried out in different solvent evnironments as described below. We used the general simulation protocal described in Chapter 2.5 to equilibrate each system. For comparison, the simulation was also done in vacuo following the same process.

5.2.2   Petentail of mean force (PMF) simulations

To understand the effect of solvent on the intermolecular interactions, PMF simlations were performed on the FBT-biTh molecules *in vacuo*, and in CB or DIO and the results are

reported in Chapter 3. Each system was built with two FBT-biTh molecules placed face to face with a center of mass distance of 4.0 nm in a box with size 6 nm × 6 nm × 6 nm, then solvate with CB or DIO solvent to make solution box. After a 500 ps equlibration to remove any overlap and strains, a pull code was used to apply umbrella sampling method to generate a series of sample windows. For the system *in vacuo*, the periodic boundary conditions (PBC) and the *NPT* ensemble were turned off and the cut-off was set to zero to keep the box from shrinking. A 2 ns *NVT* simulation was applied for data collection. For the systems with solvent, both *NVT* and *NPT* ensembles were used for equilibrium, and the final *NPT* ensemble was carried out for 5 ns for data collection.

5.2.3   Solvent drying simulations

To explore the dynamics of the OSC during the film formation process, we designed a solvent drying protocol where solvent molecules are removed from the system during the course of the simulation. We first solvated 100 FBT-biTh molecules with approximately 60,000 CB molecules and 450 DIO molecules to represent a 20 mg/ml FBT-biTh in a CB solution with 1.5 (w/w) DIO. The system was first equilibrated for an extended time using *NVT* and *NPT* ensembles. Then the peroidic boundary condition (PBC) along the *z* direction was turned off and two artifical walls were placed at the bottom and top of the simulation box to prevent molecules from moving across the boundarys. The nonbonding parameters for silicon were used for the artifical walls. In the drying simulation, the *NVT* ensemble was applied to keep the box from shrinking. Since the primary solvent during drying is CB, and it is expected that CB will evaproate at a faster rate than DIO, we only removed the CB molecules from the system. At the beginning of each drying cycle, the CB molecules on the surface (~0.8 nm) of the simulation box were mapped, and a large fraction

(>90%) of random CB molecules were removed from the system. The remaining molecules undergo a short 500 ps *NVT* simulation to equlibrate, and then another maping and removing of CB was be applied. This simulation cycle was carried continuely until the number of CB molecules were not enough to cover the entire surface.

5.2.4 Aggregation ratio

The calculation of the aggregation ratio of the OSC in the solution phase requires an accurate assignment of the molecules that paticipate in the aggregration and the molecules remains diffusing in the solutions. Typetically, the dynamics of the solute molecules in the solution can be charactized into three states: Diffusion, aggregate, and a metastable state where the molecules are transitioning between the diffusion and aggregation states. Representative snapshots in Figure 5.3 depict the molecules in the diffsuion and aggregation states. We analysized all solute molecules in the solution over many small time frames during the entire simulation window. For each molecule, the diffusion length over every time frame and the relative orientation to a given reference point were extracted.
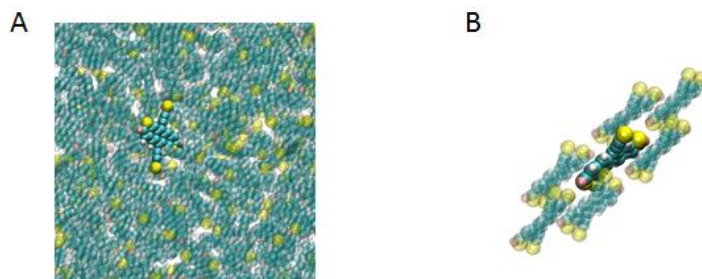
Figure 5.3. Representative MD snapshots show the solute molecule at two different states: (A) The molecule is in the diffusion state, (B) The molecule is in the aggregate state. The alkyl chain on each solute molecule and all solvent molecules were omitted for charity.

If the molecule is constantly moving over the time and its position and orientation are changing, the molecule is considered in the diffusion state. On the contrary, if the molecule

has a non-significant diffusion length over the time and the conformation is relatively "frozen" to the reference point, the molecule is considered in the aggragate state. As we observe every molecule individually within small time frames, as a molecule switces states between the adjecent time frame, the molecule is considered in the metastable transition state. From this approach, we can calculate the molecule aggregation ratio as defined by the number of molecules in the aggregate to the number of total solute molecules.

5.2.5 Nucleation in solution

To explore the nucleation of OSC in solution, different solvent environment were developed with various OSC concentrations. Each solution was first equlibrated with the standard simulation protocol described in Chapter 2.5. Then, for each equilibrated system, a vacuum gap space was inserted into the box to introduce an vacuum-solution interface. The PBC along the z direction was turned off and two artifical walls were placed at the bottom and top of the simulation box to prevent molecules from moving across the boundarys. The nonbonding parameters for silicon atom were used for the artifical walls. Finally, an *NVT* assemble was applied to the new vacuum-solution system to prevent the air space from shrinking. The order parameter, mean square displacement and aggregation ratio method were applied to the trajectories of the systems to analyze the dynamic process.

5.3 Results and Discussion

5.3.1 Oligomers in solution – conformation and aggregation

5.3.1.1 Conformation definitions

Before we begin the discussion of the conformational analysis, it is important to define how the conformations are represented. To better understand the conformational change of each oligomer, we assigned each conformation with respect to the position of the sulfer

atom on the adject units. As denoted in Figure 5.2, distinct dihedrals between each unit are marked by a different color. We make use of the notation *anti* (or A) to refer to the conformation of any two moieties along the oligomer backbone where neighboring sulfur atoms are oriented in opposite directions, while *syn* (or S) is used to represent situations where the neighboring sulfur atoms are pointed on the same side of the backbone. Since there are six dihedrals for the molecules with bithiophene (biTh) and four dihedrals for molecules with thienothiophehe (TT), each conformation can be described with six or four orientation parameters. Therefore, the representative molecules in the Figure 5.2 can be described as SASSAS (top) and ASSA (bottom).
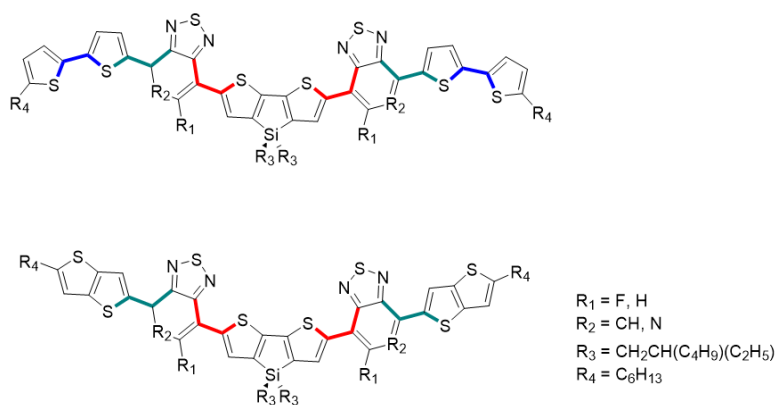
Figure 5.4. Representative oligomer conformations and dihedral angle color codes. For the top molecule, the SASSAS conformation is represented, while the bottom molecule represents the ASSA conformation.

5.3.1.2 Oligomer in solvent – conformation analysis

Figures 5.5 – 5.8 shows the dihedral change of four oligomers in CB and DIO solution. According to previous definition, the dihedral angle for *syn* conformation is 0 degrees, while the angle for *anti* conformation is 180 degrees. As shown in Figure 5.5, the rotation frequency decreases along the molecule backbone from the the exterior to the interior. This

behavior is constant for all the oligmers studied. As an example for the bithiophene (biTh) groups, denoted with blue in the image, shows a significant tendency to rotate in CB. As one moves more towards the center of the molecule, however, the dihedrals rotate (red and green depictions) to a much lower extent. This trend was excepted, as moving from head/tail to the center, the module unit size increase, and therefore, the rotation energy also increased.
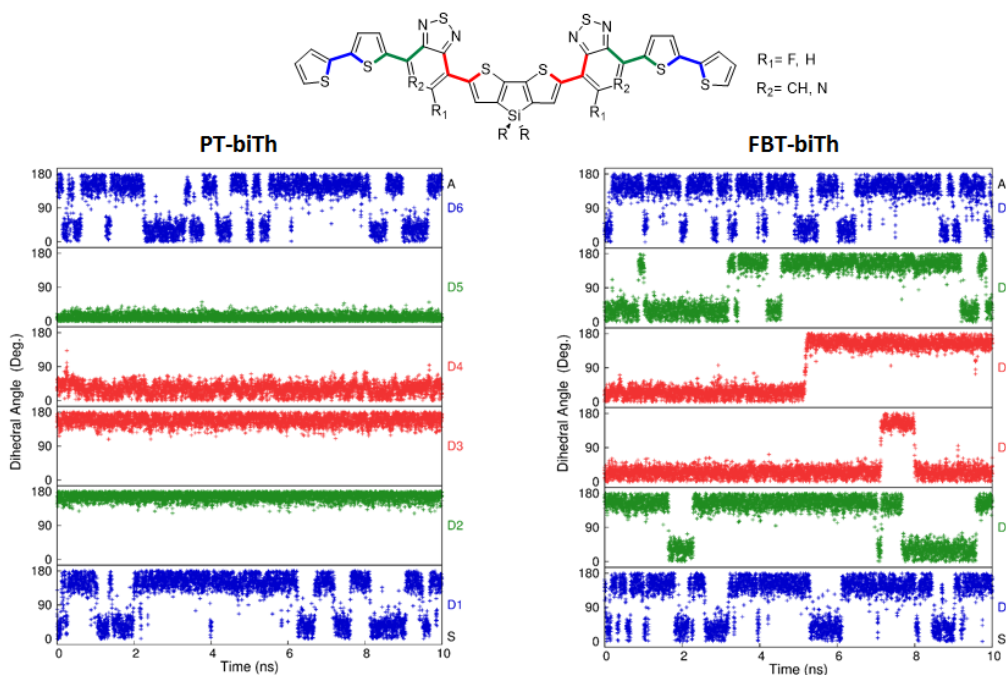
Figure 5.5. Dihedral angle analysis for the oligomers with bithiophene as ending groups in CB.
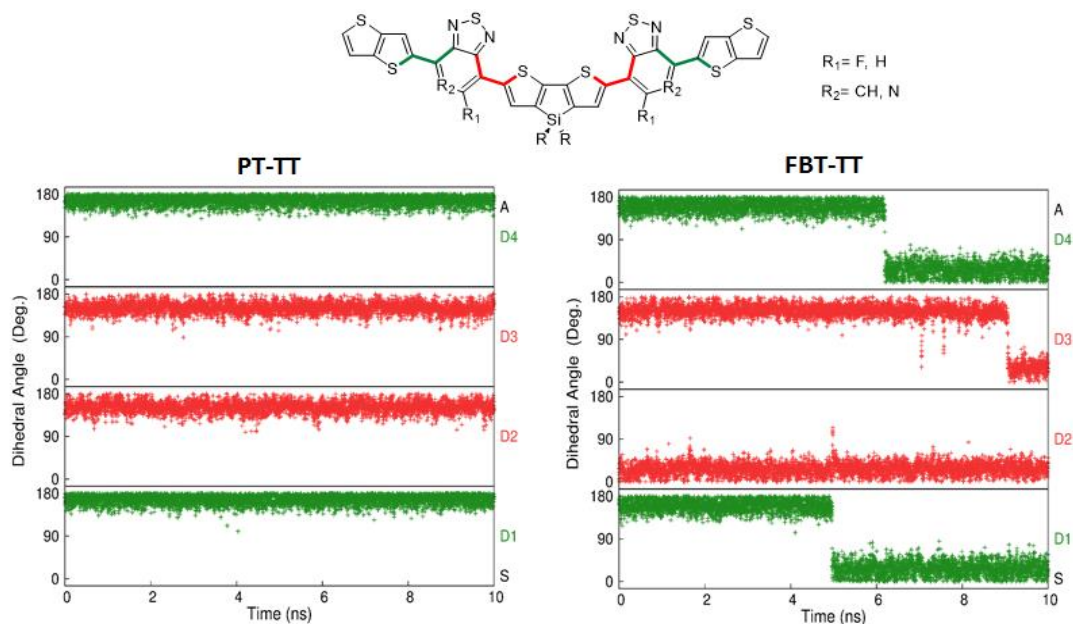
Figure 5.6. Dihedral angle analysis for the oligomers with thieno-thiophene as ending groups in CB.

Comparing the systems as either having the PT or FBT acceptor unit, the dihedral angle rotation frequency is larger for FBT, Figures 5.5 and 5.6. This suggests that PT stabilizes the moleuclar structure moreso than FBT. This is an interesting finding as fluorination is often reported in the literature to "lock in" distinctive intramolecular conformations; here in Figure 5.5, the PT interacting with its neighbors demonstrates a larger resistance to re-orientation than the fluorine atom substitution of FBT.

There is also a significant influence of the solvent on the intramolecular rotations when going from CB to DIO, Figures 5.7 and 5.8. Though there are still noticeable rotations in the exterior biTh units, the overall tendency for the different rotamers to be accessed decreases in DIO when compared to CB.
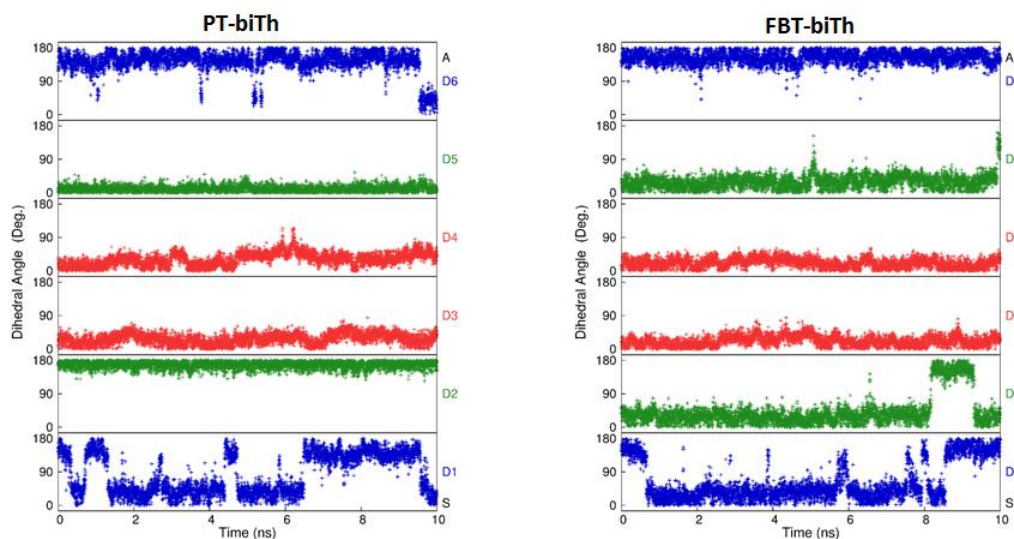
Figure 5.7. Dihedral angle analysis for the oligomers with bithiophene as ending groups in DIO.
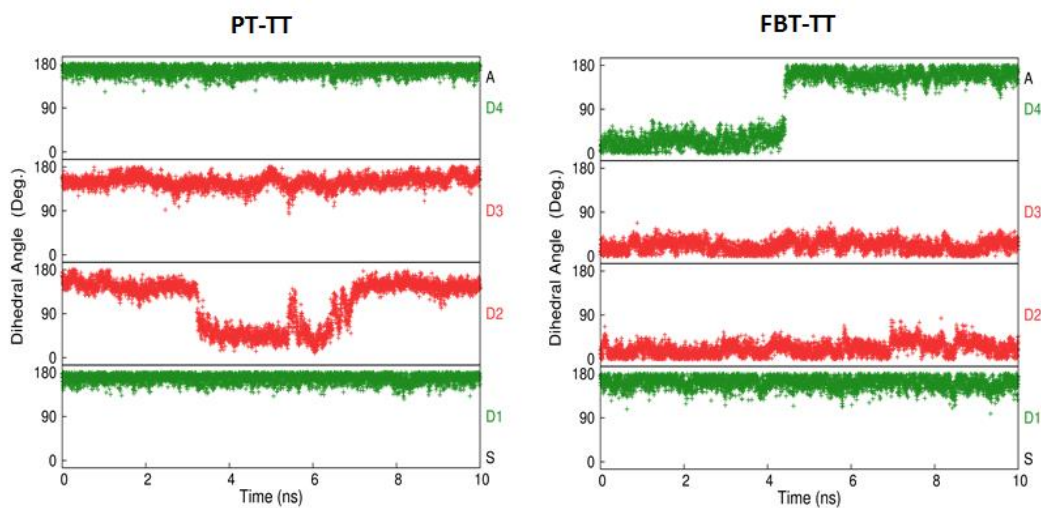
Figure 5.8. Dihedral angle analysis for the oligomers with thienothiophene as ending groups in DIO.

To explore these trends further, we repeated the simulations with several different initial rotamer conformations. Figures 5.10 to 5.17 show the dihedral angle change of different conformations of each oligomer in CB or DIO. As an example, in Figure 5.10, we explored

137

three conformations: AAAAAA, AASAAA and AASSAA, and solvated each conformation with CB. For each conformation, the tendency for rotation of any unit decreases on going from the exterior to the interior of the molecule. Again, when considering DIO (Figures 5.13 to 5.16), there is a notable change in the rotational behavior of the molecules when compared to CB, with the amount of rotation of the moieties being much smaller than what is observed for CB. As such, the molecules are more likely to maintain their initial conformations. This tendency is especially significant for the inner dihedrals, as shown in FBT-biTh (Figure 5.13), where innermost (red) dihedrals maintain the initial conformation over the full simulation.
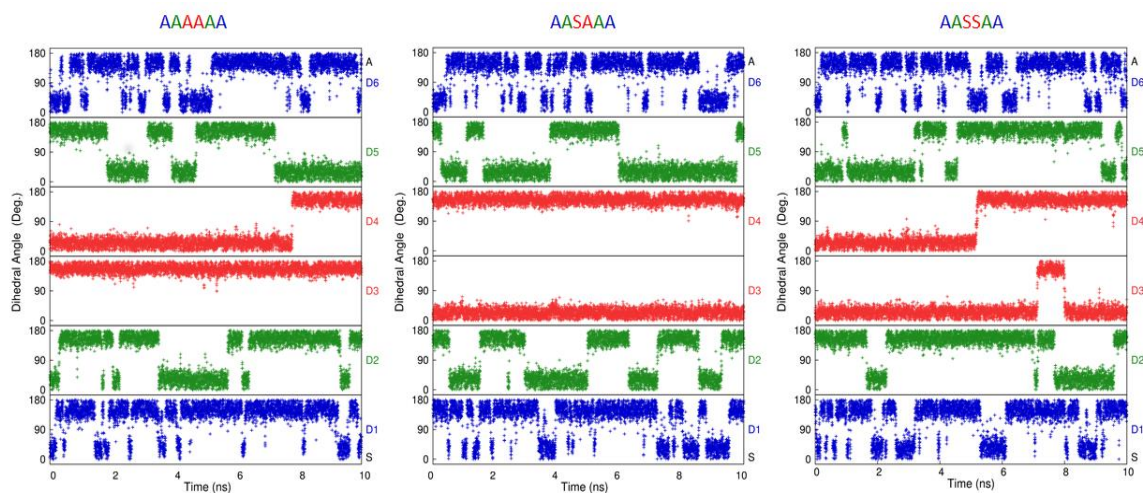
Figure 5.9. Three conformations of FBT-biTh in CB.
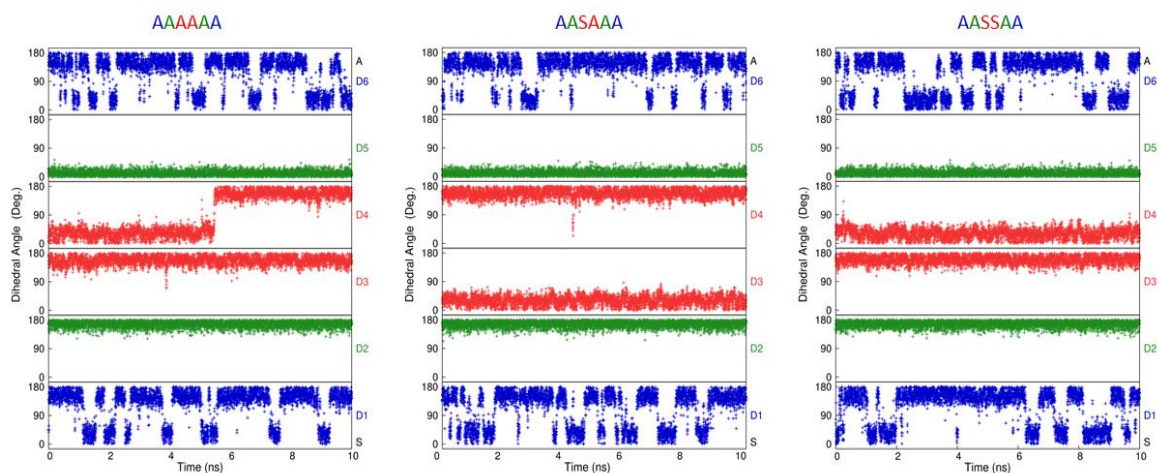
Figure 5.10. Three conformations of PT-biTh in CB.
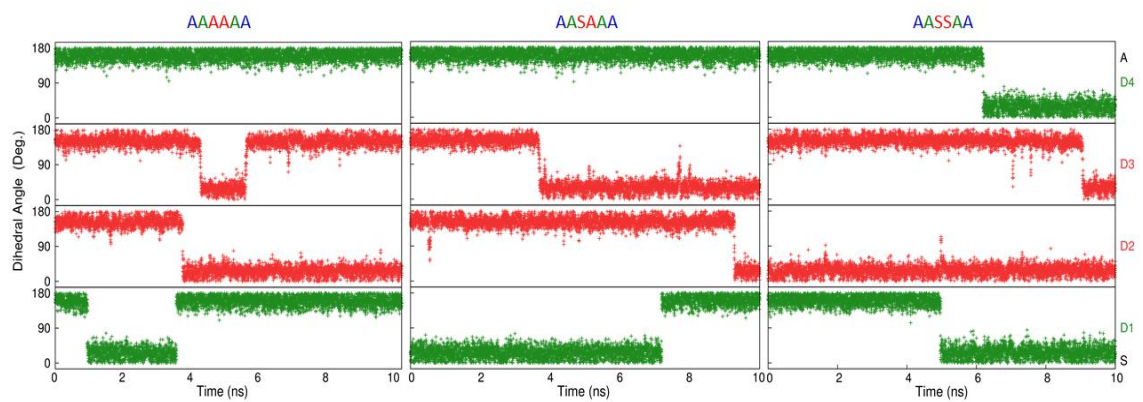
Figure 5.11. Three conformations of FBT-TT in CB.
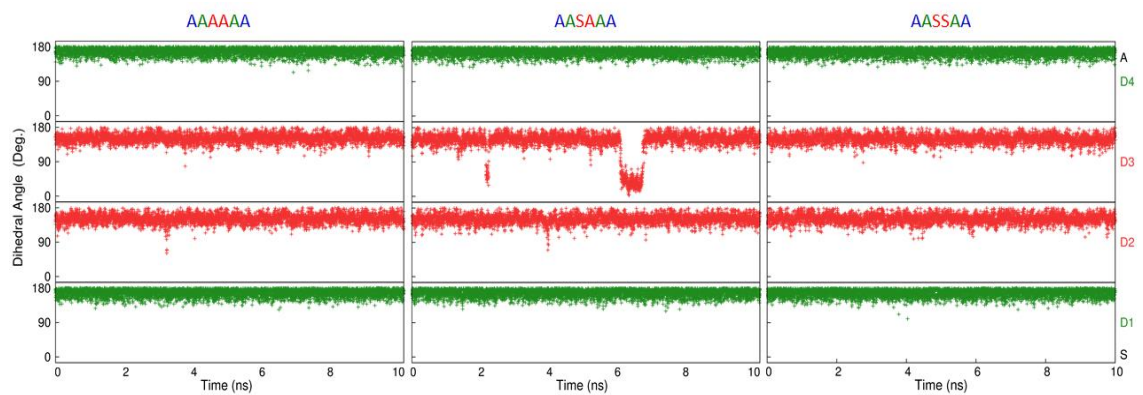
Figure 5.12. Three conformations of PT-TT in CB.
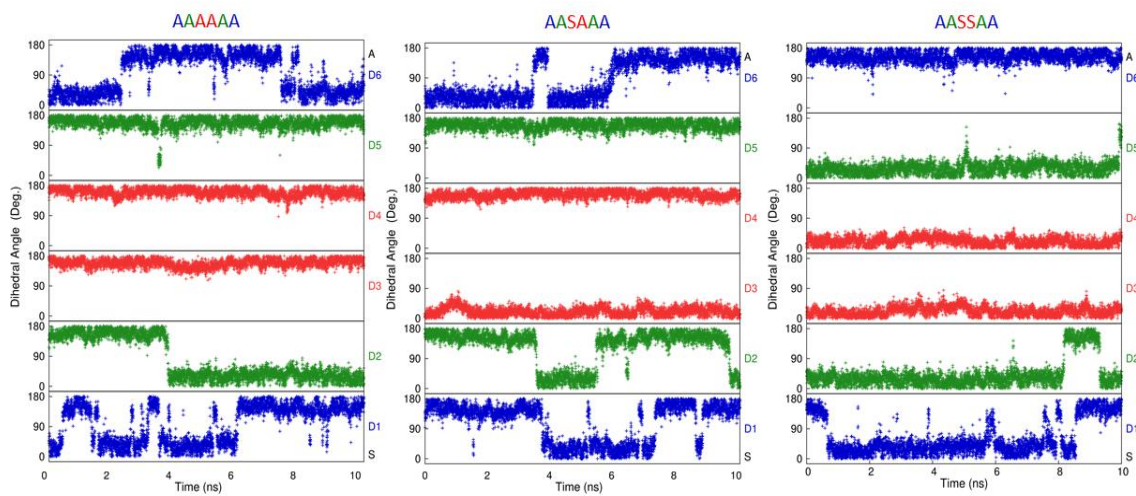
Figure 5.13. Three conformations of FBT-biTh in DIO.
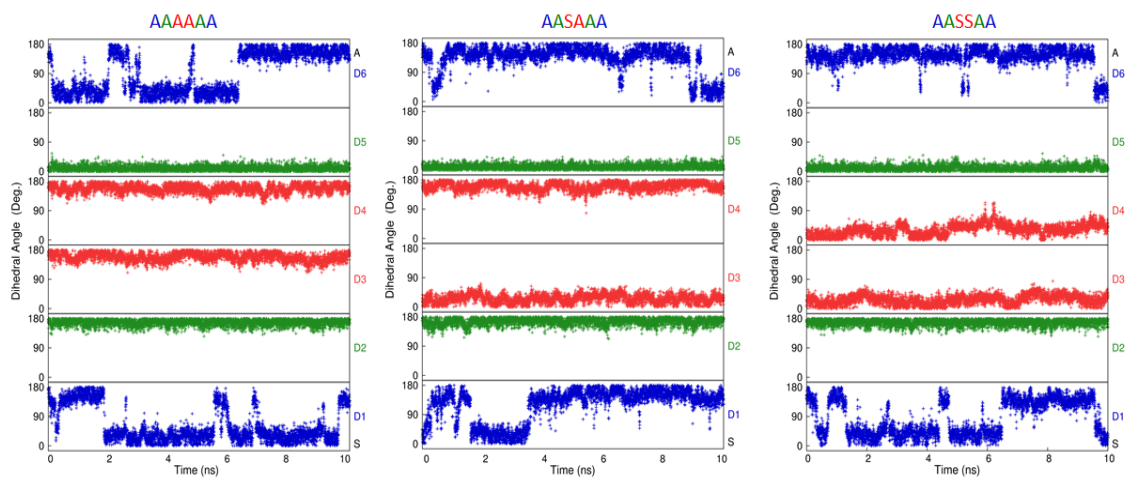
Figure 5.14. Three conformations of PT-biTh in DIO.
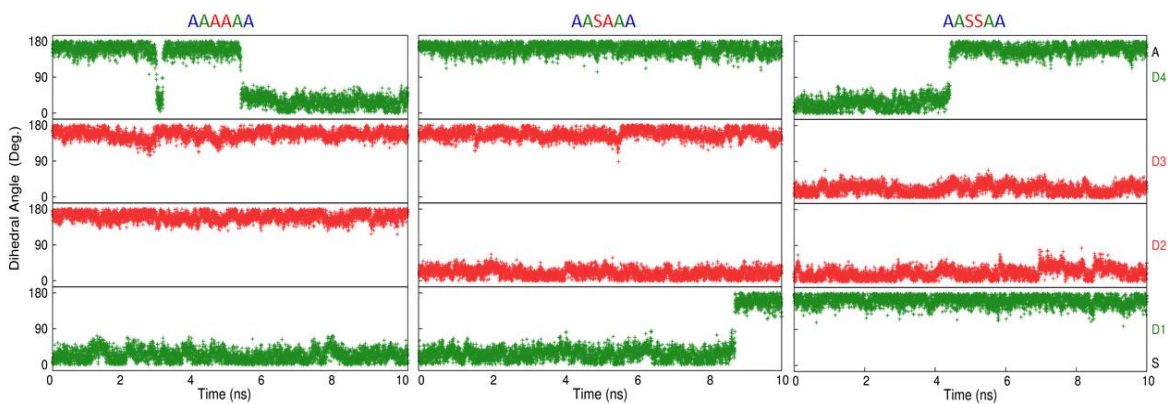
Figure 5.15. Three conformations of FBT-TT in DIO.
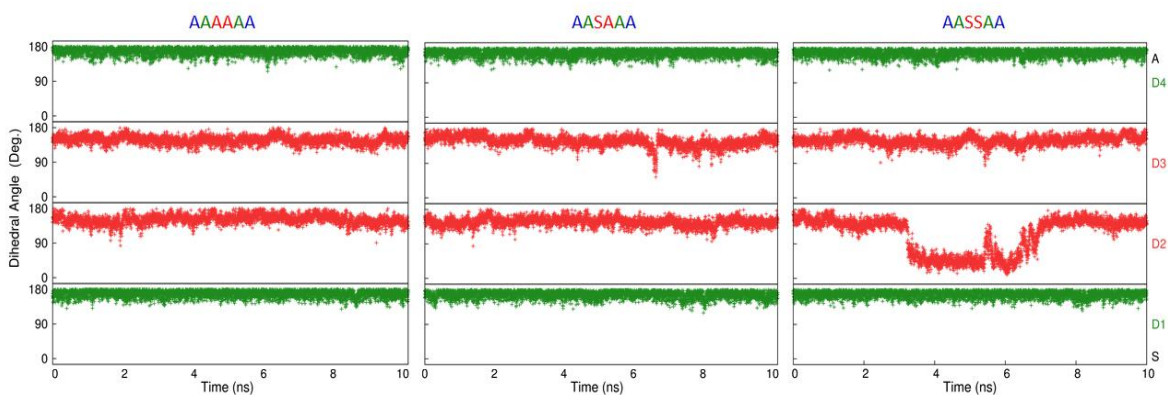
Figure 5.16. Three conformations of PT-TT in DIO.

Tables 5.1 and 5.2 summarize the structural preferences found in the different solutions. Notably, the preferred conformations are directly related to the nature of electron-accepting unit. When FBT is the acceptor and the oligomers are in CB, the center of the molecule prefers an AS conformation, which will make the molecule take on a more linear shape. On the other hand, the PT acceptor prefers to induce the AA configuration, which leads to more of a "banana shape", as shown in the Figure 5.1. In DIO, however, the situation changes. As noted, the relative amount of intramolecular rotation is dramatically reduced

in DIO when compared to CB. Hence, the oligomers tend to maintain the initial conformations that were adopted at the beginning of the simulation.

Table 5.1. Preferred final oligomer conformations in CB as a function of the oligomer conformation used at the start of the MD simulation. A and S orientations are shown in Figure 5.2; X represents cases where no preferred orientation can be confirmed.

Initial Conformation	FBT-biTh	PT-biTh	FBT-TT	PT-TT
	Final Preferred Conformation			
AAAAAA	XXASXX	XAAASX	ASAA	AAAA
AASAAA	XXSAXX	XASASX	ASXA	AAAA
AASSAA	XXSXXX	XAASSX	XSAX	AAAA

Table 5.2. Preferred final oligomer conformations in DIO as a function of the oligomer conformation used at the start of the MD simulation. A and S orientations are shown in Figure 5.2; X represents cases where no preferred orientation can be confirmed.

Initial Conformation	FBT-biTh	PT-biTh	FBT-TT	PT-TT
	Final Preferred Conformation			
AAAAAA	XSAAAX	XAAASX	SAAX	AAAA
AASAAA	XXSAAX	XASASA	SASA	AAAA
AASSAA	SSSSSA	XASSAA	ASSA	AAAA

The study of these oligomers in the different solvent environments clearly shows how the solvent can affect molecular conformations. This is important as it shows how the processing environment can impact the molecular structure Further, when considering the formulations of the processing solvent, we can see from these simulations that the choice of primary and additive solvent can impact the preferred molecular configuration, as here CB provides an environment where the molecular structure can change readily, while DIO

(which would presumably be the main solvent remaining towards the end of the drying process) does not allow for much molecular reorientation – *i.e.* the molecule will be "stuck" in the conformation developed in the primary solvent.

5.3.1.3 Inter-chromophore interactions in solution

Now that we have an understanding of how the solvent impacts the molecular structure, we want to explore the molecular dynamics when more than one chromophore is in solution. Here we chose the FBT-biTh as the target molecule for study. We performed potential of mean force (PMF) simulations for FBT-biTh *in vacuo* and in CB and DIO (Figure 5.17). When *in vacuo*, FBT-biTh presents a large intermolecular interaction energy of 30 kcal/mol when the center-of-mass (COM) distance between the two FBT-biTh is about 0.4 nm. However, when the molecules are solvated in CB and DIO, the interaction profiles change substantially. In CB, the two FBT-biTh oligomers still present a negative/attractive interaction energy (~1 kcal/mol), suggesting that the molecules prefer to interact / aggregate. The situation differs in DIO, though, where the FBT-biTh oligomers show a repulsive interaction. This is an unexpected finding as one may expect that the FBT-biTh with the large aromatic core will prefer to aggregate in the predominantly alkane-based solvent. However, the PMF simulation suggests that the FBT-biTh are repulsive in DIO solution and are less likely to form large aggregate. These results are consistent with the larger-scale aggregation studies (see below), and literature reports that FBT-biTh films formed from CB:DIO solvent blends are less dense than those from CB alone.[12]
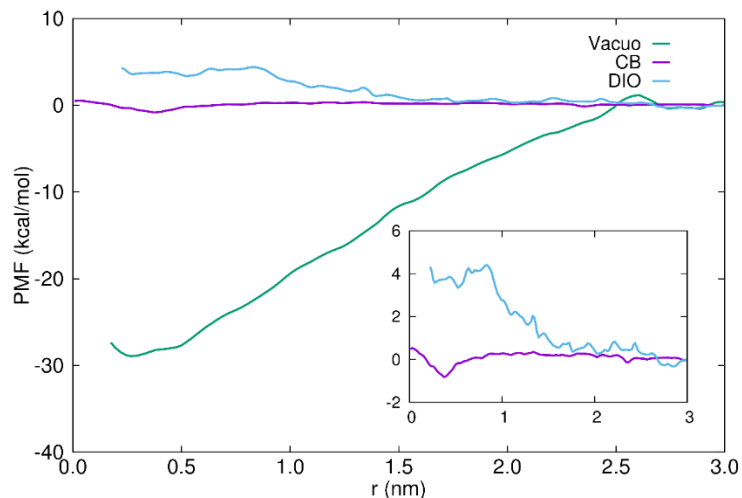
Figure 5.17. PMF calculated of two FBT-biTh molecules in vacuo, CB and DIO.

To explore this further, we modeled concentrated solutions with FBT-biTh in CB and DIO. Figure 5.18 (A) and (B) shows the radius distribution function of CB and DIO solutions with 6% (w/w) FBT-biTh, calculated after 30 ns simulation. Different initial configurations were used, each showing consistent results across the study. In CB, the formation of local aggregation presents as sharp peaks in Figure 5.18 (A), while in DIO the distribution of the molecules is still random.
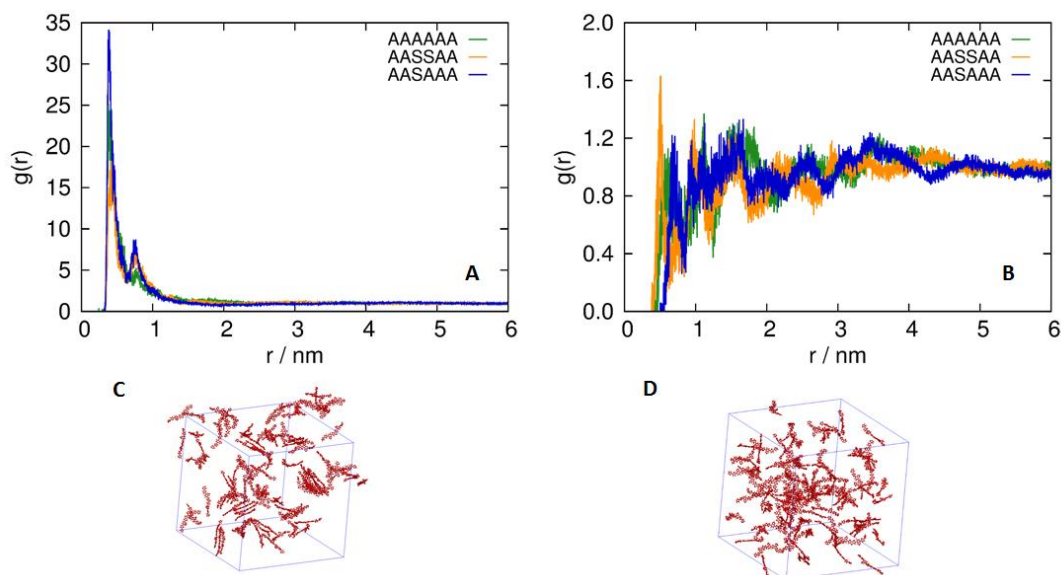
Figure 5.18. RDF of 6% FBT-biTh in (A) CB and (B) DIO, (C-D). Two representative snapshots of the two solution systems. FBT-biTh molecules are shown in red. The alkyl chains and solvent molecules are omitted for clarity.

Concerning the molecular conformations, the terminal thiophene rings, as for the isolated molecules in solution, freely change their orientation; hence, we ignored the contribution from this moiety and plotted the distribution the remaining distributions, Figure 5.19. As expected, the conformation in CB is more diverse than in DIO, with no specific conformation dominating the distribution. In DIO, however, approximately 25% of the molecules have the XASAAX conformation, note that this conformation is asymmetric with respect to the center of the molecule.
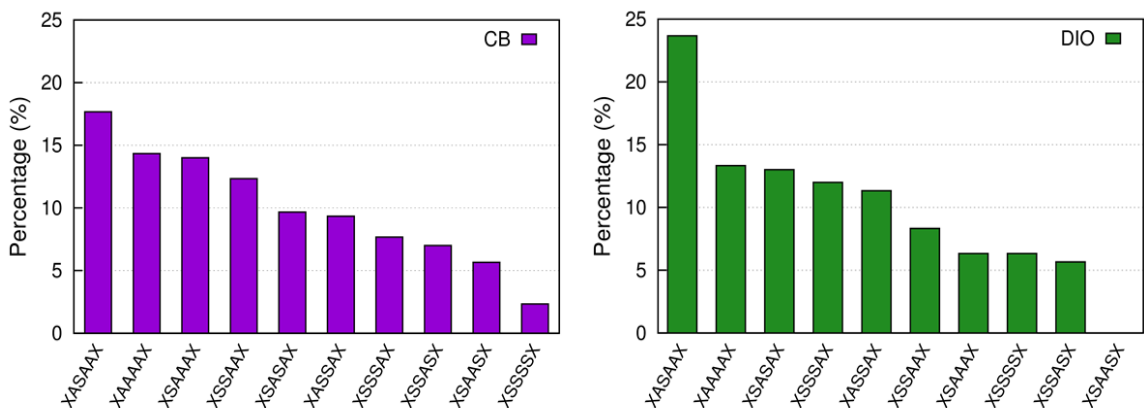
Figure 5.19. FBT-biTh conformation population in CB and DIO.

If we only consider the symmetry of the molecule as shown in Figure 5.20, the population of asymmetric conformations are significantly larger in DIO solution comparing to CB solution. This suggests that although the conformation of the oligomer in the DIO is preserved, in a concentrated solution, the interaction between molecules will lead to a preference of an asymmetric conformation. This change leads to the molecule having a more linear configuration, which may assist in the formation of aggregates.
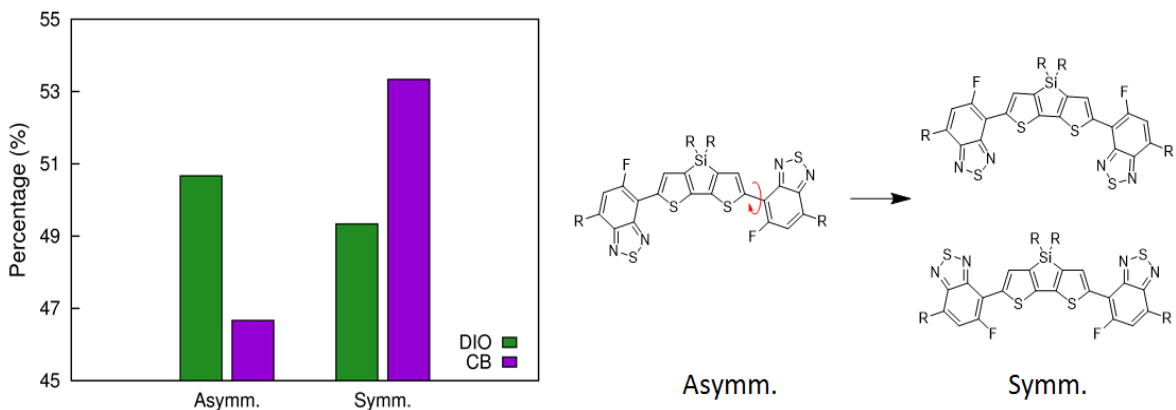
Figure 5.20. Symmetric and asymmetric population in CB and DIO/

This result is consistent with the results of the PMF simulations, where the molecules become asymmetric, as shown in Figure 5.21, even though the molecules start with a symmetric configuration (AA). The blue molecule was fixed in position in each PMF simulation, as the red molecule being pulled close to the blue molecule, the center core rotated to form an asymmetric conformation in all simulations.
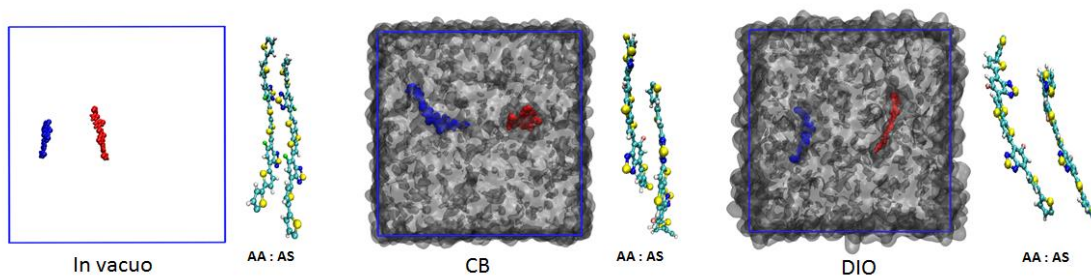
Figure 5.21. Snapshots from PMF simulation in vacuo, CB and DIO solutions. The molecule in red was pulled toward the blue molecule. The configurations of the two molecules at the closest point in each environment were extracted and placed along the side of simulation box to show close-up orientations. The alkyl chains on each molecule were omitted for clarity.

We also examined more dilute solutions to confirm the hypothesis. As the concentration increases from 1% to 6%, the change of each conformation is not significant in CB and the number of symmetric (combine AA and SS) conformations is comparable to the number of asymmetric conformation (SA). However, the asymmetric population increases from being small in the 1% solution to large in the 6% solution in DIO; here, it appears that the AA conformations switch more readily to the SA conformations (Figure 5.22).

147
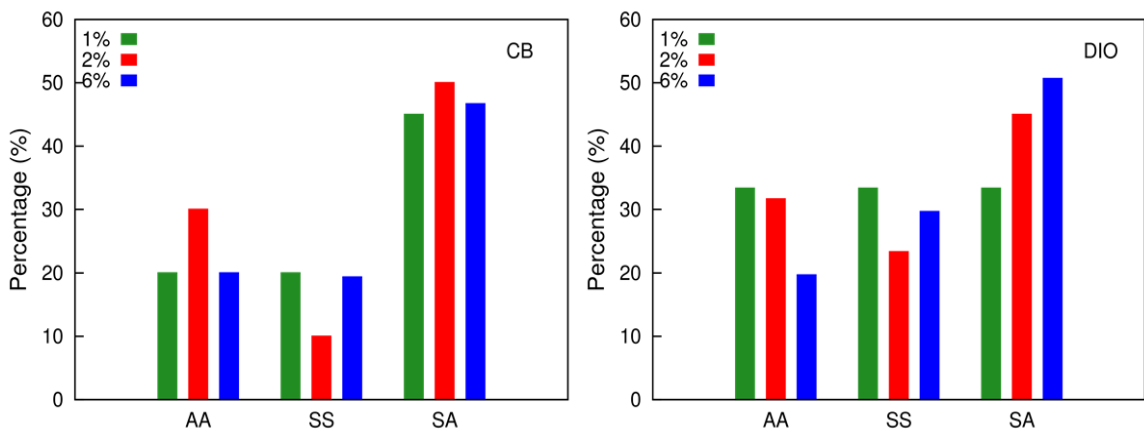
Figure 5.22. Conformation population determined by the inner molecular unit of 1%, 2% and 6% FBT-biTh in CB and DIO.

5.3.1.4 Oligomer aggregation

One of the key issues to understand is how the small amount of additive in the solution changes the morphologies of the OSC during solvent drying process. DIO is a high boiling point additive, therefore, it is expected that the concentration of DIO increases as CB evaporates. To mimic this process, we made several models with FBT-biTh, CB, and DIO. The concentration of DIO increases from 5% to 50% to 90% (w/w) to represent different states during the drying process. As shown in Figure 5.23, when we set the concentration of FBT-biTh at 5% and 10%, however, these were close to the saturation limit and due to the long alkyl chains on the backbone, the molecules started to form disordered aggregation during the equilibrium step. If we decrease the solution concentration to 2%, the individual molecule was isolated in the solution and the contact between two molecules were too rare for aggregation to occur in the MD simulation time frame (Figure 5.24).
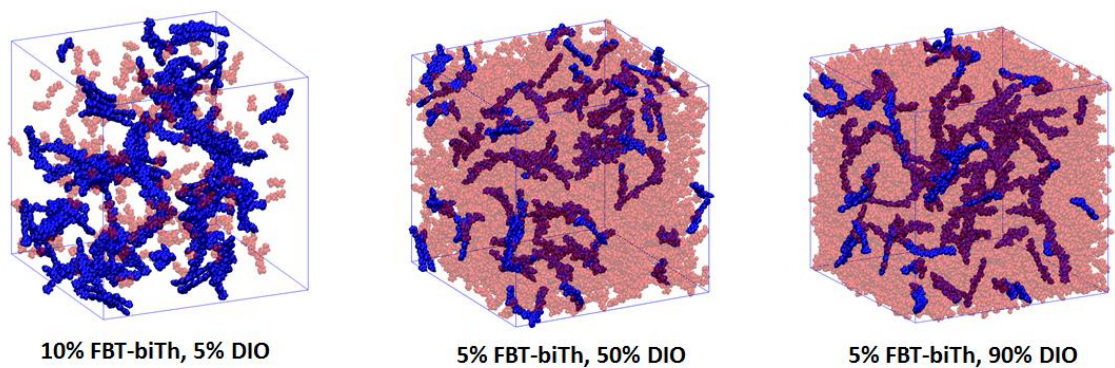
Figure 5.23. Representative snapshot of 100 FBT-biTh molecules in CB solution with 5%, 50% and 90% DIO. Blue: FBT-biTh, Red: DIO. The CB molecules and alkyl chains on FBT-biTh were omitted for clarity.
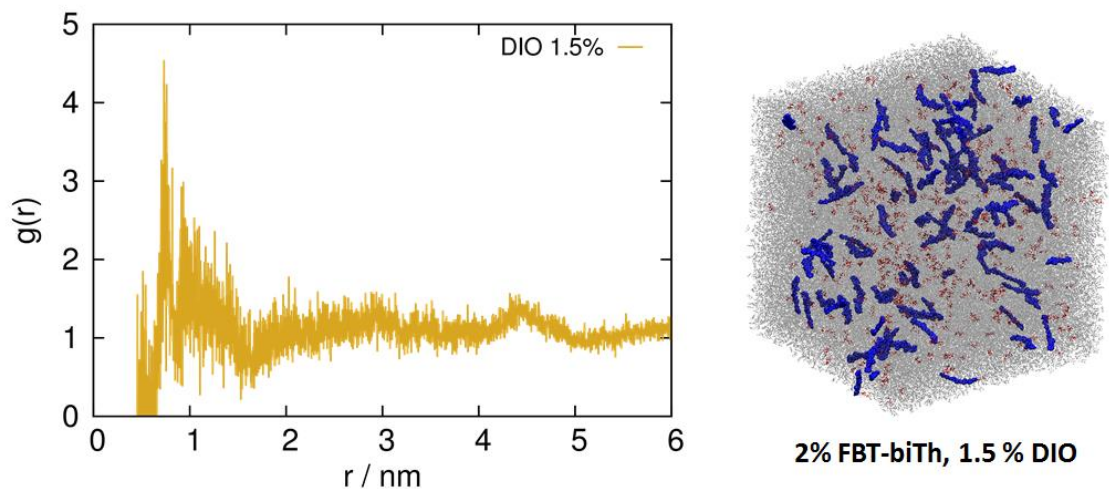
Figure 5.24. Radius distribution function of 2% FBT-biTh in CB solution with 1.5% DIO as additive. Grey: CB, red: DIO, blue: FBT-biTh. All alkyl chains on the FBT-biTh molecules are omitted for clarity.

Therefore, we conducted a solvent drying simulation to remove CB molecules out of the simulation box to model CB evaporation. As shown in Figure 5.25, while the solvent level dropped, the concentration of DIO increases, so we can track the dynamics of the solute molecules.
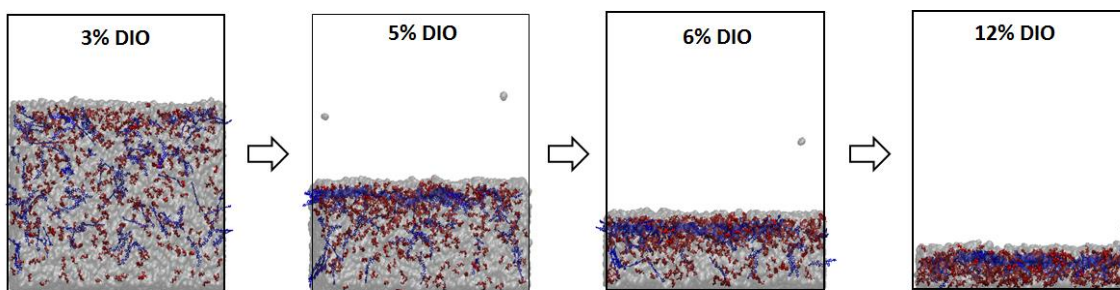
Figure 5.25. Representative snapshots from a drying process of FBT-biTh solution with 1.5% DIO. Grey: CB, red: DIO, blue: FBT-biTh. All alkyl chains on the FBT-biTh molecules are omitted for clarity.

We extracted several intermediate snapshots during the drying process and calculated the RDF of each image, as shown in Figure 5.26. The first peak was observed at about 0.4 nm while the concentration of DIO was 5%, with the concentration increasing, the second and third peaks started to form at 0.8 nm and 1.1 nm, respectively, which indicated the formation of ordered aggregates. This is confirmed from the selected snapshots shown in Figure 5.27, where ordered aggregates start to form at 3.5% DIO and keep expending through 10% DIO systems.
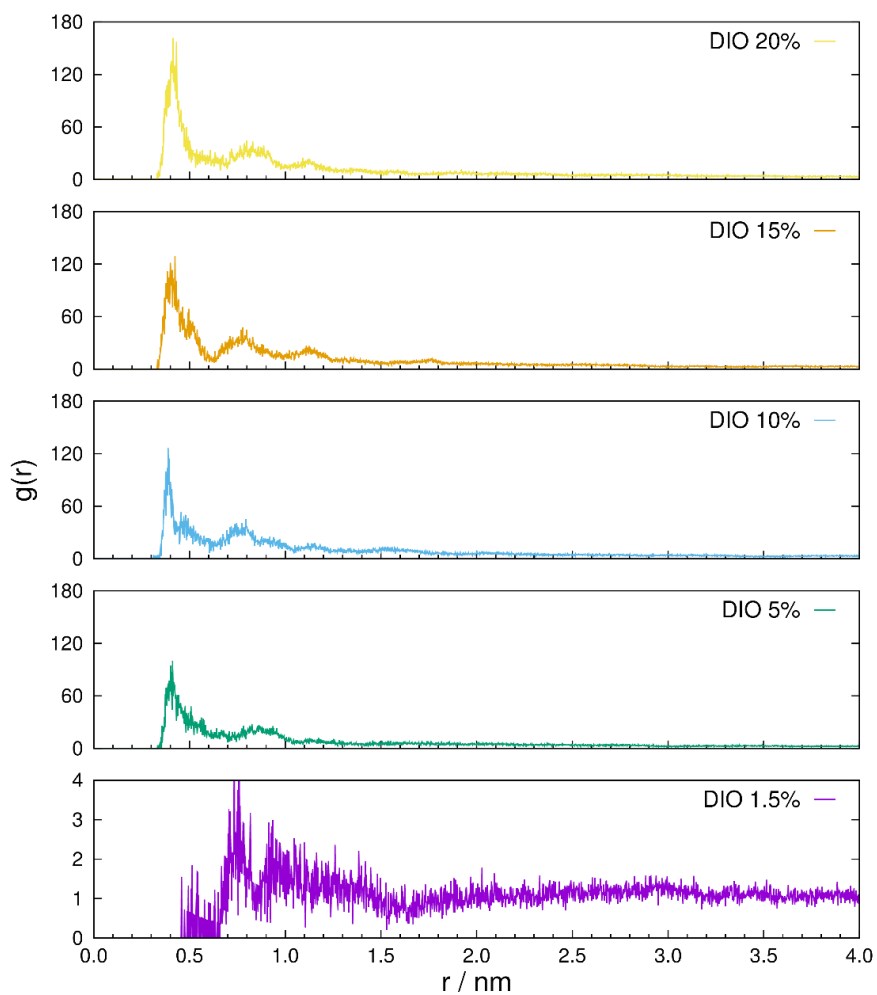
Figure 5.26. RDF of FBT-biTh molecule in the CB-DIO solution at different DIO concentrations drying solvent drying simulation.
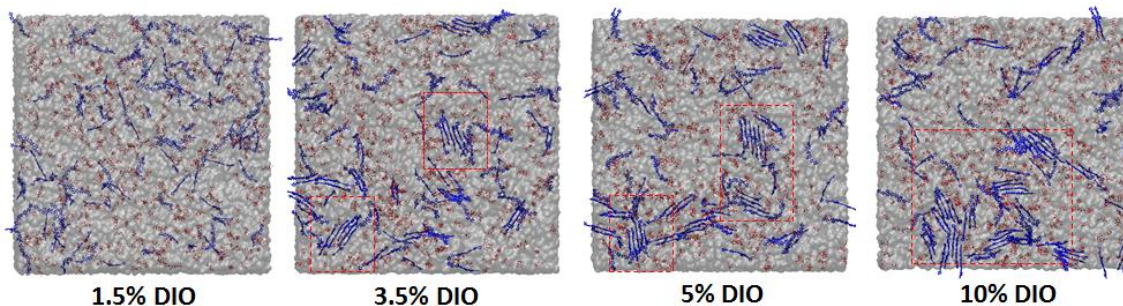
Figure 5.27. Representative snapshots from drying simulation shows the formation of aggregation of FBT-biTh. Grey: CB, red: DIO, blue: FBT-biTh. All alkyl chains on the FBT-biTh molecules are omitted for clarity.

We note interesting trends in terms of the position and orientation of the FBT-biTh molecules as drying proceeds. As shown in Figure 5.27, the molecular backbones in the aggregates take on a vertical orientation with respect to the liquid–vacuum interface. The position and orientation of the FBT-biTh molecules in the solution is critical to initiate the aggregation process.

To further confirm this, we selected a top region of the simulation box, which is 25% of the total depth at each step. Then we calculated the percentage of the solute and DIO molecules in this region to the total solute or DIO molecules in the system. Figure 5.28 shows the result of the percentage as a function of the DIO concentration during drying. Clearly, the concentration of solute and DIO both increased, especially on the top region of the simulation box, presented as the blue and red dots. As we performed the drying in a short equilibration time step, this result could have been a result of the limited relaxation time after the CB was removed. When we extended the equilibration time to 10 ns, the percentage of DIO (green rectangle line) slowly dropped back, indicating the extend equilibration time allowed the DIO to diffuse through the system. However, the percentage of solute on the top region was not affected by this. As shown by the green triangle line,

the percentage of FBT-biTh on the surface remained after the extended equilibration time. It seems like the FBT-biTh does not want to merge into the solution and stays on the surface.
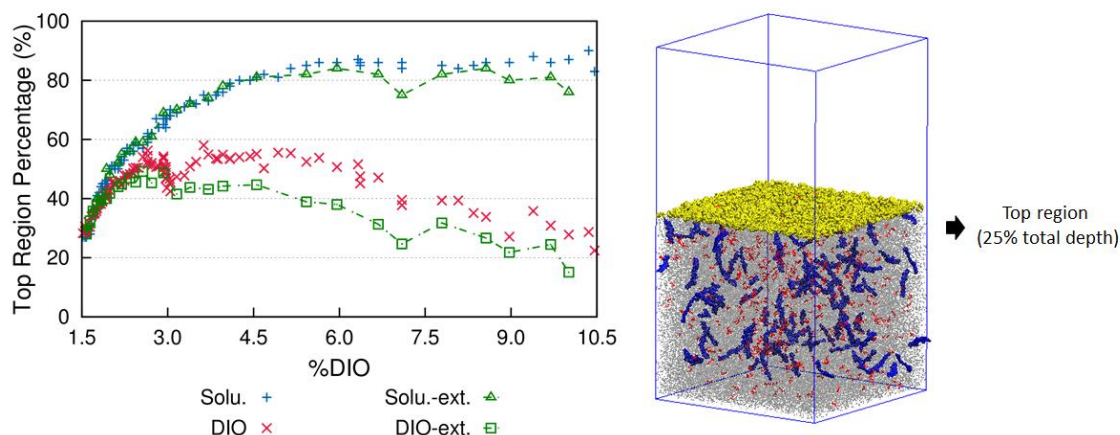
Figure 5.28. The molecular percentage of FBT-biTh and DIO on the top 25% region of the solution calculated during the solvent drying process. A Pictorial representative of the solution was also given, the thin layer marked in yellow are the CB molecular removed in each drying cycle. Grey: CB, red: DIO, blue: FBT-biTh. All alkyl chains on the FBT-biTh molecules are omitted for clarity.

To further understand this, we explored the orientation of the FBT-biTh molecules in the solutions We used two angles to determine how the molecule aligns with respect to the surface. First, we calculated the dihedral angle between the backbone central DTS unit and the *xy*-plane, defined by the surface of the solution. We also calculated the angle between the molecular long axes (defined as the vector of the backbone) and the *z*-axis, which is vertical to the surface of the solution. We calculated these two angles for each FBT-biTh and plotted the population of each angle at 20 ° intervals. As shown in Figure 5.29, with the increasing of DIO concentration, the population of two angles in the 80-100 range increases, while the first dihedral angle around 80-100 ° made the molecular backbone vertical to the surface, the second angle around 80-100 ° puts the molecule long axes along

with the solution surface. The combination of these two factors reveals that the orientation of the solute is in an upright orientation with respect to the solution surface. A close-up view of the system reveals that the primary driver for this orientation is determined by the alkyl chains. While the two alkyl chains on the termini of the molecule keep the molecular backbone parallel to the surface, and the two alkyl chains on the center DTS unit lead the molecular backbone perpendicular to the interface. As shown in Figure 5.29 (D, E), the molecules in blue and black have the same orientations in terms of the center alkyl chains on DTS pointing to the interface, while the molecule red is the only exception that has the center alkyl chains pointing down.

As discussed previously, the interaction between two FBT-biTh molecules is maximized when the backbone has maximal overlap. In this situation, the linear molecule should have the most potential to enhance the interaction. A side view of the aggregation further reveals that most of the molecules preserved the linear conformation, as shown in blue and black in Figure 5.29. The only exception is the red molecule, which has the "banana shape" conformation. This is due to the fact that while the center alkyl chains on this molecule is pointing away from the interface, the molecule has to maintain a banana shape in order to keep the terminal alkyl chain close to the interface. The mismatch of the conformation caused a disorder point in this structure and can potentially affect the charge transfer in the film.
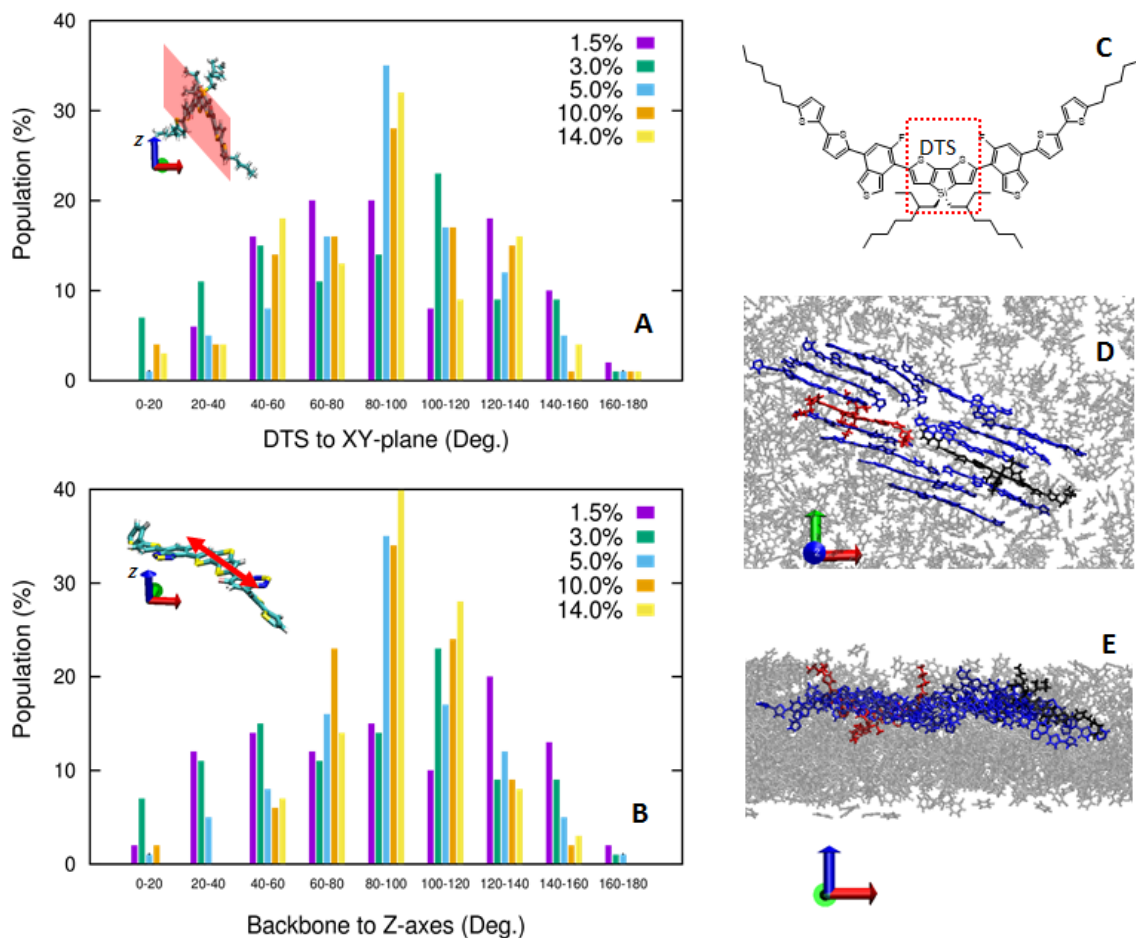
Figure 5.29. A: Angle distribution of the DTS unit to the xy plane of the FBT-biTh molecule. The xy plane is defined as the surface of the vac-solution system. B: Angle distribution of the FBT-biTh backbone to the z axes. The Z-axes was defined as the vector perpendicular to the vac-solution interface. C: Chemical structure of the FBT-biTh shows the inner DTS unit. D: A top view snapshot of one aggregate in the solution during drying process. The red and black molecules are highlighted to represent the two different orientations to the vac-solution interface. Grey: CB molecules. Red, blue, black: FBT-biTh. All hydrogen atoms on the FBT-biTh molecules are omitted for clarity.

These aggregation studies did not result in large clusters of ordered molecules. This was due a function of i) the rotational freedom on each molecule make it too difficult to aggregate in an orderly fashion, as the molecules can change conformation in solution; and ii) aggregation is by nature a slow event, and the model system size and the time given in

155

the simulation is not sufficient for large aggregates to form. Although these drying simulations can provide an initial view of the formation of local clusters, the nature of the molecule limited further study of the aggregation.

5.3.2 Nucleation in nano-confined, supersaturated solutions

With the experience we gained from the rotamer simulations, we explored another molecular model. We have studied the phase transitions of ADT molecules in pervious chapters. The rigid backbone and large conjugated area of these molecules make them a good candidate for charge transfer materials. To understand the relationship between the nucleation and the concentration of solute, we prepared several ADT-toluene models with fixed ADT concentration. As described previously, these systems were prepared with two impenetrable walls. To better represent the environment from the experiment, each system was also created with a vacuum space on the z direction. We adapted NVT simulation to equlibrate these systems and observe the nucleation of ADT in each solution.

To analyze nucleation events, we determined the order parameters of each system, Figure 5.30. The initial aggregation was observed above 60% diF-TES-ADT solution and at 70% concentration, the maximum order was achieved. In the 10% to 50% diF-TES-ADT solutions, although the systems are super satrurated solutuion, the simulation approach is not sufficient for the molecules to form aggregates. We extended the simulation time up to 300 ns, for solutions above 70%, the molecular ordering increased along with the simulation time. However, no further aggregation was developed over this time frame at 60% and below, Figure 5.31-5.32. This suggests that 70% is a critical concentration for the simulation to achieve orderred aggregations. On the other hand, the order parameters of diF-TES-ADT dropped between 70% to 99%, this was due to the space between molecules

156

was not enough for diF-TES-ADT to reorientat in order to form ordered aggregations. As

shown in Figure 5.33, the molecular ordering does increase with simulation time. However,

due to the limited space between molecules, the aggregation of diF-TES-ADT can only

form small ordered domains with many disordered molecules along the boundaries.
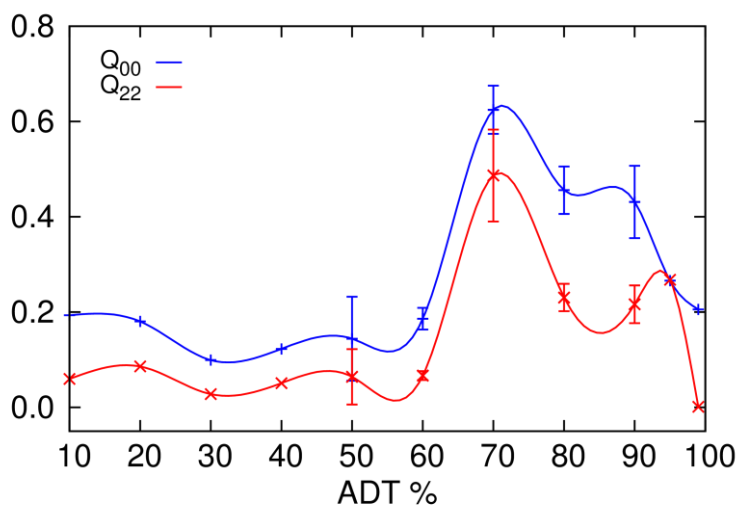
Figure 5.30. The long axes (Q_{00}) and short (Q_{22}) order parameters of the diF-TES-ADT as function of the diF-TES-ADT concentration.
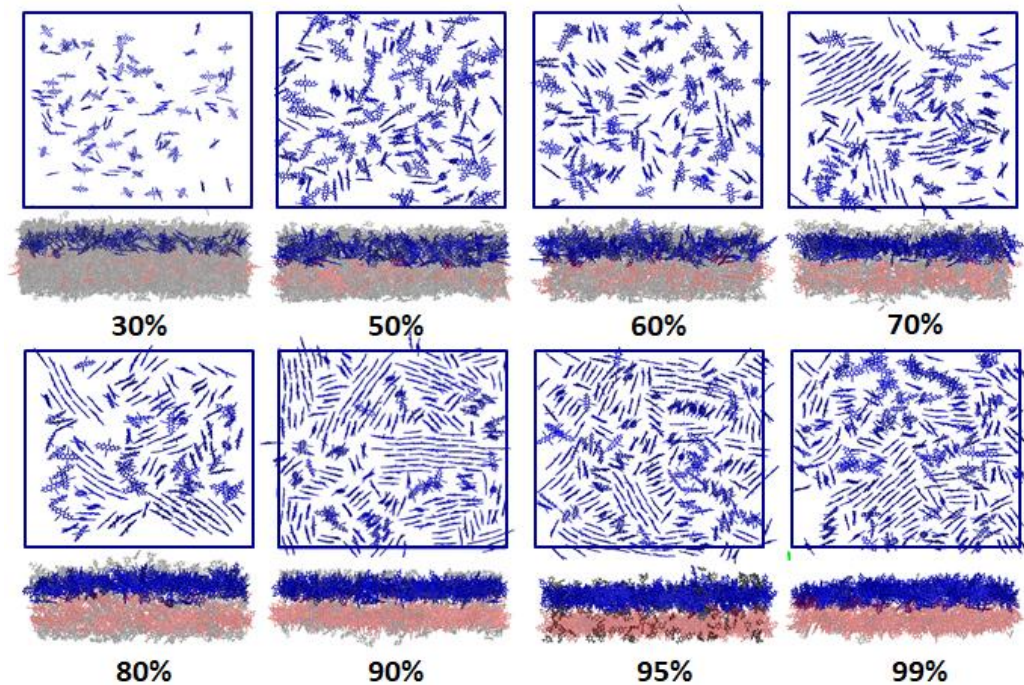
Figure 5.31. Top-view and side-view snapshots of diF-TES-ADT solution at different concentration. Blue: diF-TES-ADT in the top monolayer, red: diF-TES-ADT in the bottom layer. Grey: Toluene. All toluene molecules in the top view snapshots were omitted for clarity.
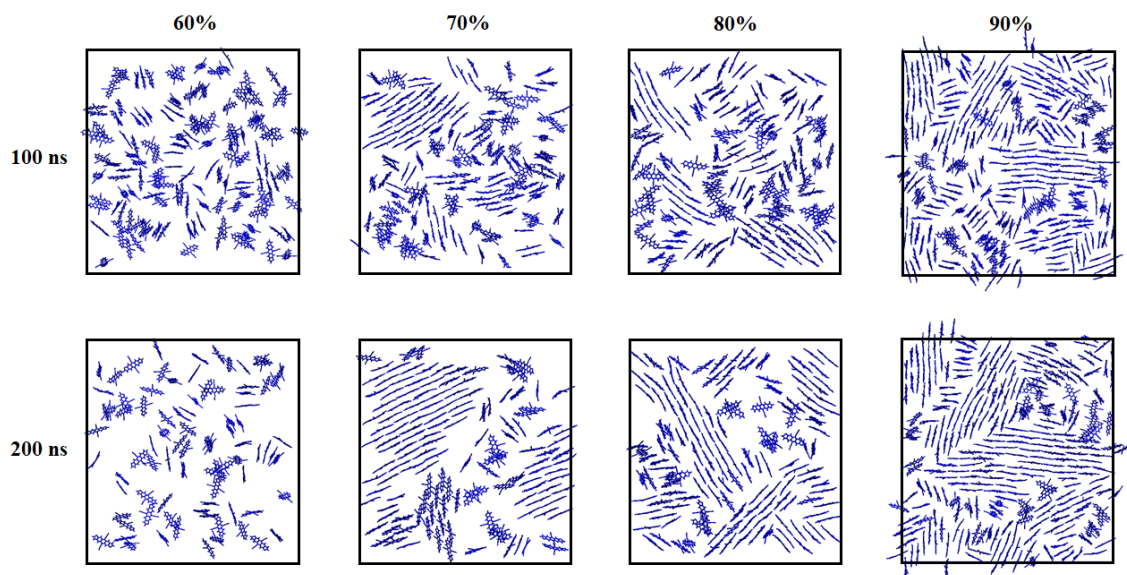
Figure 5.32. Top monolayer of diF-TES-ADT solution at different concentration simulated after 100 ns and 200 ns. All toluene molecules in the top view snapshots were omitted for clarity.
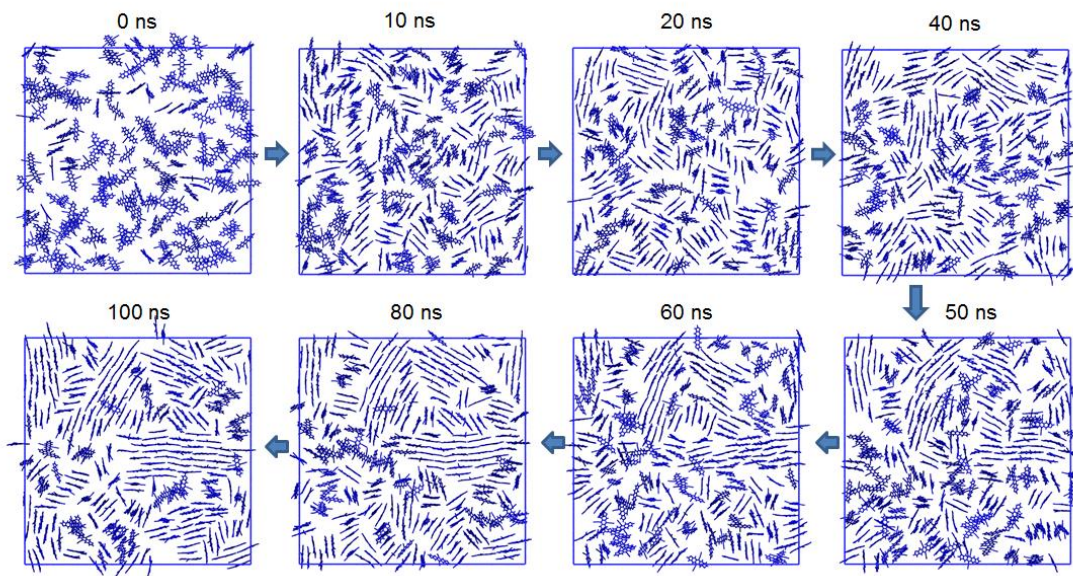
Figure 5.33. Snapshots of the 90% diF-TES-ADT solution during along simulation time. Toluene molecules were omitted for clarity.

Figure 5.30 suggests that the 70% solution has the largest ordering parameter in all systems. We extracted the two different monolayers develoted from this simulation. The first monolayer refers to the layer close to the solution-vacuum interface, while the second monolayer is the layer in contact with the artifical silicon wall in the simulation. As shown in Figure 5.34, three large ordered domains were formed at 200 ns in the first monolayer, the domains were separated by small disordered aggregates of diF-TES-ADT. Further virstuallization of this monolayer at 250 ns reveals that these small aggregations were mostly solvated in toluene, as represented as the yellow molecules. This suggested that while the larger domain was formed, the solvent molecules were pushed away from the crystalline domains. We also noticed that the degree of order on the second monolayer was significantly lower than the first monolayer. Since these two layers are in different contact environment, this suggested that the interface of solution–vacuum increases the molecular ordering. This may due to the alkyl chain effect that was discussed in the rotamer

simulation, as tge TES groups preferred to align to the solution–vacuum interface. Interactions among the non-bonding silicon surface and the solvent molecules could also be a potential driver for the observations.
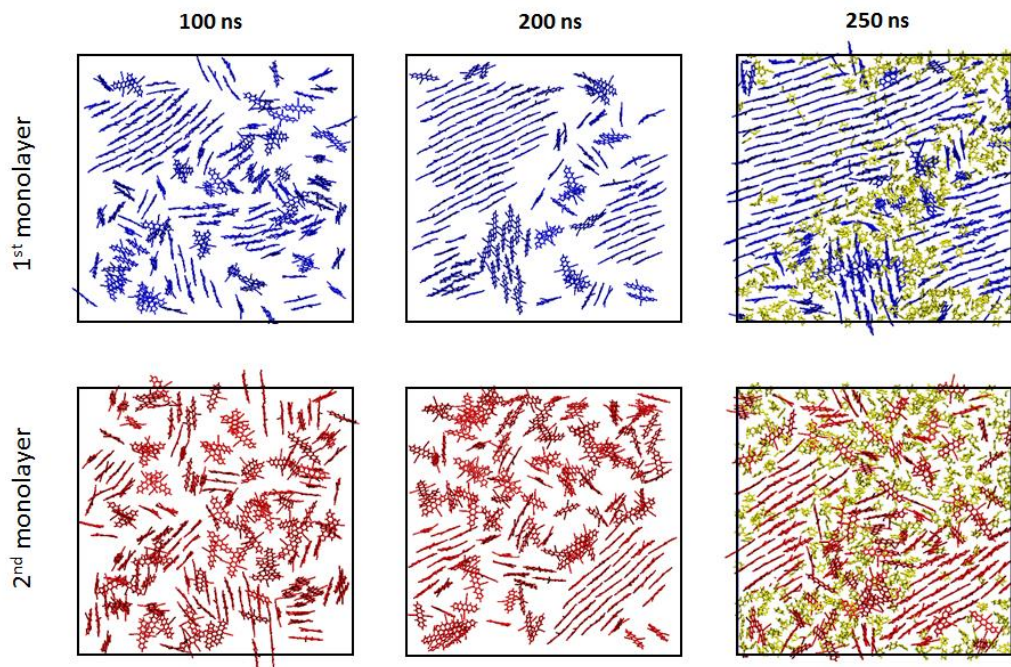
Figure 5.34. Snapshots of 70% diF-TES-ADT solution during along simulation time. Snapshots shows two monolayers in the system, blue and red molecules are diF-TES-ADT in the 1st and 2nd monolayers respectively. The toluene molecules (yellow) in the 100 ns, 200 ns snapshots and all hydrogen atoms are omitted for clarity.

We next evaluated the states of aggregation in the different solutions with the aggregation ratio method. As a test, we first selected the 60% and 70% diF-TES-ADT solutions, as there is little aggregation in the 60% solution and the highest degree of aggregation was found for the 70 % solution. The selected molecules in aggregate states were marked in red. As shown in Figure 5.35, the method can provide reasonable identification of the molecules that maintain an ordered structure. With the clear identification of each

molecules' state, we can further analyze their properties or dynamics during the aggregation process.
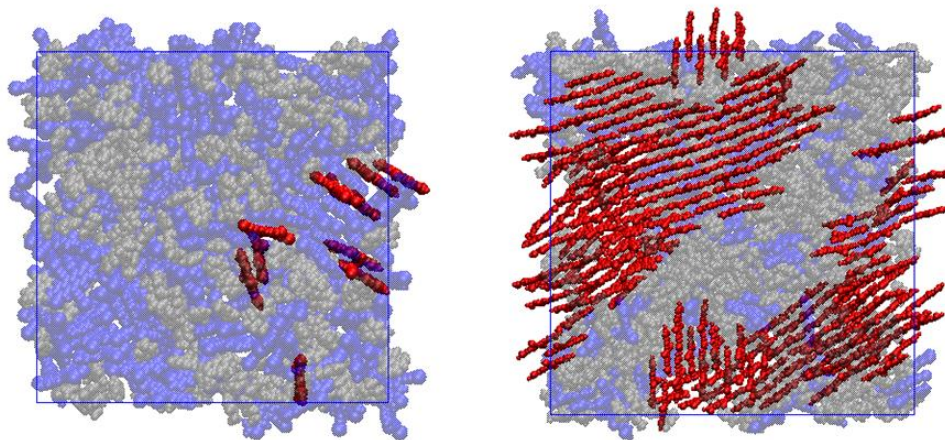
Figure 5.35. Molecules at different states characterized from the aggregation analysis. Left: 60% solution; Right: 70% solution. Red and blue: diF-TES-ADT molecules. Gray: toluene. All alkyl chains on diF-TES-ADT were omitted for clarity.

We calculated the MSD of the molecules in the aggregate and diffusing in the solution. The results are shown in Figure 5.36 (A). As expected, while the molecules diffuse in the solution, the MSD is linear in the time frame, meaning that the molecule is moving at a constant rate in the solution. On the other hand, when the molecules start to become part of an aggregate, there is an immediate increase of the displacement, suggesting a faster motion of the molecule. Once the molecule becomes part of the aggregate, the rate drops to almost zero. The diffusion rate, or diffusion coefficient (D_s), is directly related with the MSD, here in Figure 5.36 (B), while the molecule is detaching or attaching to the main cluster, the diffusion coefficient is significantly larger than the one that is diffusing in the solution.
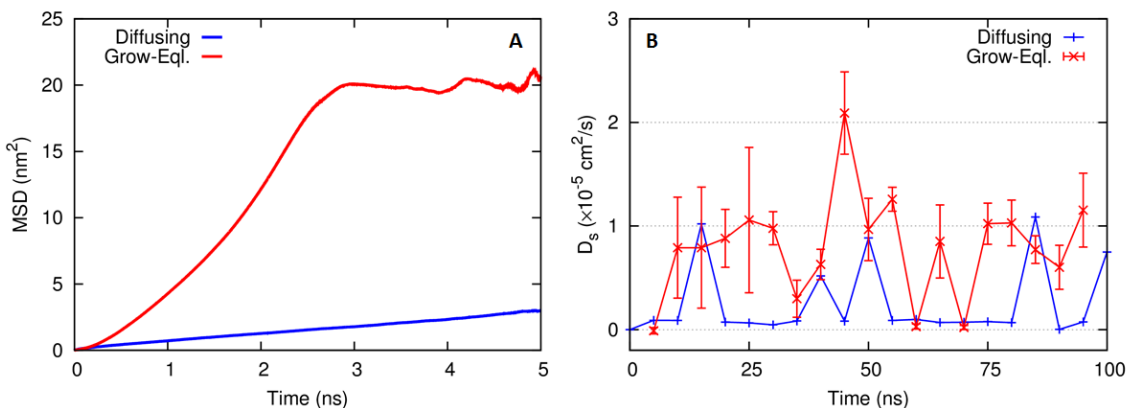
Figure 5.36. Mean square displacement (A) and diffusion coefficient (B) of the molecules in diffusion state and aggregation state.

To further capture this process, we selected three molecules in the solution that went through this process and calculated the change of diffusion coefficient over the entire time. The result is shown in Figure 5.37. The whole process can be separated into three steps:

Step 1: The green molecule is in a meta-stable state on the edge of one small cluster, as shown in the snapshot, with the molecular backbone only partly interacting with the main cluster (*e.g.* a weakly interacting state). However, since it is part of the cluster, the diffusion coefficient of this molecule is almost negligible over the first 40 ns. At the same time, the red and blue molecules are diffusing in the solution and interacting with each other. There is a significant fluctuation on their diffusion coefficients.

Step 2. At a given time, the red and blue molecules approach the green molecule. Due to the weak interaction between the green molecule and the cluster, the molecule is easily detached from the cluster and interacts with the other two molecules. This caused an immediate increase in the diffusion coefficients during the 40-50 ns time frame.

162

Step 3. Since the molecules are close to the bigger cluster, the three molecules eventually re-attach to the cluster, and after a few steps of reorientation, they became part of the cluster. This process happens within a short time frame and once it finished, the diffusion coefficients for each of the three molecules drops to zero.
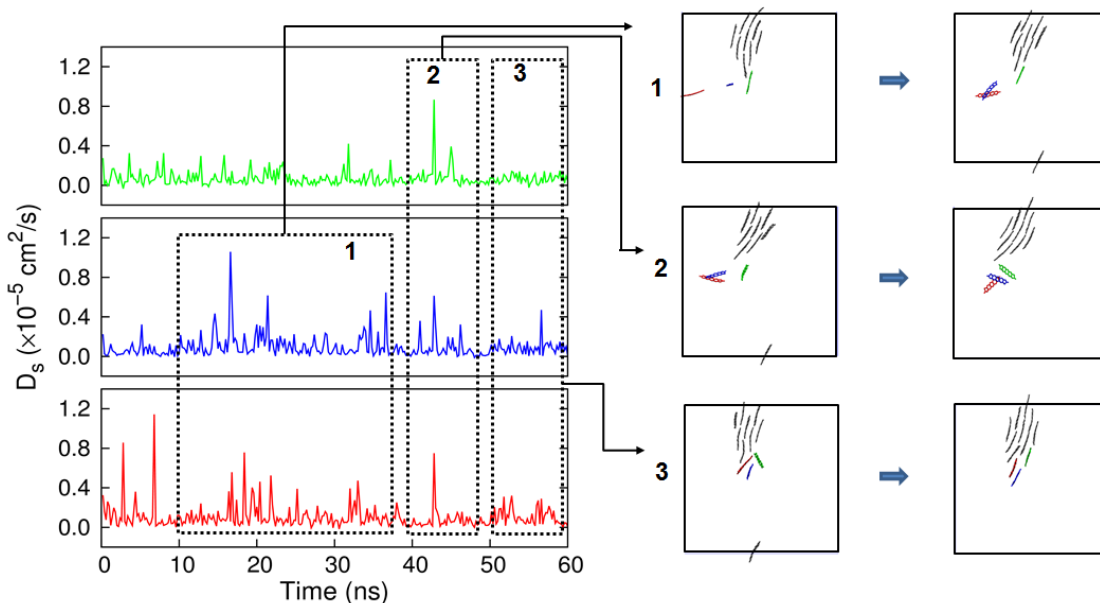
Figure 5.37. Selected diffusion coefficient of three diF-TES-ADT molecules form local aggregation in the toluene solution.

The study of these systems reveals that the aggregation of solute in the solution phase is indeed a rare event, and that several conditions need to be satisfied in order to trigger the process. First, the molecules need to have a fairly high local concentration. In our simulation models, even though the overall concentration of the system is supersaturated, the condition is still not sufficient to initiate aggregation. However, when the local centration is quite large ($> 70\%$), small clusters formed almost immediately. Second, since this is a rear event, a sufficiently long simulation time is necessary to capture the process. As revealed in Figure 5.37, the initial interaction between the red and blue molecules lasted

over 40 ns before they started to contact with the local small cluster. However, once the molecules interact in an favorable fashion with the cluster, they attach to the cluster and the final structure is formed within 10 ns, which is a relatively fast timescale. This indicates that the number of small local clusters are important to accelerate the aggregation process.

Since the state of molecule can be identified from the solution, we further calculated the aggregation ratio as defined by the number of molecules in an aggregated state *vs.* the total number of solute molecules. The change of molecule ratio as a function of the solute concentration is shown in Figure 5.38. For this analysis, we also considered non-fluorinated TES-ADT and the isomers. As discussed previously, the synthetic sample of diF-TES-ADT and TES-ADT are often mixtures of the *anti* and *syn* isomers, therefore the aggregation of the molecule can be affected by the impurity of the isomers. Here we made pure *anti* and pure *syn* isomer systems as well as a 50/50 mixture of the *anti* and *syn* isomer. For each system, we calculated the aggregated molecule ratio. The pure system is marked with (P) and the mixture was marked as (M). For the mixture, we calculated aggregated molecules against the same isomer instead of the total molecules as marked by the dashed line.
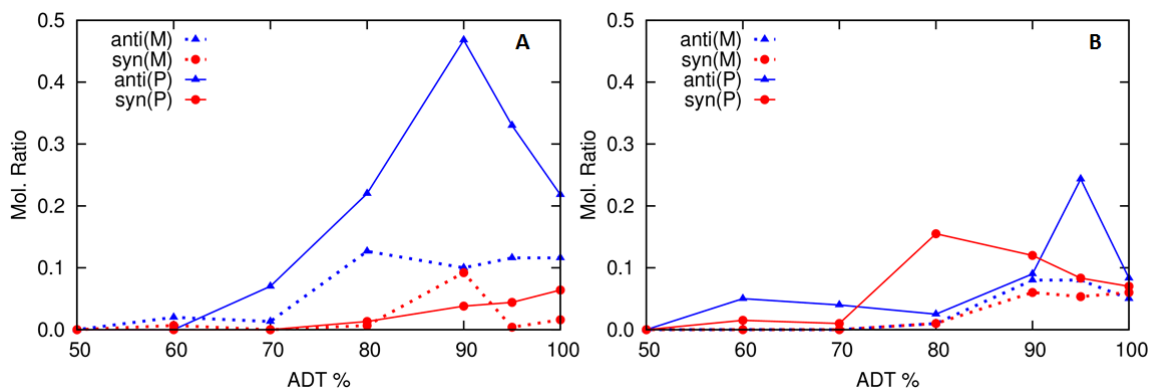
Figure 5.38. The ratio of molecules that form aggregation to the total solute molecules in the solution as a function of the concentration. A: diF-TES-ADT, B: TES-ADT.

As shown in Figure 5.38, the pure *anti* diF-TES-ADT system was the only one that presented a high aggregation ratio, and the ratio increases from 60% to 90% and dropped afterwards, which agrees with previous results. Interestingly, the *syn* isomer of diF-TES-ADT results in almost no molecules achieving an ordered state in the simulation. The ratio also drops in the mixture of these two isomers, suggested that the *syn* diF-TES-ADT in the solution will break the aggregation.

The *anti* TES-ADT also showed an increased aggregation ratio at higher concentration, although the ratio was significantly lower than the diF-TES-ADT. This may in part be due to the limited simulation time, but could also be a factor of the fluorine atom. Further extension of the simulation time at higher concentration may potentially increase the ratio. However, the fact that TES-ADT showed aggregation at higher concentration may suggest that it has a lower nucleation rate or more difficult than diF-TES-ADT in terms of nucleation. Since the *anti* diF-TES-ADT is the only molecule shows significant increase in the aggregation, we further analyzed the increase of aggregation ratio as a function of the time. We took the 70%, 80% and 90% solutions and equilibrated for 300 ns for data

analysis and the results are shown in Figure 5.39. As expected, the aggregation ratio had a

linear relationship with the simulation time and did not decrease in the 300 ns time frame.

We fit a linear trendline along each concentration points slope of each trend line should

represented the nucleation rate of the molecule. As shown in Figure 5.39, the nucleation

rate was consistent across different systems. The only difference was when the first

nucleate developed from the solution, obviously, for the most concentrated solution, the

nucleation happened almost immediately (within 10 ns) and it took about 50 ns

equilibration time in the 70 % and 80% solution before the aggregation ratio to increase.
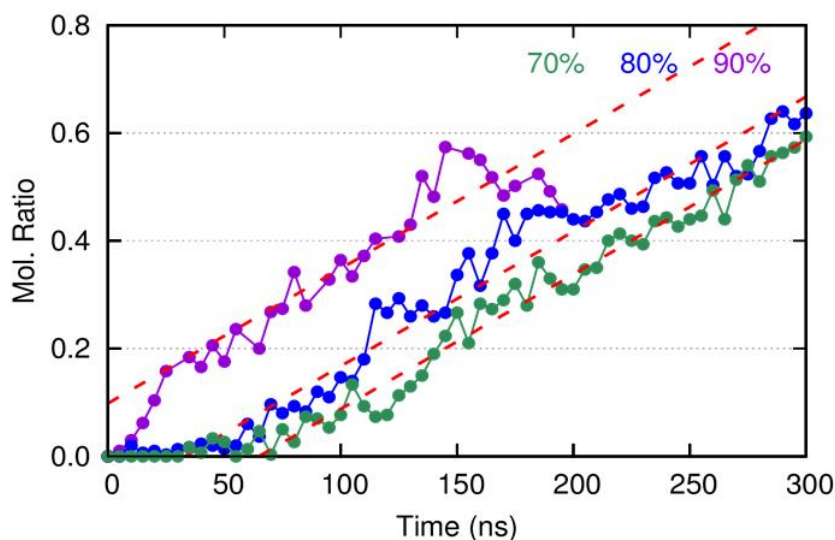
Figure 5.39. The ratio of molecules that form aggregation to the total solute molecules as a function of the simulation time of 70%, 80% and 90% diF-TES-ADT solution.

5.4 Conclusion

In the first part of this chapter, we studied the conformation of four molecules in different

solvent environments. The results show that while the molecules are synthesized with an

alternating donor-acceptor structure, the choice of acceptor unit plays a role on the

preferred conformations in solution. Further the simulations of these rotamers in the solvent environments also reveals that choice of solvent can have a significant result on the conformation of the molecules. While the molecule in CB are more flexible, the rotation of the molecular backbone in the DIO solution are decreased. At the same time, the FBT acceptor tend to lead to an asymmetric pattern of the two dihedral angles that connect the acceptors to the central donor groups, while the PT acceptor leads to a more symmetric pattern. In the case study with FBT-biTh, the molecules prefer to form ordered aggregates in CB and maintain more random configurations in DIO, which suggests that the intermolecular interaction are affected by the processing agent; this agrees with the experimental study by Bazan, Amassian, and co-workers[12] that showed that films developed from CB-DIO co-solvents, where the DIO evaporates after CB, presents a lower density structure when compared to the CB processed films. We used drying simulations to study the aggregation of such molecule from the solvent blend, with the results suggesting that the alkyl chains on the molecular backbone are important to orienting the molecules at the solvent–vacuum interface. Such features can optimize the molecular conformation to form a better ordered aggregation.

In the second part of the chapter, we further explored the aggregation and nucleation of a series of TES-ADT molecules and their derivatives in toluene. The simulations allowed us to distinguish molecules in different states in the solution environment, and analyze attributes such as molecular diffusion and nucleation events. The methods developed here can be further extended to study similar systems in different solution phase.

CHAPTER 6

STRUCTURE–FUNCTION RELATIONSHIPS OF MULTI-COMPONENT ORGANIC DYES

6.1 Introduction

In the past two decades, great effort has been made to improve the performance of organic based electronic devices, from the design of novel organic molecules to the development of processing and device fabrication techniques. However, due to the complexity of the chemical structure of organic semiconductors (OSC) and the unresolved mechanisms that are involved in the formation of solid-state morphologies, there remains a lack of fundimental understanding concerning structure–function relationships across scales. Hence, the experimental design and development of new materials often follows an Edisonian approach.

As a complement to the experimental work, theoritical approaches are entensively developed to help understand the properties of OSC and bridge the gap between chemical design and material functionality. Previously, we have made use of molecular dynamic (MD) simulations to understand the properties of OSC. Quantum-chemical methods, and in particular density functional theory (DFT)-based approaches, are also commonly used to understand the geometric, electronic, redox, and optical properties of OSC. The results derived from such calculations can provide valuable insight across materials scales – though here the focus is on molecular-scale features – that can be used in the design of OSC.

In case of organic photovolatics (OPV), the traditional bulk hedrojunction (BHJ) solar cells use fullerene based acceptors, such as phenyl-C61-butyric acid methyl ester (PC61BM) and phenyl-C71-butyric acid methyl ester (PC71BM). Although these acceptors provide large electron mobilities and enhance the formation of pure fullerene phases in two component OSC blends, they lack tunable electronic and optical properties, and absorption intensities in the visible region are relatively weak. Further, fullerene derivatives tend to have considerable synthetic cost. Hence, there has been a push to develop non-fullerene based acceptor materials for a variety of applications.

In this chapter, we report collaborative efforts with two synthetic chemistry groups – that of Professor Greg Welch (University of Calgary, Canada) and Dr. Clément Cabanetos (University of Angers, France) – to develop new electron deficient chromophores for OSC.[1-4] The novel dyes reported in these collaborations were developed through distinctive combinations of π-conjugated chromophores. Our focus was to make use of quantum-chemical methods to develop models to describe the electronic, redox, and optical properties of these molecules, both as isolated (as in solution) molecules and complexes in the solid state.

6.2   Computational Methods

All density functional theory (DFT) and time-dependent DFT (TDDFT) calculations were carried out at the optimally tuned (OT)-ωB97X-D/6-31g(d,p) level of theory. The optimized ω parameter for each molecule was used for all subsequent calculations, including the (optimized) rotational scans and dimer configurations. All optimized, unconstrained geometries were confirmed as minima on the potential energy surface through normal mode analyses. To reduce the computational cost, alkyl groups in each

molecule were truncated to methyl groups. The Gaussian09 (Revision A.02)[5] software suite was used for the DFT and TDDFT calculations. Absorption spectra were simulated through convolution of the vertical transition energies and oscillator strengths with Gaussian functions chaaracterized by a full width at half-maximum (fwhm) of 0.33 eV.

6.3 Results and discussion

6.3.1 An unsymmetrical, panchromatic non-fullerene acceptor

We begin by describing the initial collaboration with the Welch group. Their previous studies on N-annulated perylene diimides (PDI) revealed good organic solvent solubility, and when blended with π-conjugated polymers resulted in organic solar cells with reasonable performance.[6, 7] Here, they designed a new unsymmetrical molecule (PDI-DPP-IQ, A) by combining the PDI with thienyl diketopyrrolopyrrole (DPP) and indoloquinoxaline (IQ) organic units connected via C–C bonds in a linear fashion. The new molecule in the solid state demostrated considerable red shifts in the optical absorption after post-deposition solvent vapor annealing (SVA). Note that the molecule is expected to form multiple rotational isomers due to the C-C connection between the subunits, therefore the calculations on such an unsymmetrical molecule also considered serveal isomer configurations as shown in Figure 6.1.
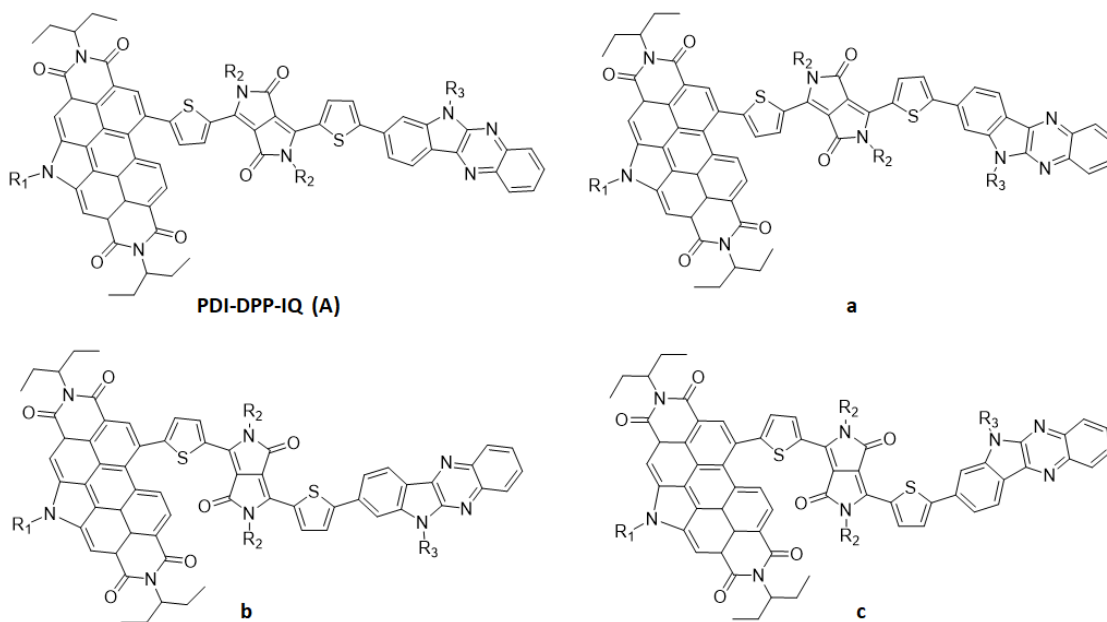
Figure 6.1. Chemical structures of PDI-DPP-IQ and three rotational isomers. R_1 = hexyl, R_2 and R_3 = octyl.

The molecular design is expected to lead to a chromophore that absorbs in different regions of the visible spectrum (*i.e.* panchromatic absorption), due to the fact that PDI (400-600 nm), DPP (425-650 nm), and IQ (300-400 nm) each have different principal absorptions. Further, previous studies on dyes containing DPP[6] and IQ[8] units with linear alkyl side chains showed considerable solid-state structural reorganization due to SVA. Thus, the new molecule design was expected to have similar properties with such post-deposition SVA treatments.

The electrochemical properties of compounds A were determined by cyclic voltammetry (CV) by our experimental colleagues.[4] The ionization potential (IP) and electron affinity (EA) were estimated to be 3.7 eV and 5.2 eV, respectively, by correlating the onsets of oxidation and reduction to the normal hydrogen electrode (NHE), assuming the IP of Fc/Fc+ to be 4.80 eV.

We determined the IP and EA of the molecules in Figure 6.2, and examined the nature and energy of the froniter molecular orbitals through DFT calculations. The results are shown in Table 6.1. The (gas phase) EA of 2.2 eV and IP of 6.0 eV determined at the OT-ωB97X-D/6-31g(d,p) level of theory compare reasonably well to the CV data. Pictorial representations of the frontier molecular orbitals show that the LUMO mainly resides on the PDI moiety while the HOMO resides on the DPP moiety, a goal of the molecular design.

Table 6.1. Select DFT and TDDFT data for PDI-DPP-IQ (A) and three rotational isomers as determined at the OT-ωB97X-D/6-31g(d,p) level of theory

Materials	Tuned ω	Relative Energy (kcal/mol)	IP^a (eV)	EA^b (eV)	$S_0 \rightarrow S_1$ (eV [nm])	f	Electronic Configuration of the $S_0 \rightarrow S_1$ Transition
A	0.123	0.00	6.00	2.21	2.37 [523]	1.27	HOMO → LUMO + 1 (85%) HOMO → LUMO (9%)
Rotational isomers							
a	0.123	2.25	6.03	2.20	2.39 [518]	1.30	HOMO → LUMO + 1 (92%)
b	0.125	13.44	6.04	2.16	2.48 [500]	1.06	HOMO → LUMO + 1 (94%)
c	0.125	12.33	6.07	2.16	2.47 [503]	0.96	HOMO → LUMO + 1 (90%)

^{a}IP = ionization potential. ^{b}EA = electron affinity.
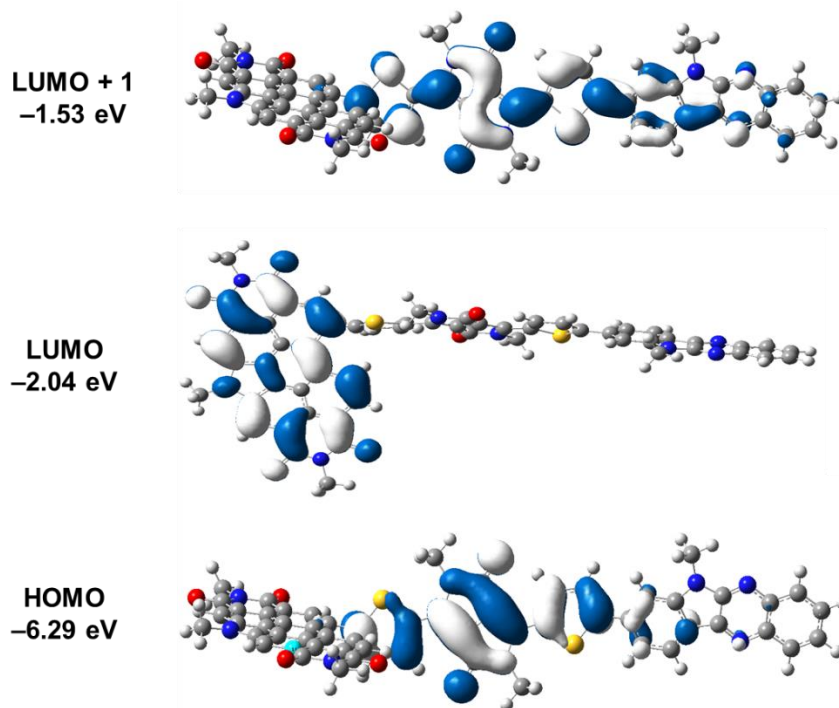
Figure 6.2. Pictorial representations of select frontier molecular orbitals of PDI-DPP-IQ (A) as determined at the OT-ωB97X-D/6-31g(d,p) level of theory.

The experimental UV-Vis spectrum shows that compound 1 exhibits panchromatic optical absorption. In solution, high intensity optical transitions are observed from ~ 300–650 nm with a tail extending beyond 700 nm. Maximum absorption occurs from ~ 510–560 nm with a peak at ~ 535 nm. TDDFT calculations at the TD-OT-oB97X-D/6-31g(d,p) level of theory provide excited-state transitions and a simulated absorption spectrum that agree reasonably well with experiment (Table 6.2). Analyses of the natural transition orbitals (NTO) reveal that the $S_0 \rightarrow S_1$ transition resides mainly on the DPP moiety, arising from a one-electron transition that is predominantly HOMO $\rightarrow$ LUMO+1 (Figure 6.3 and Figure 6.4). Confirming the panchromatic design paradigm, the mid-energy transitions can be clearly identified as taking place mainly on the PDI moiety (S_0 - S_2; S_0 - S_3; S_0 - S_4; S_0 – S_7; Figure 6.5−6.8), while the higher-energy transitions are associated with the IQ unit.

173

Table 6.2. First ten excited states of the optimized PDI-DPP-IQ (A) structure as determined at the TD-OT-ωB97X-D/6-31g(d,p) level of theory

Excited State	Energy [λ] (eV [nm])	f
1	2.37 [523]	1.27
2	2.63 [471]	0.16
3	2.75 [450]	0.57
4	3.08 [403]	0.11
5	3.32 [373]	0.02
6	3.43 [361]	0.00
7	3.50 [354]	0.66
8	3.69 [335]	0.31
9	3.72 [333]	0.00
10	3.76 [330]	0.00

$\lambda = 0.96$

hole   electron
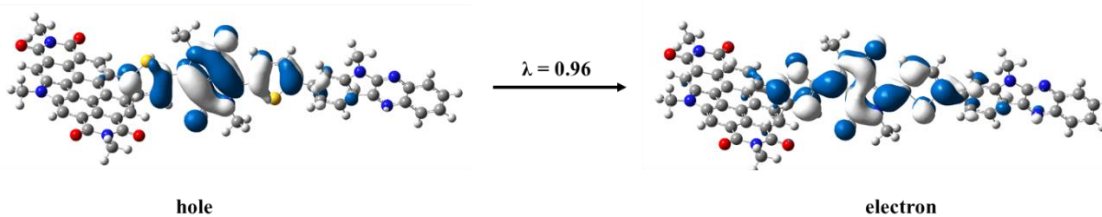
Figure 6.3. Pictorial representations of the natural transition orbitals (NTO) for the $S_0 \rightarrow S_1$ of PDI-DPP-IQ (A) as determined at the TD-OT-ωB97X-D/6-31g(d,p) level of theory. λ is the fraction of the hole–particle contribution to the excitation.
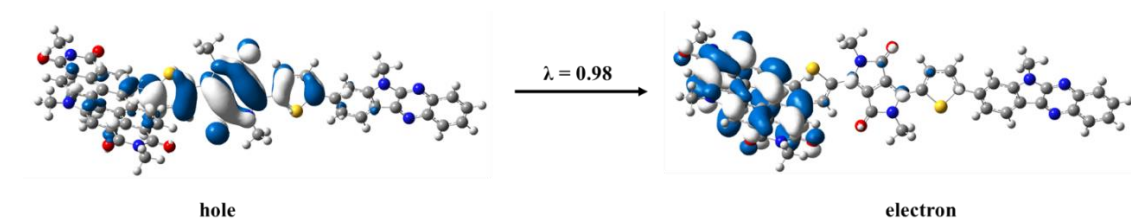
Figure 6.4. Pictorial representations of the natural transition orbitals (NTO) for the $S_0 \rightarrow S_2$ of PDI-DPP-IQ (A) as determined at the TD-OT-ωB97X-D/6-31g(d,p) level of theory. λ is the fraction of the hole–particle contribution to the excitation.
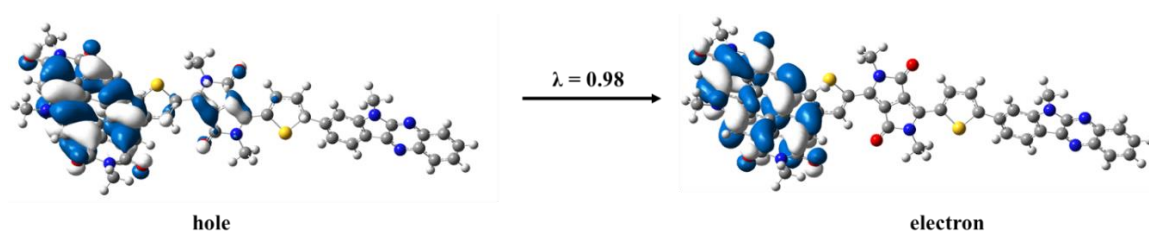
Figure 6.5. Pictorial representations of the natural transition orbitals (NTO) for the $S_0 \rightarrow S_3$ of PDI-DPP-IQ (A) as determined at the TD-OT-ωB97X-D/6-31g(d,p) level of theory. λ is the fraction of the hole–particle contribution to the excitation.
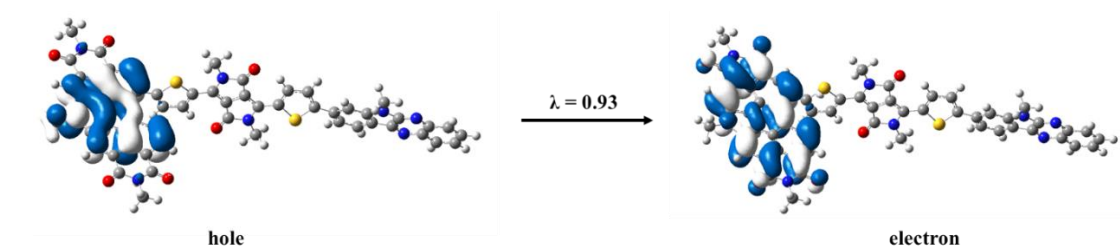
Figure 6.6. Pictorial representations of the natural transition orbitals (NTO) for the $S_0 \rightarrow S_4$ of PDI-DPP-IQ (A) as determined at the TD-OT-ωB97X-D/6-31g(d,p) level of theory. λ is the fraction of the hole–particle contribution to the excitation.
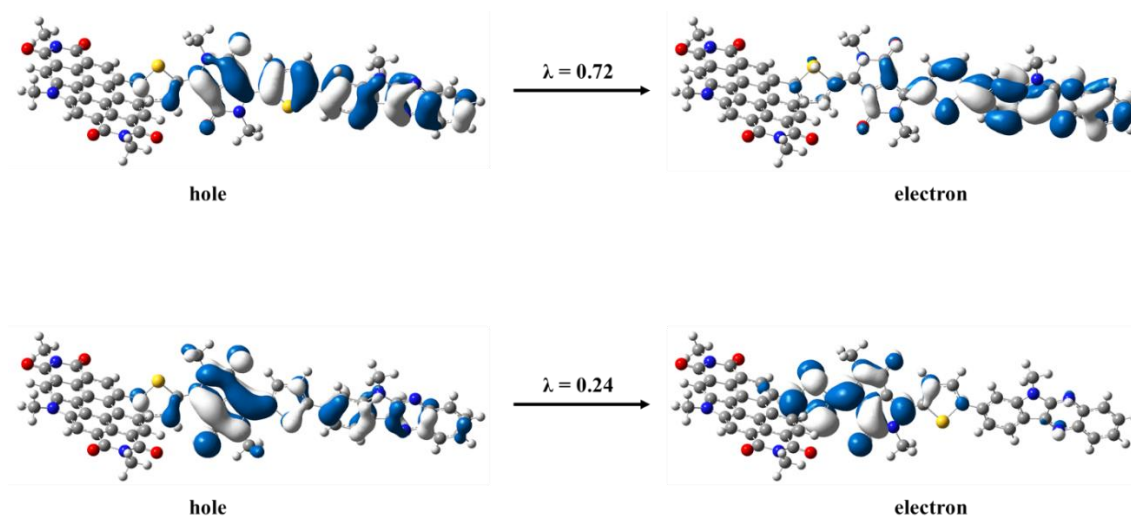
Figure 6.7. Pictorial representations of the natural transition orbitals (NTO) for the $S_0 \rightarrow S_7$ of PDI-DPP-IQ (A) as determined at the TD-OT-ωB97X-D/6-31g(d,p) level of theory. λ is the fraction of the hole–particle contribution to the excitation.

Solid-state materials derived from compound A show a dramatic change in the optical abosrption spectrum when compared to solution. In particular, the lowest-energy absorption red-shifts for A in the solid state when compared to solution. We hypothesized that a potential reason for the red-shift could be due to a change in the preferred conformation of A in the solid state. To explore this hypothesis, we examined the potential energy surface (PES) related to conformation changes around the C-C bond between the PDI unit and DPP units of A. The PES, shown in Figure 6.9, reveals that the lowest energy point in A has a dihedral angle between these units of ~81°, suggesting that the PDI and DPP units prefer to be nearly perpendicular to each other in the gas phase (and, preseumably, in solution). For each structure optimized with a constrained dihedral angle between the PDI and DPP units, we used TDDFT to examine how the change in molecular conformation would affect the excited-state characteristics and simulated the absorption spectra. The results in Figure 6.10 reveal that when the dihedral between PDI moiety and

176

DPP moiety changes from 0 to 90 degrees, there is a energy shift in the lowest energy

absorption band from ~ 600 – 700 nm, the energy shift is also associated with an intensity

loss of the peak at ~620 nm. The red shift and intensity change agrees with the trends

observed experimentally when A goes from solution to the solid-state. Hence, it is apparent

that the red-shifted absorption in the solid-state can be attributed, at least in part, to a

planarizaiton of the chromophore.
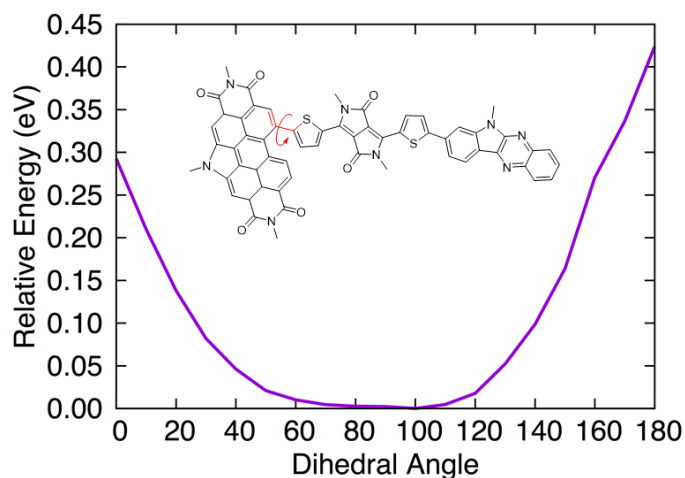
Figure 6.8. Potential energy surface for twisting the PDI moiety in PDI-DPP-IQ (A) as determined at the TD-OT-ωB97X-D/6-31g(d,p) level of theory. For each PDI twist, the dihedral angle highlighted in red was frozen at the associated angle and the remainder of the molecule was allowed to minimize through a DFT optimization; no normal mode analyses were carried out on these constrained geometries. These geometries were then used in the follow-up TDDFT calculations reported in Figure 6.9.
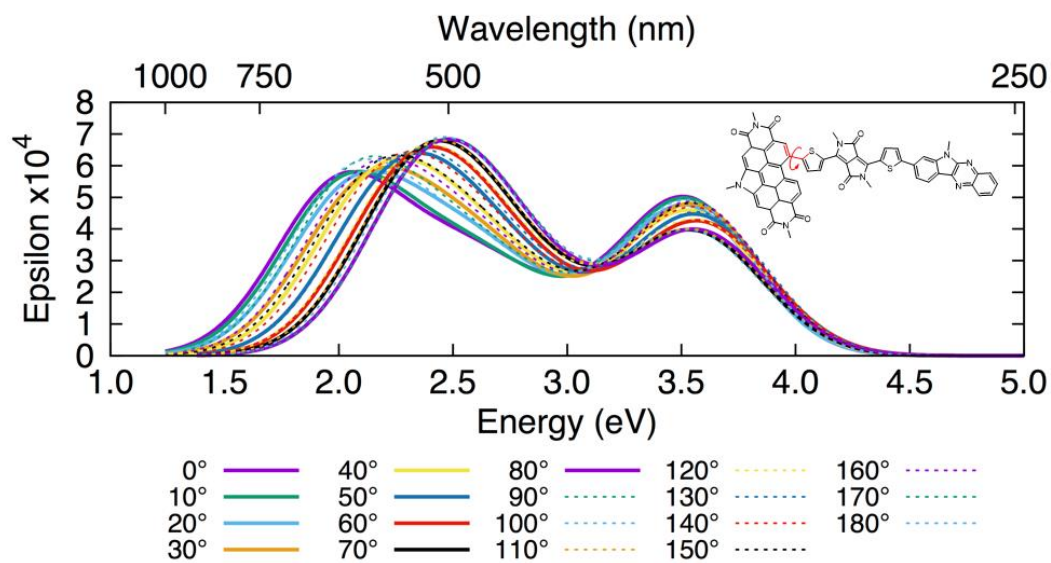
Figure 6.9. Simulated absorption spectra of PDI-DPP-IQ (A) as a function of the orientation of the PDI group as determined at the TD-OT-ωB97X-D/6-31g(d,p) level of theory. Absorption spectra were simulated through convolution of the vertical transition energies and oscillator strengths with Gaussian functions characterized by a full width at half-maximum (fwhm) of 0.33 eV.

We then simulated the absorption spectra of a planar configuration of A, as shown in Figure 6.10. The molecular $S_0 \rightarrow S_1$ transition moves to lower energy (by 0.24 eV) when compared to the optimized structure, and the oscillator strength increases modestly (Tables 6.2 and 6.3). These results are consistent with the expectation that the π electrons are more delocalized in the planar configuration; inspection of the NTO for the $S_0 \rightarrow S_1$ transition of a planar configuration of A (Figure 6.14 and 6.15) shows that the hole and electron are more delocalized, extending on to the PDI, when compared to the optimized structure.

Further changes in the optical spectra are observed upon SVA treatment of the thin film. In partciular, a blue shift is observed in the lowest energy absorption band from ~ 600 nm to ~ 700 nm, the intensity and position of the peak for the PDI unit decreases while the high-energy band for IQ unit retains. To explore the relationship between the changes in

film structure and optical characteristics with SVA, TDDFT calculations were carried out on A as a function of (i) the degree of twist within the molecular backbone and (ii) the potential formation of head-to-tail dimers. Figure 6.11 presents a comparison of the simulated absorption spectra based on the TDDFT results of the monomer and dimer models of 1. Consideration of a dimer of A where the optimized geometry of the isolated molecule is maintained reveals that the low-energy absorption band is comprised of two electronic transitions at nearly the same energy as that of the isolated molecule; the hole and electron NTO for these transitions are localized on only one of the two molecules in the dimer (Figure 6.12 and 6.13). Hence, simple aggregation without a change in molecular configuration cannot fully explain the presence of the low energy optical transitions that appear with SVA. Consideration of a dimer model composed of planar A results in a modest red shift of the first low-energy transition with appreciable oscillator strength (by 0.05 eV, Table 6.4) when compared to the isolated, planar A. For this dimer, the $S_0 \rightarrow S_1$ transition is forbidden (some 0.20 eV lower in energy than the $S_0 \rightarrow S_1$ transition for isolated, planar A), and it is the $S_0 \rightarrow S_2$ and $S_0 \rightarrow S_4$ transitions that are mainly responsible for the observed low-energy band with increased oscillator strength when compared to isolated A in both the twisted and planar conformations. NTO for the planar dimer $S_0 \rightarrow S_2$ transition show that both the hole and electron reside mainly on the DPP and PDI moieties (Figure 6.16) of both molecules in the dimer. From these models, it is apparent that both reorganization of A to a planar configuration and/or the formation of aggregates of such planar molecules can lead to the experimentally observed low-energy optical transitions that appear after SVA. While this analysis includes only a few possibilities concerning molecular reorganization and aggregation, it reveals how the consideration of

such geometric transformations and post-processing procedures can be accounted for during molecular design stage.
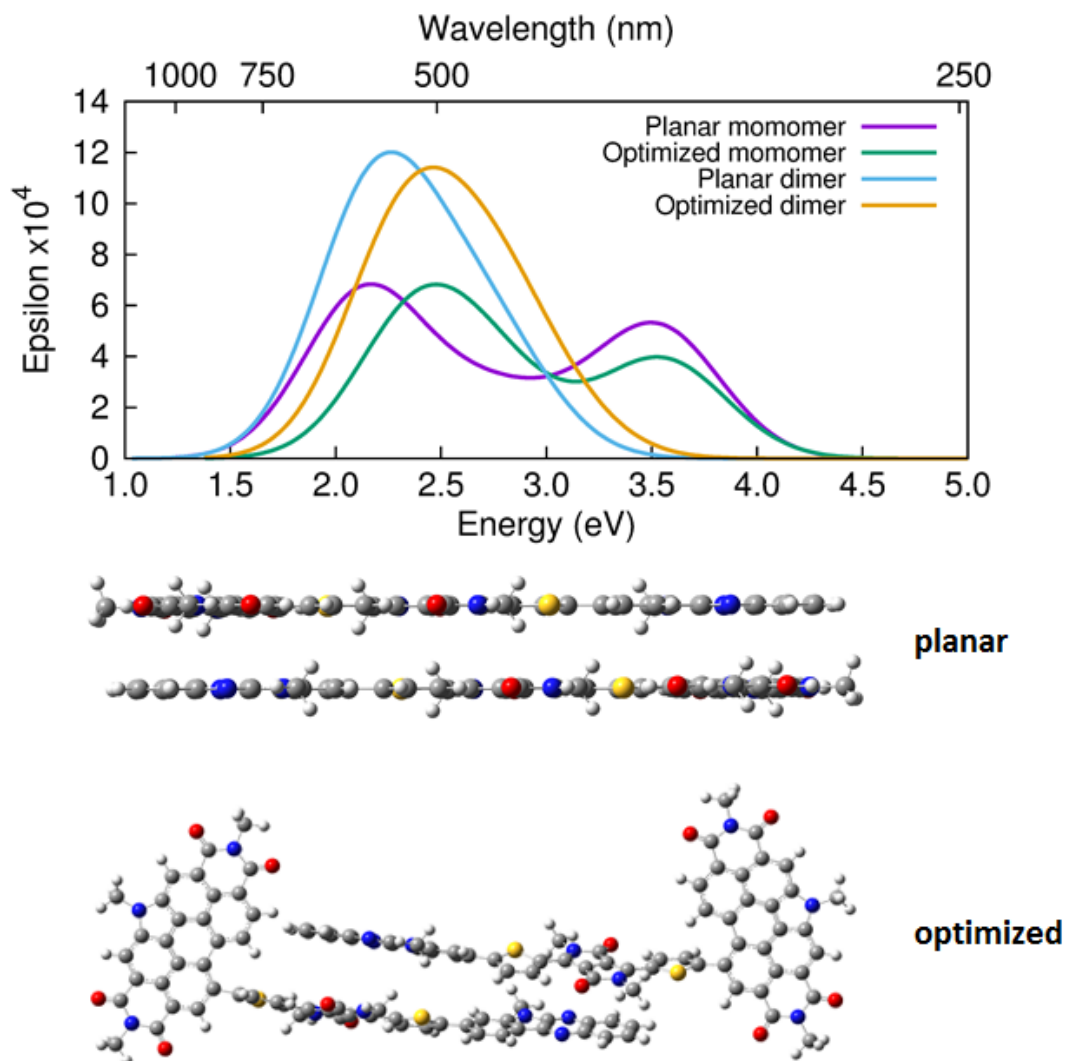
Figure 6.10. Simulated absorption spectra of isolated A, in both its fully optimized ("monomer - optimized") and constrained as fully planar structure ("monomer - planar"), and a dimer of A, where the dimer is made up of either the fully optimized structures ("dimer - optimized") or the fully constrained planar structures ("dimer - planar"), as determined at the TD-OT-ωB97X-D/6-31g(d,p) level of theory. Absorption spectra were simulated through convolution of the vertical transition energies and oscillator strengths with Gaussian functions characterized by a full width at half-maximum (fwhm) of 0.33 eV. Representative images of the dimers are provided for reference.
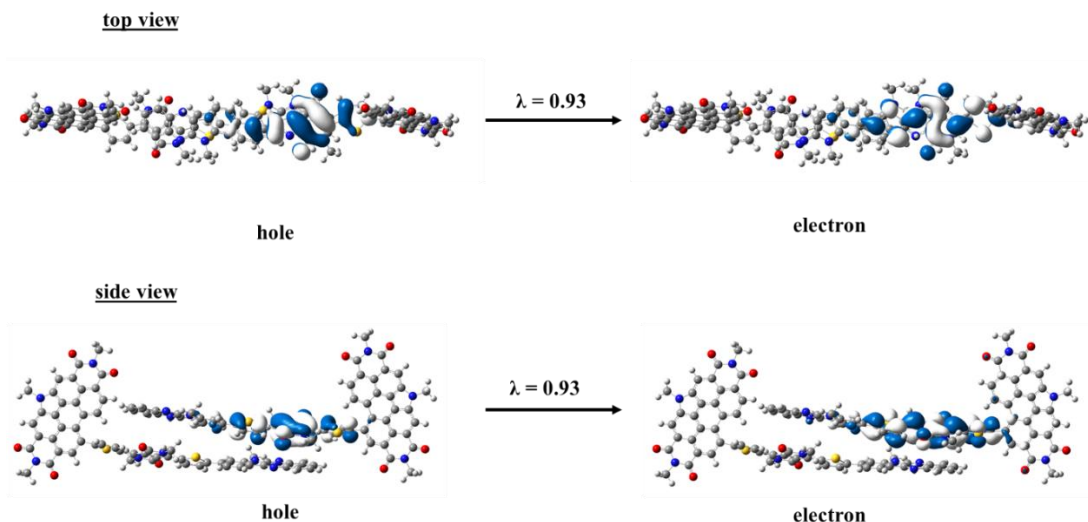
Figure 6.11. Pictorial representations of the natural transition orbitals (NTO) for the $S_0 \rightarrow S_1$ of the "optimized" dimer of PDI-DPP-IQ (A) as determined at the TD-OT-ωB97X-D/6-31g(d,p) level of theory. Both top and side views are presented. λ is the fraction of the hole–particle contribution to the excitation. Here, the optimized geometric structure of 1 is maintained, and a dimer is formed by stacking two molecules in a head-to-tail fashion with a separation of 3.5 Å.
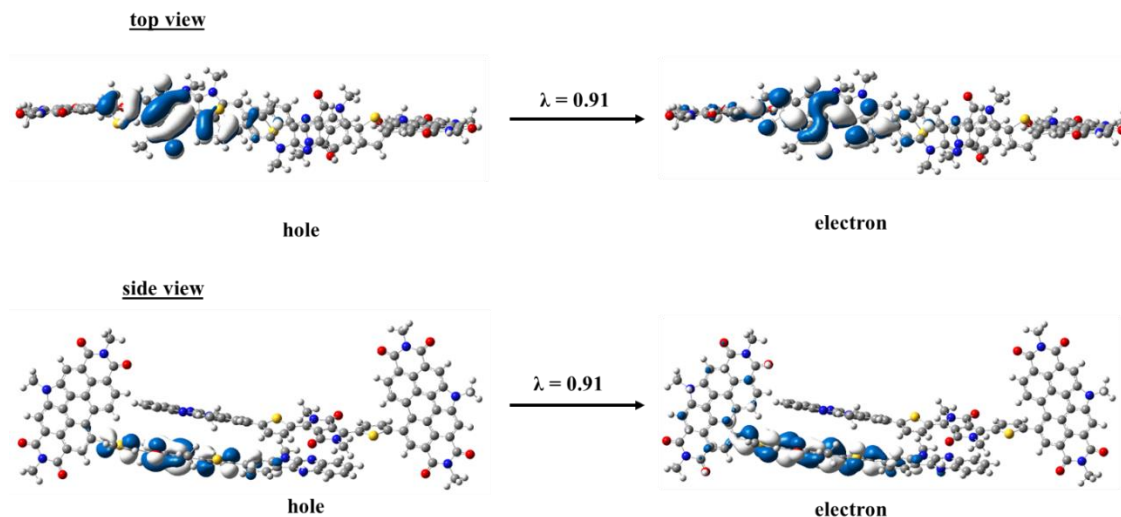
Figure 6.12. Pictorial representations of the natural transition orbitals (NTO) for the $S_0 \rightarrow S_2$ of the "optimized" dimer of PDI-DPP-IQ (A) as determined at the TD-OT-ωB97X-D/6-31g(d,p) level of theory. Both top and side views are presented. λ is the fraction of the hole–particle contribution to the excitation. Here, the optimized geometric structure of 1 is maintained, and a dimer is formed by stacking two molecules in a head-to-tail fashion with a separation of 3.5 Å.
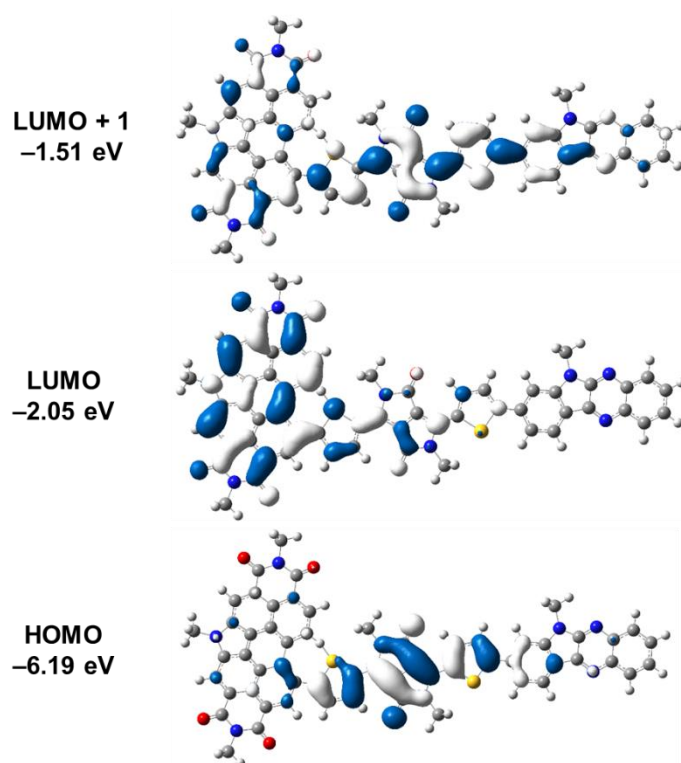
Figure 6.13. Pictorial representations of select frontier molecular orbitals of planar PDI-DPP-IQ (A) as determined at the OT-ωB97X-D/6-31g(d,p) level of theory. For this planar configuration, all dihedral angles among the aromatic moieties are set to 0^0. Note that while the LUMO and LUMO+1 energies are essentially the same as that for the fully optimized 1, the HOMO is energetically destabilized by 0.1 eV.
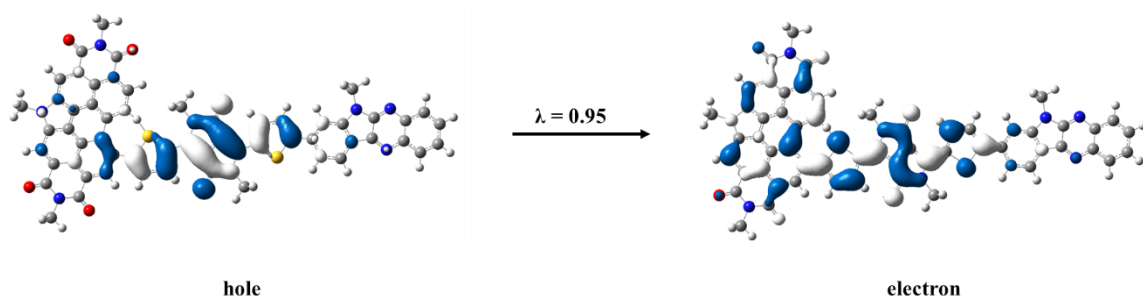
Figure 6.14. Pictorial representations of the natural transition orbitals (NTO) for the $S_0 \rightarrow S_1$ of PDI-DPP-IQ (A) in the planar configuration as determined at the TD-OT-ωB97X-D/6-31g(d,p) level of theory. λ is the fraction of the hole–particle contribution to the excitation. For this planar configuration, all dihedral angles among the aromatic moieties are set to 0^0.

Table 6.3. First ten excited states of the planar PDI-DPP-IQ (A) structure as determined at the TD-OT-ωB97X-D/6-31g(d,p) level of theory.

Excited State	Energy [λ] (eV [nm])	f
1	2.13 [582]	1.58
2	2.62 [473]	0.39
3	2.86 [434]	0.25
4	3.09 [401]	0.16
5	3.30 [376]	0.02
6	3.37 [368]	0.00
7	3.40 [364]	0.34
8	3.55 [349]	0.67
9	3.63 [342]	0.25
10	3.77 [329]	0.03

Table 6.4. First ten excited states of a "planar" dimer of PDI-DPP-IQ (A) as determined at the TD-OT-ωB97X-D/6-31g(d,p) level of theory.

Excited State	Energy [λ] (eV [nm])	f
1	1.93 [641]	0.00
2	2.08 [596]	0.93
3	2.19 [566]	0.00
4	2.23 [555]	1.78
5	2.52 [492]	0.29
6	2.55 [486]	0.00
7	2.63 [471]	0.44
8	2.65 [468]	0.00
9	2.82 [440]	0.29
10	2.82 [440]	0.00

hole

$\lambda = 0.58$

electron

hole

$\lambda = 0.38$

electron

side view

hole

$\lambda = 0.58$

electron

hole

$\lambda = 0.38$

electron
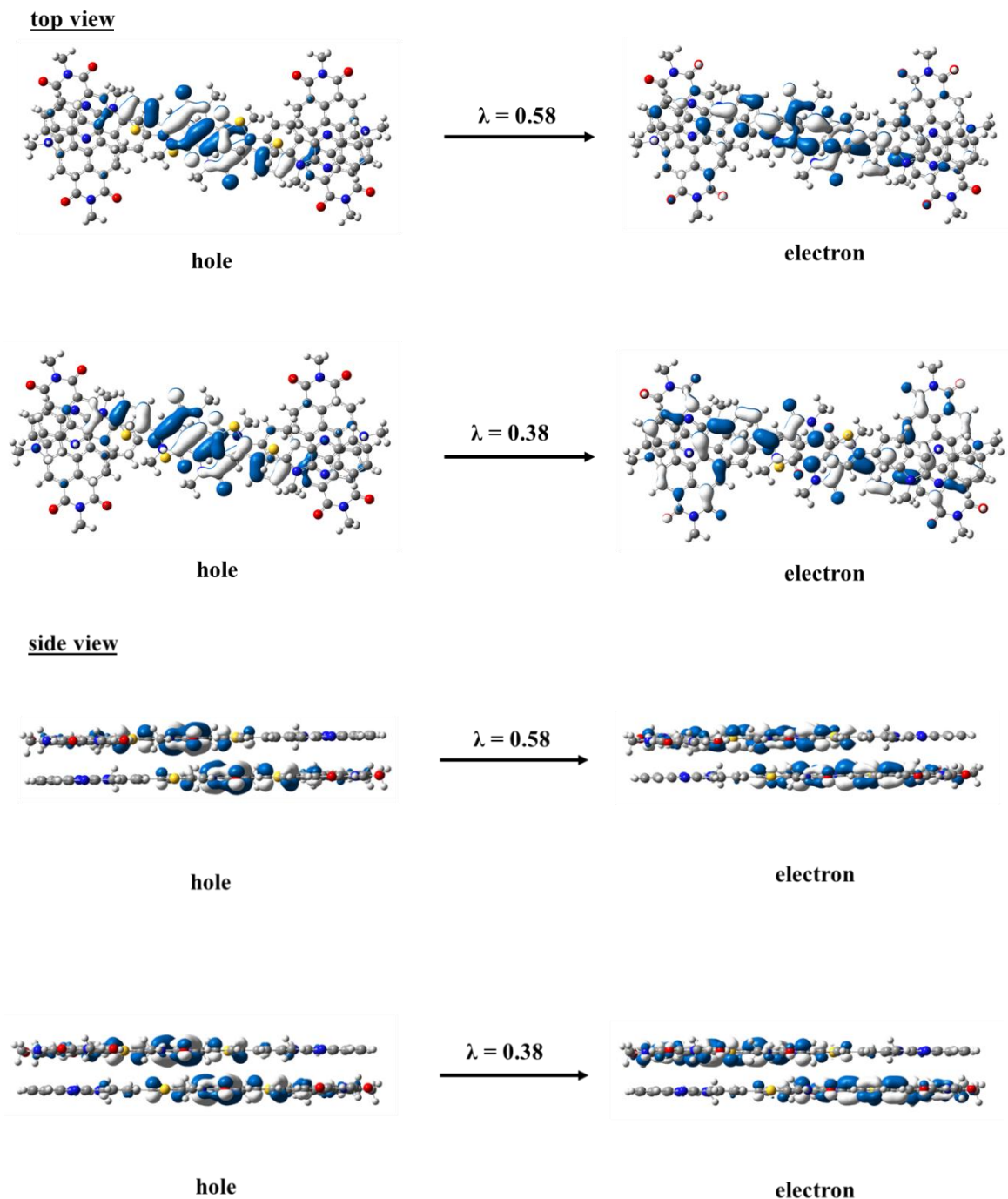
Figure 6.15. Pictorial representations of the natural transition orbitals (NTO) for the $S_0 \rightarrow S_2$ of the planar dimer of PDI-DPP-IQ (A) as determined at the TD-OT-ωB97X-D/6-31g(d,p) level of theory. Both top and side views are presented. λ is the fraction of the hole–particle contribution to the excitation.

6.3.2 Bromination and Nitration of a Benzothioxanthene

The perylene-diimide (PDI) moiety in compound A is one class of the most explored rylene dye for the preparation of electron transporting materials,[9-11] due to its optoelectronic properties, chemical flexiablity to be tailored into molecular structures, as well as its excellent thermal and photochemical stabilities.[11-15] Despite the excellent electronic properties, effort are still undertaken to functionalize the chemical stuructures to bring solubility and further tune the molecular optoelectronic characteristics.

Among these efforts, the N-(alkyl)benzothioxanthene-3,4-dicarboximide (BTXI), a sulfur containing rylene-imide dye (Figure 6.16), has recently been implemented by Cabanetos and co-workers. Due to the potential of this new building block, the functionalization of the BTXI core was studied to introduce new derivatives available for palladium-catalyzed cross coupling reactions. We studied different bromination and nitration derivatives of BTXI, synthesized by Cabanetos[16] groups. The approach affords these new building blocks to various metal-catalyzed reactions and extend the scope of design principles,[1] which serves as a key step toward the preparation of new π-conjugated molecules for OSC.
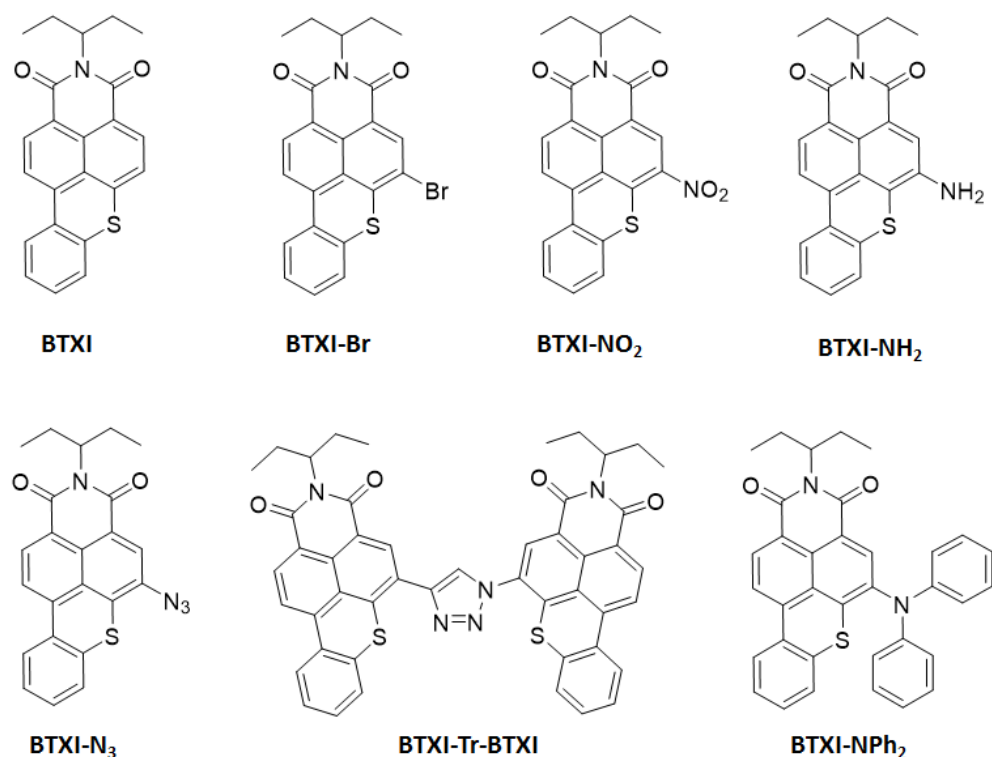
Figure 6.16. Chemical structures of the BTXI derivatives studied in this chapter.

6.3.2.1 Bromination of BTXI

The synthesis of brominated BTXI was carried out Cabanetos and co-workers started from the BTXI derivative, with the compound exposed to a dilute solution of bromine (gas) and the formation of a single product was efficiently monitored by thin layer chromatography. The monobrominated BTXI was confirmed through mass-spectroscopy and nuclear magnetic resonance (NMR).[2] To determine the position of the bromine atom, DFT calculations were carried out at the OT-ωB97X-D/6-31g(d,p) level of theory, with the range-separation parameter tuned for each molecular species and the alkyl group truncated to methyl group to reduce the computational cost (see Table 6.5). Eight monobrominated derivatives were identified, and the geometries were optimized and confirmed to be minima on the potential energy surface through normal mode analyses. (Figure 6.17)

Table 6.5. Range-separation parameter for each molecular species calculated at ωB97X-D/6-31g(d,p) level of theory

	Range-separation parameter
BTXI	0.1943
Br-BTXI(1)	0.1635
Br-BTXI(2)	0.1644
Br-BTXI(3)	0.1673
Br-BTXI(4)	0.1671
Br-BTXI(5)	0.1655
Br-BTXI(6)	0.1661
Br-BTXI(7)	0.1649
Br-BTXI(8)	0.1639
2Br-BTXI(1, 7)	0.1657
2Br-BTXI(2, 7)	0.1572
2Br-BTXI(3, 7)	0.1601
2Br-BTXI(4, 7)	0.1597
2Br-BTXI(5, 7)	0.1585
2Br-BTXI(6, 7)	0.1593
2Br-BTXI(7, 8)	0.1578

The DFT calculations suggest that the lowest energy Br-BTXI has the bromine atom located on the rylene core at the β-position with regards to the sulphur atom (position 7). The free energy (ΔG) for the reaction is –44.20 kcal/mol (see Table 6.6). Further DFT calculations were carried out to understand why additional bromine in the reaction mixture did not lead to further BTXI bromination. Starting with the low-energy monobrominated BTXI, a second bromine atom was added at the remaining carbon atoms. Inspection of the Br-BTXI HOMO shows that there is considerable electron density at most of the remaining

free carbon atoms (see Figure 6.18), suggesting that bromination could occur at any of these locations. The thermodynamically favored position for the formation of a dibrominated BTXI is at the 5 position; notably, this position is the second most favorable when considering monobromination (Figure 6.17). The free energy for reaction to form (stepwise) 5,7-dibrominated BTXI is –32.17 kcal/mol (Table 6.7). Given thermodynamic driving force for the addition of a second bromine, it is hypothesized that it is a kinetic barrier that is responsible for the lack of formation of the dibrominated system.
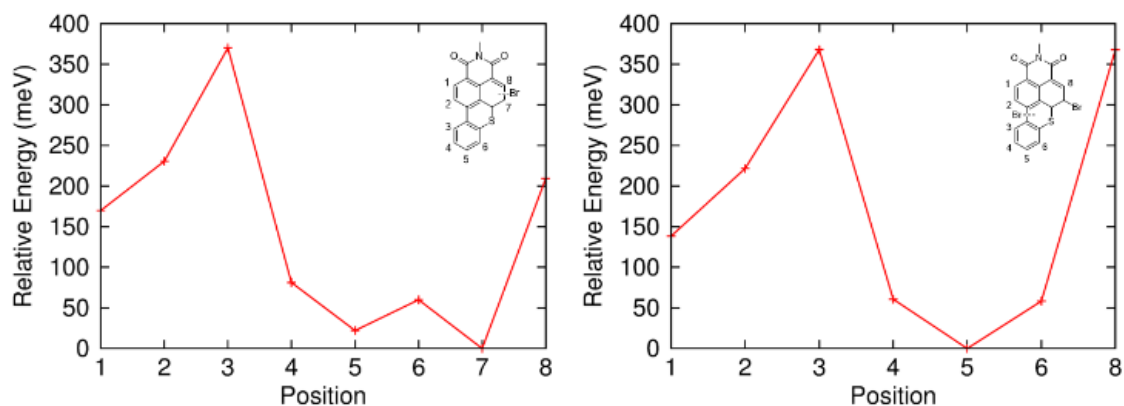
Figure 6.17. Relative energy of monobrominated (Left) and dibrominated (Right) Br-BTXI derivatives calculated at the OT-ωB97X-D/6-31g(d, p) level of theory.
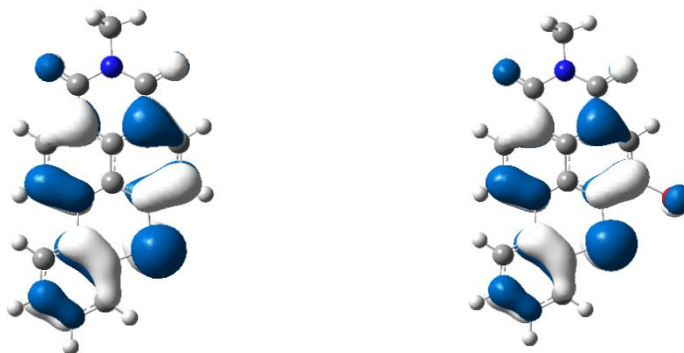
Figure 6.18. HOMO of BTXI (Left) and a monobrominated Br-BTXI with the bromine at the β-position with regards to the sulphur atom (Right).

Table 6.6. Change of enthalpy and Gibbs free energies of the reactions to form a monobrominated Br-BTXI.

	ΔH (kcal/mol)	*ΔG (kcal/mol)*
Br-BTXI(1)	*-39.95*	*-40.59*
Br-BTXI(2)	*-38.46*	*-37.87*
Br-BTXI(3)	*-35.14*	*-34.72*
Br-BTXI(4)	*-41.91*	*-42.23*
Br-BTXI(5)	*-43.14*	*-43.23*
Br-BTXI(6)	*-42.40*	*-42.60*
Br-BTXI(7)	*-43.79*	*-44.20*
Br-BTXI(8)	*-38.86*	*-39.13*

Table 6.7. Change of enthalpy and Gibbs free energies of the reactions to form a dibrominated
Br-BTXI.

	ΔH (kcal/mol)	*ΔG (kcal/mol)*
2Br-BTXI(1, 7)	*-29.45*	*-28.62*
2Br-BTXI(2, 7)	*-27.63*	*-25.80*
2Br-BTXI(3, 7)	*-24.12*	*-22.30*
2Br-BTXI(4, 7)	*-32.45*	*-28.50*
2Br-BTXI(5, 7)	*-32.79*	*-32.17*
2Br-BTXI(6, 7)	*-31.35*	*-30.56*
2Br-BTXI(7, 8)	*-24.25*	*-22.96*

6.3.2.2   Nitration of BTXI

The low-energy nitro-substitution site for each unique and potential BTXI-NO$_2$ derivative was determined by DFT calculations at the OT-ωB97X-D/6-31g(d,p) level of theory. Determination of the relative free energies (ΔG) of the potential mono-nitro products (Figure 6.19 and Table 6.8) reveals that NO$_2$ has a thermodynamic preference for the position labelled 4, but positions 5, 6, and 7 being relatively close in energy. This prediction, however, did not agree with NMR measurements.[16] Hence, we postulate that the nitration on position 7 is potentially due to kinetic preference.
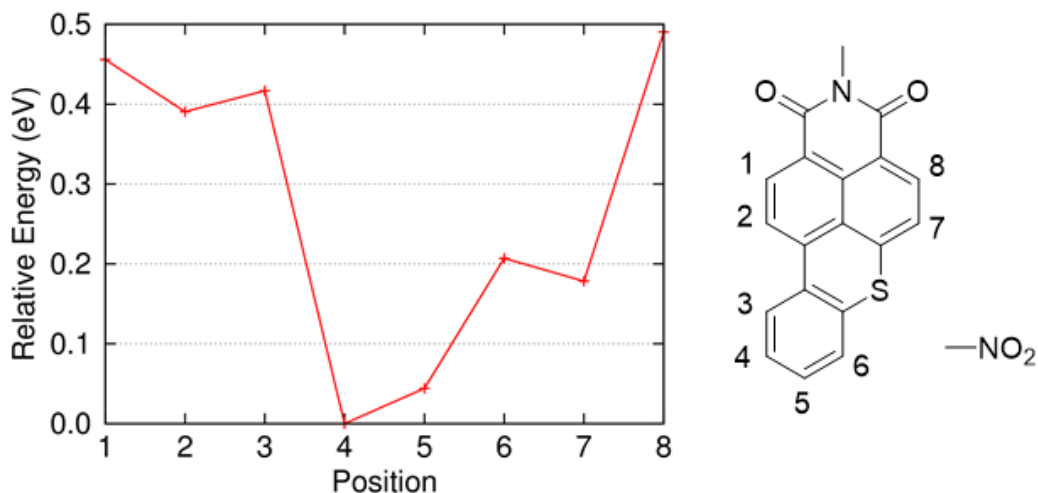
Figure 6.19. Relative energies of BTXI-NO2 derivatives calculated at the OT-oB97xD/6-31G(d,p) level of theory. NB: the alkyl group was truncated to a methyl to reduce the computational cost.

Table 6.8. Change of enthalpy and Gibbs free energies of the reactions to form BTXI-NO$_2$.

	ΔH (kcal/mol)	ΔG (kcal/mol)
BTXI-NO$_2$(1)	-35.43	-35.11
BTXI-NO$_2$ (2)	-36.49	-34.89
BTXI-NO$_2$ (3)	-33.16	-31.40
BTXI-NO$_2$ (4)	-44.90	-43.95
BTXI-NO$_2$ (5)	-40.09	-38.96
BTXI-NO$_2$ (6)	-37.31	-35.73
BTXI-NO$_2$ (7)	-40.46	-39.12
BTXI-NO$_2$ (8)	-34.48	-33.79

The absorption and emission spectra measured by Cabanetos and co-workers revealed that the main transitions of BTXI, BTXI-Br, BTXI-N$_3$ and BTXI-Tr-BTXI located at 480 nm can be assigned to a localized π-π^* transition of the polyaromatic BTXI core, which is slightly affected by the presence of substituents. The BTXI-NH$_2$ has a broad and structureless absorption and emission bands which are significantly red-shifted. This band was assigned to a charge transfer (CT) transition, indicative of push pull effect between the amino and naphthalimide parts of the molecule. This feature is more significant for the BTXI-NPh$_2$.

Simulated absorption and emission spectra derived from TDDFT reveals that the absorption and emission spectrum of BTXI-NH$_2$ is significantly red-shifted when compared to other BTXI derivatives, which agree well with the experimental results (Figure 6.20). To further investigate the CT transition between BTXI core and substitution,

NTO analyses were carried out for the transitions with significant oscillator strength for each derivative (Table 6.9 and Figure 6.21-6.30). For BTXI-NH2 and BTXI-NPh2, the NTO analyses reveals that the transitions are mainly between the amino and naphtalimide moieties, which also agrees with the experimental assignment.
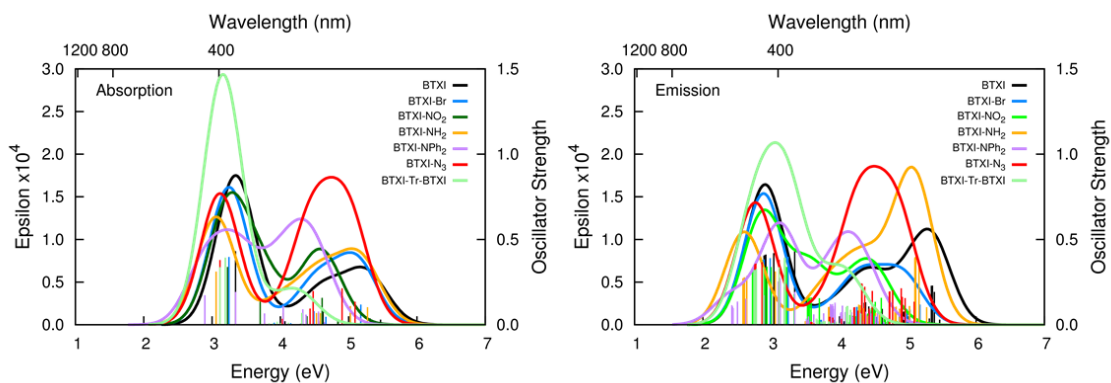
Figure 6.20. Simulated absorption (left) and emission (right) spectra of BTXI derivatives as determined at the OT-ωB97X-D/6-31g(d,p) level of theory. The spectra were simulated through convolution of the vertical transition energies and oscillator strengths with Gaussian functions characterized by a full width at half-maximum (fwhm) of 0.33 eV.

Table 6.1. First ten excited states for the BTXI derivatives as determined at the TD-OT-ωB97X-D/6-31g(d,p) level of theory.

Excited State	BTXI		BTXI-Br		BTXI-NO$_2$		BTXI-N$_3$		BTXI-NH$_2$		BTXI-NPh$_2$		BTXI-Tr-BTXI	
	Energy [λ] (eV [nm])	f	Energy [λ] (eV [nm])	f	Energy [λ] (eV [nm])	f	Energy [λ] (eV [nm])	f	Energy [λ] (eV [nm])	f	Energy [λ] (eV [nm])	f	Energy [λ] (eV [nm])	f
1	3.28 [378]	0.4151	3.25 [382]	0.3974	3.23 [384]	0.3386	3.12 [398]	0.3794	3.06 [405]	0.3116	2.90 [428]	0.1725	3.12 [398]	0.3373
2	4.01 [309]	0.0224	3.91 [317]	0.0116	3.71 [335]	0.1549	3.74 [331]	0.0027	3.77 [329]	0.0134	3.35 [370]	0.1924	3.19 [388]	0.3931
3	4.24 [292]	0.0057	4.15 [299]	0.0093	3.96 [313]	0.0004	3.85 [322]	0.0013	4.04 [307]	0.0682	3.77 [329]	0.0666	3.83 [323]	0.0084
4	4.26 [291]	0.0002	4.22 [294]	0.0002	4.04 [307]	0.0062	4.03 [308]	0.0346	4.24 [292]	0.0002	4.04 [307]	0.1119	3.89 [318]	0.0081
5	4.53 [273]	0.0928	4.49 [276]	0.0799	4.22 [294]	0.0002	4.21 [294]	0.0002	4.53 [274]	0.0686	4.11 [301]	0.0028	3.95 [314]	0.0175
6	4.68 [265]	0.0007	4.64 [267]	0.0098	4.39 [282]	0.0508	4.43 [280]	0.0949	4.58 [270]	0.0681	4.33 [286]	0.0905	4.01 [309]	0.0099
7	4.76 [261]	0.0128	4.67 [266]	0.0468	4.51 [275]	0.0040	4.48 [277]	0.1976	4.67 [266]	0.0007	4.38 [283]	0.0595	4.11 [302]	0.0014
8	5.08 [244]	0.069	4.97 [249]	0.0001	4.61 [269]	0.1574	4.64 [267]	0.0004	5.02 [247]	0.1097	4.56 [272]	0.0769	4.12 [301]	0.0117
9	5.20 [239]	0.0363	5.02 [247]	0.0691	4.64 [267]	0.0019	4.90 [253]	0.2139	5.13 [242]	0.0061	4.56 [272]	0.0195	4.17 [298]	0.0005
10	5.40 [230]	0.0831	5.18 [239]	0.1179	4.84 [256]	0.0220	5.09 [243]	0.1345	5.28 [235]	0.1023	4.65 [267]	0.0157	4.31 [287]	0.0691

Figure 6.21. Pictorial representations of the natural transition orbitals (NTO) for the $S_0 \rightarrow S_1$ transitions of NH2-BTXI as determined at the TD-OT-ωB97X-D/6-31g(d,p) level of theory. λ is the fraction of the hole–particle contribution to the excitation.

Figure 6.22. Pictorial representations of the natural transition orbitals (NTO) for the $S_0 \rightarrow S_1$ transitions of N3-BTXI as determined at the TD-OT-ωB97X-D/6-31g(d,p) level of theory. λ is the fraction of the hole–particle contribution to the excitation.

$\lambda = 0.57$

$S_0 \rightarrow S_7$

$\lambda = 0.40$

Hole   Electron

Figure 6.23. Pictorial representations of the natural transition orbitals (NTO) for the $S_0 \rightarrow S_7$ transitions of N3-BTXI as determined at the TD-OT-ωB97X-D/6-31g(d,p) level of theory. λ is the fraction of the hole–particle contribution to the excitation.

$S_0 \rightarrow S_9$

$\lambda = 0.50$

$\lambda = 0.32$

$\lambda = 0.12$

Hole

Electron

Figure 6.24. Pictorial representations of the natural transition orbitals (NTO) for the $S_0 \rightarrow S_9$ transitions of N3-BTXI as determined at the TD-OT-ωB97X-D/6-31g(d,p) level of theory. λ is the fraction of the hole–particle contribution to the excitation.

Figure 6.25. Pictorial representations of the natural transition orbitals (NTO) for the $S_0 \rightarrow S_{10}$ transitions of N3-BTXI as determined at the TD-OT-ωB97X-D/6-31g(d,p) level of theory. λ is the fraction of the hole–particle contribution to the excitation.

Figure 6.26. Pictorial representations of the natural transition orbitals (NTO) for the $S_0 \rightarrow S_1$ transitions of NPh2-BTXI as determined at the TD-OT-ωB97X-D/6-31g(d,p) level of theory. λ is the fraction of the hole–particle contribution to the excitation.

198

Figure 6.27. Pictorial representations of the natural transition orbitals (NTO) for the $S_0 \rightarrow S_2$ transitions of NPh2-BTXI as determined at the TD-OT-ωB97X-D/6-31g(d,p) level of theory. λ is the fraction of the hole–particle contribution to the excitation.

Figure 6.28. Pictorial representations of the natural transition orbitals (NTO) for the $S_0 \rightarrow S_4$ transitions of NPh2-BTXI as determined at the TD-OT-ωB97X-D/6-31g(d,p) level of theory. λ is the fraction of the hole–particle contribution to the excitation.

Figure 6.29. Pictorial representations of the natural transition orbitals (NTO) for the $S_0 \rightarrow S_1$ transitions of NO2-BTXI as determined at the TD-OT-ωB97X-D/6-31g(d,p) level of theory. λ is the fraction of the hole–particle contribution to the excitation.

Figure 6.30. Pictorial representations of the natural transition orbitals (NTO) for the $S_0 \rightarrow S_8$ transitions of NO_2-BTXI as determined at the TD-OT-ωB97X-D/6-31g(d,p) level of theory. λ is the fraction of the hole–particle contribution to the excitation.

6.3.3 Replacing PDI with BTXI in dyes

The use of PDI and DPP fragments enables an a strong visible light absorption and high electron affinity. The reorganization of these molecule during SVA to form a planar head-to-tail configurations also contributes to a unprecedented 'red-shifts' in the optical absorption spectrum. Further, the functionlization of the BTXI dye opens new doors to the design of new π-conjugated materials used in optoelectronics. Although the new building blocks provide new strategy in the design of OSC, the role of these moieties play are still unclear, therefore, it is important to understand how these building blocks modify key molecular and material characteristics in order to enhance the design strategies.

We studied three OSCs (Figure 6.31) synthesized by Cabanetos, Welch, and co-workers using the PDI, DPP and BTXI building blocks.[4] The synthesized compounds show different charge-carrier transport characteristics, and offer a distinctive path to create OSC that span a range of device performance metrics.[4]

PDI-DPP-PDI (1)   PDI-DPP-BTXI (2)   BTXI-DPP-BTXI (3)
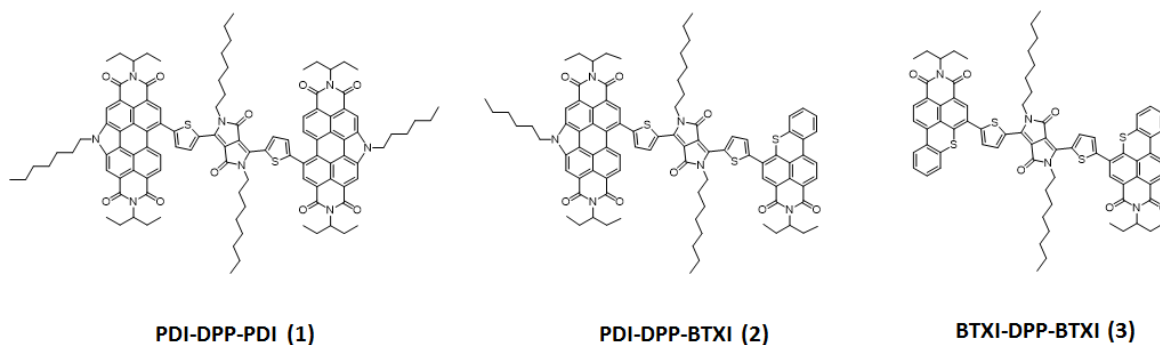
Figure 6.31. Chemical structures of the three molecules studied in this section.

The electrochemical properties of compounds 1-3 were determined by cyclic voltammetry by our experimental colleagues.[4] Overall, the IP appears to be dictated by the DPP core, falling between 5.2 to 5.3 eV. For compounds 1 and 2, the EAs (ca. 3.7 eV) appear to be

dictated by the PDI units. For compound 3 containing only BTXI terminal groups and no PDI, the EA appears to be dictated by DPP with some influence from BTXI, which results in a large decrease in the EA from 3.7 to 3.3 eV. This result suggests that BTXI is significantly more electron rich than PDI.

Table 6.10. Select DFT and TDDFT data for 1, 2 and 3 as determined at the OT-ωB97X-D/6-31g(d,p) level of theory.

Compound	Tuned ω	IP(eV)	EA(eV)	Reorganization Energy (eV)		$S_0 \rightarrow S_1$ (eV[nm])	f	Electronic configuration
				Hole	Electron			
1	0.123	6.18	2.21	0.43	0.38	2.45 [506]	1.00	HOMO $\rightarrow$ LUMO (12%) HOMO $\rightarrow$ LUMO + 2(83%)
2	0.124	6.05	2.19	0.48	0.39	2.45 [506]	0.96	HOMO $\rightarrow$ LUMO (3%) HOMO $\rightarrow$ LUMO + 1 (88%) HOMO $\rightarrow$ LUMO + 2 (5%)
3	0.118	5.94	1.67	0.49	0.31	2.40 [516]	1.10	HOMO $\rightarrow$ LUMO (88%) HOMO $\rightarrow$ LUMO + 2 (10%)

These experimental IP and EA assignments were confirmed through the evaluation of frontier molecular orbitals and IP and EA, as determined by DFT calculations at the OT-ωB97X-D/6-31g(d,p) level of theory. The results are presented in Figure 6.32-6.34. The highest-occupied molecular orbitals (HOMO: 1, –6.45 eV, and 2, –6.33 eV) for 1 and 2 reside on the DPP moiety, while the lowest-occupied molecular orbitals (LUMO; 1, –2.06 eV, and 2, –2.03 eV) are localized on the PDI units. For 3, the assignment of IP and EA being a function of DPP with some influence from BXTI is also confirmed through evaluation of the frontier molecular orbitals. Here the HOMO (–6.19 eV) is mainly

localized on the DPP core, though it does extend onto the BTXI sulfur atoms, while the LUMO (–1.50 eV) is delocalized across the DPP and BTXI π-conjugated framework; note that though there is more π electron delocalization of the LUMO of 3 when compared to 1 and 2, the greater reducing power of PDI results in a more energetically stabilized LUMO when it is part of the full molecular construct. Overall, the frontier molecular orbital energies follow the redox potential trends. Further, adiabatic IP and EA (AIP and AEA, respectively) determined at the OT-ωB97X-D/6-31g(d,p) level of theory correspond well with experiment. The subsequent replacement of PDI with BTXI results in an energetic destabilization of both the AIP (6.18 eV for 1, 6.05 eV for 2, and 5.94 eV for 3) and AEA (–2.21 eV for 1, –2.19 eV for 2, and –1.67 eV for 3). Finally, we also note that the intramolecular reorganization energies for hole (0.43 eV for 1, 0.48 eV for 2, and 0.49 eV for 3) and electron (0.38 eV for 1, 0.39 eV for 2, and 0.31 eV for 3) transport are rather considerable in these systems; for the acenes, for instance, the reorganization energies are typically of the order of 0.10 eV. These large reorganization energies, which constitute the sum of the geometric relaxation processes that molecules undergo during the oxidation and reduction events that occur as charges move through the molecular materials, stem in part from considerable changes in the dihedral angles between the DPP and PDI or BTXI when the molecule is oxidized or reduced.
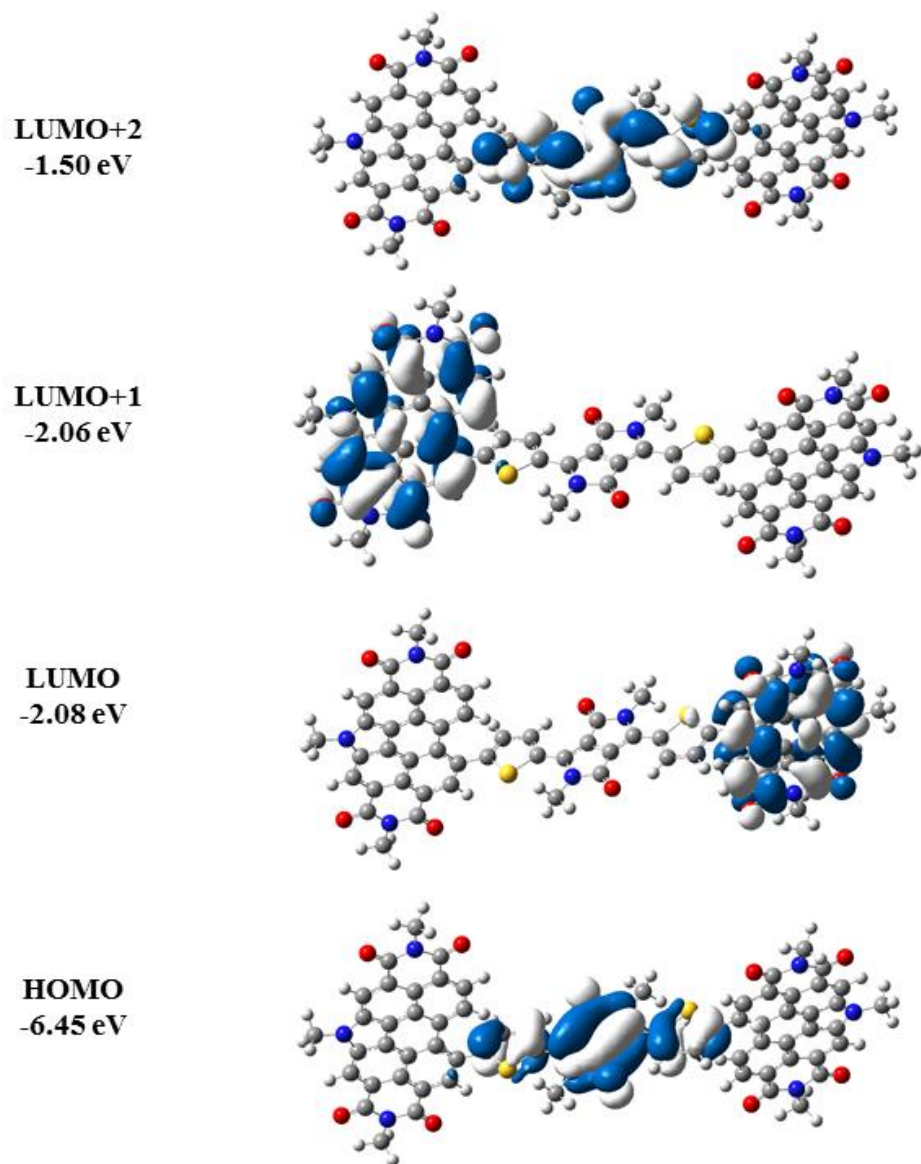
Figure 6.32. Pictorial representations of select frontier molecular orbitals of compound 1 as determined at the OT-ωB97X-D/6-31g(d,p) level of theory.
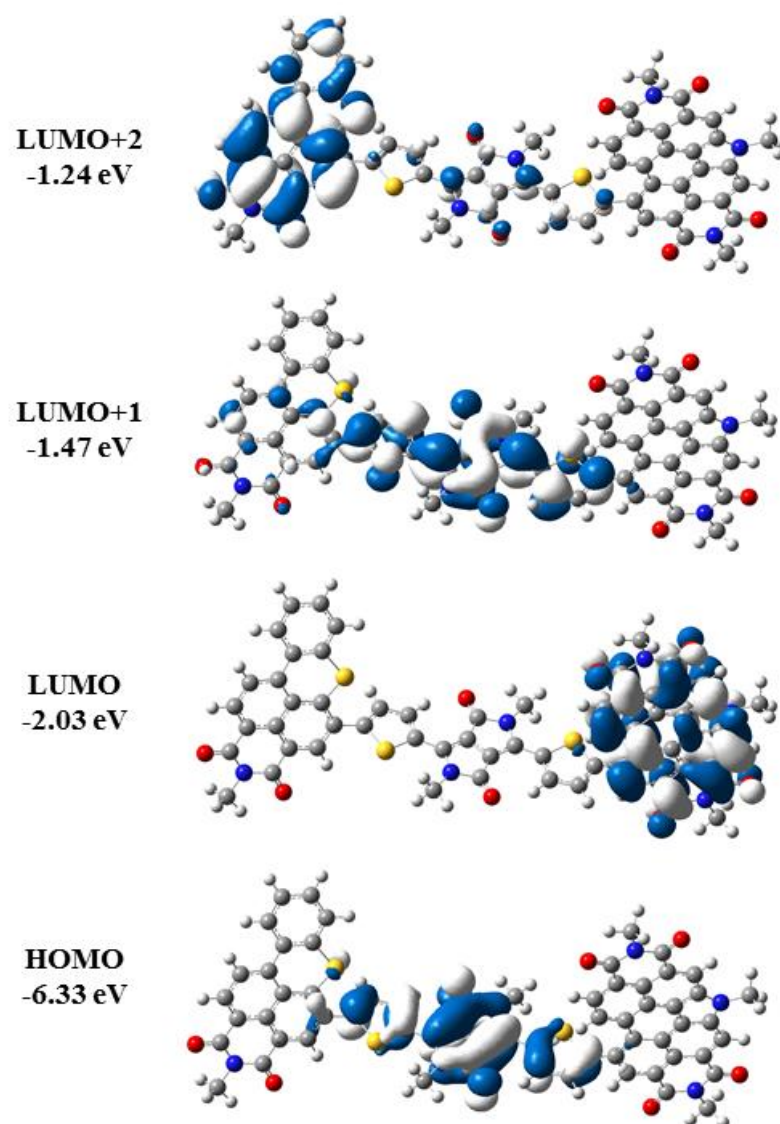
Figure 6.33. Pictorial representations of select frontier molecular orbitals of 2 as determined at the OT-ωB97X-D/6-31g(d,p) level of theory.
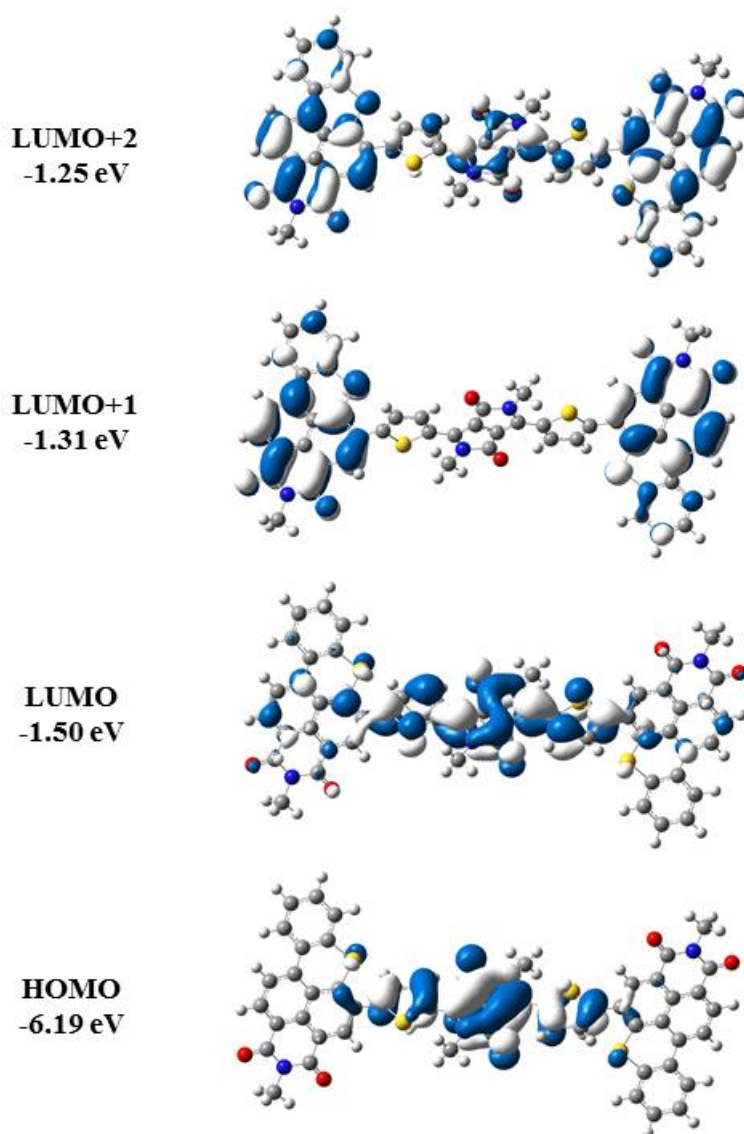
Figure 6.34. Pictorial representations of select frontier molecular orbitals of **3** as determined at the OT-ωB97X-D/6-31g(d,p) level of theory.

The optical properties of compounds 1, 2, and 3 were determined experimentally by UV-vis spectroscopy.[4] To assist in the understanding of the optical characteristics, we performed time-dependent DFT (TD-DFT) calculations at the OT-ωB97X-D/6-31g(d,p) level of theory. The results agreed reasonably well with experiment (Figure 6.35-6.37); it should be noted that while the TD-DFT calculations reproduce the experimental trends in

terms of transition energies, the relative intensities of the DPP-based and PDI-based transitions are inconsistent. For 1 and 2, the $S_0 \rightarrow S_1$ transitions (both at 2.45 eV; 506 nm) are centralized on the DPP core, which is a function of the highly twisted nature of the PDI moieties with respect to the DPP; in each case, the transitions mainly involve DPP-localized orbitals (HOMO$\rightarrow$LUMO+2 for 1, and HOMO$\rightarrow$LUMO+1 for 2). These DPP-centric transitions for 1 and 2 are confirmed by natural transition orbital (NTO) analyses, where the hole and electron wavefunctions are located on the DPP moiety (Figure 6.38). The next transitions with significant oscillator strength [$S_0 \rightarrow S_4$ for 1 (2.75 eV) and $S_0 \rightarrow S_3$ for 2 (2.75 eV)] are PDI localized. For 3, though it is generally more planar and the LUMO extends into the BTXI, the hole and electron NTO for the $S_0 \rightarrow S_1$ transition (HOMO$\rightarrow$LUMO) are also DPP localized. We furthered calculated NTO for higher-lying excited states of the compound, shown in Figure 6.39; for these transitions, there is more DPP character associated with each transition. This result confirms the idea that BTXI is neither a strong donor nor acceptor with respect to DPP.
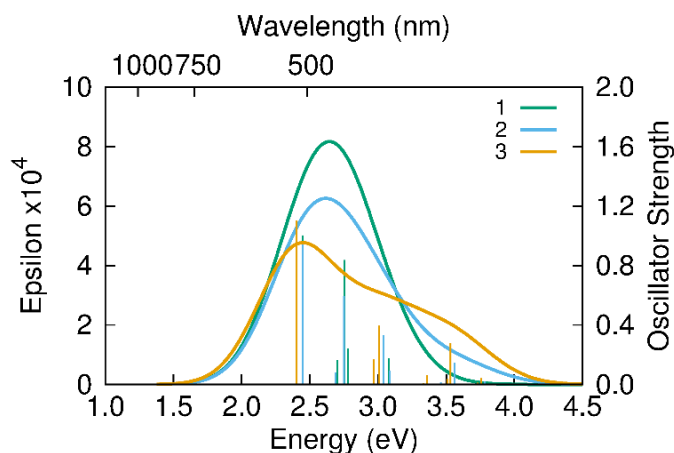
Figure 6.35. Simulated absorption spectra of 1, 2, and 3 as determined at the TD-OT-ωB97X-D/6-31g(d,p) level of theory. Absorption spectra were simulated through convolution of the vertical transition energies and oscillator strengths with Gaussian functions characterized by a full width at half-maximum (fwhm) of 0.33 eV.
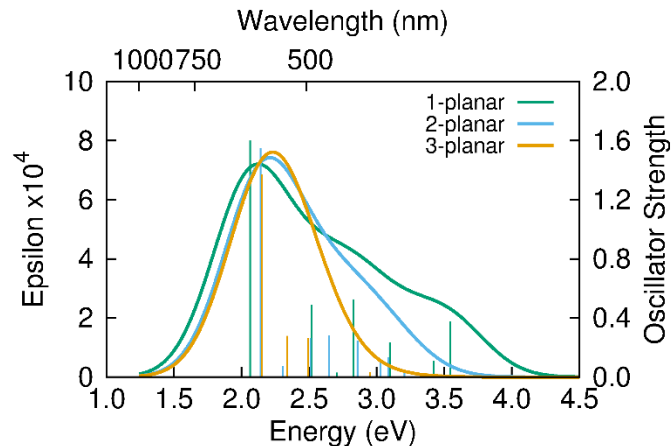
Figure 6.36. Simulated absorption spectra of constrained planar 1, 2, and 3 as determined at the TD-OT-ωB97X-D/6-31g(d,p) level of theory. Absorption spectra were simulated through convolution of the vertical transition energies and oscillator strengths with Gaussian functions characterized by a full width at half-maximum (fwhm) of 0.33 eV.
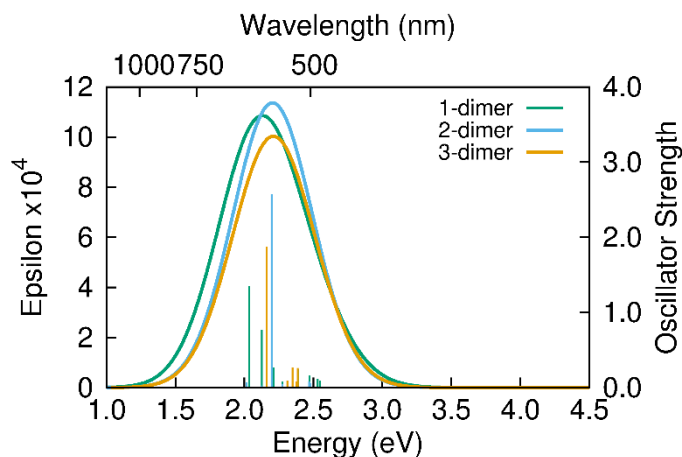
Figure 6.37. Simulated absorption spectra of constrained planar dimers of 1, 2, and 3 as determined at the TD-OT-ωB97X-D/6-31g(d,p) level of theory. Absorption spectra were simulated through convolution of the vertical transition energies and oscillator strengths with Gaussian functions characterized by a full width at half-maximum (fwhm) of 0.33 eV.
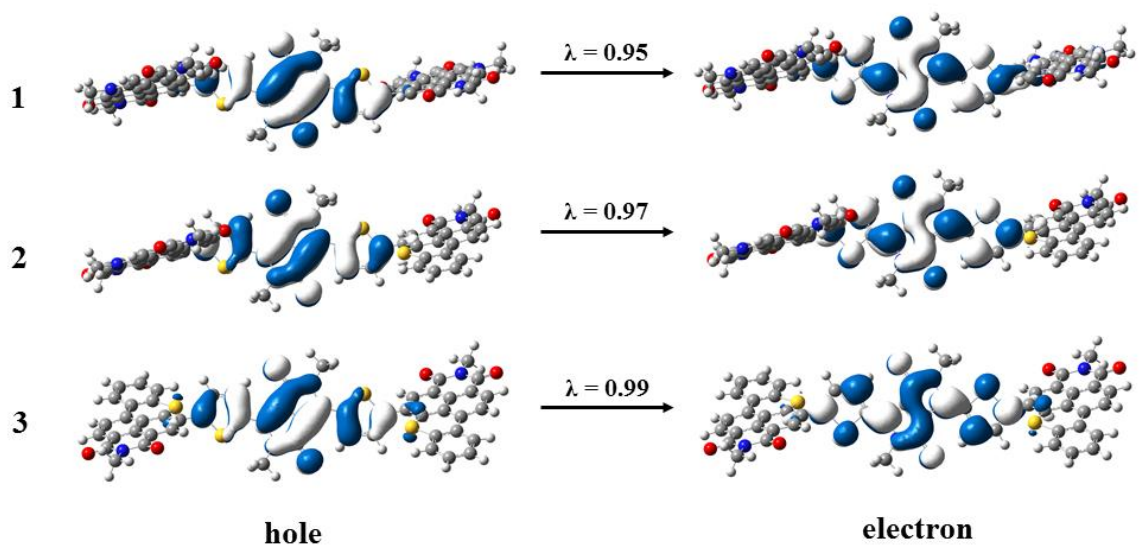
Figure 6.38. Pictorial representations of natural transition orbitals (NTO) of the $S_0 \rightarrow S_1$ of compound 1, 2 and 3 as determined at the TD-OT-ωB97X-D/6-31g(d,p) level of theory. λ is the fraction of the hole-electron contribution to the excitation.
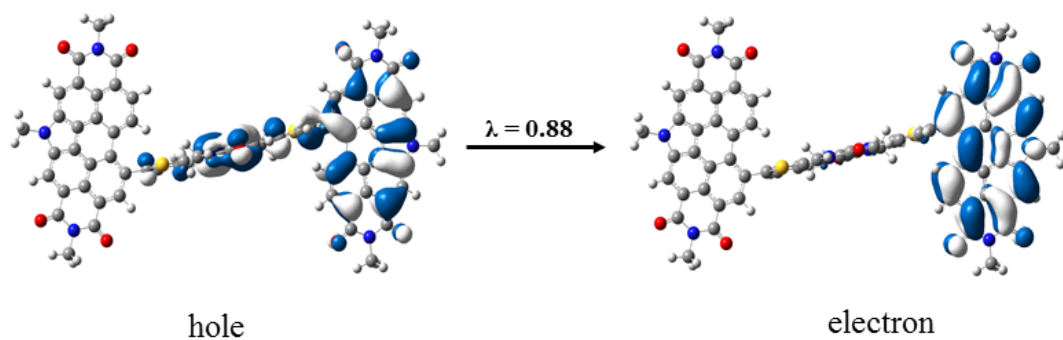
Figure 6.39. Pictorial representations of the natural transition orbitals (NTO) for the $S_0 \rightarrow S_2$ transition of 1 as determined at the TD-OT-ωB97X-D/6-31g(d,p) level of theory. λ is the fraction of the hole–particle contribution to the excitation.

hole   electron
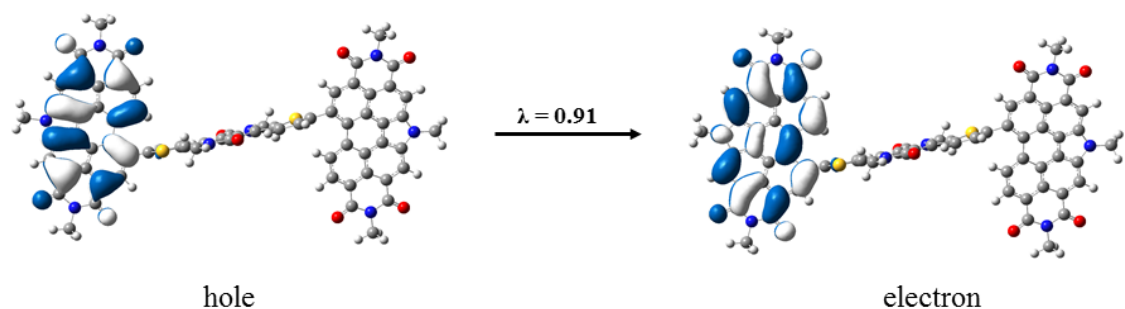
Figure 6.40. Pictorial representations of the natural transition orbitals (NTO) for the $S_0 \rightarrow S_4$ transition of 1 as determined at the TD-OT-ωB97X-D/6-31g(d,p) level of theory. λ is the fraction of the hole–particle contribution to the excitation.

hole   electron
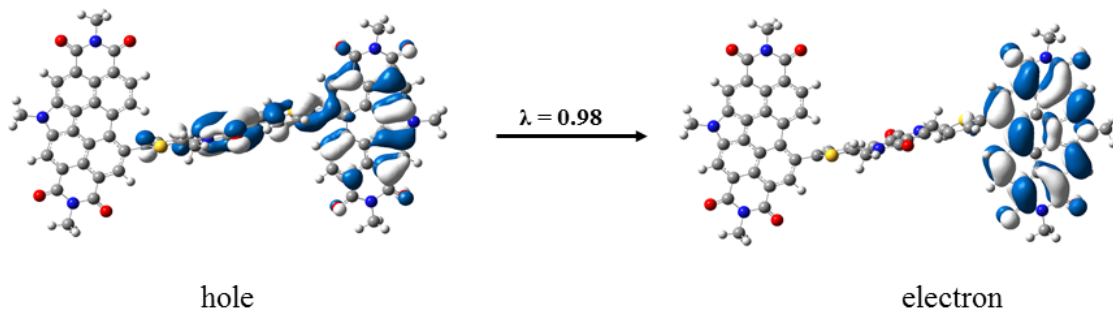
Figure 6.41. Pictorial representations of the natural transition orbitals (NTO) for the $S_0 \rightarrow S_5$ transition of 1 as determined at the TD-OT-ωB97X-D/6-31g(d,p) level of theory. λ is the fraction of the hole–particle contribution to the excitation.

hole   electron
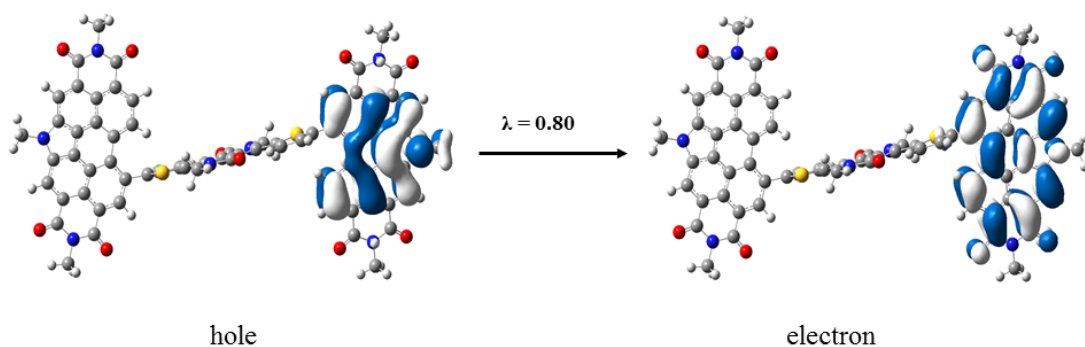
Figure 6.42. Pictorial representations of the natural transition orbitals (NTO) for the $S_0 \rightarrow S_6$ transition of 1 as determined at the TD-OT-ωB97X-D/6-31g(d,p) level of theory. λ is the fraction of the hole–particle contribution to the excitation.
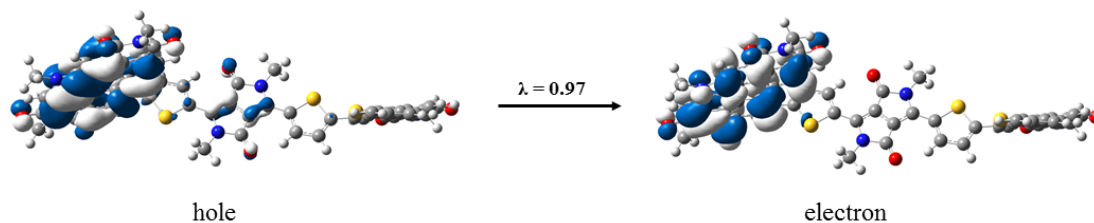
Figure 6.43. Pictorial representations of the natural transition orbitals (NTO) for the $S_0 \rightarrow S_3$ transition of 2 as determined at the TD-OT-ωB97X-D/6-31g(d,p) level of theory. λ is the fraction of the hole–particle contribution to the excitation.
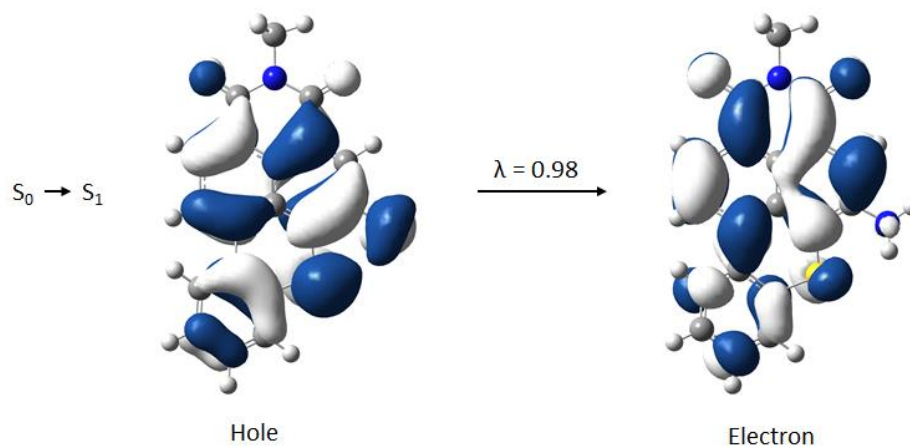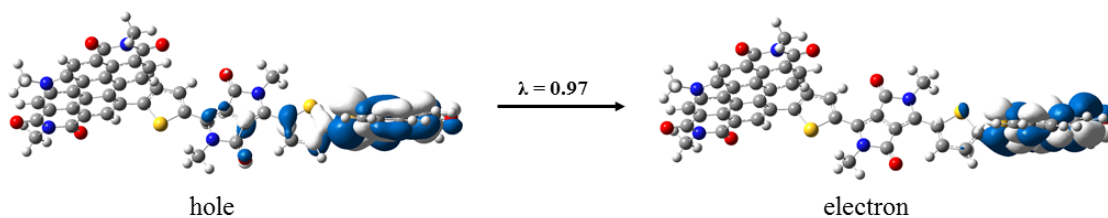

Figure 6.44. Pictorial representations of the natural transition orbitals (NTO) for the $S_0 \rightarrow S_4$ transition of 2 as determined at the TD-OT-ωB97X-D/6-31g(d,p) level of theory. λ is the fraction of the hole–particle contribution to the excitation.
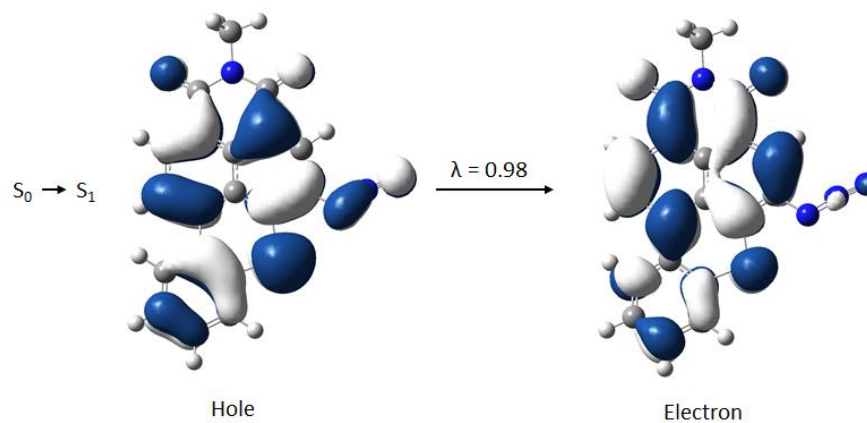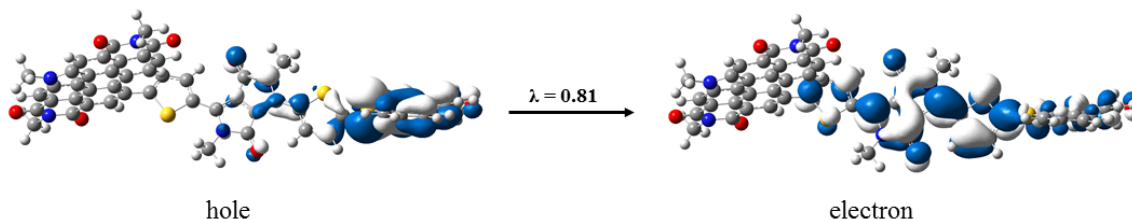

Figure 6.45. Pictorial representations of the natural transition orbitals (NTO) for the $S_0 \rightarrow S_8$ transition of 2 as determined at the TD-OT-ωB97X-D/6-31g(d,p) level of theory. λ is the fraction of the hole–particle contribution to the excitation.
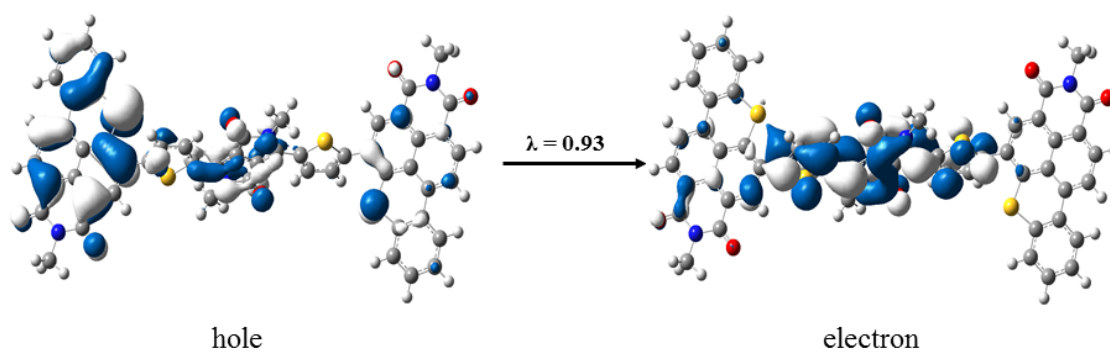
Figure 6.46. Pictorial representations of the natural transition orbitals (NTO) for the $S_0 \rightarrow S_3$ transition of 3 as determined at the TD-OT-ωB97X-D/6-31g(d,p) level of theory. λ is the fraction of the hole–particle contribution to the excitation.
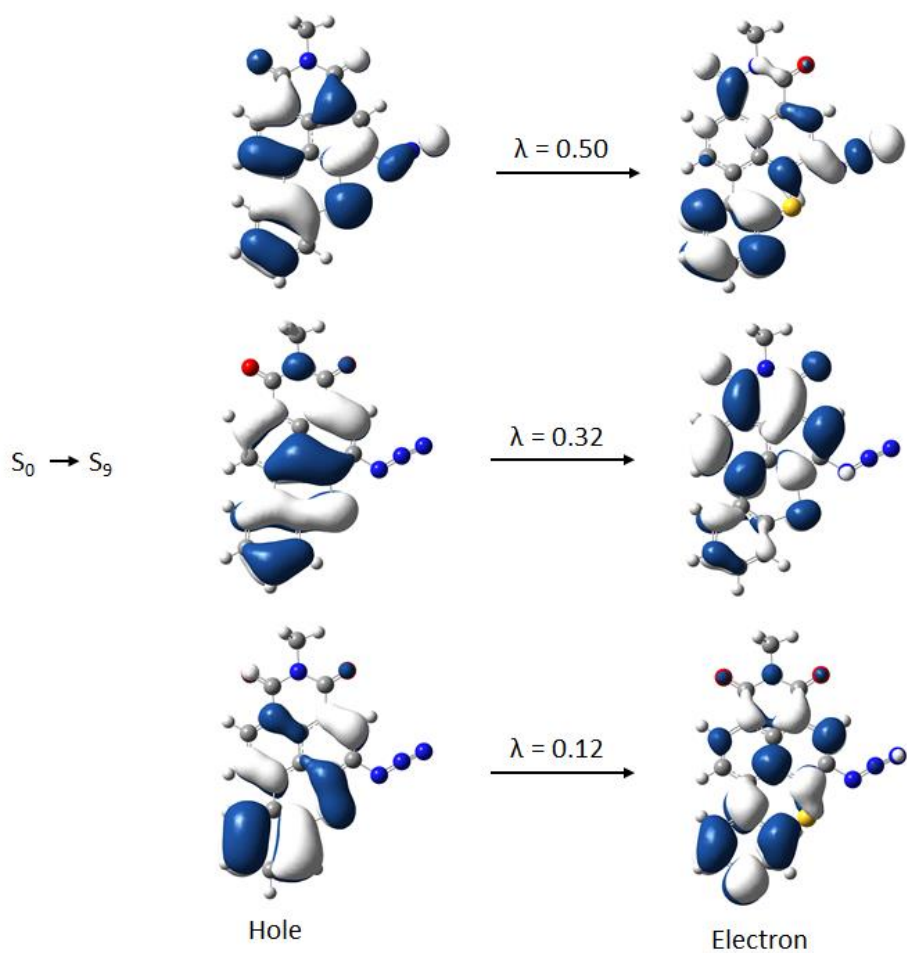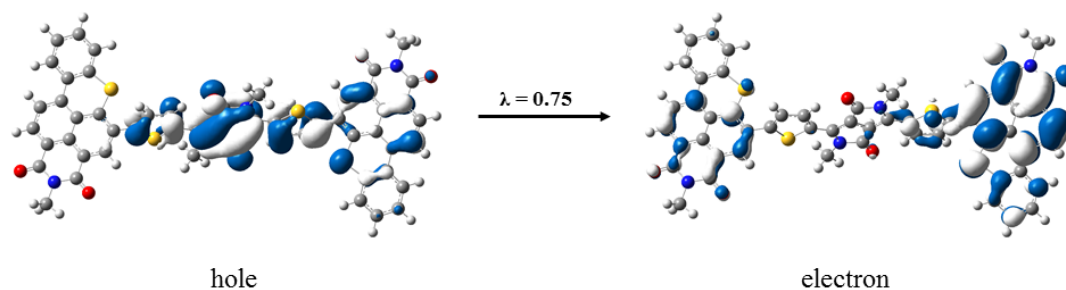

Figure 6.47. Pictorial representations of the natural transition orbitals (NTO) for the $S_0 \rightarrow S_4$ transition of 3 as determined at the TD-OT-ωB97X-D/6-31g(d,p) level of theory. λ is the fraction of the hole–particle contribution to the excitation.
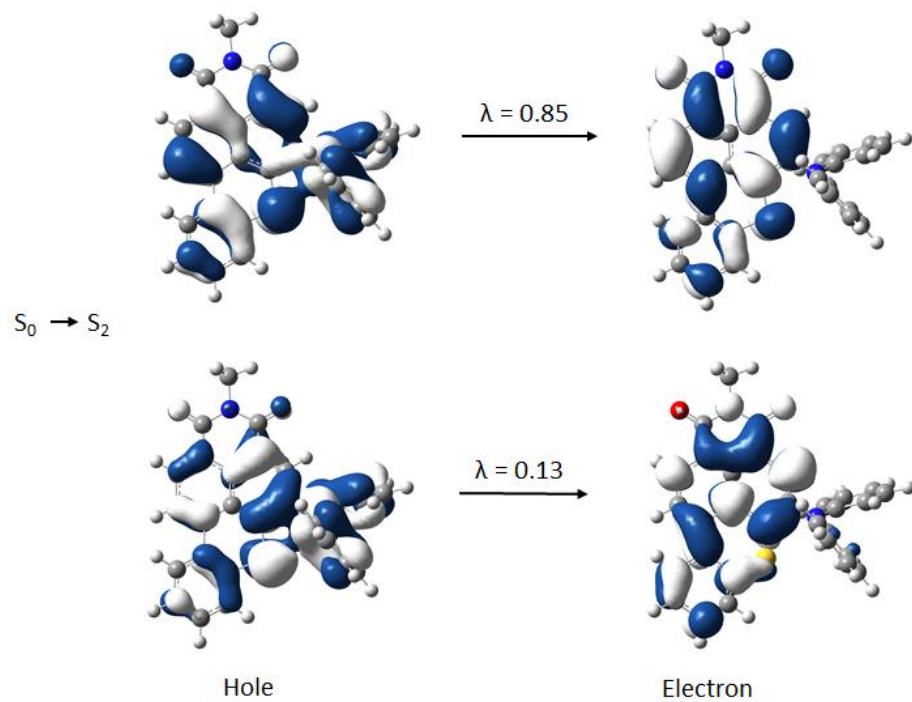

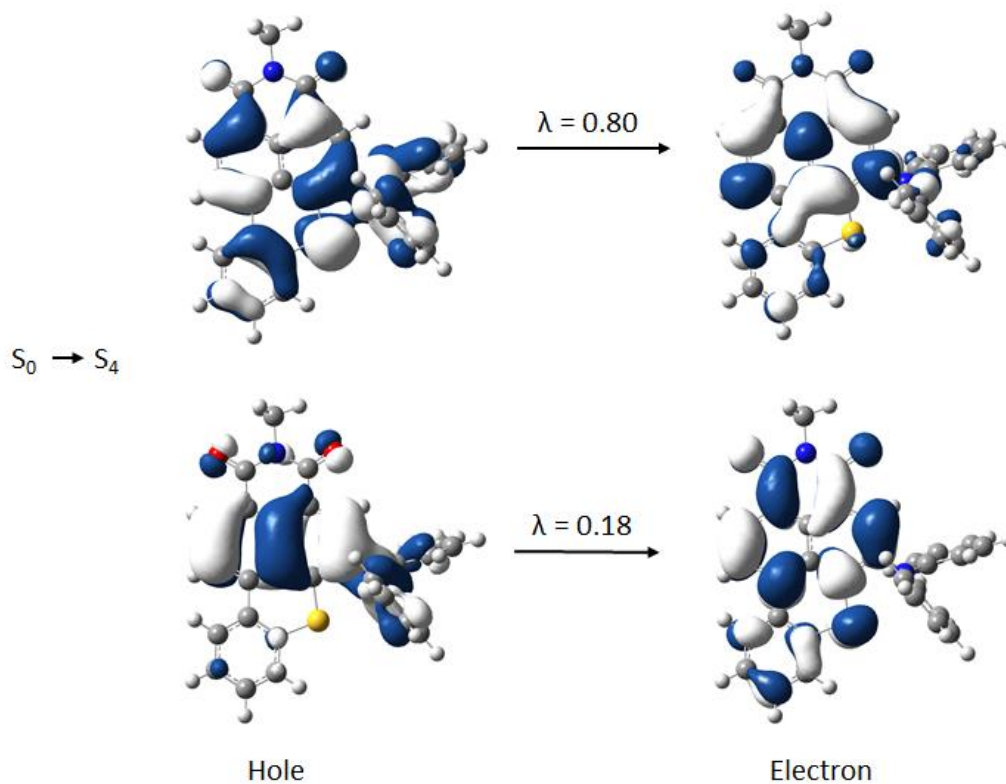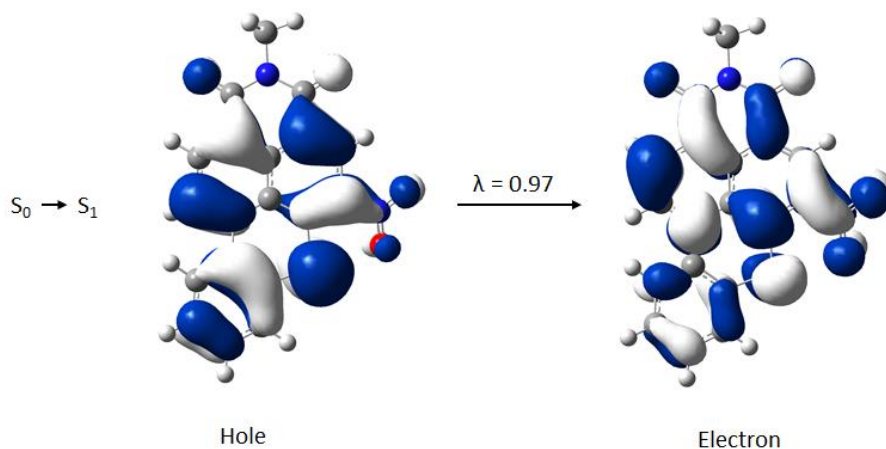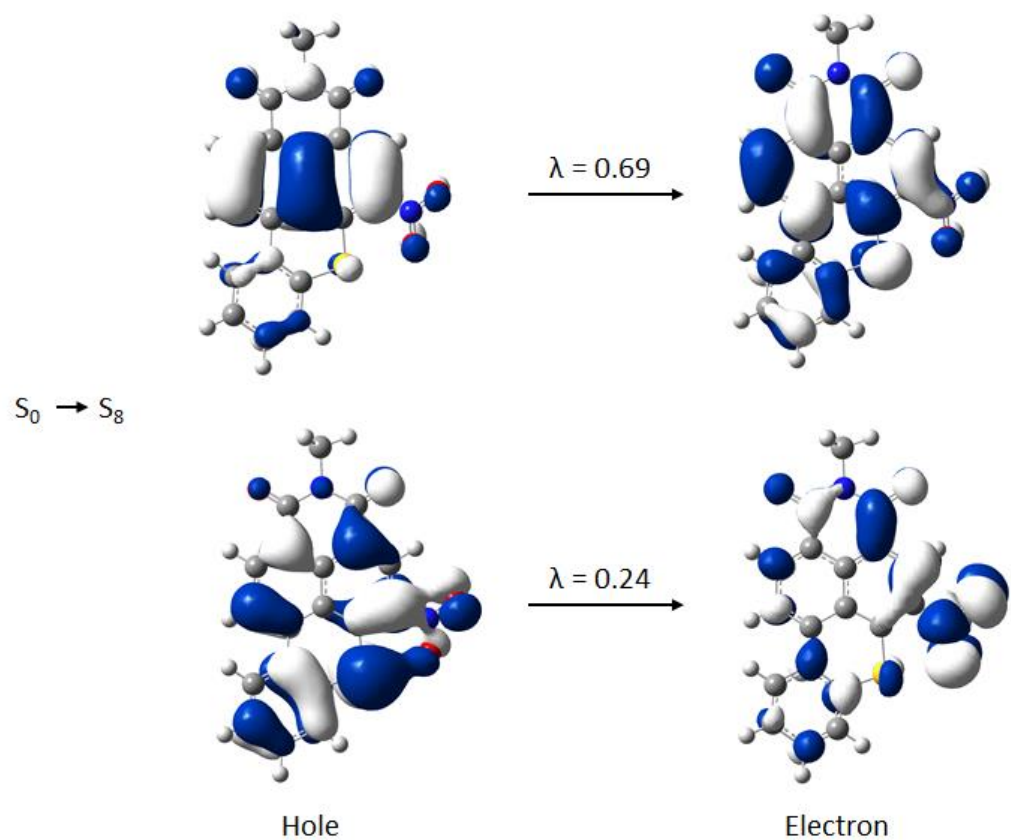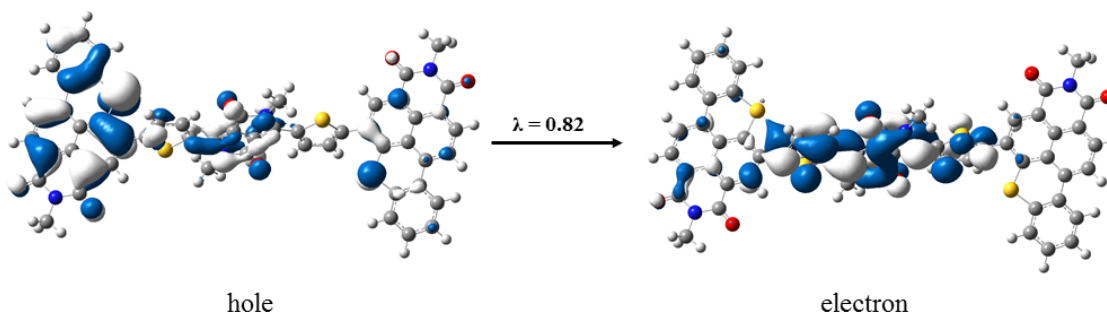**Figure 6.48.** Pictorial representations of the natural transition orbitals (NTO) for the $S_0 \rightarrow S_8$ transition of 3 as determined at the TD-OT-ωB97X-D/6-31g(d,p) level of theory. λ is the fraction of the hole–particle contribution to the excitation.

As with the previous study on the PDI-DPP-IQ molecule showed a structural reorganization in the solid-state upon post-deposition SVA treatment, thin film of compounds 1, 2, and 3 were exposed to tetrahydrofuran (THF) vapor for varying times, and the optical absorption spectra of each film were measured. The absorption band of all compounds have shown different changes upon SVA, such as onset sharpening, increasing intensity, red-shift and appearance of fine structure across the absorption profile, which are typical for DPP containing molecules.[4, 17, 18] Ultimately, the replacement of PDI with BTXI does not inhibit the response observed by UV-vis spectroscopy, further suggesting that the DPP core plays a significant role in the molecular reorganization responsible for the changes observed in the absorption profile upon SVA.

To investigate the relationship between possible changes in molecular structure and optical characteristics with SVA, further TDDFT calculations were carried out as a function of the degree of twist within the molecular structure (among the DPP and rylene-based substituents) and the potential to form tightly packed dimers with coplanar structures; the results are presented in Figure 6.49-6.54. The PES of 1, shown in Figure 6.49, reveals again that the lowest energy point has a dihedral angle between these units of ~ 90°, suggesting that the PDI and DPP units prefer to be perpendicular to each other in the gas phase. Further TDDFT calculations at each twist angle reveals that the planar configuration of 1 results a red shift of the $S_0 \rightarrow S_1$ transition when comparing to the optimized structure (Figure 6.50). The formation of a coplanar conformation, though higher in energy, leads to a significant red shift of the $S_0 \rightarrow S_1$ transition (by ~0.4 eV). For 2 and 3, however, the already more coplanar conformation between the DPP and BTXI moieties in the optimized structure limits changes in $S_0 \rightarrow S_1$ transition energies if fully planar configurations are considered.

Instead, the potential to form closer contacts among the π systems of neighboring, coplanar molecules can lead to the appearance of lower-energy transitions (by ~0.2 eV) in 2 and 3. In each case, the low-lying transitions with appreciable oscillator strength reveal some charge-transfer-like character from the DPP to the respective rylene-based substituents. (Figure 6.52-6.54)
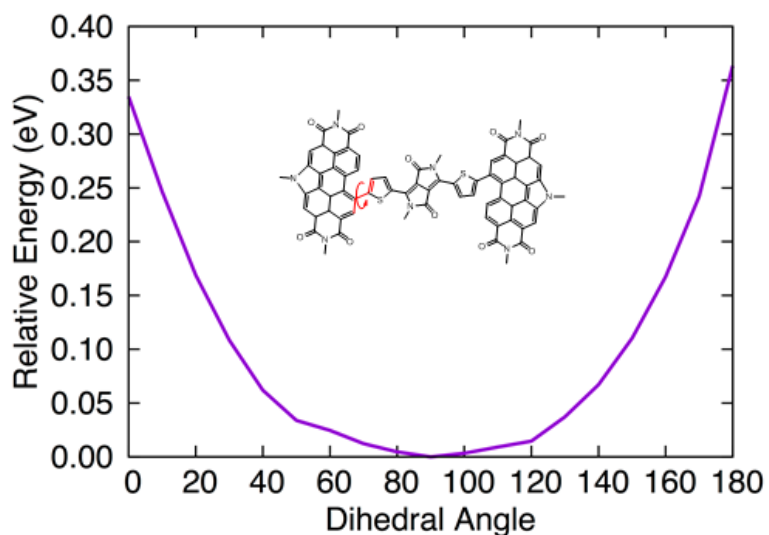
Figure 6.49. Potential energy surface for twisting the PDI moiety in PDI-DPP-PDI (1) as determined at the TD-OT-ωB97X-D/6-31g(d,p) level of theory.
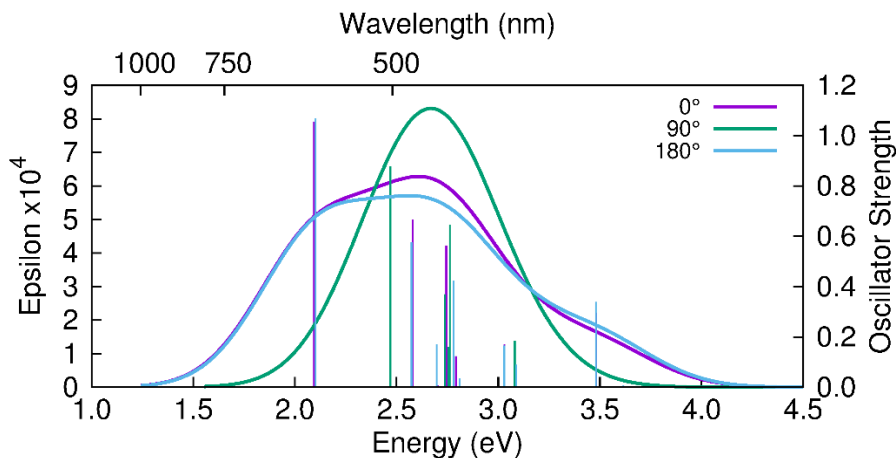
Figure 6.50. Simulated absorption spectra of PDI-DPP-PDI (1) at three different orientations of the PDI group as determined at the TD-OT-ωB97X-D/6-31g(d,p) level of theory. Absorption spectra were simulated through convolution of the vertical transition energies and oscillator strengths with Gaussian functions characterized by a full width at half-maximum (fwhm) of 0.33 eV.
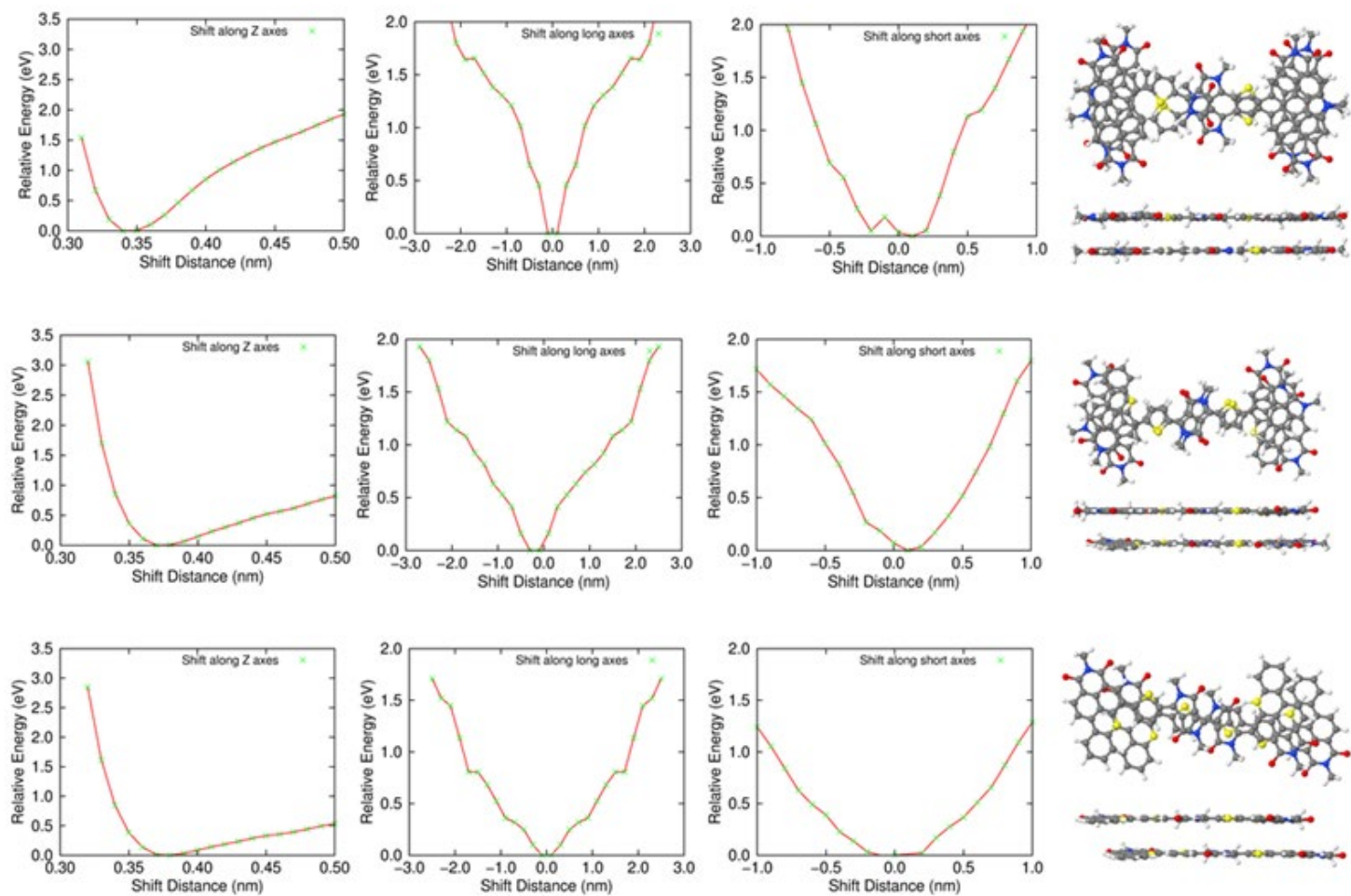
Figure 6.1. Potential energy surface (PES) for the stacking of two, planar configurations of 1 (A), 2 (B) and 3 (C) as determined at the OT-ωB97X-D/6-31g(d,p) level of theory. The molecules were oriented so that the dimer had no net dipole moment, as depicted in the right of the figure.

Table 6.11. First ten excited states of the constrained planar configurations of 1, 2, and 3 as determined at the TD-OT-ωB97X-D/6-31g(d,p) level of theory. The geometry of the planar for this calculation was based on the PES shown in Figures 6.51.

Excited State	Energy [λ] (eV [nm])			f		
	1	**2**	**3**	**1**	**2**	**3**
1	2.06 [601]	2.45 [506]	2.40 [516]	1.60	0.96	1.10
2	2.52 [493]	2.69 [461]	2.97 [418]	0.49	0.08	0.17
3	2.70 [459]	2.75 [451]	3.01 [413]	0.03	0.59	0.39
4	2.83 [439]	3.04 [408]	3.34 [372]	0.53	0.33	0.01
5	2.86 [433]	3.08 [402]	3.36 [369]	0.01	0.09	0.06
6	3.06 [405]	3.44 [361]	3.42 [363]	0.00	0.00	0.00
7	3.10 [401]	3.46 [358]	3.51 [353]	0.23	0.01	0.04
8	3.33 [372]	3.56 [348]	3.53 [351]	0.00	0.14	0.28
9	3.42 [363]	3.77 [329]	3.73 [332]	0.11	0.00	0.01
10	3.54 [350]	3.78 [328]	3.76 [330]	0.38	0.02	0.04

Table 6.10. First ten excited states of the constrained planar dimers of 1, 2 and 3 as determined at the TD-OT-ωB97X-D/6-31g(d,p) level of theory. The geometry of the planar dimer for this calculation was based on the PES shown in Figures 6.51.

Excited State	Energy [λ] (eV [nm]) (Dimer)			f (Dimer)		
	1	**2**	**3**	**1**	**2**	**3**
1	1.84 [674]	1.47 [711]	2.04 [607]	0.01	0.00	0.00
2	2.03 [610]	2.02 [615]	2.16 [574]	1.35	0.07	1.87
3	2.13 [583]	2.12 [585]	2.22 [559]	0.77	0.02	0.01
4	2.19 [566]	2.20 [564]	2.24 [553]	0.00	2.57	0.01
5	2.21 [560]	2.27 [545]	2.26 [549]	0.26	0.05	0.01
6	2.28 [545]	2.31 [537]	2.28 [545]	0.08	0.00	0.01
7	2.39 [519]	2.31 [536]	2.31 [537]	0.24	0.02	0.09
8	2.47 [501]	2.43 [511]	2.35 [528]	0.16	0.00	0.26
9	2.53 [490]	2.47 [502]	2.38 [521]	0.12	0.08	0.08
10	2.55 [487]	2.48 [501]	2.39 [519]	0.09	0.05	0.26

top view

λ = 0.79

λ = 0.16

side view

λ = 0.79

λ = 0.16

hole

electron
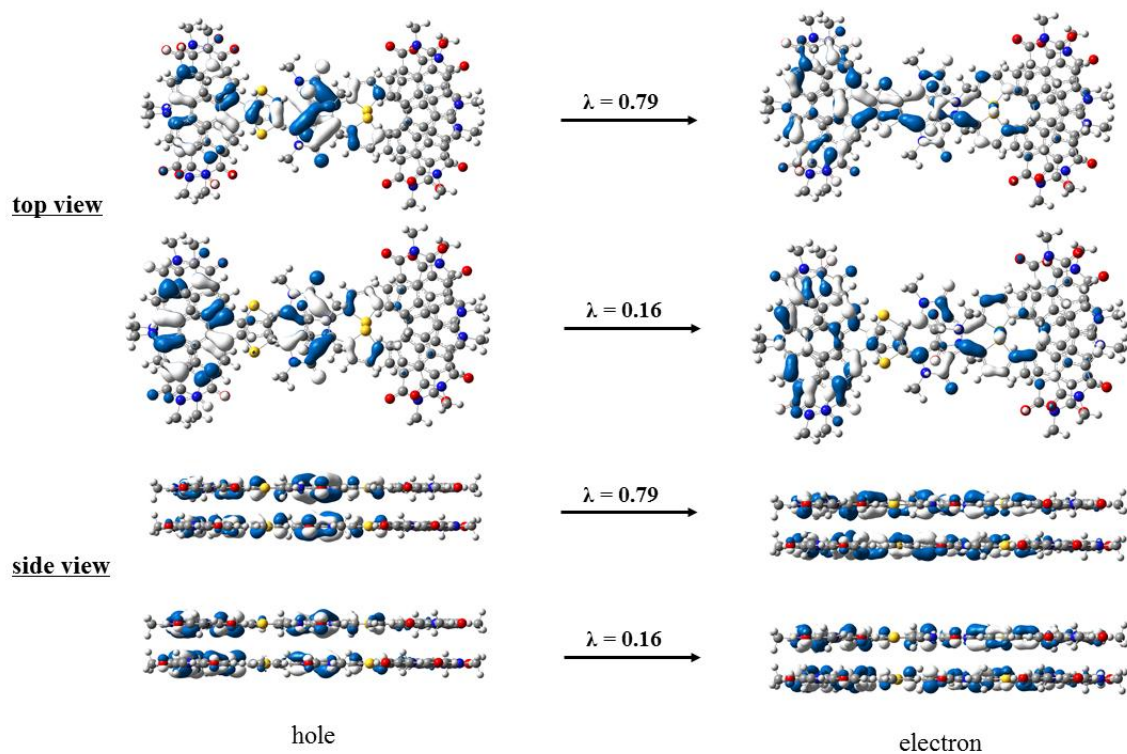
Figure 6.52. Pictorial representations of the natural transition orbitals (NTO) for the $S_0 \rightarrow S_2$ transition of the planar dimer of 1 as determined at the TD-OT-ωB97X-D/6-31g(d,p) level of theory. Both top and side views are presented. λ is the fraction of the hole–particle contribution to the excitation.
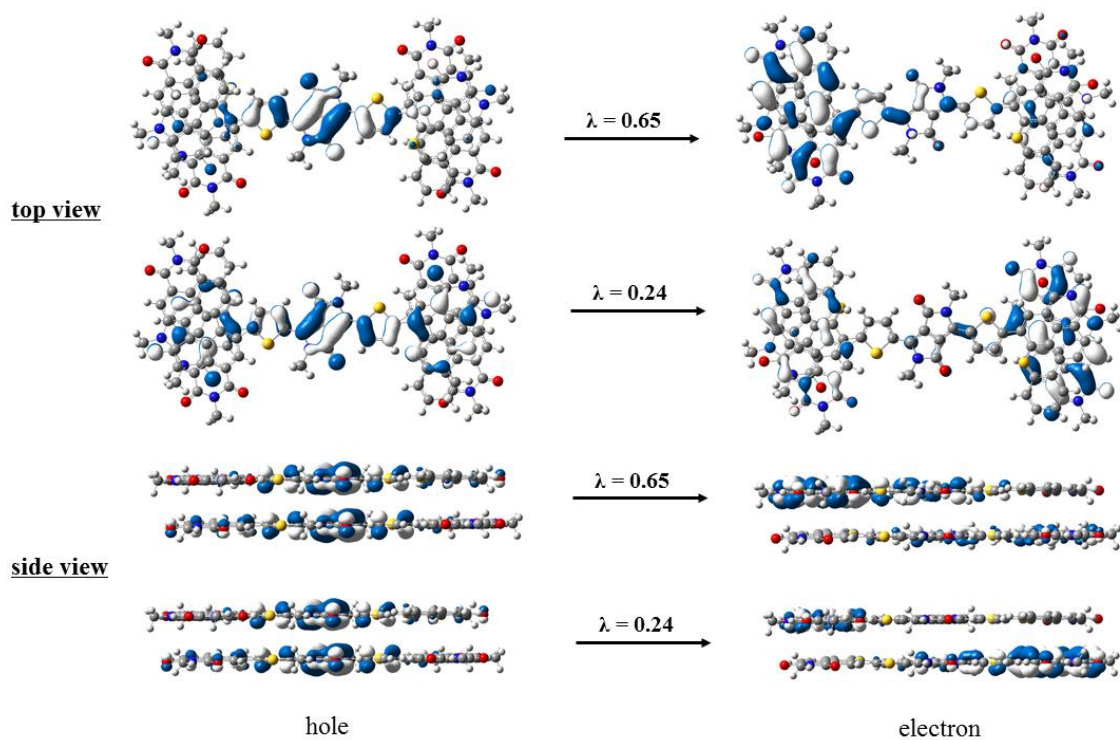
Figure 6.53. Pictorial representations of the natural transition orbitals (NTO) for the $S_0 \rightarrow S_4$ transition of the planar dimer of 2 as determined at the TD-OT-ωB97X-D/6-31g(d,p) level of theory. Both top and side views are presented. λ is the fraction of the hole–particle contribution to the excitation.
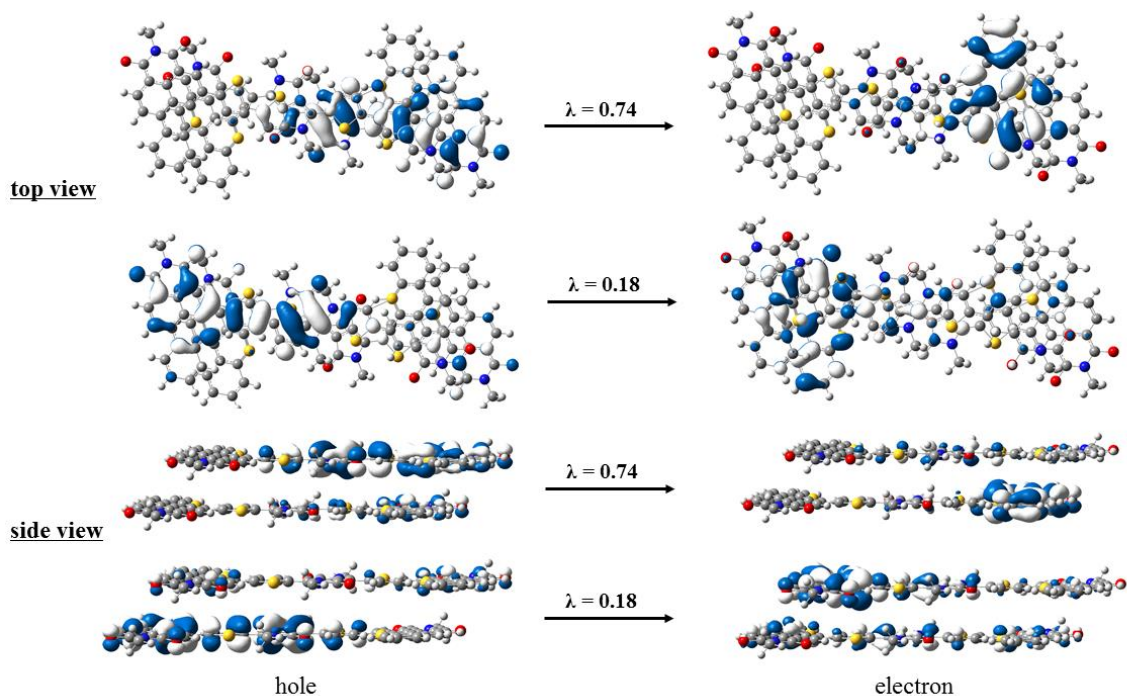
Figure 6.54. Pictorial representations of the natural transition orbitals (NTO) for the $S_0 \rightarrow S_2$ transition of the planar dimer of 3 as determined at the TD-OT-ωB97X-D/6-31g(d,p) level of theory. Both top and side views are presented. λ is the fraction of the hole–particle contribution to the excitation.

6.4 Conclusion

In this chapter, we made use of DFT to study the electronic and optical characteristics of new dyes for OSC. For the unsymmetrical PDI-DPP-IQ molecule, our calculation of IP, EA, excited-state transition and absorption spectrum agree reasonably with experiment assignments. The analysis using NTO method confirms the panchromatic design paradigm, while the mid-energy transition is mainly on the PDI unit, the higher-energy transitions are associated with the IQ moiety. By applying the TDDFT analysis on each configuration from the potential energy surface of the twisting of the PDI unit, we revealed that the shift of absorption band is associated with the molecular reorganization and the formation of a planar dimer configurations during SVA.

In the determination of the bromination and nitration position on the BTXI building block, we confirmed the first and second bromination positions from both energy and frontier molecular orbital evaluation. The disagreement of the nitration position with the NMR measurement may be attritbuted to the knitic perfernces, though more work is needed to confirm this assertion. Finally, we studied three additional dyes where PDI is replaced with the BTXI building block. The optical properties determined by TDDFT reveals that BTXI was neither a strong donor nor acceptor with respect to DPP unit. We further evaluated the formation of co-facial dimers on change of optical characteristics. In each molecule, there are some charge-transfer like character associated with the DPP and rylene-based substituents. This effort demonstrates how appropriate theoretical approaches can assist synthetic chemists to understand the behavior of new OSC and provide fundamental understanding on the structure–function relationships to further improve material performance.

CHAPTER 7

PERSPECTIVE

7.1 Summary

The exploration of functional organic semiconductors (OSC) has garnered enormous attention over the past few decades. Due to continued advances in theoretical methods and computational techniques, theoretical approaches to investigate structure–function relationships in OSC holds great promise to bring fundamental understanding to the often complicated physicochemical features of OSC. One of the chief issues that hinders the advance OSC adoption in commercial electronics applications is fundamental lack of understanding as to how the molecular structure affects the solid-state morphology, which in turn impacts the OSC properties pertinent to their use in a variety of semiconductor devices. In this dissertation, we developed and deployed computational models, making use of both classical molecular dynamics (MD) simulations and quantum chemical approaches, to investigate OSC structure–property relationships with the ultimate goal of extending knowledge as to the intricate connections between molecular structure, processing, morphology, and electronic and optical response.

The first model consisted of a number of OSC bulk crystals. We were particularly interested in exploring phase transitions, as a deeper insight of these mechanisms can aid in understanding how post-processing thermal treatments can influence material packing and morphology and provide a reverse-engineering perspective as to how these materials assemble. Further, we explored the impact of superheating in MD simulations. Our results revealed how providing free space for the molecules to move in the simulation gave more opportunity for increased disorder – either through the introduction of voids into the

supercell or the creation of free surfaces – and a dramatic reduction in superheating. For the small, rigid ADT molecules, the melting temperatures calculated from the slab models showed very good agreement with experiment. The same strategy, though had a lesser effect on lowering the simulated melt transitions of TES-ADT crystals. However, during the melting procedure, distinct solid-solid phase transitions was observed in the temperature range consistent with the experimentally reported melting temperature; we hypothesize that this solid-solid phase transition, related to a reorientation of the TES-ADT molecules in the unit cell, may lead to breaks in the crystals and facilitate melting at lower temperatures.

We then developed and applied large-scale simulations on unary, binary, and ternary mixture models, using both Lennard-Jones (LJ) particles and molecules, to explore the free energy of mixing (ΔG_m) as a function of material composition. The knowledge developed through these simulations can help us understand the solution processing of OSC, which often involves multi-components that vary in concentrations. We implemented the two-phase dynamic (2PT) model to determine the entropy of the liquid systems and, in turn, determine ΔG_m. For the unary and binary models, our results show reasonable agreement with experiment. In many of the systems under investigation, mixing was determined to be predominantly entropy driven, highlighting the need of robust methods to determine this thermodynamic function.

We then examined how the solution environment can impact the structure and aggregation of OSC molecular building blocks in solution. Our studies revealed significant solvent effects for each attribute. For instance, preferred rotamer configurations for donor-acceptor oligomers can be greatly influenced by the choice of processing solvent, and their ability

225

to assemble/aggregate in solution can also be modulated by the solvent environment. We further developed an approach to study the impact of solvent drying on oligomer structure and dynamics. Here, the presence of the vacuum–solution interface played an important role as alkyl chains on the periphery of the oligomer preferentially extended into this interface, leading to an alignment of the oligomer backbones at this interface. Such features can be a key characteristic in the relative molecular ordering of thin-film OSC developed from solution processing. Similar effects were observed for diF TES ADT in toluene solutions, where the triethylsilyl side groups appended to the ADT backbone preferentially aligned at the vacuum–solution interface. These simulations reveled large-scale nucleation from supersaturated solutions, with important details arising as to how relative concentrations in these supersaturated states influence the relative molecular packing order that can be achieved (within the timescale of the simulation). We also developed an analysis approach to distinguish molecules at different states of aggregation, providing us the ability to study molecular behavior during different states of nucleation and growth.

Our final study focused on the application of quantum chemical approaches to explore distinctive electronic and optical properties of OSC, which were shown to change as a function of material processing. Density functional theory (DFT) and time-dependent DFT (TDDFT) calculations were used to examine how conformational changes and molecular dimerization/complexation arising from solvent vapor annealing (SVA) can alter the observed optical characteristics of the material. We further used these methods to explore the development of new chromophore building blocks for OSC, and how their incorporation into multi-chromophoric dyes can alter the electronic, redox, and optical properties.

7.2 Future work

While this thesis made considerable progress in terms of method and model development and providing insight into the structure–processing–function paradigm of OSC, we are still only scratching the surface of the intricacies of OSC. A number of advances are still needed to extend our knowledge and further explore the complicated relationships that connect molecular structure and OSC properties.

One such modification is to ensure that MD force fields are accurate representations of the systems under study. Currently, most force fields are developed for a general materials class and modified on a case-by-case fashion. Due to limited experimental measurements on OSC molecules and materials, the parameterization of distinct bond, angle, and dihedral parameters relies on the quantum chemical calculations. Such calculations generally treat the target as an isolated gas-phase molecule at absolute zero temperature, ignoring environmental influences. Further, these calculations can be time and resource consuming. Applications of machine learning, for instance, are starting to transform the development of force fields in small molecular systems with limited chemistry. Developing these approaches for larger, and in particular π-conjugated molecules can be a particularly important advance for the field.

Further, there continues to be a need to bring simulations closer to experiment. We have shown, for instance, how one can overcome superheating effects in MD simulations by creating slab models that provide the boundaries from which melting will first occur. However, we still need to incorporate other empirical parameters, including impurities, multi-scale disorder, and defects. These features are a critical part of the nature of the samples and will greatly impact measured materials properties. Therefore, accounting for

these attributes can bring the models closer to experiment and bring forward deeper understanding pertaining to structure–function relationships.

The size (number of atoms and/or length) and time domains of the MD simulations also need to be better correlated with respect to experiment. For instance, in our solution models, we have a small, finite number of molecules available to explore aspects related to nucleation and growth. Hence, there is little opportunity to explore rare events that are expected to be observed in much larger ensembles. There have wide-ranging suggestions to overcome such situations, such as automatically inserting solutes molecules into the system to maintain supersaturated conditions or add an external potential to change the intermolecular interaction energies. Despite different approaches to accelerate the nucleation process, the MD simulation of such rare events requires careful modification and extended studies. One of the most popular approaches is to develop coarse grained (CG) models by neglecting some of the atomistic degrees of freedom and reduce computational complexity, therefore significantly increases the simulation time scale. The use of CG models in the study of OSC can be an important step forward, provided that too much molecular-scale information is not lost in the CG model.

Given these considerations, one would expect that theoretical investigations would be able to truly capture the hierarchical characteristics of OSC. Such advances, in turn, could aid in the development of machine-driven design and discovery of OSC.

REFERENCES

Chapter 1 References

1.   Eley, D. D., Phthalocyanines as Semiconductors. *Nature* **1948,** *162* (4125), 819-819.

2.   Paasch, G.; Lindner, T.; Rost-Bietsch, C.; Karg, S.; Riess, W.; Scheinert, S., Operation and properties of ambipolar organic field-effect transistors. *Journal of Applied Physics* **2005,** *98* (8), 084505.

3.   Png, R.-Q.; Chia, P.-J.; Tang, J.-C.; Liu, B.; Sivaramakrishnan, S.; Zhou, M.; Khong, S.-H.; Chan, H. S. O.; Burroughes, J. H.; Chua, L.-L.; Friend, R. H.; Ho, P. K. H., High-performance polymer semiconducting heterostructure devices by nitrene-mediated photocrosslinking of alkyl side chains. *Nature materials* **2010,** *9* (2), 152-158.

4.   Tang, C. W.; VanSlyke, S. A., Organic electroluminescent diodes. *Applied Physics Letters* **1987,** *51* (12), 913-915.

5.   Riede, M.; Mueller, T.; Tress, W.; Schueppel, R.; Leo, K., Small-molecule solar cells—status and perspectives. *Nanotechnology* **2008,** *19* (42), 424001.

6.   Yang, F.; Shtein, M.; Forrest, S. R., Controlled growth of a molecular bulk heterojunction photovoltaic cell. *Nature materials* **2005,** *4* (1), 37-41.

7.   Yuan, Y.; Giri, G.; Ayzner, A. L.; Zoombelt, A. P.; Mannsfeld, S. C. B.; Chen, J.; Nordlund, D.; Toney, M. F.; Huang, J.; Bao, Z., Ultra-high mobility transparent organic thin film transistors grown by an off-centre spin-coating method. *Nature communications* **2014,** *5* (1), 3005.

8.   Jurchescu, O. D.; Subramanian, S.; Kline, R. J.; Hudson, S. D.; Anthony, J. E.; Jackson, T. N.; Gundlach, D. J., Organic Single-Crystal Field-Effect Transistors of a Soluble Anthradithiophene. *Chemistry of Materials* **2008,** *20* (21), 6733-6737.

9.   Subramanian, S.; Park, S. K.; Parkin, S. R.; Podzorov, V.; Jackson, T. N.; Anthony, J. E., Chromophore Fluorination Enhances Crystallization and Stability of Soluble Anthradithiophene Semiconductors. *Journal of the American Chemical Society* **2008,** *130* (9), 2706-2707.

10.   Mamada, M.; Katagiri, H.; Mizukami, M.; Honda, K.; Minamiki, T.; Teraoka, R.; Uemura, T.; Tokito, S., syn-/anti-Anthradithiophene Derivative Isomer Effects on Semiconducting Properties. *ACS applied materials & interfaces* **2013,** *5* (19), 9670-9677.

11.   Payne, M. M.; Parkin, S. R.; Anthony, J. E., Functionalized Higher Acenes: Hexacene and Heptacene. *Journal of the American Chemical Society* **2005,** *127* (22), 8028-8029.

12.   Payne, M. M.; Parkin, S. R.; Anthony, J. E.; Kuo, C.-C.; Jackson, T. N., Organic Field-Effect Transistors from Solution-Deposited Functionalized Acenes with Mobilities as High as 1 cm2/V·s. *Journal of the American Chemical Society* **2005,** *127* (14), 4986-4987.

13.   Davey, R. J., Polymorphism in Molecular Crystals Joel Bernstein. Oxford University Press, New York, 2002. ISBN 0198506058. *Crystal Growth & Design* **2002,** *2* (6), 675-676.

14.   Desiraju, G. R., Crystal Engineering: A Holistic View. *Angewandte Chemie International Edition* **2007,** *46* (44), 8342-8356.

15.   Kuhnert-Brandstätter, M.; Sollinger, H. W., Thermal analytical and infrared spectroscopic investigations on polymorphic organic compounds—VI. *Microchimica Acta* **1990,** *102* (1), 137-149.

16.   Threlfall, T. L., Analysis of organic polymorphs. A review. *Analyst* **1995,** *120* (10), 2435-2460.

17.   Yu, L.; Li, X.; Pavlica, E.; Koch, F. P. V.; Portale, G.; da Silva, I.; Loth, M. A.; Anthony, J. E.; Smith, P.; Bratina, G.; Kjellander, B. K. C.; Bastiaansen, C. W. M.; Broer, D. J.; Gelinck, G. H.; Stingelin, N., Influence of Solid-State Microstructure on the Electronic Performance of 5,11-Bis(triethylsilylethynyl) Anthradithiophene. *Chemistry of Materials* **2013,** *25* (9), 1823-1828.

18.   Sorli, J. C.; Ai, Q.; Granger, D. B.; Gu, K.; Parkin, S.; Jarolimek, K.; Telesz, N.; Anthony, J. E.; Risko, C.; Loo, Y.-L., Impact of Atomistic Substitution on Thin-Film Structure and Charge Transport in a Germanyl-ethynyl Functionalized Pentacene. *Chemistry of Materials* **2019,** *31* (17), 6615-6623.

19.   Newman, C. R.; Frisbie, C. D.; da Silva Filho, D. A.; Brédas, J.-L.; Ewbank, P. C.; Mann, K. R., Introduction to Organic Thin Film Transistors and Design of n-Channel Organic Semiconductors. *Chemistry of Materials* **2004,** *16* (23), 4436-4451.

20.   Bredas, J. L., Yang, H., Someya, T., Horowitz, G., Podzorov, V., Loo, Y.L., Shin, T., Malliaras, G., Arias, A., Frisbie, C., Torsi, L., Kane, M., Katz, H., DeLongchamp, D., Sirringhaus, H., Wang, L., Maliakal, A., *Organic Field Effect Transistors*. CRC Press Taylor and Francis Group: 2007.

21.   Smith, J.; Hamilton, R.; McCulloch, I.; Stingelin-Stutzmann, N.; Heeney, M.; Bradley, D. D. C.; Anthopoulos, T. D., Solution-processed organic transistors based on semiconducting blends. *Journal of Materials Chemistry* **2010,** *20* (13), 2562-2574.

22.   Lee, W. H.; Park, Y. D., Organic Semiconductor/Insulator Polymer Blends for High-Performance Organic Transistors. *Polymers* **2014,** *6* (4), 1057-1073.

23.   Virkar, A. A.; Mannsfeld, S.; Bao, Z.; Stingelin, N., Organic Semiconductor Growth and Morphology Considerations for Organic Thin-Film Transistors. *Advanced materials* **2010,** *22* (34), 3857-3875.

24.   Jiang, L.; Fu, Y.; Li, H.; Hu, W., Single-Crystalline, Size, and Orientation Controllable Nanowires and Ultralong Microwires of Organic Semiconductor with Strong Photoswitching Property. *Journal of the American Chemical Society* **2008,** *130* (12), 3937-3941.

25.   Jones, B. A.; Ahrens, M. J.; Yoon, M.-H.; Facchetti, A.; Marks, T. J.; Wasielewski, M. R., High-Mobility Air-Stable n-Type Semiconductors with Processing

Versatility: Dicyanoperylene-3,4:9,10-bis(dicarboximides). *Angewandte Chemie International Edition* **2004,** *43* (46), 6363-6366.

26. Kelley, T. W.; Baude, P. F.; Gerlach, C.; Ender, D. E.; Muyres, D.; Haase, M. A.; Vogel, D. E.; Theiss, S. D., Recent Progress in Organic Electronics: Materials, Devices, and Processes. *Chemistry of Materials* **2004,** *16* (23), 4413-4422.

27. Laquindanum, J. G.; Katz, H. E.; Dodabalapur, A.; Lovinger, A. J., n-Channel Organic Transistor Materials Based on Naphthalene Frameworks. *Journal of the American Chemical Society* **1996,** *118* (45), 11331-11332.

28. Ostroverkhova, O.; Cooke, D. G.; Hegmann, F. A.; Anthony, J. E.; Podzorov, V.; Gershenson, M. E.; Jurchescu, O. D.; Palstra, T. T. M., Ultrafast carrier dynamics in pentacene, functionalized pentacene, tetracene, and rubrene single crystals. *Applied Physics Letters* **2006,** *88* (16), 162101.

29. Sung, A.; Ling, M. M.; Tang, M. L.; Bao, Z.; Locklin, J., Correlating Molecular Structure to Field-Effect Mobility: The Investigation of Side-Chain Functionality in Phenylene−Thiophene Oligomers and Their Application in Field Effect Transistors. *Chemistry of Materials* **2007,** *19* (9), 2342-2351.

30. Tang, M. L.; Okamoto, T.; Bao, Z., High-Performance Organic Semiconductors: Asymmetric Linear Acenes Containing Sulphur. *Journal of the American Chemical Society* **2006,** *128* (50), 16002-16003.

31. Tang, M. L.; Roberts, M. E.; Locklin, J. J.; Ling, M. M.; Meng, H.; Bao, Z., Structure Property Relationships: Asymmetric Oligofluorene−Thiophene Molecules for Organic TFTs. *Chemistry of Materials* **2006,** *18* (26), 6250-6257.

32. Tang, Q.; Jiang, L.; Tong, Y.; Li, H.; Liu, Y.; Wang, Z.; Hu, W.; Liu, Y.; Zhu, D., Micrometer- and Nanometer-Sized Organic Single-Crystalline Transistors. *Advanced materials* **2008,** *20* (15), 2947-2951.

33. Tang, Z.; Wang, Y.; Podsiadlo, P.; Kotov, N. A., Biomedical Applications of Layer-by-Layer Assembly: From Biomimetics to Tissue Engineering. *Advanced materials* **2006,** *18* (24), 3203-3224.

34. Li, R.; Khan, H. U.; Payne, M. M.; Smilgies, D.-M.; Anthony, J. E.; Amassian, A., Heterogeneous Nucleation Promotes Carrier Transport in Solution-Processed Organic Field-Effect Transistors. *Advanced Functional Materials* **2013,** *23* (3), 291-297.

35. Velardez, G. F.; Alavi, S.; Thompson, D. L., Molecular dynamics studies of melting and solid-state transitions of ammonium nitrate. *The Journal of Chemical Physics* **2004,** *120* (19), 9151-9159.

36. Halls, J. J. M.; Walsh, C. A.; Greenham, N. C.; Marseglia, E. A.; Friend, R. H.; Moratti, S. C.; Holmes, A. B., Efficient photodiodes from interpenetrating polymer networks. *Nature* **1995,** *376*, 498.

37. Yu, G.; J.Gao; C.Hummelen, J.; Wudl, F.; Heeger, A. J., Ploymer Photovoltaic Cells: Enhanced Efficiencies via a Network of Internal Donor-Acceptor Heterojunctions. *Science* **1995,** *270*, 1789.

38.   Peet, J.; Kim, J. Y.; Coates, N. E.; Ma, W. L.; Moses, D.; Heeger, A. J.; Bazan, G. C., Efficiency enhancement in low-bandgap polymer solar cells by processing with alkane dithiols. *Nature materials* **2007,** *6* (7), 497-500.

39.   Yao, Y.; Hou, J.; Xu, Z.; Li, G.; Yang, Y., Effects of Solvent Mixtures on the Nanoscale Phase Separation in Polymer Solar Cells. *Advanced Functional Materials* **2008,** *18* (12), 1783-1789.

40.   Liu, J.; Walker, B.; Tamayo, A.; Zhang, Y.; Nguyen, T.-Q., Effects of Heteroatom Substitutions on the Crystal Structure, Film Formation, and Optoelectronic Properties of Diketopyrrolopyrrole-Based Materials. *Adv. Funct. Mater.* **2013,** *23* (1), 47-56.

41.   Liao, H.-C.; Ho, C.-C.; Chang, C.-Y.; Jao, M.-H.; Darling, S. B.; Su, W.-F., Additives for morphology control in high-efficiency organic solar cells. *Materials Today* **2013,** *16* (9), 326-336.

42.   Perez, L. A.; Rogers, J. T.; Brady, M. A.; Sun, Y.; Welch, G. C.; Schmidt, K.; Toney, M. F.; Jinnai, H.; Heeger, A. J.; Chabinyc, M. L.; Bazan, G. C.; Kramer, E. J., The Role of Solvent Additive Processing in High Performance Small Molecule Solar Cells. *Chemistry of Materials* **2014,** *26* (22), 6531-6541.

43.   Kwon, S.; Kang, H.; Lee, J.-H.; Lee, J.; Hong, S.; Kim, H.; Lee, K., Effect of Processing Additives on Organic Photovoltaics: Recent Progress and Future Prospects. *Advanced Energy Materials* **2017,** *7* (10), 1601496.

44.   Zhao, W.; Zhang, S.; Zhang, Y.; Li, S.; Liu, X.; He, C.; Zheng, Z.; Hou, J., Environmentally Friendly Solvent-Processed Organic Solar Cells that are Highly Efficient and Adaptable for the Blade-Coating Method. *Adv Mater* **2018,** *30* (4).

45.   Liang, Y.; Xu, Z.; Xia, J.; Tsai, S.-T.; Wu, Y.; Li, G.; Ray, C.; Yu, L., For the Bright Future—Bulk Heterojunction Polymer Solar Cells with Power Conversion Efficiency of 7.4%. *Advanced materials* **2010,** *22* (20), E135-E138.

46.   Lou, S. J.; Szarko, J. M.; Xu, T.; Yu, L.; Marks, T. J.; Chen, L. X., Effects of Additives on the Morphology of Solution Phase Aggregates Formed by Active Layer Components of High-Efficiency Organic Solar Cells. *Journal of the American Chemical Society* **2011,** *133* (51), 20661-20663.

47.   Giri, G.; Li, R.; Smilgies, D.-M.; Li, E. Q.; Diao, Y.; Lenn, K. M.; Chiu, M.; Lin, D. W.; Allen, R.; Reinspach, J.; Mannsfeld, S. C. B.; Thoroddsen, S. T.; Clancy, P.; Bao, Z.; Amassian, A., One-dimensional self-confinement promotes polymorph selection in large-area organic semiconductor thin films. *Nature communications* **2014,** *5* (1), 3573.

48.   Niazi, M. R.; Li, R.; Qiang Li, E.; Kirmani, A. R.; Abdelsamie, M.; Wang, Q.; Pan, W.; Payne, M. M.; Anthony, J. E.; Smilgies, D.-M.; Thoroddsen, S. T.; Giannelis, E. P.; Amassian, A., Solution-printed organic semiconductor blends exhibiting transport properties on par with single crystals. *Nature communications* **2015,** *6* (1), 8598.

Chapter 2 References

1.   Kanimozhi, C.; Yaacobi-Gross, N.; Burnett, E. K.; Briseno, A. L.; Anthopoulos, T. D.; Salzner, U.; Patil, S., Use of side-chain for rational design of n-type diketopyrrolopyrrole-based conjugated polymers: what did we find out? *Physical Chemistry Chemical Physics* **2014,** *16* (32), 17253-17265.

2.   Yost, S. R.; Wang, L.-P.; Van Voorhis, T., Molecular Insight Into the Energy Levels at the Organic Donor/Acceptor Interface: A Quantum Mechanics/Molecular Mechanics Study. *The Journal of Physical Chemistry C* **2011,** *115* (29), 14431-14436.

3.   Mosconi, E.; Azpiroz, J. M.; De Angelis, F., Ab Initio Molecular Dynamics Simulations of Methylammonium Lead Iodide Perovskite Degradation by Water. *Chemistry of Materials* **2015,** *27* (13), 4885-4892.

4.   van Speybroeck, V.; Meier, R. J., A recent development in computational chemistry: chemical reactions from first principles molecular dynamics simulations. *Chemical Society Reviews* **2003,** *32* (3), 151-157.

5.   Niu, S.; Hall, M. B., Theoretical Studies on Reactions of Transition-Metal Complexes. *Chemical Reviews* **2000,** *100* (2), 353-406.

6.   Torrent, M.; Solà, M.; Frenking, G., Theoretical Studies of Some Transition-Metal-Mediated Reactions of Industrial and Synthetic Importance. *Chemical Reviews* **2000,** *100* (2), 439-494.

7.   Feynman, R. P., *The Feynman lectures on physics*. Reading, Mass. : Addison-Wesley Pub. Co., c1963-1965.: 1963.

8.   Vanommeslaeghe, K.; Guvench, O.; MacKerell, A. D., Jr., Molecular mechanics. *Curr Pharm Des* **2014,** *20* (20), 3281-3292.

9.   Warshel, A.; Levitt, M., Theoretical studies of enzymic reactions: Dielectric, electrostatic and steric stabilization of the carbonium ion in the reaction of lysozyme. *Journal of Molecular Biology* **1976,** *103* (2), 227-249.

10.   Gaunt, J. A., A Theory of Hartree's Atomic Fields. *Mathematical Proceedings of the Cambridge Philosophical Society* **1928,** *24* (2), 328-342.

11.   Becke, A. D., Perspective: Fifty years of density-functional theory in chemical physics. **2014,** *140* (18), 18A301.

12.   Kawanabe, Y.; Moulé, A. J.; Faller, R., Molecular Dynamics Study of the Local Structure of Photovoltaic Polymer PCDTBT. *J. Chem. Eng. Data* **2014,** *59* (10), 2982-2986.

13.   Bernardes, C. E.; Joseph, A., Evaluation of the OPLS-AA force field for the study of structural and energetic aspects of molecular organic crystals. *The journal of physical chemistry. A* **2015,** *119* (12), 3023-3034.

14.   Bernardes, C. E. S.; Joseph, A., Evaluation of the OPLS-AA Force Field for the Study of Structural and Energetic Aspects of Molecular Organic Crystals. *The Journal of Physical Chemistry A* **2015,** *119* (12), 3023-3034.

15.   William L. Jorgensen, D. S. M., Julian Tirado-Rives, Development and Testing of the OPLS All-Atom Force Field on Conformational Energetics and Properties of Organic Liquids. *J. Am. Chem. Soc* **1996,** *118*, 11225-11236.

16.   Jorgensen, W. L.; Maxwell, D. S.; Tirado-Rives, J., Development and Testing of the OPLS All-Atom Force Field on Conformational Energetics and Properties of Organic Liquids. *J. Am. Chem. Soc.* **1996,** *118*, 11225-11236.

17.   Jorgensen, W. L.; Tirado-Rives, J., The OPLS [optimized potentials for liquid simulations] potential functions for proteins, energy minimizations for crystals of cyclic peptides and crambin. *Journal of the American Chemical Society* **1988,** *110* (6), 1657-1666.

18.   Jorgensen, W. L.; Tirado-Rives, J., Potential energy functions for atomic-level simulations of water and organic and biomolecular systems. *Proceedings of the National Academy of Sciences of the United States of America* **2005,** *102* (19), 6665-6670.

19.   Berendsen, H. J. C.; Vanderspoel, D.; Vandrunen, R., GROMACS: A message-passing parallel molecular dynamics implementation. *Comput. Phys. Commun.* **1995,** *91*, 43-56.

20.   Hess, B.; Kutzner, C.; Spoel, D. v. d.; Lindahl, E., GROMACS 4: Algorithms for Highly Efficient, Load-Balanced, and Scalable Molecular Simulation. *J. Chem. Theory Comput.* **2008,** *4* (3), 435-447.

21.   Jorgensen, W. L.; Schyman, P., Treatment of Halogen Bonding in the OPLS-AA Force Field; Application to Potent Anti-HIV Agents. *Journal of chemical theory and computation* **2012,** *8* (10), 3895-3801.

22.   Kutzner, C.; van der Spoel, D.; Fechner, M.; Lindahl, E.; Schmitt, U. W.; de Groot, B. L.; Grubmuller, H., Speeding up parallel GROMACS on high-latency networks. *Journal of computational chemistry* **2007,** *28* (12), 2075-2084.

23.   Plimpton, S., Fast Parallel Algorithms for Short-Range Molecular Dynamics. *Journal of Computational Physics* **1995,** *117* (1), 1-19.

24.   Berendsen, H. J. C.; Postma, J. P. M.; Gunsteren, W. F. v.; DiNola, A.; Haak, J. R., Molecular dynamics with coupling to an external bath. *The Journal of Chemical Physics* **1984,** *81* (8), 3684-3690.

25.   Parrinello, M.; Rahman, A., Polymorphic transitions in single crystals: A new molecular dynamics method. *Journal of Applied Physics* **1981,** *52* (12), 7182-7190.

26.   Essmann, U.; Perera, L.; Berkowitz, M. L.; Darden, T.; Lee, H.; Pedersen, L. G., A smooth particle mesh Ewald method. *The Journal of Chemical Physics* **1995,** *103* (19), 8577-8593.

27.   Torrie, G. M.; Valleau, J. P., Nonphysical sampling distributions in Monte Carlo free-energy estimation: Umbrella sampling. *Journal of Computational Physics* **1977,** *23* (2), 187-199.

28.   Kumar, S.; Bouzida, D.; Swendsen, R. H.; Kollman, P. A.; Rosenberg, J. M., The Weighted Histogram Analysis Method for Free-Energy Calculations on Biomolecules. I. The Method. *Journal of computational chemistry* **1992,** *13* (8), 1011-1021.

29.   Roux, B., The calculation of the potential of mean force using computer simulations. *Comput. Phys. Commun.* **1995,** *91*, 275-282.

30.   Hildebrand, J. H.; Scott, R. L., The Entropy of Solution of Nonelectrolytes. *The Journal of Chemical Physics* **1952,** *20* (10), 1520-1521.

31.   Hansen, C. M., The Three Disensional Solubility Parameter and Solvent Diffusion Coefficient. *Journal of Paint Technology* **1967,** *39* (104).

32.   Belmares, M.; Blanco, M.; Goddard, W. A., 3rd; Ross, R. B.; Caldwell, G.; Chou, S. H.; Pham, J.; Olofson, P. M.; Thomas, C., Hildebrand and Hansen solubility parameters from molecular dynamics with applications to electronic nose polymer sensors. *J Comput Chem* **2004,** *25* (15), 1814-26.

33. Tummala, N. R.; Mehraeen, S.; Fu, Y.-T.; Risko, C.; Brédas, J.-L., Materials-Scale Implications of Solvent and Temperature on [6,6]-Phenyl-C61-butyric Acid Methyl Ester (PCBM): A Theoretical Perspective. *Advanced Functional Materials* **2013,** *23* (46), 5800-5813.

34. Zhang, Y.; Voth, G. A., Combined Metadynamics and Umbrella Sampling Method for the Calculation of Ion Permeation Free Energy Profiles. *Journal of Chemical Theory and Computation* **2011,** *7* (7), 2277-2283.

35. Widom, B., Some Topics in the Theory of Fluids. *The Journal of Chemical Physics* **1963,** *39* (11), 2808-2812.

36. Kofke, D. A., Gibbs-Duhem integration: a new method for direct evaluation of phase coexistence by molecular simulation. *Molecular Physics* **1993,** *78* (6), 1331-1336.

37. Lai, P. K.; Hsieh, C. M.; Lin, S. T., Rapid determination of entropy and free energy of mixtures from molecular dynamics simulations with the two-phase thermodynamic model. *Phys Chem Chem Phys* **2012,** *14* (43), 15206-13.

38. Lin, S.-T.; Blanco, M.; Goddard, W. A., The two-phase model for calculating thermodynamic properties of liquids from molecular dynamics: Validation for the phase diagram of Lennard-Jones fluids. *The Journal of Chemical Physics* **2003,** *119* (22), 11792-11805.

39. Michael P. Allen, D. J. T., *Computer simulation of liquids*. 2 ed.; Oxford: Oxford University Press, 2017.

40. Pascal, T. A.; Goddard, W. A., Hydrophobic Segregation, Phase Transitions and the Anomalous Thermodynamics of Water/Methanol Mixtures. *The Journal of Physical Chemistry B* **2012,** *116* (47), 13905-13912.

41. Zhang, H.; Duquesne, M.; Godin, A.; Niedermaier, S.; Palomo del Barrio, E.; Nedea, S. V.; Rindt, C. C. M., Experimental and in silico characterization of xylitol as seasonal heat storage material. *Fluid Phase Equilibria* **2017,** *436*, 55-68.

42. Minakov, D. V.; Levashov, P. R.; Fokin, V. B., Vibrational spectrum and entropy in simulation of melting. *Computational Materials Science* **2017,** *127*, 42-47.

43. Vadhana, V.; Ayappa, K. G., Structure and Dynamics of Octamethylcyclotetrasiloxane Confined between Mica Surfaces. *J Phys Chem B* **2016,** *120* (11), 2951-67.

44. Lim, H. K.; Lee, H.; Kim, H., A Seamless Grid-Based Interface for Mean-Field QM/MM Coupled with Efficient Solvation Free Energy Calculations. *J Chem Theory Comput* **2016,** *12* (10), 5088-5099.

45. Caro, M. A.; Laurila, T.; Lopez-Acevedo, O., Accurate schemes for calculation of thermodynamic properties of liquid mixtures from molecular dynamics simulations. *J Chem Phys* **2016,** *145* (24), 244504.

46. Wang, J.; Chakraborty, B.; Eapen, J., Absolute thermodynamic properties of molten salts using the two-phase thermodynamic (2PT) superpositioning method. *Phys Chem Chem Phys* **2014,** *16* (7), 3062-9.

47. Pascal, T. A.; Goddard, W. A., 3rd, Interfacial thermodynamics of water and six other liquid solvents. *J Phys Chem B* **2014,** *118* (22), 5943-56.

48. Lai, P.-K.; Lin, S.-T., Rapid determination of entropy for flexible molecules in condensed phase from the two-phase thermodynamic model. *RSC Advances* **2014,** *4* (19).

49.	Chen, M.; Pendrill, R.; Widmalm, G.; Brady, J. W.; Wohlert, J., Molecular Dynamics Simulations of the Ionic Liquid 1-n-Butyl-3-Methylimidazolium Chloride and Its Binary Mixtures with Ethanol. *J Chem Theory Comput* **2014,** *10* (10), 4465-79.

50.	Li, C.; Medvedev, G. A.; Lee, E.-W.; Kim, J.; Caruthers, J. M.; Strachan, A., Molecular dynamics simulations and experimental studies of the thermomechanical response of an epoxy thermoset polymer. *Polymer* **2012,** *53* (19), 4222-4230.

51.	Jeon, J.; Kim, H.; Goddard, W. A., 3rd; Pascal, T. A.; Lee, G. I.; Kang, J. K., The Role of Confined Water in Ionic Liquid Electrolytes for Dye-Sensitized Solar Cells. *J Phys Chem Lett* **2012,** *3* (4), 556-9.

52.	Caleman, C.; van Maaren, P. J.; Hong, M.; Hub, J. S.; Costa, L. T.; van der Spoel, D., Force Field Benchmark of Organic Liquids: Density, Enthalpy of Vaporization, Heat Capacities, Surface Tension, Isothermal Compressibility, Volumetric Expansion Coefficient, and Dielectric Constant. *J Chem Theory Comput* **2012,** *8* (1), 61-74.

53.	Pascal, T. A.; Lin, S. T.; Goddard, W. A., 3rd, Thermodynamics of liquids: standard molar entropies and heat capacities of common solvents from 2PT molecular dynamics. *Phys Chem Chem Phys* **2011,** *13* (1), 169-81.

54.	Pascal, T. A.; He, Y.; Jiang, S.; Goddard, W. A., Thermodynamics of Water Stabilization of Carboxybetaine Hydrogels from Molecular Dynamics Simulations. *The Journal of Physical Chemistry Letters* **2011,** *2* (14), 1757-1760.

55.	Huang, S. N.; Pascal, T. A.; Goddard, W. A., 3rd; Maiti, P. K.; Lin, S. T., Absolute Entropy and Energy of Carbon Dioxide Using the Two-Phase Thermodynamic Model. *J Chem Theory Comput* **2011,** *7* (6), 1893-901.

56.	Berens, P. H.; Mackay, D. H. J.; White, G. M.; Wilson, K. R., Thermodynamics and quantum corrections from molecular dynamics for liquid water. *The Journal of Chemical Physics* **1983,** *79* (5), 2375-2389.

57.	Caro, M. A.; Laurila, T.; Lopez-Acevedo, O., Accurate schemes for calculation of thermodynamic properties of liquid mixtures from molecular dynamics simulations. *J. Chem. Phys.* **2016,** *145* (24), 244504.

58.	Caro, M. A.; Lopez-Acevedo, O.; Laurila, T., Redox Potentials from Ab Initio Molecular Dynamics and Explicit Entropy Calculations: Application to Transition Metals in Aqueous Solution. *Journal of Chemical Theory and Computation* **2017,** *13* (8), 3432-3441.

59.	Bennett, C. H., Efficient estimation of free energy differences from Monte Carlo data. *Journal of Computational Physics* **1976,** *22* (2), 245-268.

60.	Dewar, A.; Camp, P. J., Computer simulations of bent-core liquid crystals. *Physical review. E, Statistical, nonlinear, and soft matter physics* **2004,** *70* (1 Pt 1), 011704.

61.	Goldstein, H.; Poole, C.; Safko, J., *Classical Mechanics*. 3 ed.; Addison-Wesley: London, 2001.

62.	Thomas, L. H., The calculation of atomic fields. *Mathematical Proceedings of the Cambridge Philosophical Society* **1927,** *23* (5), 542-548.

63.	Hohenberg, P.; Kohn, W., Inhomogeneous Electron Gas. *Physical Review* **1964,** *136* (3B), B864-B871.

64.	Kohn, W.; Sham, L. J., Self-Consistent Equations Including Exchange and Correlation Effects. *Physical Review* **1965,** *140* (4A), A1133-A1138.

65.	Dirac, P. A. M., Note on Exchange Phenomena in the Thomas Atom. *Mathematical Proceedings of the Cambridge Philosophical Society* **1930,** *26* (3), 376-385.

66.   Slater, J. C., A Simplification of the Hartree-Fock Method. *Physical Review* **1951,** *81* (3), 385-390.

67.   Perdew, J. P.; Yue, W., Accurate and simple density functional for the electronic exchange energy: Generalized gradient approximation. *Physical Review B* **1986,** *33* (12), 8800-8802.

68.   Perdew, J. P.; Burke, K.; Ernzerhof, M., Generalized Gradient Approximation Made Simple. *Physical Review Letters* **1996,** *77* (18), 3865-3868.

69.   Lee, C.; Yang, W.; Parr, R. G., Development of the Colle-Salvetti correlation-energy formula into a functional of the electron density. *Physical Review B* **1988,** *37* (2), 785-789.

70.   Armiento, R.; Mattsson, A. E., Functional designed to include surface effects in self-consistent density functional theory. *Physical Review B* **2005,** *72* (8), 085108.

71.   Sun, G.; Kürti, J.; Rajczy, P.; Kertesz, M.; Hafner, J.; Kresse, G., Performance of the Vienna ab initio simulation package (VASP) in chemical applications. *Journal of Molecular Structure: THEOCHEM* **2003,** *624* (1), 37-45.

72.   Perdew, J. P.; Ruzsinszky, A.; Csonka, G. I.; Vydrov, O. A.; Scuseria, G. E.; Constantin, L. A.; Zhou, X.; Burke, K., Restoring the Density-Gradient Expansion for Exchange in Solids and Surfaces. *Physical Review Letters* **2008,** *100* (13), 136406.

73.   Tao, J.; Perdew, J. P.; Staroverov, V. N.; Scuseria, G. E., Climbing the Density Functional Ladder: Nonempirical Meta--Generalized Gradient Approximation Designed for Molecules and Solids. *Physical Review Letters* **2003,** *91* (14), 146401.

74.   Becke, A. D., A new mixing of Hartree‐Fock and local density‐functional theories. **1993,** *98* (2), 1372-1377.

75.   Perdew, J. P.; Ernzerhof, M.; Burke, K., Rationale for mixing exact exchange with density functional approximations. **1996,** *105* (22), 9982-9985.

76.   Zhao, Y.; Truhlar, D. G., Density Functionals with Broad Applicability in Chemistry. *Accounts of Chemical Research* **2008,** *41* (2), 157-167.

77.   Iikura, H.; Tsuneda, T.; Yanai, T.; Hirao, K., A long-range correction scheme for generalized-gradient-approximation exchange functionals. **2001,** *115* (8), 3540-3544.

78.   Toulouse, J.; Colonna, F.; Savin, A., Long-range--short-range separation of the electron-electron interaction in density-functional theory. *Physical Review A* **2004,** *70* (6), 062505.

79.   Yanai, T.; Tew, D. P.; Handy, N. C., A new hybrid exchange–correlation functional using the Coulomb-attenuating method (CAM-B3LYP). *Chemical Physics Letters* **2004,** *393* (1), 51-57.

80.   Brémond, É.; Pérez-Jiménez, Á. J.; Sancho-García, J. C.; Adamo, C., Range-separated hybrid density functionals made simple. **2019,** *150* (20), 201102.

81.   Day, P. N.; Pachter, R.; Nguyen, K. A., Analysis of nonlinear optical properties in donor–acceptor materials. **2014,** *140* (18), 184308.

82.   Chai, J.-D.; Head-Gordon, M., Long-range corrected hybrid density functionals with damped atom–atom dispersion corrections. *Physical Chemistry Chemical Physics* **2008,** *10* (44), 6615-6620.

83.   Kendall, R. A.; Jr., T. H. D.; Harrison, R. J., Electron affinities of the first‐row atoms revisited. Systematic basis sets and wave functions. **1992,** *96* (9), 6796-6806.

84.   Woon, D. E.; Jr., T. H. D., Gaussian basis sets for use in correlated molecular calculations. III. The atoms aluminum through argon. **1993,** *98* (2), 1358-1371.

85.   Runge, E.; Gross, E. K. U., Density-Functional Theory for Time-Dependent Systems. *Physical Review Letters* **1984,** *52* (12), 997-1000.

86.   Martin, R. L., Natural transition orbitals. **2003,** *118* (11), 4775-4777.

87.   Amos, A. T.; Hall, G. G.; Jones, H., Single determinant wave functions. **1961,** *263* (1315), 483-493.

Chapter 3 References

1.   Takahashi, N.; Hikosaka, M.; Yamamoto, T., Computer Simulation of Melting of Polymer Crystals. *Phys. B* **1996,** *219-220*, 420-422.

2.   Arnstein, S. A.; Sherrill, C. D., Substituent effects in parallel-displaced pi-pi interactions. *Phys. Chem. Chem. Phys.* **2008,** *10* (19), 2646-55.

3.   Tsuzuki, S.; Honda, K.; Azumi, R., Model Chemistry Calculations of Thiophene Dimer Interactions: Origin of π-Stacking. *J. Am. Chem. Soc.* **2002,** *124* (41), 12200-12209.

4.   Hohenstein, E. G.; Sherrill, C. D., Effects of Heteroatoms on Aromatic π−π Interactions: Benzene−Pyridine and Pyridine Dimer. *J. Phys. Chem. A* **2009,** *113* (5), 878-886.

5.   Hohenstein, E. G.; Duan, J.; Sherrill, C. D., Origin of the Surprising Enhancement of Electrostatic Energies by Electron-Donating Substituents in Substituted Sandwich Benzene Dimers. *J. Am. Chem. Soc.* **2011,** *133* (34), 13244-13247.

6.   Wheeler, S. E.; Bloom, J. W., Anion-pi Interactions and Positive Electrostatic Potentials of N-heterocycles Arise from the Positions of the Nuclei, not Changes in the pi-electron Distribution. *Chem. Commun.* **2014,** *50* (76), 11118-21.

7.   Sutton, C.; Risko, C.; Brédas, J.-L., Noncovalent Intermolecular Interactions in Organic Electronic Materials: Implications for the Molecular Packing vs Electronic Properties of Acenes. *Chem. Mater.* **2016,** *28* (1), 3-16.

8.   Hallani, R. K.; Thorley, K. J.; Mei, Y.; Parkin, S. R.; Jurchescu, O. D.; Anthony, J. E., Structural and Electronic Properties of Crystalline, Isomerically Pure Anthradithiophene Derivatives. *Adv. Funct. Mater.* **2016,** *26* (14), 2341-2348.

9.   Gryn'ova, G.; Corminboeuf, C., Noncovalent Molecular Electronics. *J. Phys. Chem. Lett.* **2018,** *9* (9), 2298-2304.

10.   Jeziorski, B.; Moszynski, R.; Szalewicz, K., Perturbation Theory Approach to Intermolecular Potential Energy Surfaces of van der Waals Complexes. *Chem. Rev.* **1994,** *94* (7), 1887-1930.

11.   Sinnokrot, M. O.; Sherrill, C. D., Highly Accurate Coupled Cluster Potential Energy Curves for the Benzene Dimer: Sandwich, T-Shaped, and Parallel-Displaced Configurations. *The journal of physical chemistry. A* **2004,** *108* (46), 10200-10207.

12.   Sinnokrot, M. O.; Sherrill, C. D., Substituent Effects in π−π Interactions: Sandwich and T-Shaped Configurations. *J. Am. Chem. Soc.* **2004,** *126* (24), 7690-7697.

13.   Podeszwa, R.; Bukowski, R.; Szalewicz, K., Potential Energy Surface for the Benzene Dimer and Perturbational Analysis of π−π Interactions. *The journal of physical chemistry. A* **2006,** *110* (34), 10345-10354.

14.   Ringer, A. L.; Figgs, M. S.; Sinnokrot, M. O.; Sherrill, C. D., Aliphatic C−H/π Interactions: Methane−Benzene, Methane−Phenol, and Methane−Indole Complexes. *The journal of physical chemistry. A* **2006,** *110* (37), 10822-10828.

15.   Sinnokrot, M. O.; Sherrill, C. D., High-Accuracy Quantum Mechanical Studies of π−π Interactions in Benzene Dimers. *The journal of physical chemistry. A* **2006,** *110* (37), 10656-10668.

16.   Podeszwa, R.; Szalewicz, K., Physical Origins of Interactions in Dimers of Polycyclic Aromatic Hydrocarbons. *Phys. Chem. Chem. Phys.* **2008,** *10* (19), 2735-46.

17. Wheeler, S. E.; Houk, K. N., Substituent Effects in the Benzene Dimer are Due to Direct Interactions of the Substituents with the Unsubstituted Benzene. *J. Am. Chem. Soc.* **2008,** *130* (33), 10854-10855.

18. Wheeler, S. E.; McNeil, A. J.; Müller, P.; Swager, T. M.; Houk, K. N., Probing Substituent Effects in Aryl−Aryl Interactions Using Stereoselective Diels−Alder Cycloadditions. *J. Am. Chem. Soc.* **2010,** *132* (10), 3304-3311.

19. Wheeler, S. E., Understanding Substituent Effects in Noncovalent Interactions Involving Aromatic Rings. *Acc. Chem. Res.* **2013,** *46* (4), 1029-1038.

20. Kirkland-York, S.; Gallow, K.; Ray, J.; Loob, Y.-l.; McCormick, C., Temperature-Induced Ordering and Gelation of Star Micelles based on ABA Triblocks Synthesized via Aqueous RAFT Polymerization. *Soft Matter* **2009,** *5*, 2179-2182

21. Beckingham, B. S.; Ho, V.; Segalman, R. A., Melting Behavior of Poly(3-(2′-ethyl)hexylthiophene). *Macromolecules* **2014,** *47* (23), 8305-8310.

22. Treat, N. D.; Westacott, P.; Stingelin, N., The Power of Materials Science Tools for Gaining Insights into Organic Semiconductors. *Annu. Rev. Mater. Res.* **2015,** *45* (1), 459-490.

23. Yu, L.; Davidson, E.; Sharma, A.; Andersson, M. R.; Segalman, R.; Muller, C., Isothermal Crystallization Kinetics and Time-Temperature-Transformation of the Conjugated Polymer: Poly(3-(2'-ethyl)hexylthiophene). *Chem. Mater.* **2017,** *29* (13), 5654-5662.

24. Heinz, H.; Vaia, R. A.; Farmer, B. L., Relation between Packing Density and Thermal Transitions of Alkyl Chains on Layered Silicate and Metal Surfaces. *Langmuir* **2008,** *24* (8), 3727-3733.

25. Antony, L. W.; Jackson, N. E.; Lyubimov, I.; Vishwanath, V.; Ediger, M. D.; de Pablo, J. J., Influence of Vapor Deposition on Structural and Charge Transport Properties of Ethylbenzene Films. *ACS Cent. Sci.* **2017,** *3* (5), 415-424.

26. Root, S. E.; Jackson, N. E.; Savagatrup, S.; Arya, G.; Lipomi, D. J., Modelling the Morphology and Thermomechanical Behaviour of Low-Bandgap Conjugated Polymers and Bulk Heterojunction Films. *Energy Environ. Sci.* **2017,** *10* (2), 558-569.

27. Soldera, A., Comparison Between the Glass Transition Temperatures of the Two PMMA Tacticities: A Molecular Dynamics Simulation Point of View. *Maromol. Symp.* **1998,** *133*, 21-32.

28. Watt, S. W.; Chisholm, J. A.; Jones, W.; Motherwell, S., A Molecular Dynamics Simulation of the Melting Points and Glass Transition Temperatures of myo- and neo-Inositol. *J. Chem. Phys.* **2004,** *121* (19), 9565-9573.

29. Root, S. E.; Savagatrup, S.; Printz, A. D.; Rodriquez, D.; Lipomi, D. J., Mechanical Properties of Organic Semiconductors for Stretchable, Highly Flexible, and Mechanically Robust Electronics. *Chem. Rev.* **2017,** *117* (9), 6467-6499.

30. Lu, K.; Li, Y., Homogeneous Nucleation Catastrophe as a Kinetic Stability Limit for Superheated Crystal. *Phys. Rev. Lett.* **1998,** *80* (20), 4474-4477.

31. Luo, S.-N.; Ahrens, T. J., Superheating Systematics of Crystalline Solids. *Appl. Phys. Lett.* **2003,** *82* (12), 1836-1838.

32. Chen, Q.; Sirota, E. B.; Zhang, M.; Chung, T. C. M.; Milner, S. T., Free Surfaces Overcome Superheating in Simulated Melting of Isotactic Polypropylene. *Macromolecules* **2015,** *48* (24), 8885-8896.

33. Velardez, G. F.; Alavi, S.; Thompson, D. L., Molecular Dynamics Studies of Melting and Solid-State Transitions of Ammonium Nitrate. *J. Chem. Phys.* **2004,** *120* (19), 9151-9.

34. Jayaraman, S.; Maginn, E. J., Computing the Melting Point and Thermodynamic Stability of the Orthorhombic and Monoclinic Crystalline Polymorphs of the Ionic Liquid 1-n-butyl-3-methylimidazolium Chloride. *J. Chem. Phys.* **2007,** *127* (21), 214504.

35. Takahashi, N.; Yamamoto, T.; Hikosaka, M., Surface Melting of an n-Alkane Crystallite. *Prog. Theor. Phys. Suppl.* **2000,** *138*, 414-415.

36. Laquindanum, J. G.; Katz, H. E.; Lovinger, A. J., Synthesis, Morphology, and Field-Effect Mobility of Anthradithiophenes. *J. Am. Chem. Soc.* **1998,** *120* (4), 664-672.

37. Payne, M. M.; Odom, S. A.; Parkin, S. R.; Anthony, J. E., Stable, Crystalline Acenedithiophenes with up to Seven Linearly Fused Rings. *Org. Lett.* **2004,** *6* (19), 3325-3328.

38. Payne, M. M.; Parkin, S. R.; Anthony, J. E.; Kuo, C.-C.; Jackson, T. N., Organic Field-Effect Transistors from Solution-Deposited Functionalized Acenes with Mobilities as High as 1 cm2/V·s. *J. Am. Chem. Soc* **2005,** *127* (14), 4986-4987.

39. Lehnherr, D.; Tykwinski, R. R., Conjugated Oligomers and Polymers Based on Anthracene, Tetracene, Pentacene, Naphthodithiophene, and Anthradithiophene Building Blocks. *Aust. J. Chem.* **2011,** *64* (7), 919-929.

40. Lehnherr, D.; Waterloo, A. R.; Goetz, K. P.; Payne, M. M.; Hampel, F.; Anthony, J. E.; Jurchescu, O. D.; Tykwinski, R. R., Isomerically Pure syn-Anthradithiophenes: Synthesis, Properties, and FET Performance. *Org. Lett.* **2012,** *14* (14), 3660–3663.

41. Berendsen, H. J. C.; Vanderspoel, D.; Vandrunen, R., GROMACS: A message-passing parallel molecular dynamics implementation. *Comput. Phys. Commun.* **1995,** *91*, 43-56.

42. Hess, B.; Kutzner, C.; Spoel, D. v. d.; Lindahl, E., GROMACS 4: Algorithms for Highly Efficient, Load-Balanced, and Scalable Molecular Simulation. *J. Chem. Theory Comput.* **2008,** *4* (3), 435-447.

43. Bernardes, C. E.; Joseph, A., Evaluation of the OPLS-AA force field for the study of structural and energetic aspects of molecular organic crystals. *The journal of physical chemistry. A* **2015,** *119* (12), 3023-3034.

44. William L. Jorgensen, D. S. M., and Julian Tirado-Rives, Development and Testing of the OPLS All-Atom Force Field on Conformational Energetics and Properties of Organic Liquids. *J. Am. Chem. Soc.* **1996,** *118*, 11225-11236.

45. Schwarz, K. N.; Kee, T. W.; Huang, D. M., Coarse-grained simulations of the solution-phase self-assembly of poly(3-hexylthiophene) nanostructures. *Nanoscale* **2013,** *5* (5), 2017-2027.

46. Do, K.; Risko, C.; Anthony, J. E.; Amassian, A.; Brédas, J.-L., Dynamics, Miscibility, and Morphology in Polymer:Molecule Blends: The Impact of Chemical Functionality. *Chem. Mater.* **2015,** *27* (22), 7643-7651.

47. Mamada, M.; Katagiri, H.; Mizukami, M.; Honda, K.; Minamiki, T.; Teraoka, R.; Uemura, T.; Tokito, S., syn-/anti-Anthradithiophene derivative isomer effects on semiconducting properties. *ACS Appl. Mater. Interfaces* **2013,** *5* (19), 9670-9677.

48. Bussi, G.; Donadio, D.; Parrinello, M., Canonical Sampling Through Velocity Rescaling. *J. Chem. Phys.* **2007,** *126* (1), 014101.

49.   Berendsen, H. J. C.; Postma, J. P. M.; van Gunsteren, W. F.; DiNola, A.; Haak, J. R., Molecular Dynamics with Coupling to an External Bath. *J. Chem. Phys.* **1984,** *81* (8), 3684-3690.

50.   Parrinello, M.; Rahman, A., Polymorphic Transitions in Single Crystals: A New Molecular Dynamics Method. *J. Appl. Phys.* **1981,** *52* (12), 7182-7190.

51.   Essmann, U.; Perera, L.; Berkowitz, M. L.; Darden, T.; Lee, H.; Pedersen, L. G., A smooth particle mesh Ewald method. *J. Chem. Phys.* **1995,** *103* (19), 8577-8593.

52.   Kumar, S.; Bouzida, D.; Swendsen, R. H.; Kollman, P. A.; Rosenberg, J. M., The Weighted Histogram Analysis Method for Free-Energy Calculations on Biomolecules. I. The Method. *Journal of computational chemistry* **1992,** *13* (8), 1011-1021.

53.   Palczynski, K.; Heimel, G.; Heyda, J.; Dzubiella, J., Growth and Characterization of Molecular Crystals ofpara-Sexiphenyl by All-Atom Computer Simulations. *Cryst. Growth Des.* **2014,** *14* (8), 3791-3799.

54.   Taylor, R.; Macrae, C. F., Rules governing the crystal packing of mono- and dialcohols. *Acta Crystallographica Section B* **2001,** *57* (6), 815-827.

55.   Bruno, I. J.; Cole, J. C.; Edgington, P. R.; Kessler, M.; Macrae, C. F.; McCabe, P.; Pearson, J.; Taylor, R., New software for searching the Cambridge Structural Database and visualizing crystal structures. *Acta Crystallographica Section B* **2002,** *58* (3 Part 1), 389-397.

56.   Macrae, C. F.; Edgington, P. R.; McCabe, P.; Pidcock, E.; Shields, G. P.; Taylor, R.; Towler, M.; van de Streek, J., Mercury: visualization and analysis of crystal structures. *J. Appl. Crystallogr.* **2006,** *39* (3), 453-457.

57.   Macrae, C. F.; Bruno, I. J.; Chisholm, J. A.; Edgington, P. R.; McCabe, P.; Pidcock, E.; Rodriguez-Monge, L.; Taylor, R.; van de Streek, J.; Wood, P. A., Mercury CSD 2.0 - new features for the visualization and investigation of crystal structures. *Journal of Applied Crystallography* **2008,** *41* (2), 466-470.

58.   Thorley, K. J.; Finn, T. W.; Jarolimek, K.; Anthony, J. E.; Risko, C., Theory-Driven Insight into the Crystal Packing of Trialkylsilylethynyl Pentacenes. *Chem. Mater.* **2016,** *29* (6), 2502-2512.

59.   Ryno, S. M.; Risko, C.; Bredas, J. L., Impact of Molecular Packing on Electronic Polarization in Organic Crystals: the Case of Pentacene vs TIPS-pentacene. *J. Am. Chem. Soc.* **2014,** *136* (17), 6421-6427.

60.   Lutsko, J. F.; Wolf, D.; Phillpot, S. R.; Yip, S., Molecular-Dynamics Study of Lattice-Defect-Nucleated Melting in Metals Using an Embedded-Atom-Method Potential. *Phys. Rev. B* **1989,** *40* (5), 2841-2855.

61.   K. Lu, Y. L., Homogeneous Nucleation Catastrophe as a Kinetic Stability Limit for Superheated Crystal. *Phys. Rev. Lett.* **1998,** *80* (20), 4474-4477.

62.   Zhang, L.; Jin, Z. H.; Zhang, L. H.; Sui, M. L.; Lu, K., Superheating of Confined Pb Thin Films. *Phys. Rev. Lett.* **2000,** *85* (7), 1484-1847.

63.   Payne, M. M.; Parkin, S. R.; Anthony, J. E.; Kuo, C.-c.; Jackson, T. N., Organic Field-Effect Transistors from Solution-Deposited Functionalized Acenes with Mobilities as High as 1 cm2/Vs. *J. Am. Chem. Soc* **2005,** *127*, 4986-4987.

64.   Loo, Y.-L., Solution-Processable Organic Semiconductors for Thin-Film Transistors: Opportunities for Chemical Engineers. *AIChE Journal* **2007,** *53* (5), 1066-1074.

65.   Hailey, A. K.; Petty, A. J.; Washbourne, J.; Thorley, K. J.; Parkin, S. R.; Anthony, J. E.; Loo, Y. L., Understanding the Crystal Packing and Organic Thin-Film Transistor Performance in Isomeric Guest-Host Systems. *Adv. Mater.* **2017,** *29* (23), 170048.

66.   Yu, L.; Li, X.; Pavlica, E.; Koch, F. P. V.; Portale, G.; da Silva, I.; Loth, M. A.; Anthony, J. E.; Smith, P.; Bratina, G.; Kjellander, B. K. C.; Bastiaansen, C. W. M.; Broer, D. J.; Gelinck, G. H.; Stingelin, N., Influence of Solid-State Microstructure on the Electronic Performance of 5,11-Bis(triethylsilylethynyl) Anthradithiophene. *Chem. Mater.* **2013,** *25* (9), 1823-1828.

Chapter 4 References

1.   Bolognesi, B.; Lorenzo Gotor, N.; Dhar, R.; Cirillo, D.; Baldrighi, M.; Tartaglia, G. G.; Lehner, B., A Concentration-Dependent Liquid Phase Separation Can Cause Toxicity upon Increased Protein Expression. *Cell Reports* **2016,** *16* (1), 222-231.

2.   Yadegari, A.; Fahimipour, F.; Rasoulianboroujeni, M.; Dashtimoghadarm, E.; Omidi, M.; Golzar, H.; Tahriri, M.; Tayebi, L., 10 - Specific considerations in scaffold design for oral tissue engineering. In *Biomaterials for Oral and Dental Tissue Engineering*, Tayebi, L.; Moharamzadeh, K., Eds. Woodhead Publishing: 2017; pp 157-183.

3.   Lee, K.-Y.; Blaker, J. J.; Heng, J. Y. Y.; Murakami, R.; Bismarck, A., pH-triggered phase inversion and separation of hydrophobised bacterial cellulose stabilised Pickering emulsions. *Reactive and Functional Polymers* **2014,** *85*, 208-213.

4.   Baghaban-Eslaminejad, M.; Oryan, A.; Kamali, A.; Moshiri, A., Chapter 25 - The role of nanomedicine, nanotechnology, and nanostructures on oral bone healing, modeling, and remodeling. In *Nanostructures for Oral Medicine*, Andronescu, E.; Grumezescu, A. M., Eds. Elsevier: 2017; pp 777-832.

5.   Banani, S. F.; Lee, H. O.; Hyman, A. A.; Rosen, M. K., Biomolecular condensates: organizers of cellular biochemistry. *Nature Reviews Molecular Cell Biology* **2017,** *18* (5), 285-298.

6.   Isono, Y.; Nakajima, M., Membrane Phase Separation of Aqueous/Alcohol Biphase Mixture and Its Application for Enzyme Bioreactor. In *Progress in Biotechnology*, Endo, I.; Nagamune, T.; Katoh, S.; Yonemoto, T., Eds. Elsevier: 2000; Vol. 16, pp 63-68.

7.   Cardon, L. K.; Ragaert, K. J.; De Santis, R.; Gloria, A., 2 - Design and fabrication methods for biocomposites. In *Biomedical Composites (Second Edition)*, Ambrosio, L., Ed. Woodhead Publishing: 2017; pp 17-36.

8.   Indulkar, A. S.; Gao, Y.; Raina, S. A.; Zhang, G. G. Z.; Taylor, L. S., Exploiting the Phenomenon of Liquid–Liquid Phase Separation for Enhanced and Sustained Membrane Transport of a Poorly Water-Soluble Drug. *Molecular Pharmaceutics* **2016,** *13* (6), 2059-2069.

9.   Halls, J. J. M.; Walsh, C. A.; Greenham, N. C.; Marseglia, E. A.; Friend, R. H.; Moratti, S. C.; Holmes, A. B., Efficient photodiodes from interpenetrating polymer networks. *Nature* **1995,** *376*, 498.

10.   Yu, G.; J.Gao; C.Hummelen, J.; Wudl, F.; Heeger, A. J., Ploymer Photovoltaic Cells: Enhanced Efficiencies via a Network of Internal Donor-Acceptor Heterojunctions. *Science* **1995,** *270*, 1789.

11.   Peet, J.; Kim, J. Y.; Coates, N. E.; Ma, W. L.; Moses, D.; Heeger, A. J.; Bazan, G. C., Efficiency enhancement in low-bandgap polymer solar cells by processing with alkane dithiols. *Nature materials* **2007,** *6* (7), 497-500.

12.   Yao, Y.; Hou, J.; Xu, Z.; Li, G.; Yang, Y., Effects of Solvent Mixtures on the Nanoscale Phase Separation in Polymer Solar Cells. *Advanced Functional Materials* **2008,** *18* (12), 1783-1789.

13.   Liu, J.; Walker, B.; Tamayo, A.; Zhang, Y.; Nguyen, T.-Q., Effects of Heteroatom Substitutions on the Crystal Structure, Film Formation, and Optoelectronic Properties of Diketopyrrolopyrrole-Based Materials. *Adv. Funct. Mater.* **2013,** *23* (1), 47-56.

14.   Liao, H.-C.; Ho, C.-C.; Chang, C.-Y.; Jao, M.-H.; Darling, S. B.; Su, W.-F., Additives for morphology control in high-efficiency organic solar cells. *Materials Today* **2013,** *16* (9), 326-336.

15.   Perez, L. A.; Rogers, J. T.; Brady, M. A.; Sun, Y.; Welch, G. C.; Schmidt, K.; Toney, M. F.; Jinnai, H.; Heeger, A. J.; Chabinyc, M. L.; Bazan, G. C.; Kramer, E. J., The Role of Solvent Additive Processing in High Performance Small Molecule Solar Cells. *Chemistry of Materials* **2014,** *26* (22), 6531-6541.

16.   Kwon, S.; Kang, H.; Lee, J.-H.; Lee, J.; Hong, S.; Kim, H.; Lee, K., Effect of Processing Additives on Organic Photovoltaics: Recent Progress and Future Prospects. *Advanced Energy Materials* **2017,** *7* (10), 1601496.

17.   Zhao, W.; Zhang, S.; Zhang, Y.; Li, S.; Liu, X.; He, C.; Zheng, Z.; Hou, J., Environmentally Friendly Solvent-Processed Organic Solar Cells that are Highly Efficient and Adaptable for the Blade-Coating Method. *Adv Mater* **2018,** *30* (4).

18.   Zhao, W.; Ye, L.; Zhang, S.; Sun, M.; Hou, J., A universal halogen-free solvent system for highly efficient polymer solar cells. *Journal of Materials Chemistry A* **2015,** *3* (24), 12723-12729.

19.   Zhao, J.; Li, Y.; Yang, G.; Jiang, K.; Lin, H.; Ade, H.; Ma, W.; Yan, H., Efficient organic solar cells processed from hydrocarbon solvents. *Nature Energy* **2016,** *1* (2).

20.   Zhang, Y.; Voth, G. A., Combined Metadynamics and Umbrella Sampling Method for the Calculation of Ion Permeation Free Energy Profiles. *Journal of Chemical Theory and Computation* **2011,** *7* (7), 2277-2283.

21.   Widom, B., Some Topics in the Theory of Fluids. *The Journal of Chemical Physics* **1963,** *39* (11), 2808-2812.

22.   Kofke, D. A., Gibbs-Duhem integration: a new method for direct evaluation of phase coexistence by molecular simulation. *Molecular Physics* **1993,** *78* (6), 1331-1336.

23.   Lai, P. K.; Hsieh, C. M.; Lin, S. T., Rapid determination of entropy and free energy of mixtures from molecular dynamics simulations with the two-phase thermodynamic model. *Phys Chem Chem Phys* **2012,** *14* (43), 15206-13.

24.   Pascal, T. A.; Lin, S. T.; Goddard, W. A., 3rd, Thermodynamics of liquids: standard molar entropies and heat capacities of common solvents from 2PT molecular dynamics. *Phys Chem Chem Phys* **2011,** *13* (1), 169-81.

25.   Zhang, H.; Duquesne, M.; Godin, A.; Niedermaier, S.; Palomo del Barrio, E.; Nedea, S. V.; Rindt, C. C. M., Experimental and in silico characterization of xylitol as seasonal heat storage material. *Fluid Phase Equilibria* **2017,** *436*, 55-68.

26.   Minakov, D. V.; Levashov, P. R.; Fokin, V. B., Vibrational spectrum and entropy in simulation of melting. *Computational Materials Science* **2017,** *127*, 42-47.

27.   Vadhana, V.; Ayappa, K. G., Structure and Dynamics of Octamethylcyclotetrasiloxane Confined between Mica Surfaces. *J Phys Chem B* **2016,** *120* (11), 2951-67.

28.   Lim, H. K.; Lee, H.; Kim, H., A Seamless Grid-Based Interface for Mean-Field QM/MM Coupled with Efficient Solvation Free Energy Calculations. *J Chem Theory Comput* **2016,** *12* (10), 5088-5099.

29.   Caro, M. A.; Laurila, T.; Lopez-Acevedo, O., Accurate schemes for calculation of thermodynamic properties of liquid mixtures from molecular dynamics simulations. *J Chem Phys* **2016,** *145* (24), 244504.

30.   Wang, J.; Chakraborty, B.; Eapen, J., Absolute thermodynamic properties of molten salts using the two-phase thermodynamic (2PT) superpositioning method. *Phys Chem Chem Phys* **2014,** *16* (7), 3062-9.

31.   Pascal, T. A.; Goddard, W. A., 3rd, Interfacial thermodynamics of water and six other liquid solvents. *J Phys Chem B* **2014,** *118* (22), 5943-56.

32.   Lai, P.-K.; Lin, S.-T., Rapid determination of entropy for flexible molecules in condensed phase from the two-phase thermodynamic model. *RSC Advances* **2014,** *4* (19).

33.   Chen, M.; Pendrill, R.; Widmalm, G.; Brady, J. W.; Wohlert, J., Molecular Dynamics Simulations of the Ionic Liquid 1-n-Butyl-3-Methylimidazolium Chloride and Its Binary Mixtures with Ethanol. *J Chem Theory Comput* **2014,** *10* (10), 4465-79.

34.   Li, C.; Medvedev, G. A.; Lee, E.-W.; Kim, J.; Caruthers, J. M.; Strachan, A., Molecular dynamics simulations and experimental studies of the thermomechanical response of an epoxy thermoset polymer. *Polymer* **2012,** *53* (19), 4222-4230.

35.   Jeon, J.; Kim, H.; Goddard, W. A., 3rd; Pascal, T. A.; Lee, G. I.; Kang, J. K., The Role of Confined Water in Ionic Liquid Electrolytes for Dye-Sensitized Solar Cells. *J Phys Chem Lett* **2012,** *3* (4), 556-9.

36.   Caleman, C.; van Maaren, P. J.; Hong, M.; Hub, J. S.; Costa, L. T.; van der Spoel, D., Force Field Benchmark of Organic Liquids: Density, Enthalpy of Vaporization, Heat Capacities, Surface Tension, Isothermal Compressibility, Volumetric Expansion Coefficient, and Dielectric Constant. *J Chem Theory Comput* **2012,** *8* (1), 61-74.

37.   Pascal, T. A.; He, Y.; Jiang, S.; Goddard, W. A., Thermodynamics of Water Stabilization of Carboxybetaine Hydrogels from Molecular Dynamics Simulations. *The Journal of Physical Chemistry Letters* **2011,** *2* (14), 1757-1760.

38.   Huang, S. N.; Pascal, T. A.; Goddard, W. A., 3rd; Maiti, P. K.; Lin, S. T., Absolute Entropy and Energy of Carbon Dioxide Using the Two-Phase Thermodynamic Model. *J Chem Theory Comput* **2011,** *7* (6), 1893-901.

39.   Lin, S.-T.; Blanco, M.; Goddard, W. A., The two-phase model for calculating thermodynamic properties of liquids from molecular dynamics: Validation for the phase diagram of Lennard-Jones fluids. *The Journal of Chemical Physics* **2003,** *119* (22), 11792-11805.

40.   Berens, P. H.; Mackay, D. H. J.; White, G. M.; Wilson, K. R., Thermodynamics and quantum corrections from molecular dynamics for liquid water. *The Journal of Chemical Physics* **1983,** *79* (5), 2375-2389.

41.   Zhao, J.; Li, Y.; Yang, G.; Jiang, K.; Lin, H.; Ade, H.; Ma, W.; Yan, H., Efficient organic solar cells processed from hydrocarbon solvents. *Nature Energy* **2016,** *1* (2), 15027.

42.   Berendsen, H. J. C.; van der Spoel, D.; van Drunen, R., GROMACS: A message-passing parallel molecular dynamics implementation. *Computer Physics Communications* **1995,** *91* (1), 43-56.

43.   Abraham, M. J.; Spoel, D. v. d.; Lindahl, E.; Hess, B.; team, t. G. d., *GROMACS User Manual version 5.0.5*. 2015.

44.   M. J. Frisch, G. W. T., H. B. Schlegel, G. E. Scuseria, M. A. Robb, J. R. Cheeseman, G. Scalmani, V. Barone, G. A. Petersson, H. Nakatsuji, X. Li, M. Caricato, A. Marenich, J. Bloino, B. G. Janesko, R. Gomperts, B. Mennucci, H. P. Hratchian, J. V. Ortiz, A. F. Izmaylov, J. L. Sonnenberg, D. Williams-Young, F. Ding, F. Lipparini, F. Egidi, J. Goings, B. Peng, A. Petrone, T. Henderson, D. Ranasinghe, V. G. Zakrzewski, J. Gao, N. Rega, G.

Zheng, W. Liang, M. Hada, M. Ehara, K. Toyota, R. Fukuda, J. Hasegawa, M. Ishida, T. Nakajima, Y. Honda, O. Kitao, H. Nakai, T. Vreven, K. Throssell, J. A. Montgomery, Jr., J. E. Peralta, F. Ogliaro, M. Bearpark, J. J. Heyd, E. Brothers, K. N. Kudin, V. N. Staroverov, T. Keith, R. Kobayashi, J. Normand, K. Raghavachari, A. Rendell, J. C. Burant, S. S. Iyengar, J. Tomasi, M. Cossi, J. M. Millam, M. Klene, C. Adamo, R. Cammi, J. W. Ochterski, R. L. Martin, K. Morokuma, O. Farkas, J. B. Foresman, and D. J. Fox *Gaussian 09, Revision A.02*, Gaussian, Inc.: Wallingford CT, 2016.

45.   Marenich, A. V.; Jerome, S. V.; Cramer, C. J.; Truhlar, D. G., Charge Model 5: An Extension of Hirshfeld Population Analysis for the Accurate Description of Molecular Interactions in Gaseous and Condensed Phases. *Journal of Chemical Theory and Computation* **2012,** *8* (2), 527-541.

46.   Plimpton, S., Fast Parallel Algorithms for Short-Range Molecular Dynamics. *Journal of Computational Physics* **1995,** *117* (1), 1-19.

47.   Henk Bekker, H. B., Ej Dijkstra, S. Achterop, R Vondrumen, D Vanderspoel, A. M. Sijbers, H Keegstra, Mkr Renardus, Gromacs: A parallel computer for molecular dynamics simulations. In *Physics Computing '92*, RA DeGroot, J. N., Ed. World Scientific Publishing: Singapore, 1993; p 5.

48.   Berendsen, H. J. C.; Postma, J. P. M.; Gunsteren, W. F. v.; DiNola, A.; Haak, J. R., Molecular dynamics with coupling to an external bath. *The Journal of Chemical Physics* **1984,** *81* (8), 3684-3690.

49.   Parrinello, M.; Rahman, A., Polymorphic transitions in single crystals: A new molecular dynamics method. *Journal of Applied Physics* **1981,** *52* (12), 7182-7190.

50.   Humphrey, W.; Dalke, A.; Schulten, K., VMD: Visual molecular dynamics. *Journal of Molecular Graphics* **1996,** *14* (1), 33-38.

51.   Bennett, C. H., Efficient estimation of free energy differences from Monte Carlo data. *Journal of Computational Physics* **1976,** *22* (2), 245-268.

52.   Ben‑Naim, A.; Marcus, Y., Solvation thermodynamics of nonionic solutes. *The Journal of Chemical Physics* **1984,** *81* (4), 2016-2027.

53.   Stryland, W. V. W. J. C., Density measurements of compressed solid and liquid argon. *Canadian Journal of Physiscs* **1968,** *46*, 811.

54.   Gedde, U. W., *Ploymer Physics*. Springer Netherlands: United Kingdom, 1995.

55.   Jorgensen, W. L.; Schyman, P., Treatment of Halogen Bonding in the OPLS-AA Force Field; Application to Potent Anti-HIV Agents. *Journal of chemical theory and computation* **2012,** *8* (10), 3895-3801.

56.   Pascal, T. A.; Goddard, W. A., Hydrophobic Segregation, Phase Transitions and the Anomalous Thermodynamics of Water/Methanol Mixtures. *The Journal of Physical Chemistry B* **2012,** *116* (47), 13905-13912.

57.   Belmares, M.; Blanco, M.; Goddard, W. A., 3rd; Ross, R. B.; Caldwell, G.; Chou, S. H.; Pham, J.; Olofson, P. M.; Thomas, C., Hildebrand and Hansen solubility parameters from molecular dynamics with applications to electronic nose polymer sensors. *J Comput Chem* **2004,** *25* (15), 1814-26.

58.   Machui, F.; Abbott, S.; Waller, D.; Koppe, M.; Brabec, C. J., Determination of Solubility Parameters for Organic Semiconductor Formulations. *Macromolecular Chemistry and Physics* **2011,** *212* (19), 2159-2165.

59.   Hansen, C. M., *Hansen Solubility Parameters (A User's Handbook)*. 2 ed.; CRC Press: 2007.

60.   Zhao, J.; Li, Y.; Yang, G.; Jiang, K.; Lin, H.; Ade, H.; Ma, W.; Yan, H., Efficient organic solar cells processed from hydrocarbon solvents. *Nature Energy* **2016,** *1*, 15027.

Chapter 5 References

1.   Payne, M. M.; Parkin, S. R.; Anthony, J. E., Functionalized Higher Acenes: Hexacene and Heptacene. *Journal of the American Chemical Society* **2005,** *127* (22), 8028-8029.
2.   Mei, J.; Bao, Z., Side Chain Engineering in Solution-Processable Conjugated Polymers. *Chemistry of Materials* **2014,** *26* (1), 604-615.
3.   Tumbleston, J. R.; Yang, L.; You, W.; Ade, H., Morphology linked to miscibility in highly amorphous semi-conducting polymer/fullerene blends. *Polymer* **2014,** *55* (19), 4884-4889.
4.   Guo, Z.-H.; Ai, N.; McBroom, C. R.; Yuan, T.; Lin, Y.-H.; Roders, M.; Zhu, C.; Ayzner, A. L.; Pei, J.; Fang, L., A side-chain engineering approach to solvent-resistant semiconducting polymer thin films. *Polymer Chemistry* **2016,** *7* (3), 648-655.
5.   Zhang, W.; Mao, Z.; Zheng, N.; Zou, J.; Wang, L.; Wei, C.; Huang, J.; Gao, D.; Yu, G., Highly planar cross-conjugated alternating polymers with multiple conformational locks: synthesis, characterization and their field-effect properties. *Journal of Materials Chemistry C* **2016,** *4* (39), 9266-9275.
6.   Zhu, C.; Mu, A. U.; Lin, Y.-H.; Guo, Z.-H.; Yuan, T.; Wheeler, S. E.; Fang, L., Molecular Coplanarity and Self-Assembly Promoted by Intramolecular Hydrogen Bonds. *Organic Letters* **2016,** *18* (24), 6332-6335.
7.   Huang, H.; Yang, L.; Facchetti, A.; Marks, T. J., Organic and Polymeric Semiconductors Enhanced by Noncovalent Conformational Locks. *Chemical Reviews* **2017,** *117* (15), 10291-10318.
8.   Dickey, K. C.; Anthony, J. E.; Loo, Y.-L., Improving Organic Thin-Film Transistor Performance through Solvent-Vapor Annealing of Solution-Processable Triethylsilylethynyl Anthradithiophene. *Advanced materials* **2006,** *18* (13), 1721-1726.
9.   Dickey, K. C.; Smith, T. J.; Stevenson, K. J.; Subramanian, S.; Anthony, J. E.; Loo, Y.-L., Establishing Efficient Electrical Contact to the Weak Crystals of Triethylsilylethynyl Anthradithiophene. *Chemistry of Materials* **2007,** *19* (22), 5210-5215.
10.   Dickey, K. C.; Subramanian, S.; Anthony, J. E.; Han, L.-H.; Chen, S.; Loo, Y.-L., Large-area patterning of a solution-processable organic semiconductor to reduce parasitic leakage and off currents in thin-film transistors. *Applied Physics Letters* **2007,** *90* (24), 244103.
11.   McDowell, C.; Narayanaswamy, K.; Yadagiri, B.; Gayathri, T.; Seifrid, M.; Datt, R.; Ryno, Sean M.; Heifner, M. C.; Gupta, V.; Risko, C.; Singh, S. P.; Bazan, G. C., Impact of rotamer diversity on the self-assembly of nearly isostructural molecular semiconductors. *Journal of Materials Chemistry A* **2018,** *6* (2), 383-394.
12.   Perez, L. A.; Chou, K. W.; Love, J. A.; van der Poll, T. S.; Smilgies, D.-M.; Nguyen, T.-Q.; Kramer, E. J.; Amassian, A.; Bazan, G. C., Solvent Additive Effects on Small Molecule Crystallization in Bulk Heterojunction Solar Cells Probed During Spin Casting. *Advanced materials* **2013,** *25* (44), 6380-6384.
13.   Giri, G.; Verploegen, E.; Mannsfeld, S. C. B.; Atahan-Evrenk, S.; Kim, D. H.; Lee, S. Y.; Becerril, H. A.; Aspuru-Guzik, A.; Toney, M. F.; Bao, Z., Tuning charge transport in solution-sheared organic semiconductors using lattice strain. *Nature* **2011,** *480* (7378), 504-508.

14.   Lee, S. S.; Kim, C. S.; Gomez, E. D.; Purushothaman, B.; Toney, M. F.; Wang, C.; Hexemer, A.; Anthony, J. E.; Loo, Y.-L., Controlling Nucleation and Crystallization in Solution-Processed Organic Semiconductors for Thin-Film Transistors. *Advanced materials* **2009,** *21* (35), 3605-3609.

15.   Lee, S. S.; Loth, M. A.; Anthony, J. E.; Loo, Y.-L., Orientation-Independent Charge Transport in Single Spherulites from Solution-Processed Organic Semiconductors. *Journal of the American Chemical Society* **2012,** *134* (12), 5436-5439.

16.   Li, R.; Khan, H. U.; Payne, M. M.; Smilgies, D.-M.; Anthony, J. E.; Amassian, A., Heterogeneous Nucleation Promotes Carrier Transport in Solution-Processed Organic Field-Effect Transistors. *Advanced Functional Materials* **2013,** *23* (3), 291-297.

17.   Giri, G.; Li, R.; Smilgies, D.-M.; Li, E. Q.; Diao, Y.; Lenn, K. M.; Chiu, M.; Lin, D. W.; Allen, R.; Reinspach, J.; Mannsfeld, S. C. B.; Thoroddsen, S. T.; Clancy, P.; Bao, Z.; Amassian, A., One-dimensional self-confinement promotes polymorph selection in large-area organic semiconductor thin films. *Nature communications* **2014,** *5* (1), 3573.

18.   Niazi, M. R.; Li, R.; Qiang Li, E.; Kirmani, A. R.; Abdelsamie, M.; Wang, Q.; Pan, W.; Payne, M. M.; Anthony, J. E.; Smilgies, D.-M.; Thoroddsen, S. T.; Giannelis, E. P.; Amassian, A., Solution-printed organic semiconductor blends exhibiting transport properties on par with single crystals. *Nature communications* **2015,** *6* (1), 8598.

19.   Henk Bekker, H. B., Ej Dijkstra, S. Achterop, R Vondrumen, D Vanderspoel, A. M. Sijbers, H Keegstra, Mkr Renardus, Gromacs: A parallel computer for molecular dynamics simulations. In *Physics Computing '92*, RA DeGroot, J. N., Ed. World Scientific Publishing: Singapore, 1993; p 5.

20.   Hess, B.; Kutzner, C.; van der Spoel, D.; Lindahl, E., GROMACS 4: Algorithms for Highly Efficient, Load-Balanced, and Scalable Molecular Simulation. *Journal of Chemical Theory and Computation* **2008,** *4* (3), 435-447.

21.   Bernardes, C. E.; Joseph, A., Evaluation of the OPLS-AA force field for the study of structural and energetic aspects of molecular organic crystals. *The journal of physical chemistry. A* **2015,** *119* (12), 3023-3034.

22.   William L. Jorgensen, D. S. M., Julian Tirado-Rives, Development and Testing of the OPLS All-Atom Force Field on Conformational Energetics and Properties of Organic Liquids. *J. Am. Chem. Soc* **1996,** *118*, 11225-11236.

Chapter 6 References

1.   Andrés Castán, J. M.; Abad Galán, L.; Li, S.; Dalinot, C.; Simón Marqués, P.; Allain, M.; Risko, C.; Monnereau, C.; Maury, O.; Blanchard, P.; Cabanetos, C., Nitration of benzothioxanthene: towards a new class of dyes with versatile photophysical properties. *New Journal of Chemistry* **2020,** *44* (3), 900-905.

2.   Josse, P.; Li, S.; Dayneko, S.; Joly, D.; Labrunie, A.; Dabos-Seignon, S.; Allain, M.; Siegler, B.; Demadrille, R.; Welch, G. C.; Risko, C.; Blanchard, P.; Cabanetos, C., Bromination of the benzothioxanthene Bloc: toward new π-conjugated systems for organic electronic applications. *Journal of Materials Chemistry C* **2018,** *6* (4), 761-766.

3.   Payne, A.-J.; Li, S.; Dayneko, S. V.; Risko, C.; Welch, G. C., An unsymmetrical non-fullerene acceptor: synthesis via direct heteroarylation, self-assembly, and utility as a low energy absorber in organic photovoltaic cells. *Chemical communications* **2017,** *53* (73), 10168-10171.

4.   Payne, A.-J.; Rice, N. A.; McAfee, S. M.; Li, S.; Josse, P.; Cabanetos, C.; Risko, C.; Lessard, B. H.; Welch, G. C., Donor or Acceptor? How Selection of the Rylene Imide End Cap Impacts the Polarity of π-Conjugated Molecules for Organic Electronics. *ACS Applied Energy Materials* **2018,** *1* (9), 4906-4916.

5.   M. J. Frisch, G. W. T., H. B. Schlegel, G. E. Scuseria, M. A. Robb, J. R. Cheeseman, G. Scalmani, V. Barone, G. A. Petersson, H. Nakatsuji, X. Li, M. Caricato, A. Marenich, J. Bloino, B. G. Janesko, R. Gomperts, B. Mennucci, H. P. Hratchian, J. V. Ortiz, A. F. Izmaylov, J. L. Sonnenberg, D. Williams-Young, F. Ding, F. Lipparini, F. Egidi, J. Goings, B. Peng, A. Petrone, T. Henderson, D. Ranasinghe, V. G. Zakrzewski, J. Gao, N. Rega, G. Zheng, W. Liang, M. Hada, M. Ehara, K. Toyota, R. Fukuda, J. Hasegawa, M. Ishida, T. Nakajima, Y. Honda, O. Kitao, H. Nakai, T. Vreven, K. Throssell, J. A. Montgomery, Jr., J. E. Peralta, F. Ogliaro, M. Bearpark, J. J. Heyd, E. Brothers, K. N. Kudin, V. N. Staroverov, T. Keith, R. Kobayashi, J. Normand, K. Raghavachari, A. Rendell, J. C. Burant, S. S. Iyengar, J. Tomasi, M. Cossi, J. M. Millam, M. Klene, C. Adamo, R. Cammi, J. W. Ochterski, R. L. Martin, K. Morokuma, O. Farkas, J. B. Foresman, and D. J. Fox *Gaussian 09, Revision A.02*, Gaussian, Inc.: Wallingford CT, 2016.

6.   McAfee, S. M.; Dayneko, S. V.; Hendsbee, A. D.; Josse, P.; Blanchard, P.; Cabanetos, C.; Welch, G. C., Applying direct heteroarylation synthesis to evaluate organic dyes as the core component in PDI-based molecular materials for fullerene-free organic solar cells. *Journal of Materials Chemistry A* **2017,** *5* (23), 11623-11633.

7.   Hendsbee, A. D.; Sun, J.-P.; Law, W. K.; Yan, H.; Hill, I. G.; Spasyuk, D. M.; Welch, G. C., Synthesis, Self-Assembly, and Solar Cell Performance of N-Annulated Perylene Diimide Non-Fullerene Acceptors. *Chemistry of Materials* **2016,** *28* (19), 7098-7109.

8.   Payne, A.-J.; Welch, G. C., Optimized synthesis of π-extended squaraine dyes relevant to organic electronics by direct (hetero)arylation and Sonogashira coupling reactions. *Organic & Biomolecular Chemistry* **2017,** *15* (15), 3310-3319.

9.   Zhan, X.; Facchetti, A.; Barlow, S.; Marks, T. J.; Ratner, M. A.; Wasielewski, M. R.; Marder, S. R., Rylene and Related Diimides for Organic Electronics. *Advanced materials* **2011,** *23* (2), 268-284.

10.   Guo, X.; Facchetti, A.; Marks, T. J., Imide- and Amide-Functionalized Polymer Semiconductors. *Chemical Reviews* **2014,** *114* (18), 8943-9021.

11.   Liu, Z.; Zhang, G.; Cai, Z.; Chen, X.; Luo, H.; Li, Y.; Wang, J.; Zhang, D., New Organic Semiconductors with Imide/Amide-Containing Molecular Systems. *Advanced materials* **2014,** *26* (40), 6965-6977.

12.   Balaji, G.; Kale, T. S.; Keerthi, A.; Della Pelle, A. M.; Thayumanavan, S.; Valiyaveettil, S., Low Band Gap Thiophene−Perylene Diimide Systems with Tunable Charge Transport Properties. *Organic Letters* **2011,** *13* (1), 18-21.

13.   Li, C.; Wonneberger, H., Perylene Imides for Organic Photovoltaics: Yesterday, Today, and Tomorrow. *Advanced materials* **2012,** *24* (5), 613-636.

14.   Chen, L.; Li, C.; Müllen, K., Beyond perylene diimides: synthesis, assembly and function of higher rylene chromophores. *Journal of Materials Chemistry C* **2014,** *2* (11), 1938-1956.

15.   Würthner, F.; Saha-Möller, C. R.; Fimmel, B.; Ogi, S.; Leowanawat, P.; Schmidt, D., Perylene Bisimide Dye Assemblies as Archetype Functional Supramolecular Materials. *Chemical Reviews* **2016,** *116* (3), 962-1052.

16.   Andrés Castán, J. M.; Abad Galán, L.; Li, S.; Dalinot, C.; Simón Marqués, P.; Allain, M.; Risko, C.; Monnereau, C.; Maury, O.; Blanchard, P.; Cabanetos, C., Nitration of benzothioxanthene: towards a new class of dyes with versatile photophysical properties. *New Journal of Chemistry* **2020**.

17.   Kan, B.; Zhang, Q.; Li, M.; Wan, X.; Ni, W.; Long, G.; Wang, Y.; Yang, X.; Feng, H.; Chen, Y., Solution-Processed Organic Solar Cells Based on Dialkylthiol-Substituted Benzodithiophene Unit with Efficiency near 10%. *Journal of the American Chemical Society* **2014,** *136* (44), 15529-15532.

18.   Ryan, J. W.; Matsuo, Y., Increased Efficiency in Small Molecule Organic Solar Cells Through the Use of a 56-π Electron Acceptor – Methano Indene Fullerene. *Scientific Reports* **2015,** *5* (1), 8319.

VITA

Place of birth

Benxi, Liaoning, China

Education

B.S. Tianjin University, Tianjin, China, 2006

M.S. Tianjin University, Tianjin, China, 2010

Ph. D. University of Kentucky, Lexington, KY, 2020 (expected)

Publications

1. Shi Li, Balaji Sesha Sarath Pokur, Sean M. Ryno, Asare Nkansah, Camron De'vine, Baskar Ganapathysubramanian and Chad Risko. Determination of the Free Energies of Mixing of Organic Solutions through a Combined Molecular Dynamics and Bayesian Statistics Approach. *Journal of Chemical Information and Modeling.* Accepted. Jan. 2020. DOI: 10.1021/acs.jcim/9b01113

2. José María Andres Castan, Laura Abad Galán, Shi Li, Clément Dalinot, Pablo Simon Marques, Magali Allain, Chad Risko, Cyrille Monnereau, Olivier Maury, Philippe Blanchard and Clement Cabanetos. Nitration of the Benzothioxanthene: Towards a New Class of Dyes with Versatile Photophyscial Properties. *New Journal of Chemistry*, 2020. DOI: 10.1039/C9NJ05804D

3. Shi Li, Sean M. Ryno, Chad Risko. Exploring Thermal Transitions in Anthradithiophene-based Organic Semiconductors to Reveal Structure-Packing Relationships. *Journal of Material Chemistry C* (2018) 6, 10924-10934. DOI: 10.1039/C8TC03976C

4. Abby-Jo Payne, Nicole A. Rice, Seth M. McAfee, Shi Li, Pierre Josse, Clément Cabanetos, Chad Risko, Benoît H. Lessard, Gregory C. Welch. Donor or Acceptor? How Selection of the Rylene Imide End Cap Impacts the Polarity of π-Conjugated Molecules for Organic Electronics. *ACS Applied Energy Materials* (2018) 1, 9, 4906-4916. DOI: 10.1021/acsaem.8b00929

5. Pierre Josse, Shi Li, Sergey Dayneko, Damien Joly, Antoine Labrunie, Sylvie Dabos-Seignon, Magali Allain, Benjamin Siegler, Renaud Demadrille, Gregory C. Welch, Chad Risko, Philippe Blanchard and Clément Cabanetos. Bromination of the Benzothioxanthene Bloc: Toward New π-conjugated Systems for Organic Electronic Applications. *Journal of Material Chemistry C* (2018) 6, 761-766. DOI: 10.1039/C7TC05245F

6. Abby-Jo Payne, Shi Li, Sergey V. Dayneko, Chad Risko and Gregory C. Welch. An Unsymmetrical Non-Fullerene Acceptor: Synthesis via Direct Heteroarylation, Self-assembly, and Utility as a Low Energy Absorber in Organic Photovoltaic Cells. *Chemical Communications* (2017) 53, 10168-10171. DOI: 10.1039/C7CC90360J

Shi Li